An investigation of dielectric tunable materials for microwave tunable devices

Li Xiao, Beng

Thesis submitted to the University of Nottingham for the degree of Doctor of Philosophy

May 2011

Abstract

Today, many of the communication systems are operated in several different bandwidths. Till now, the common solution to get a multi bandwidth transmitter/receiver is to insert several fixed microwave devices with different bandwidth to the required standard. This increases the size and power consumption of trans/receiver. One solution is to develop electronically tunable microwave devices. By replacing several fixed microwave devices with a single electronically tunable device, the size and power consumptions of the transmitter/receiver can be significantly reduced.

The tunable devices are usually implemented by high permittivity tunable materials that exhibit a change of dielectric constant with respect to a DC electric field. In this work, two different types of tunable materials: ferroelectric Barium Strontium Titanate (BST) Oxide and pyrochloe Bismuth Zinc Niobate Oxide (BZN) thin films are investigated. A simple and cost effective chemical solution deposition (CSD) method has been used to prepare the thin films. In addition, two different types of microwave devices (coplanar waveguide and metal insulated metal capacitors) were fabricated to measure the microwave dielectric properties of BST and BZN thin films. The maximum errors in the measured dielectric constants are 24% due to the calibration errors.

To improve the dielectric properties of BST thin films, acceptor ions such as lithium (Li) and cobalt (Co) were doped into BST thin films. According to the measured results, the Li doped BST thin film exhibits an increase of dielectric constant and a decrease of dielectric loss, which makes it highly attractive for implementing microwave device. In contrast, the BZN thin films exhibit little dielectric tunability (3.0%) even when a large DC electric field (500kV/cm) is applied. These results demonstrate that ferroelectric BST thin films are still the only practical materials for implementing tunable microwave devices due to its high tunability.

Publications

Journals:

1. L. Xiao, K. L. Choy and I. Harrison, "Co doped BST thin films for tunable microwave applications", *Journal of surface coating technique,* vol. 205, 8-9,2989-2993, 2011.

Conference paper:

1. L. Xiao, K. L. Choy and I. Harrison, —Ferroelectric thin film for microwave devices", *International Workshop on Advanced Nanostructured materials and Thin Films for Industrial Applications,* Nottingham, UK, 10-13 November.

Acknowledgements

During the research period, I have been supported by many people. Firstly, I have to give my thanks to my principal supervisor, Dr Ian Harrison. He has given a great deal of support and useful advice on the characterization of materials. In addition, I would like to thank to Professor Kewang-Leong Choy for her supervision and advice on material synthesis.

Also I like to gratefully acknowledge the Faculty of Engineering of Nottingham University for the award of an interdisciplinary scholarship. I am very pleasant for the environment and facilities provided by the University of Nottingham.

Meanwhile, I would like to thanks to the following people who have given me very useful assistance on the synthesis and characterization of the materials, Mr Rod Dykeman, Dr Steve Bull, Dr Jingwang Yan, Dr Xianghui Hou, Dr Malcolm Woolfson and Dr Peiliang Dong. Finally I have to thank to my parents for their financial support, love and understanding. Without the help from these people, I would not be able to complete my research works.

Chapter 1: Introduction

1.1 Motivation

Over the past few decades, there has been rapid growth in microwave communication and radar systems. For example, mobile phones, GPS and WLAN are widely used around the world. Traditionally microwave systems are fabricated by implementing several separated microwave devices on a PCB, which increases the size and cost of the system. Because many of the microwave communication systems are sold in huge quantities, it is important to lower the manufacturing cost and size of the microwave devices.

In the past few decades, the development of semiconductor technology had led to enormous miniaturization of "microwave devices"[1]. However, a bigger challenge is the miniaturization of "passive microwave devices" such as filters, matching networks, and phase shifters. Passive microwave devices are usually implemented by using ceramic materials with very high dielectric constant [1]. The dimensions of passive devices are inversely related to the dielectric constant of the dielectric material. The desired features for implementation in microwave devices are high dielectric constant, low temperature coefficient of capacitance (TTC) and low loss [1].

Much effort has been directed towards developing high permittivity ferroelectric materials with dielectric constant $\varepsilon_r > 100$ and very low dielectric loss [2, 3]. For a very long time, Barium Strontium Titanate (BST) [4-7] is the most interesting material for implementing "tunable microwave devices", since it has a high dielectric constant (ε_r=300-800 [8]) that can be tuned by applying an electric field, and has relatively low loss at microwave frequencies.

In microwave systems, several fixed passive devices can be replaced by a single tunable device with lower cost and smaller size. For example, a frequency agile filter with tunable bandwidth [9] can replace several traditional filters with fixed bandwidth. Another example is in radar systems where tunable phase shifters made from BST thin films are used in phased array antennas to produce electromagnetic beam scanning [10]. Bulky and expensive mechanical devices are then not required to steer the antenna which saves space and power consumption of the radar system.

More recently, the trend of the development is to integrate the separated microwave devices into a single monolithic microwave integrated circuit (MMIC) which saves a lot of space and lowers the overall cost [1]. This leads to a further reduction in manufacturing cost and saves physical space. However, it is also important to point out that the properties of BST thin films are heavily influenced by the substrate-induced strain, film thickness, microstructure features, charge defects and other deposition parameters [7, 11-13]. Acceptor ion doping [7] is a popular way to improve the dielectric properties of the BST thin film. In the present work, acceptor ions including lithium (Li) and cobalt (Co) were doped into BST thin films and their dielectric properties were measured. According to the measured results, the possible applications for Li and Co doped BST thin films are also presented.

Another problem for the ferroelectric BST is that the desired deposition parameters (high annealing temperature, high resistive substrate materials and high oxygen pressure) of BST thin films are usually not compatible with the manufacturing process of microchips (MMICs). Thus, the performance of a BST thin film could be compromised if it has been integrated into a microchip.

To overcome these difficulties, a novel pyrochlore Bismuth Zinc Niobate (BZN) was developed. BZN is a pyrochlore structure material which exhibits a relatively high permittivity (ε_r=150 to 180 for cubic pyrochlore phase BZN) [14, 15] and a change of dielectric constant under electric field. Although this class of material was

discovered nearly 30 years ago **[14, 16]**, the possibility of implementing passive microwave devices based on BZN material was only reported several years ago **[17,18]**. BZN thin film properties are relatively independent of strain induced by the substrate **[19]**, and BZN has a low firing temperature (when a pulse KrF excimer laser was used to anneal the thin film) **[20]**. Furthermore, it has a modest temperature coefficient of capacitance (TTC =150 ppm/°C or -400 ppm/°C) **[20]** which can be tuned to zero. These features have allowed BZN thin films to be easily integrated into a microchip.

1.2 Thesis aims and outline

The work described in this thesis has two main purposes: (a) To improve dielectric properties of BST thin films. As mentioned earlier, the dielectric properties of BST can be affected by many factors such as substrate materials, strain, film thickness, etc. Therefore, it is important to understand the relationship between the physical properties and dielectric properties of BST, in order to optimise the overall performance of a BST thin film. In this work, BST thin films were doped with lithium (Li) and cobalt (Co) ions to improve their dielectric properties. The corresponding physical and dielectric properties have been investigated. (b) To investigate the potential of implementing microwave devices based on BZN thin films. Although BZN's dielectric properties are independent of the substrate materials, its dielectric properties at microwave frequencies are relatively unknown. Hence, it is still worthy to study its microwave dielectric properties.

Chapter 1 provides the motivations for this thesis. The potential applications of tunable BST materials are presented and the problems of this material, which has limited the use of BST, are also discussed. Meanwhile, an alternative tunable material

(pyrochlore BZN thin film) has also been proposed. The main advantages of BZN thin films over ferroelectric BST are discussed.

Chapter 2 provides an overview of ferroelectric BST and pyrochlore BZN thin films. The important physical and dielectric properties of these materials are presented. At the same time, the methods for improving the dielectric properties of BST and BZN films are also discussed.

Chapter 3 discusses the process of synthesizing BST and BZN thin films by using a modified sol gel technique (chelation). This chapter also provides an overview of modern characterization techniques for analyzing the crystal structures and microstructures of BST and BZN thin films.

Chapter 4 describes the procedures for fabricating microwave devices (coplanar waveguide (CPW) and metal insulated metal capacitor (MIM)).

Chapter 5 shows the basic theory of measuring microwave circuits and the methodology of characterizing dielectric thin films at microwave frequencies. In this Chapter, two types of devices (CPW and MIM capacitor) were employed to characterize the thin film's dielectric properties.

Chapter 6 BST thin films are doped with Li and Co ions to achieve lower dielectric loss and smaller leakage currents. The measured microwave results are compared

with the crystal/microstructures of the thin films. The mechanisms for the improvement of dielectric properties are also discussed.

Chapter 7 investigates the BZN thin films in two aspects: annealing temperature dependence and effect of substrate. The microwave dielectric properties of the thin film are co-studied by coplanar waveguide (CPW) and metal insulated metal (MIM) capacitor techniques.

Chapter 8 provides conclusions of the thesis based on the characterized results. A plan for future work is also presented.

References:

[1] W. Wersing, "Microwave ceramics for resonators and filters," *Solid State and Materials Science,* vol. 1, 715-731, 1996.

[2] N.Setter, D.Damjanovic *et al*,"Ferroelectric thin films: Review of materials, properties, and applications, " *J. Appl. Phys,* vol.100, 051606, 2006.

[3] O. G. Vendik, E. K. Hollmann, A. B. Kozyrev, and A. M. Prudan, "Ferroelectric Tuning of Planar and Bulk Microwave Devices," *Journal of Superconductivity,* vol. 12, No. 2, 1999.

[4] C. Berbecaru. H. V. Alexandru, *et al*, "Oxide ferroelectric (Ba,Sr)TiO3 for microwave devices," *Materials Science and Engineering B,* vol. 109, 152-159, 2004.

[5] C. R. Yang and. W. L. Zhang, W. C. Hu, "Fabrication and characteristics of La, Sc and Sn doped BST thin films by sol-gel method," *J mater Sci: Mater Electron,* vol. 19, 1197-1201, 2008.

[6] J. M. Zhu, X. H Zhu. *et al*, "Recent progress of (Ba,Sr)TiO3 thin films for tunable microwave devices," *Journal of Electronic Materials,* vol. 32, 1125-1133, 2003.

[7] T. J. Jackson. P Bao, X Wang and M. J. Lancaster, "Barium Strontium Titanate thin film varactors for room-temperature microwave device applications," *J. Phys. D: Appl. Phys,* vol. 41, 063001, 2008.

[8] D. Ghosh. J. Nath, J. P Maria, *et al*, "An electronically tunable microstrip bandpass filter using thin film Barium Strontium Titanate (BST) varactor," *IEEE Trans Microwave Theory and Techniques,* vol. 53, 2707-2711, 2005.

[9] M. H. Lim, L. D. Kim, H.G. Kim, *et al*,, "Ferroelectric thin film based electrically tunable band pass filters," *Electrochemical and Solid State Letters,* vol. 5, F25-F28, 2002.

[10] J. T. Bernhard, Frederick W. Van Keuls, *et al*, "K-Band Phased Array Antennas Based on $Ba_{0.6}Sr_{0.4}TiO_3$ Thin-Film Phase Shifters," *IEEE Trans Microwave Theory and Techniques,* vol. 48, 2504-2510, 2000.

[11] W. Chang. and C. M. Gilmore, "Influence of strain on microwave dielectric properties of (Ba,Sr)TiO3 thin films," *J. Appl. Phys,* vol. 87, 3044-3049, 2000.

[12] J.W.Choi. J.Y. Ha, C.Y Kang, *et al*, "Thickness dependent ferroelectric properties of BSTO thin films deposited by RF magnetron sputtering," *J Electroceram,* vol. 17, 141-144, 2006.

[13] S. C. Sun, M. S . Tsai, and T. Y. Tseng, "Effect of oxygen to argon ratio on propeties of (Ba,Sr)TiO3 thin films prepared by radio- frequency magnetron sputtering," *J. Appl. Phys,* vol. 82, 3482-3486, 1997.

[14] S. kamba, H. Wang, M.L. Zhang, *et al.*, "Microwave and infrared dielectric response of monoclinic Bismuth Zinc Niobate based pyrochlore ceramics with ion substitution in A site," *J. Appl. Phys,* vol. 100, 034109, 2006.

[15] Y. Zhang, S.T. Zhang, M.H. Lu, Y.F. Chen, and Z. G. Liu, "Structures and dielectric properties of $Bi_{1.5}Zn_{1.0}Nb_{1.5} - xTi_xO_7$ (x=0, 0.05,and 0.10) thin films," *Applied Physics Letters,* vol. 90, 042903, 2007.

[16] M.L. Zhang, H. Wang and X. Yao, "Effect of Ca substitution on structure and dielectric properties of Bismuth-based microwave ceramics," *J Electroceram,* vol. 21, 461-464, 2007.

[17] D.W. Kim, J.Y. Kim, H. S. Jung and K. S. Hong,, "Voltage-tunable dielectric properties of pyrochlore Bi-Zn-Nb-Ti-O solid-solution thin films," *J. Appl. Phys,* vol. 44, 6648-6653, 2005.

[18] J. W. Lu, and S. Stemmer, "Low loss, tunable Bimuth Zinc Niobate films deposited by rf magnetron sputtering," *Applied Physics Letters,* vol. 83, 2411-2413, 2003.

[19] S. Okaura, H Funakubo, M. Suzuki, H. Uchida, *et al*, "Low strain sensitivity of the dielectric property of pyrochlore Bi-Zn-Nb-O films," *Applied Physics Letters,* vol. 92, 182901, 2008.

[20] J. W. Jian, G. Cheng, T. Dechakupt, and S. T. Mckinstry,, "Low temperature crystallized pyrochlore Bismuth Zinc Niobate thin films by excimer laser annealing," *Applied Physics Letters,* vol. 87, 232905, 2005.

Chapter 2: Literature review

Chapter 2 provides an overview of ferroelectric BST and pyrochlore BZN materials. The important physical and dielectric properties of both materials are discussed in this chapter. Some of the drawbacks of the materials are also presented. In order to study the behaviour of ferroelectric and pyrochlore materials, the definition of dielectric materials must be understood first. Thus section 2.1 gives the definition and theories of dielectric material. (Deleted, since it is not related to the content in this chapter)

2.1 Dielectric material

2.1.1 Definition of dielectric and polarization

Dielectrics are the opposite of conductors and are similar to insulators. They have high resistivity and a band gap of several keV **[1].** Dielectric materials are generally ionic and carry either positive or negative charge **[2].** Under an electric field, the electrons within the dielectric material suffer displacement and create internal electric dipoles. The creation of an electric dipole forms its own field and so induced extra charges **[3].** This phenomenon is called **electric polarization.**

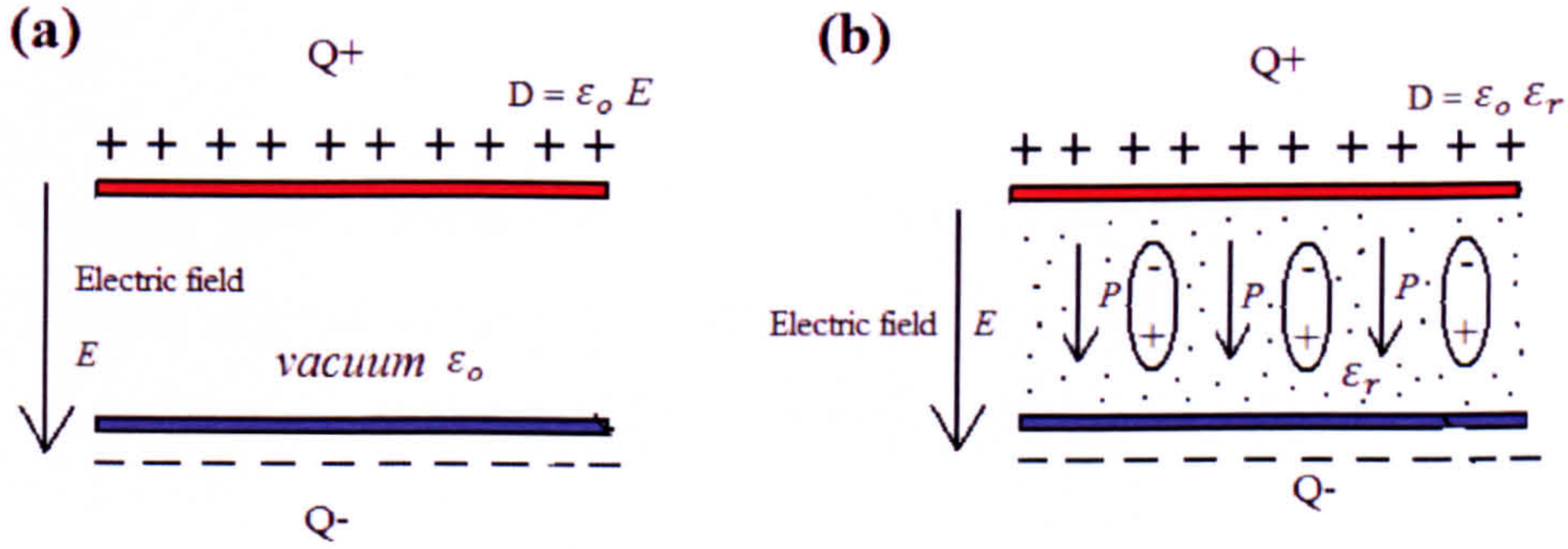

Figure 2.1 (a) Parallel capacitor with vacuum ε_0 (b) Parallel capacitor with dielectric constant ε_r (reproduced from **[3]**).

To obtain the electric polarization (P_{atom}), let us consider the displacement of a single atom inside a capacitor under the influence of an electric field. The electric polarization per each atom is expressed as: [1]

$$P_{atom} = \alpha_{elect}\, \varepsilon_o\, E \qquad (2.1)$$

where α_{atom} is the electric polarizability, ε_o is the permittivity of vacuum and E is the electric field.

The electric polarization per unit volume can be obtained by multiplying P_{atom} with the number of atom per unit volume (N).

$$P_{unit} = N\ \alpha_{elect}\, \varepsilon_o\, E \qquad (2.2)$$

2.1.2 Definition of dielectric constant

In practice, it is necessary to quantify the dielectric by using terms like dielectric constant. This can be achieved by considering the total electric polarization field (D) in the material. As shown in figure 2.1(a), in a parallel plate capacitor with no dielectric between the plates, the electric displacement field (D) of the **vacuum** parallel plate is related to the electric field (E) by the following equation: [4]

$$D = \varepsilon_o E \qquad (2.3)$$

In contrast, when a dielectric is inserted into the capacitor (figure 2.1(b)), there is an additional contribution to the electric displacement caused by the polarised atoms.

The total electric field displacement (D) can be expressed as follows: [4]

$$D = \varepsilon_o E + P \qquad (2.4)$$

By substituting 2.2 into 2.4, we have the following expression: **[2,4]**

$$D = \varepsilon_o E + P = \varepsilon_o E(1 + N\alpha_{elect}) = \varepsilon_o E \varepsilon_r \qquad (2.5)$$

where ε_o is the permittivity of the free space ($\varepsilon_o = 8.854 \times 10^{-12} F/m$) and ε_r is the relative permittivity or simply known as dielectric constant. In this work, the dielectric properties of all materials are compared by using the dielectric constant (ε_r).

2.1.3 Frequency response of a dielectric

In the previous section, the DC dielectric constant was introduced. When a low frequency AC field is applied, the polarisation of the atoms can follow the applied field and the dielectric constant is the same as the DC value. However, as the frequency is increased, the perturbation of the charges can no longer follow the changes in field and the material suffers from dielectric loss. Mathematically this can be expressed by defining the dielectric constant or permittivity as a complex number of the form $\varepsilon_r = \varepsilon_r' + \varepsilon_r''$ where the imaginary part (ε_r'') corresponds to the dielectric loss of the material. Both the real and imaginary parts of the dielectric constant are strongly affected by different the loss mechanisms. In a dielectric, there are three main classes of polarization in the material: **[5]**

(a) Electronic polarization : the displacement electrons orbiting around an atom induced by an electric field

(b) Ionic polarization: the displacement of ions caused by an electric field

(c) Orientation polarization: the alignment of polar molecules that are free to rotate in an electric field

Each of these polarisations has a different time constant associated with it and there will be regions where the dielectric constant will change. Figure 2.2 shows a typical behaviour of dielectric constant (ε_r' and ε_r'') of a dielectric material as a function of frequency.

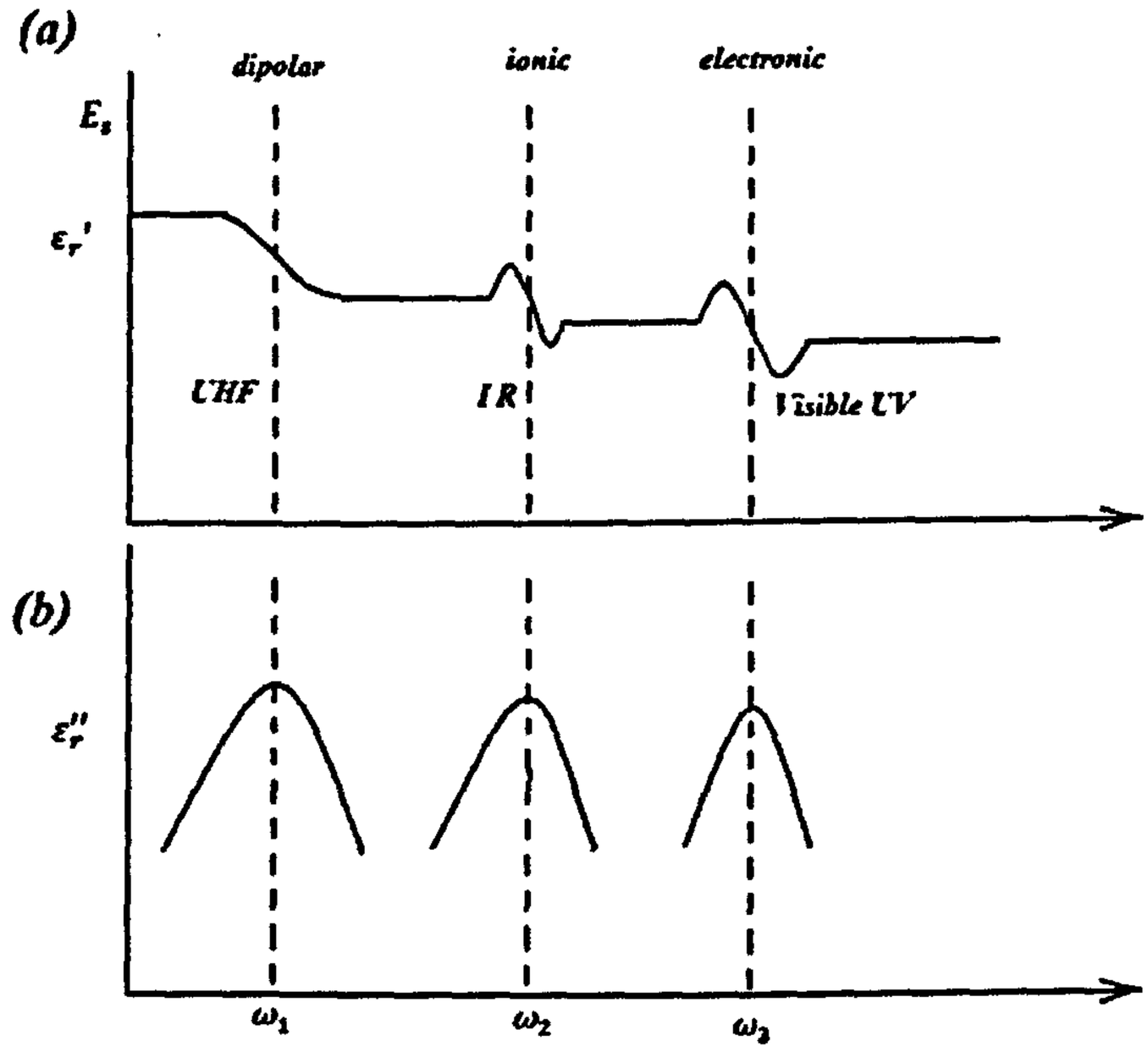

Figure 2.2 (a) Real ε' and (b) imaginary ε'' part of dielectric constant versus frequency log (ω) with three main absorption peaks $\omega_1 = 10^{10}Hz$, $10^{12}H_z < \omega_2 < 10^{13}H_z$ *and* $\omega_3 = 10^{15}Hz$ (*reproduced from* [5,6]).

According to figure 2.2, the real (ε') and imaginary (ε'') parts of the dielectric constants change significantly with respect to an increasing frequency. The frequency dependence of the material's dielectric constant due to different polarization is called dielectric dispersion. The dielectric peaks in figure 2.2 are caused by the ionic, dipolar and atomic polarizations. Despite the dielectric constant peaks, the real part of the dielectric constant of the material decreases with respect to increasing frequency. This behaviour was also observed in the measured results presented in chapter 6 and 7 of this thesis.

2.1.4 Dielectric loss and quality factor

In practice, the energy loss associated with the dielectric material is quantified by the *dissipation factor* or *loss tangent* which is defined as $tan\delta = \frac{\varepsilon_r''}{\varepsilon_r'}$. Since the imaginary part of the dielectric constant will increase along with increasing frequency, the material's dielectric loss tangent ($tan\delta$) also increases. In a parallel capacitor, the loss tangent represents the relative loss of energy to obtain a given amount of charge storage **[4]**. The inverse of loss tangent, the quality factor defined as $Q = 1/tan\delta$, is used as a figure of merit to describe the performance of microwave devices. Ideally, the larger this value then the better the device performance.

2.2. Ferroelectric BST

All ferroelectric materials have spontaneous electric polarization in which the directions of the polarization can be changed by applying an electric field. Ferroelectric materials come under a subclass of pyroelectric materials, which in turn comes from piezoelectric materials that exhibits a change of polarization under mechanical pressure **[6]**. Therefore, ferroelectric materials are also pyroelectric and piezoelectric.

For many years **[7-9]**, ferroelectric materials such as Barium Strontium Titanate (BST) have been used in a wide range of applications. It is well known that BST materials2 have high dielectric constant and their dielectric properties are dependent on both temperature and the applied electric field. In the following sections, the physical and dielectric properties of Barium Strontium Titanate (BST) are discussed.

This chapter discusses the physical and dielectric properties of BST materials. At first, a brief introduction to the crystal structures of ferroelectric BST is presented in

section 2.2.1. Sections 2.2.2 and 2.2.3 discuss the temperature dependence of polarization for ferroelectric materials. The composition dependence of dielectric properties is presented in section 2.2.4. The last three sections (2.2.5, 2.2.6 2.2.7) discuss the degradation of dielectric properties of thin film BST and the solutions for improving its dielectric properties.

2.2.1 Perovakite structure of Barium Strontium Titanate (BST)

BST material has a ABO_3 perovskite structure which is named after $CaTiO_3$ perovskite mineral **[7, 10].** The general form of BST material is $(Ba_xSr_{(1-x)})Ti_{1.0}O_3$ where $0.0<x<1.0$. Figure 2.3 shows the atomic unit cell of a perovskite BST crystal. In this figure, the A site of the crystal is occupied by either Ba^{2+} or Sr^{2+} ions whereas the *B site* is occupied by Ti^{4+}.

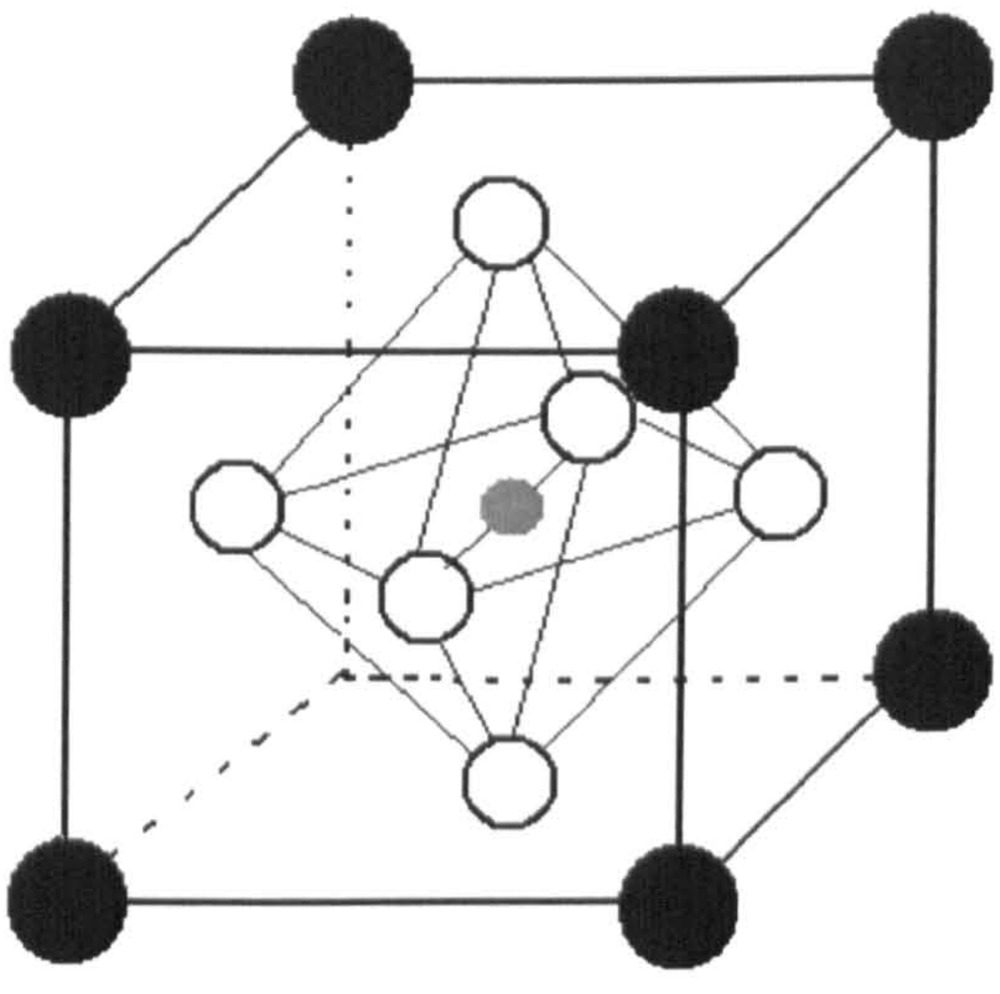

Figure 2.3 perovskite structure of ABO_3 crystal (reproduced from [8])

The perovskite structure is considered as a variation of a face-centred cubic (FCC)-structure. The large "A" site ions ($Ba^{2+} = 1.35Å$) occupy the eight corners of the crystal and O site ion (oxygen) occupies the centre of each face. The small B site ion

(Ti^{4+}=0.63Å) occupies the octahedral interstices **[4].** Because the radius of Sr^{2+}ion (1.18Å) is similar to Ba^{2+}ion, Sr^{2+}can substitute into the A site of the perovskite structure. When an electric field is applied, the B site ion is displaced from its original position in the centre of TiO_6 octahedron **[6].** This creates dipoles in the material which provide the mechanism for dielectric tunability.

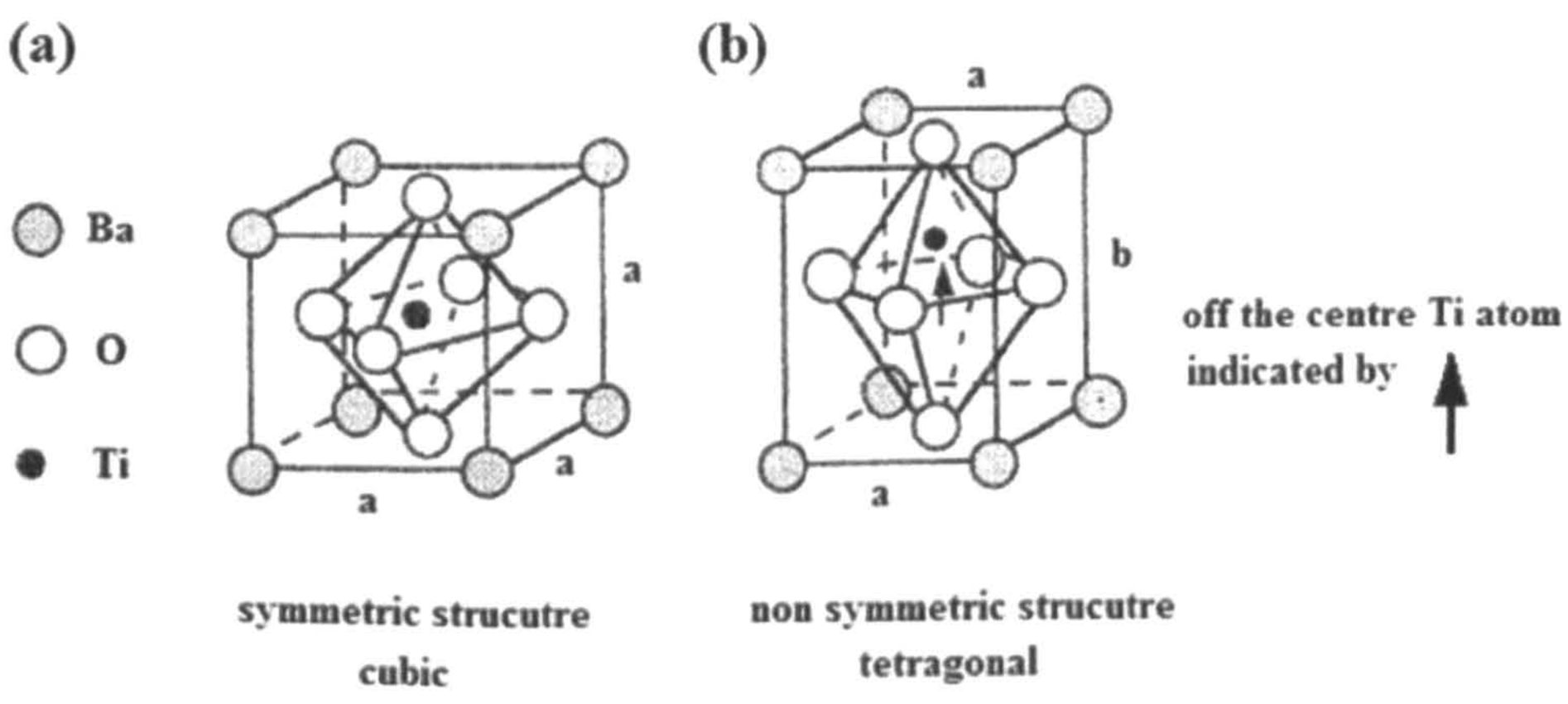

*Figure 2.4 (a) symmetric cubic BST structure (paraelectric phase) (b) non symmetric tetragonal BST structure (ferroelectric phase)***[8]**

The crystal structure of BST material is also temperature dependent. All ferroelectric materials including BST possess a ferroelectric to paraelectric phase transition temperature or *Curie* temperature (T_c). At ($T < T_c$), BST is in the ferroelectric phase which corresponds to a nonsymmetric tetragonal structure. As figure 2.4(b) shows, the Ti ion is slightly off the centre of the lattice. This leads to a permanent dipole which results in a spontaneous electric polarization within the crystal **[4].** The direction of the polarization is reversible by applying an external field. As the temperature goes above T_c, ($T > T_c$), **[4]** the thermal energy is enough to move the positions of Ti ion which form the symmetrical structure as shown in figure 2.4(a). Hence the material is in paraelectric phase in which the material does not have spontaneous polarization. The Curie temperature of the BST material can be altered by changing its composition. This provides the mechanism for changing the dielectric

properties of BST material to suit to a particular application. The compositional dependency of BST material will be further discussed in section 2.2.4. The Curie temperature of the BST material is also influenced by doping ions with radius between 1.35Å and 0.63Å, which substitute into either the A or B site of the BST crystal. The influence of ion doping will be discussed in section 2.2.7.

2.2.2Temperature dependence of hysteresis loop

As mentioned above, the ferroelectric materials exhibit spontaneous polarization and the direction of the polarization is reversible. Therefore, ferroelectric materials which including BST also have a unique characteristic of a hysteresis loop for polarization. Figure 2.5 gives a typical example of a hysteresis loop as a function of electric field. According to this graph, the response of polarization is highly nonlinear. When the electric field is reduced to zero, the corresponding polarization is not zero. At zero electric field, there are two *remnant* polarizations with opposite directions ($+P_r$and $-P_r$) **[6]**. To achieve a zero polarization, the strength of reverse electric field must be greater than the *remnant* polarization **[6]**.

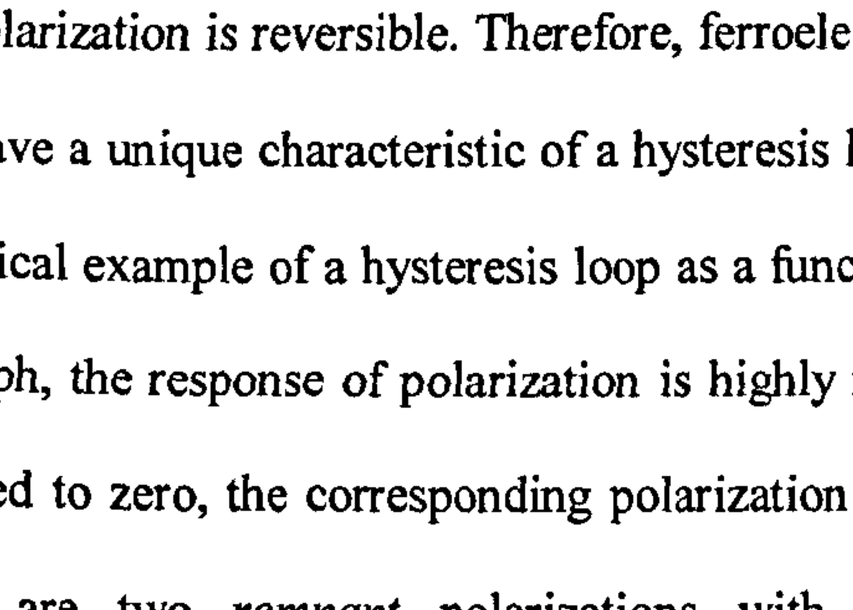

Figure 2.5 Hysteresis loop for ferroelectric polarization **[6]**

The behaviour of hysteresis loop for polarization is also tied with the crystal structure which is temperature dependent. Figure 2.6 (a), (b) and (c) shows the variation of hysteresis loop at various temperatures.

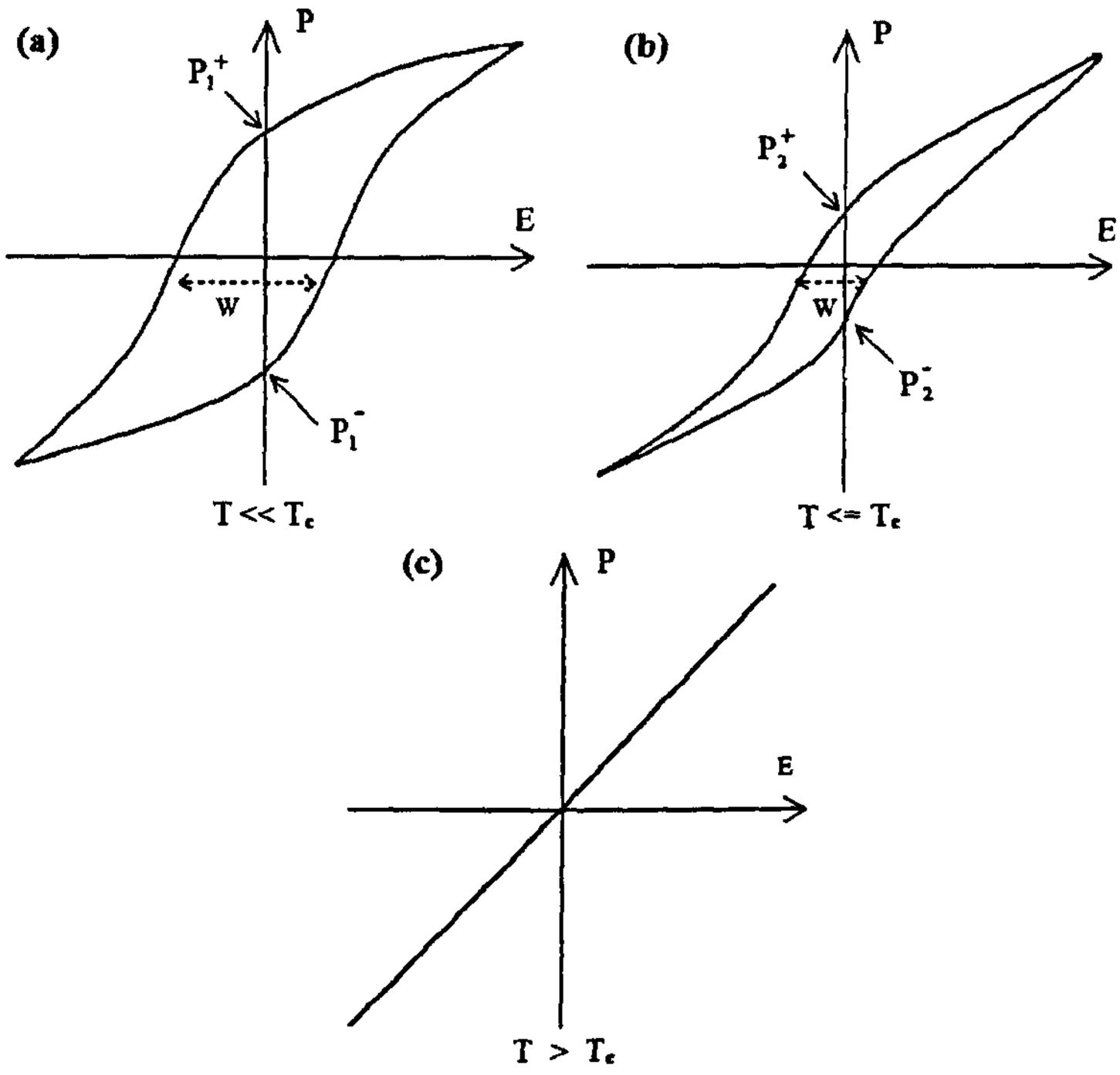

Figure 2.6 Polarization hysteresis loop (a) very low temperature ($T << T_c$) (b) low temperature ($T < T_c$) and room temperature ($T > T_c$) **[6]**

When the temperature is much lower than the *Curie* temperature ($T << T_c$), the material is in the ferroelectric state. The width (w) of the hysteresis curve is much wider and the remnant polarizations of P_1^+ and P_1^- are the highest. This is because at lower temperature, a greater electric field is needed to orient the domain **[6]** As the temperature rises close to the *Curie* temperature, a smaller reverse electric field can achieve a zero polarization and so the width (w) of the hysteresis loop is narrower. Once the temperature is well above the *Curie* temperature, the material undergoes a phase transition from tetragonal (ferroelectric) to cubic (paraelectric) in which the hysteresis loop disappears. The electric polarization is linearly related with the

electric field. Thus, ferroelectric materials do not exhibit ferroelectricity or hysteresis loops at ($T > T_c$).

2.2.3 Temperature dependence of dielectric properties

Similar to the polarization hysteresis loop, the dielectric properties of all ferroelectrics including BST are strongly temperature dependent. Figure 2.7 shows the variations of permitivity of a ferroelectric material as a function of temperature. According to this figure, the permitivity in both ferroelectric and paraelectric phases are very high. The origin of the high permittivity (dielectric constant) is the orientation polarization of B site atom (Ti) in the perovskite structure.

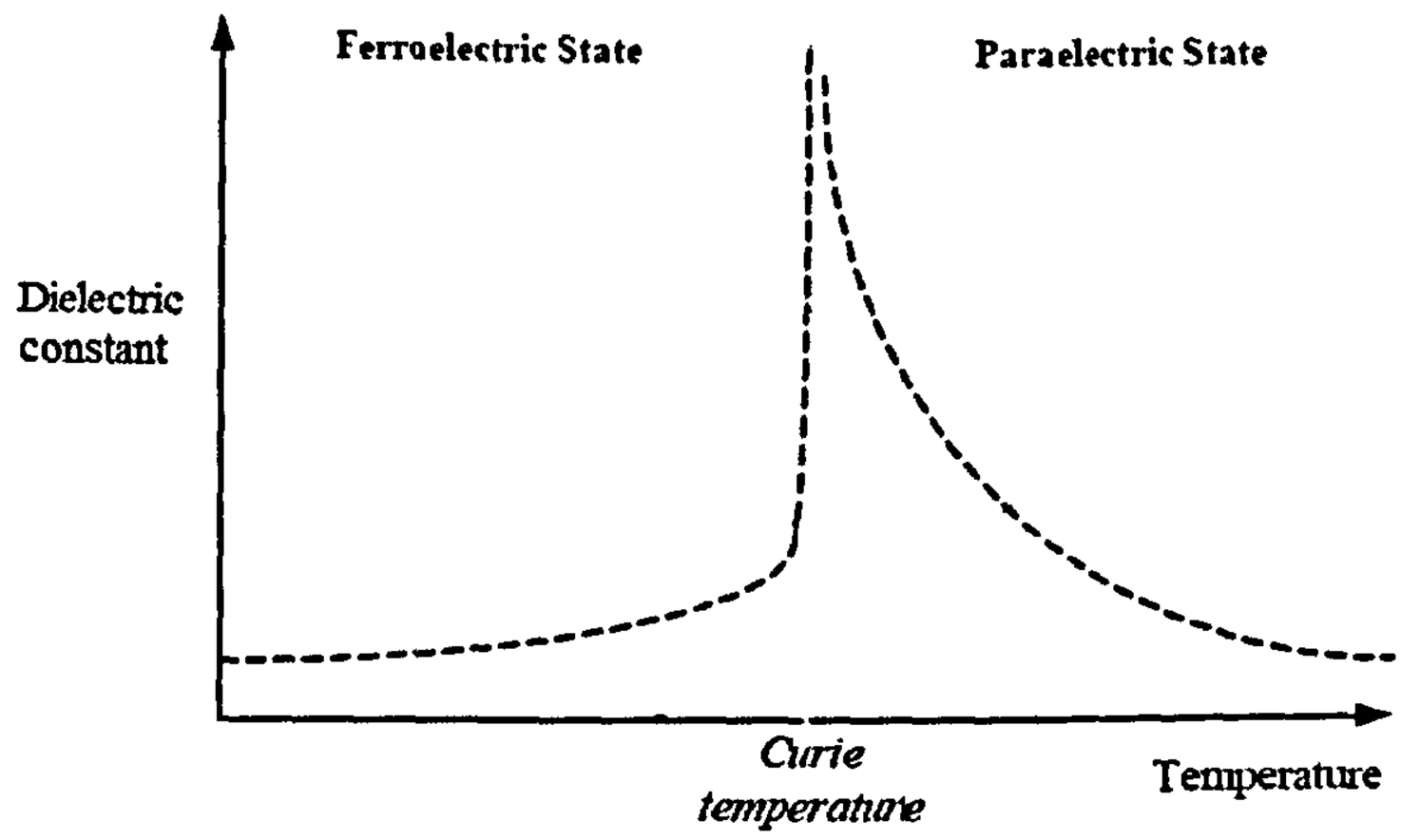

Figure 2.7 Dielectric constant of ferroelectric material versus temperature

There is a sharp peak of the dielectric constant at near *Curie* temperature where there is a structure and phase transition. In the paraelectric phase, the dielectric constant increases with increasing temperature according to *Curie-Weiss* law. This relationship can be mathematically expressed as : [8]

$$\varepsilon = \varepsilon_o + \left|\frac{C}{T-T_o}\right| \approx \left|\frac{C}{T-T_o}\right| \qquad (2.6)$$

where C is Curie constant, T is the temperature and T_o is the Curie temperature.

2.2.4 Composition dependence of BST

As mentioned in section 2.2.1, the dielectric properties of BST material are strongly affected by its composition. BST material has a general form of $Ba_xSr_{1-x}TiO_3$ $(0.0 < x < 1.0)$ which can be considered as a substantial solid solution of Barium Titanium Oxide (BTO) and Strontium Titanium Oxide (STO). Since the *Curie* temperatures for BST and STO are 120 °C and -163°C respectively, the substitution of "Sr" into BST will lower the Curie temperature. In contrast, an increase of "Ba" concentration allows the *Curie* temperature to increase. The dependence of the *Curie* temperature on its composition (Ba or Sr) is highly attractive for applications in making microwave components because it allows the dielectric properties of the material to be chosen by changing the composition 11 **[9].** Figure 2.8 shows the variation of dielectric constant of BST crystal as a function of temperature for different composition **[11]**.

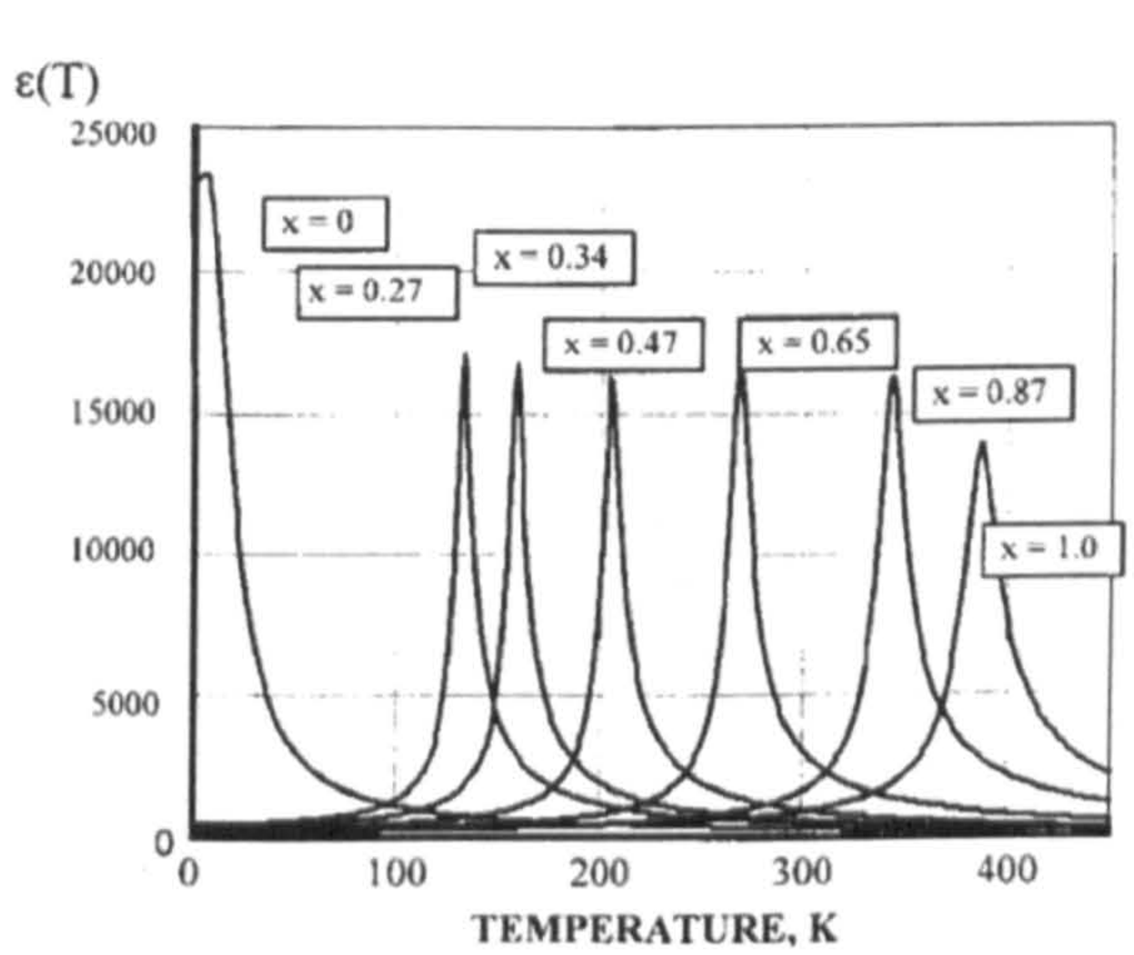

Figure 2.8 Dielectric constant of $(Ba_xSr_{1-x})TiO_3$ *where* $0.0<x<1.0$ **[11]**.

According to this figure, the *Curie* temperature gradually increases as the concentration of Ba is increased from $x = 0$ to 1.0. In figure 2.9, the dielectric loss of a BST crystal with different composition is presented as a function of temperature at 10GHz. The loss tangent slightly increases with temperature for all compositions

apart from the lowest. As the material undergoes the ferroelectric to paraelectric transition the loss tangent drops. This demonstrates that the dielectric loss of BST in the paraelectric phase is many times smaller than the loss in the ferroelectric phase. The reason is that BST in ferroelectric phase are also piezoelectrics which can induce large acoustic losses at lower GHz frequency **[12]**. In addition, ferroelectrics also exhibit polarization hysteresis loop under a changing electric field which further increases the dielectric loss of the material.

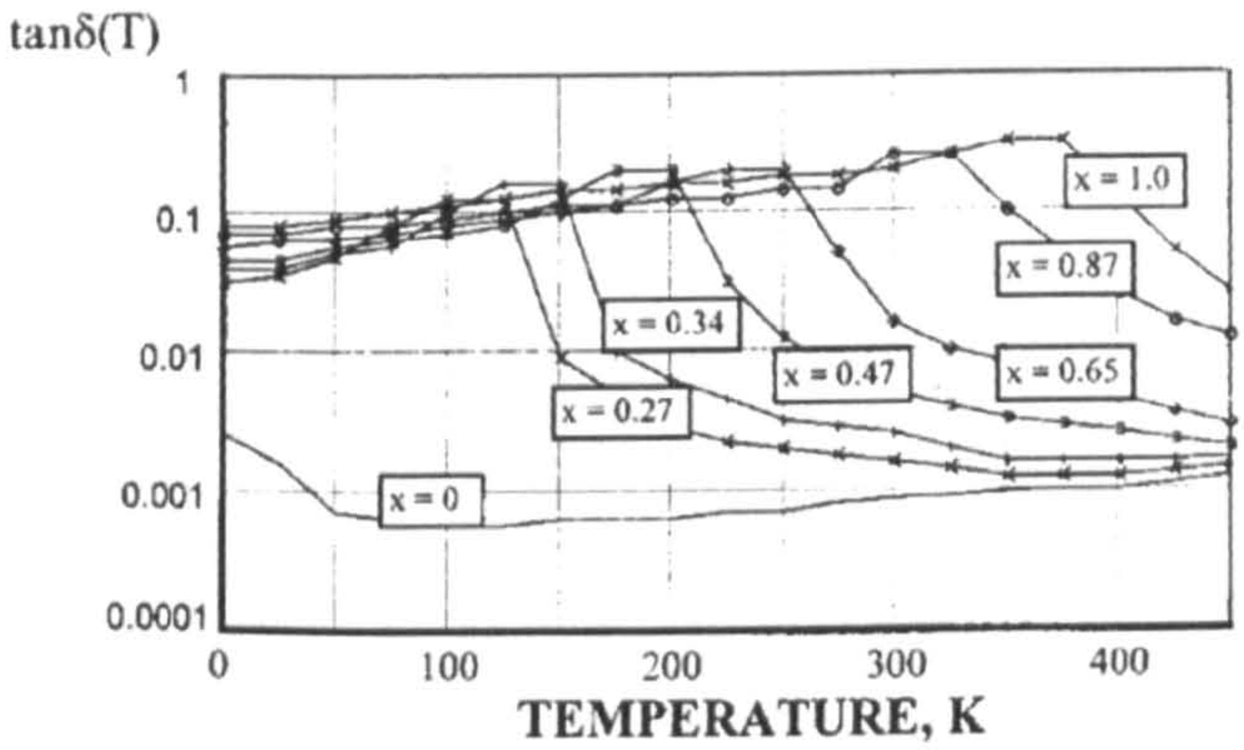

Figure 2.9 Loss tangent of $(Ba_xSr_{1-x})TiO_3$ *as a function of temperature at 10GHz* **[11]**.

In addition to the dielectric constant and dielectric loss, the dielectric tunability of BST material is also crucial for implementing microwave tunable devices. In this work, the dielectric tunability is expressed as follows:

$$tunability\ (\%) = \frac{Dielectric\ constant\ (0V) - Dielectric\ constant\ (at\ given\ voltage)}{Dielectric\ constant\ (0V)} \times 100\% \qquad (2.7)$$

Although the dielectric tunability is not presented in figure 2.8 and 2.9, it is widely believed that a large dielectric constant is proportionally associated with high tunability **[7]**. In the present work, these figures serve as a guideline for the optimisation of the dielectric properties at a given temperature.

For implementing tunable devices, it is desirable to maximise the material's tunability and dielectric constant. In a BST material system, the dielectric constant and tunability are maximized in the ferroelectric-paraelectric transition region **[7].** The temperature at which this occurs is called the Curie temperature (T_c) and can be adjusted by changing the composition between Ba and Sr in $Ba_{(1-x)}Sr_xTi_{1.0}O_3$. Previous work [12], has suggested that the $Ba_{0.5}Sr_{0.5}Ti_{1.0}O_3$material is ideally suited to implementing microwave devices (MW) because its Curie temperature is close to room temperature. In this work, all BST thin films were synthesized with the composition of $Ba_{0.5}Sr_{0.5}TiO_3$.

2.2.5 Bulk or thin film

The dielectric properties of ferroelectric thin films have been found to be substantially different from those of bulk materials in most cases. Figure 2.10 compares the dielectric constant of BST in *bulk* and *thin film* as a function of temperature.

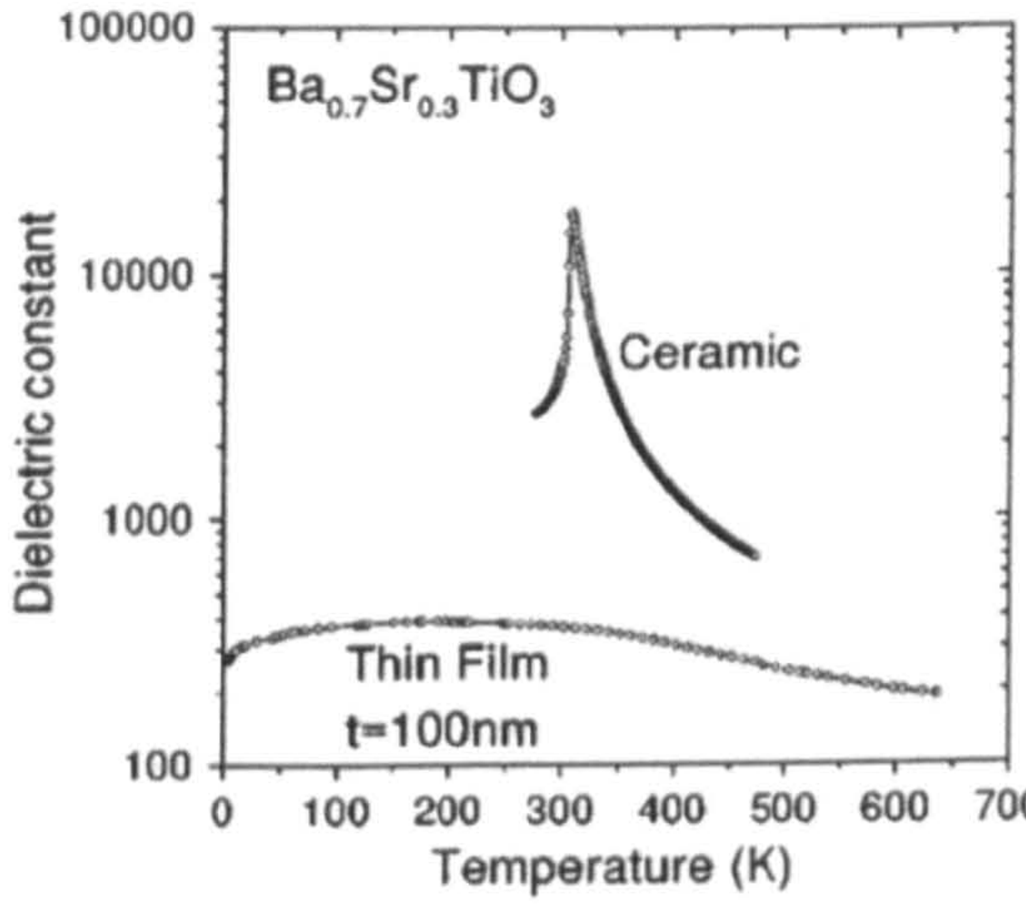

Figure 2.10 a comparison of dielectric constant between thin film BST and bulk BST **[13]**.

Although *bulk* BST has a much higher dielectric constant, it also shows a sharp dielectric peak near the *Curie* temperature. Therefore, *bulk* BST is more sensitive to the change of temperature than a ferroelectric thin film. Furthermore, the use of bulk ferroelectric requires very high DC tuning voltage for tuning the dielectric constant. This leads to an increase of power consumption. In this case, the tuning electric field is defined as:

$$E_{field} = \frac{V_{tune}}{d_{(distance)}} \tag{2.8}$$

where E_{field} is the tuning electric field, V_{tune} is the tuning DC voltage and $d_{(distance)}$ is the thickness of the thin film.

In contrast, the thin film BST requires a very low DC tuning voltage to achieve a strong electric field. The sharp dielectric peak is not found in the thin film (as shown in figure 2.10). The dielectric constant gradually decreases as the temperature goes up. These advantages make BST thin films very popular for implementing microwave components. In this work all $Ba_xSr_{1-x}TiO_3$ thin films are made in the form of thin films (<300nm).

2.2.6 Loss mechanism

However, BST thin films also have lower dielectric constants and higher losses than the *bulk* BST. The increase in dielectric loss of BST thin film is a particular problem for implementing microwave devices. In this work, the main challenge is to lower the dielectric loss of BST thin films. Many reasons have been given for the degradation of the dielectric properties. In particular, charge defects and substrate induced-strain are the most influential factors in the degradation of dielectric properties.

Influence of substrate

Strain in a ferroelectric thin film is significant because it can change the soft phonon mode, which greatly affects the dielectric constant of a ferroelectric thin film **[7]**. Film strain is caused by the mismatch between the lattice parameters and thermal expansion coefficients of the thin film and substrate. In BST thin films, the strain is mainly caused by the lattice mismatch between the substrate and thin film. It is also indicated that the lattice parameters mismatch at the deposition temperature are much more important than the mismatch at room temperature **[14]**.

A popular way to minimize this effect is to use substrates that have similar lattice parameters as BST thin films. The most frequently used substrates are MgO, SrTiO3, LaAlO3, Sapphire and LSAT. A completely strain free (- 0.1% mismatch) thin film based on LSAT has been demonstrated by *Canedy C. L* and *Li Hao* **[15]**. The other way to control the strain is to develop a compositional graded BST thin film which contains several layers of $Ba_xSr_{1-x}TiO_3$ with x varied between 0.1 and 0.7 **[16, 17]**. The layers that are close to the bottom substrate act like a buffer layer between the bottom substrate and the top layers of BST. The strain effect of BST thin films is well understood and the solutions to the problem are provided by numerical works.

Influence of charge defects

The dielectric loss of a material can be attributed to two mechanisms One: intrinsic loss which appears due to the interaction between the phonons and microwave field **[7]**. The intrinsic loss is the fundamental loss of ferroelectric material and cannot be removed by improving crystallization or microstructure of the materials. Two: extrinsic loss that is associated with (a) charge defects which excite acoustic vibrations, (b) universal relaxation law mechanism and (c) quasi-Debye contribution

[9]. Figure (2.11) illustrates this fact by comparing the dielectric loss of BST materials with and without charge defect as a function of frequency. Clearly, BST with charge defects has a much larger dielectric loss than single crystal BST and so work is required to reduce the density of charge defects.

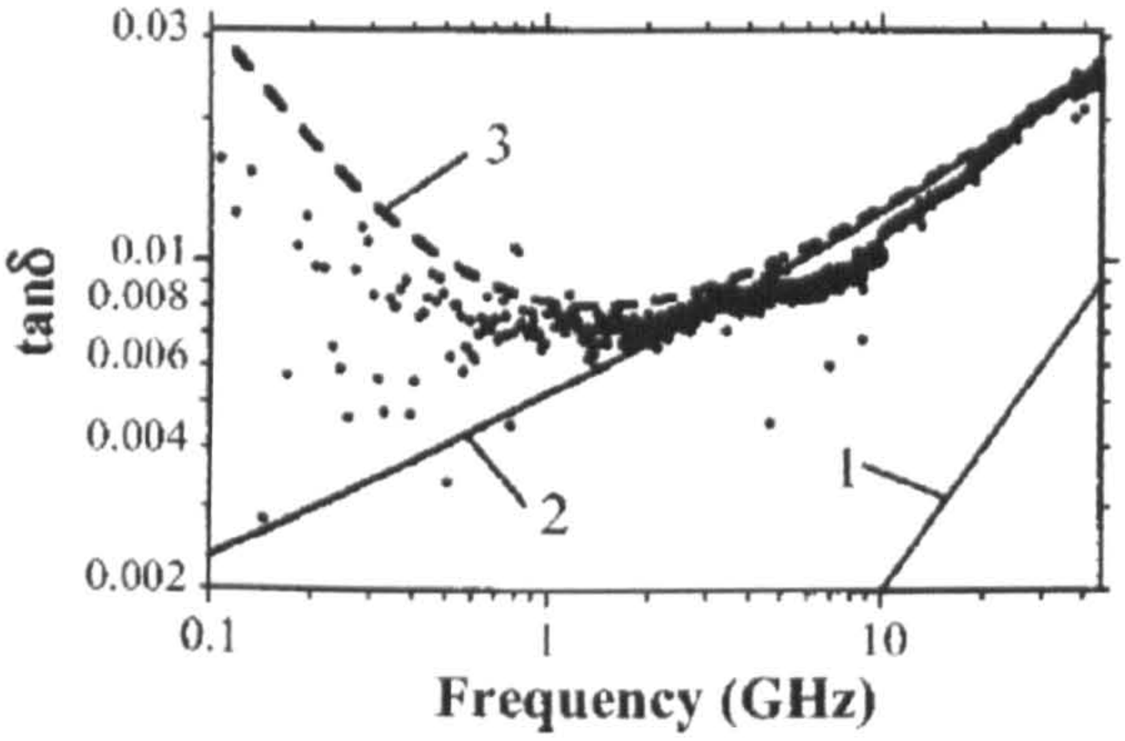

1: Single crystal BST
2: BST with charge deficit
3: BST with charge deficit and Si substrate

Figure 2.11 Dielectric loss of (1) single crystal BST (2) BST with charge deficit (3) BST with charge deficit and Si substrate **[18].**

In this work, oxygen vacancies are the main charge defects that affect the dielectric loss of BST thin film. It has been widely proved that electrons, generated from oxygen vacancies, hop between each of Ti^{4+} ion of the BST crystal providing the mechanism for dielectric loss **[19].** The density of oxygen vacancies is heavily influenced by the deposition parameters of the thin film. A straight forward way to minimize this effect is to change the oxygen pressure during annealing. However, the handling of pure oxygen has safety issues and the control of oxygen pressure is difficult.

2.2.7 The improvement of dielectric properties in BST materials by acceptor doping

As mentioned in section 2.2.1, doping is a more effective way for reducing the effects of oxygen vacancies **[20, 21].** Generally, the dopants can be distinguished into three types: acceptor, donor and stable addictives **[22].** Acceptor ions with a charge of less than 4^{+}can substitute the B site Ti^{4+} ion of the ABO_3 structure and act as electron acceptor. This prevents the reduction of Ti^{4+} to Ti^{3+} by neutralizing the donor action of the oxygen vacancies **[19].** The oxygen vacancies generate free electrons that can hop between the B (Ti^{4+}) sites and so provide the loss mechanism **[23].** The compensation for oxygen vacancies by acceptor dopants reduces the free electron concentration and so lowers the dielectric loss. Therefore, acceptor dopants are widely used to modify the dielectric properties of BST thin films.

The doped ions can substitute either the A or B site of the ABO_3structure depending on their size. Dopants such as La^{3+}(1.03Å), Er^{3+} (0.89Å), Cd^{3+}(0.95Å) and K^{1+} (1.38Å) ions **[24, 25, 26]** substitute the A site of the ABO_3 structure because the size of the dopants are close to the size of the $Ba^{2+}(1.35\dot{A})$ and $Sr^{2+}(1.18\ \dot{A})$ ions which sit on the A site. It is suggested that the doped ions which occupy the A sites do not break the cooperative vibration of Ti-O chains and hence keep the anharmonic interaction of the Ti ions. This may result in an increase of the dielectric constant or at least maintain the dielectric constant as the undoped BST **[27].**

On the other hand, the B site dopants with smaller radius including Fe^{3+}, Co^{3+}, Co^{2+}, Mn^{2+}, Mn^{3+}, Ni^{2+}, Mg^{2+}, Al^{2+}, In^{3+}, Cr^{3+} and Sc^{3+}, can replace the smaller Ti^{4+} ion (0.63Å) in the B site of the ABO_3 structure **[28].** Similar to the acceptor ions that substituted into the A site of BST crystal, the B site doping can also lead to a reduction of dielectric loss. However, this could break the cooperative vibration of Ti-O chains of the perovskite structure which lowers the

Curie temperature. Therefore, this leads to a smaller dielectric constantand dielectric tunability.

To date, numerous works ([24], [29], [30], [26], [31], [23], [32], [32] and [33]) have been carried out to study the effects of ion doped BST thin films. The following table (2.1) shows a list of examples of ion doped BST materials.

Type of dopant	*Deposition methods*	*Characterization Methods*	*Dielectric properties*	
Fe	*Sol gel*	*MIM capacitor*	*ε_r=170, tunability = 21% and tan_δ=0.012 at 100MHz*	[24]
Bi	*Sol gel*	*MIM capacitor*	*ε_r=242, tunability =31.5% and tan_δ=0.015 at 100MHz*	[24]
Mg	*Sol gel*	*Interdigital capacitor (IDC)*	*Average ε_r= 245 and tan_δ=0.08 at 15GHz*	[24]
K	*Sol gel*	*IDC*	*Average ε_r= 260 and tan_δ=0.078 at 15GHz*	[24]
Li	*Screen Print*	*IDC*	*Capacitance of IDC increases from 0.63 pF to 0.46 pF as the frequency increased from 1 GHz to 6.4 GHz. tan_δ=0.016 at 3GHz*	[29]
Li	*Screen print*	*IDC*	*ε_r= 265 and tan_δ=0.0055 at 7GHz*	[30]
La	*Sol gel*	*MIM capacitor*	*22.16% tunability under 10V ε_r= 209 (0V) at 100KHz*	[26]
W	*RF sputtering*	*MIM capacitor*	*ε_r= 239 with 1% of W at 100KHz tan_δ=0.022 with 1% W at 100KHz*	[31]
Co	*PLD*	*MIM capacitor*	*tan_δ=0.039 and tunability = 18.7% at 100KHz under 200KV/cm*	[23]
Y	*PLD*	*MIM capacitor*	*ε_r= 232 at 100kHz with 1.5% Y under 0V tan_δ=0.032 at 100kHz with 1.5% Y under 0V*	[32]
Cr	*Sol gel*	*MIM capacitor*	*ε_r= 426 at 100KHz with 5% Cr tan_δ=0.0065 at 100 KHz with 5% Cr*	[33]

Table 2.1 examples of ion doped BST thin films

According to this table, most of the work has been carried out at low frequency (<100MHz). The dielectric properties at low frequency could be completely different from the dielectric properties at microwave frequency. Therefore, the need for studying the effect of ion doping on the microwave properties of BST thin film is strong.

Among all types of acceptor dopants, cobalt (Co) and lithium (Li) ions are particularly interesting. Cobalt (Co) is a well known acceptor type dopant. By doping BST materials with Co ion, a reduction of leakage of current and dielectric loss can be achieved at the same time. Compared with Co, very little attention has been given to the Lithium doped BST. So far, two works **[29, 30]** has been found to describe the crystal structure and dielectric properties of BST thin film doped with Li ion.

However, these works do not provide any information about the effects on the material's microstructure and only one 3wt% Li doped $Ba_{0.5}Sr_{0.5}Ti_{1.0}O_3$ thin films was studied. Furthermore, the measured results of Li doped BST at microwave frequency [29, 30] are obtained from measuring an interdigital capacitor (IDC). The relative complexity of the IDC geometry makes the modelling of IDC very difficult and one must rely in practice on simpler quasistatic or semi-empirical models **[34]**. This results in large errors in the measured dielectric results. Hence the interest for studying the effects of Li doping on the dielectric properties of BST thin film is still strong.

In this work, various concentrations of Li and Co ions were doped into BST thin films to modify their crystal and microstructures. As suggested in section 2.2.4, the composition of the BST thin film is chosen to be $Ba_{0.5}Sr_{0.5}Ti_{1.0}O_3$ which exhibits very high dielectric constant and tunability at room temperature. The dielectric properties of the thin films were characterized at microwave frequencies (>1GHz) by employing a simpler coplanar waveguide (CPW). The simplicity of CPW geometry

does not reply on semi-empirical models. Therefore, the coplanar waveguide (CPW) geometry allows a more accurate characterization of its microwave properties. The geometry and fabrication process of CPW are presented in chapter 4. The measured dielectric results of the Co and Li doped BST films are discussed in chapter 7.

2.3 Alternative tunable material (BZN)

2.3.1 Introduction

Barium Strontium Titanate (BST) is not the only material that has been used to implement the tunable microwave devices. In the past decade, much work has been devoted to the search for new materials that exhibit lower dielectric low tangent and higher dielectric tunability.

STO materials are widely considered as the most likely candidate to replace the ferroelectric BST. STO is in a paraelectric state at room temperature (>300K) with very little tunability. When the temperature drops to 77K, this material exhibits very high tunability and small dielectric loss. Therefore, the overall loss of the microwave system can be dramatically reduced by the incorporation of high temperature superconductor materials (HTS) **[35]** and **[36]**. However, the cost of maintaining a low working temperature (77K) is too high which prevents STO being used in room temperature microwave devices.

Pyrochlore Bismuth Zinc Niobate (BZN) ceramic was initially developed in 1970s for high permittivity ceramic capacitors. Only recently have people started to consider it as a potential candidate to replace the BST due to its low dielectric loss (0.005), relatively high dielectric constant (120 at 0MV/cm) and significant dielectric

tunability (45% at 3MV/cm) **[37]**. These parameters are comparable to the latest BST technology. According to *Hiroshi Funakubo and Shingo Okaura* **[38]**, very high stability in dielectric property has been discovered in BZN thin films with respect to thermal strain of the substrates. It is also known that the tunable temperature coefficient (TTC) of bismuth based materials are relatively low (-400ppm/°C for α phase and +200ppm/°C for β phase **[39]**) and by the selection of the correct doping can be tuned to zero. This allows the material to be integrated into a microchip relatively easily. Generally, the pyrochlore BZN offers a combination of advantages of low dielectric loss, modest TTC and substrate independent dielectric properties over the traditional BST ferroelectric. These advantages have attracted numerous researchers **[40, 41 42]** to work on pyrochlore BZN microwave devices.

2.3.2 Structures of pyrochlore BZN

The general formula of a pyrochlore BZN material is $A_2B_2O_7$. In pyrochlore BZN, the larger Bi ion occupies the "A" site position of $A_2B_2O_7$ with eight fold coordination. The smaller Nb ion occupies the "B" site of $A_2B_2O_7$ with six fold coordination **[39]**. The medium sized zinc ion occupies both the A and B sites of the $A_2B_2O_7$ structure. The general composition of BZN material is $(Bi_{3x}Zn_{2-3x})(Zn_xNb_{2-x})O_7$. The material exhibits cubic (α-phase) phase when x = 0.5 $Bi_{1.5}Zn_{1.0}Nb_{1.5}O_7$ and monoclinic-zirconolite phase (β-phase) when x = 2/3 $Bi_{2.0}(Zn_{1/3}Nb_{2/3})O_7$, respectively **[39]**.

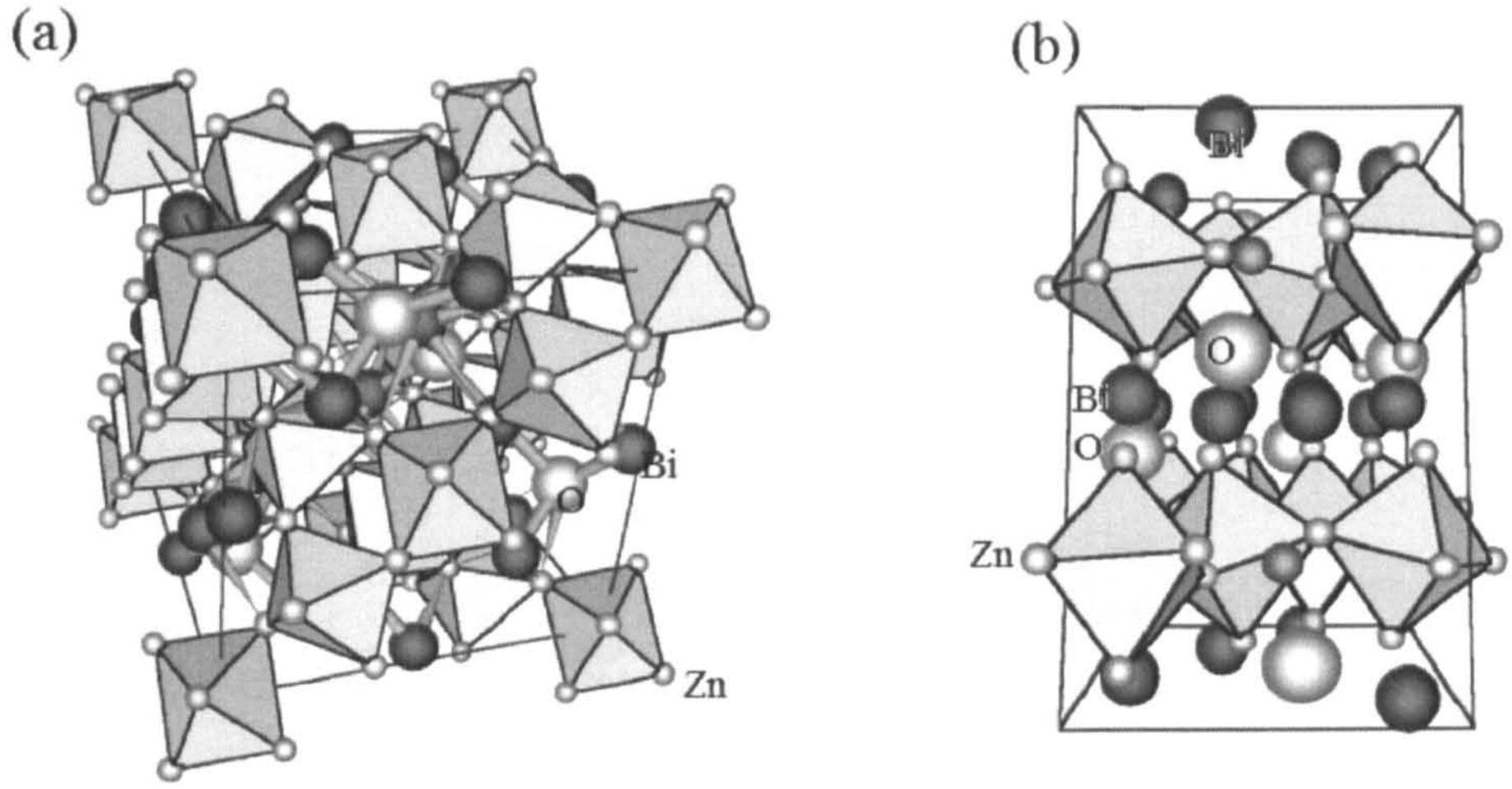

Bi is the large dark atom O is the while atom Zn is the smaller gray atom

Figure 2.12 (a) Schematic structure of the cubic pyrochlore BZN and (b) monoclinic-zirconolite phase of BZN **[37].**

The schematics of cubic phase and monoclinic-zirconolite phase BZN crystals are shown in figure 2.12(a) and (b) **[37].** The structure of cubic pyrochlore BZN is considered as a derivative of the fluorite structure AO_2 where the A site is split into A and B sites for BZN **[37].** However, the unit cell of BZN is twice as large as AO_2. In cubic pyrochlore BZN, the larger "A" cations are eight fold coordinated with oxygen which form a distorted cube. The smaller "B" cations which are sixfold coordinated with oxygen forms a distorted octahedral **[37].** One of the seven oxygen atoms is bonded to A site cations **[37].**

On the other hand, the monoclinic–zirconolite phase BZN can be considered as a derivative of the cubic pyrochlore structured BZN. The crystal structures of monoclinic phase BZN are too complicated to be discussed in this thesis and the distribution of Zn and Nb ions in monoclinic BZN are not of interest to this work. However, the distribution and location of ions in pyrochlore BZN are presented in work by *I. Levin* and *T. G. Amos* **[43].**

2.3.3 Dielectric properties of BZN

Influence of dielectric relaxation

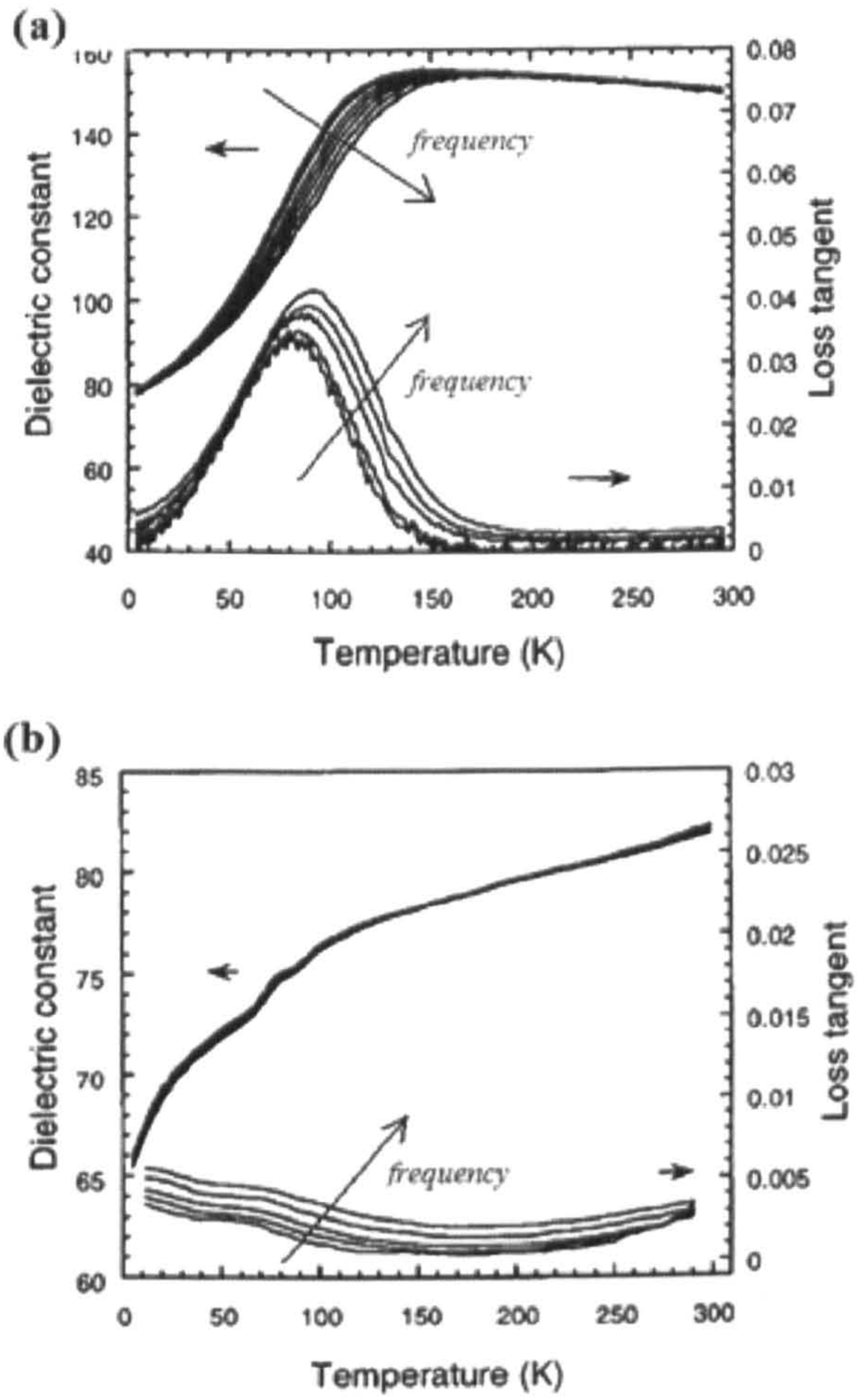

Figure 2.13 (a) Dielectric constant and loss for cubic BZN thin film versus temperature (b) Dielectric constant and loss for monoclinic BZN thin film (*reproduced from* **[44]**).

Figures 2.13(a) and (b) compare the dielectric properties of cubic and monoclinic BZN thin films as a function of temperature. According to figure 2.13(b), the monoclinic BZN has no frequency dispersion of dielectric constant and dielectric loss.

Although the dielectric constant decreases rapidly at below 100K, the corresponding dielectric loss remains below 0.005. In figure 2.13(a), a frequency dispersion of dielectric constant and loss are observed around 100K. The dielectric constant decreases from 150 to 80 as the measuring temperature decreases towards 0K. As the measured frequency increases, the peak of dielectric loss increases and shifts to higher temperature.

Since frequency relaxation is observed in cubic BZN, the dielectric loss in this material is much higher than in monoclinic BZN. The source of dielectric loss is frequency relaxation in cubic BZN thin films. The origin of frequency relaxation is attributed to the hopping of the A and O'sites atoms in a cubic pyrcohlore structure **[45].** The detailed analysis for the cause of frequency relaxation is given in many reports **[46, 47].**

Tunabilities of cubic and monoclinic BZN

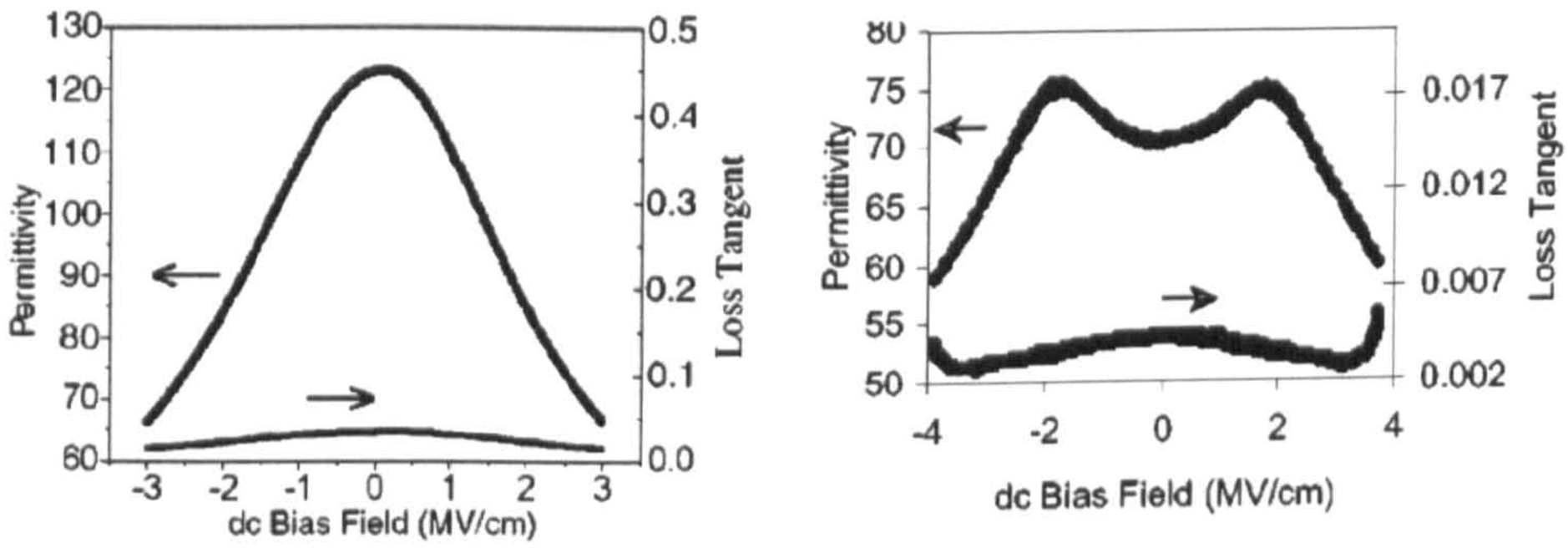

Figure 2.14 (a) Dielectric tunability of cubic BZN (b) Dielectric tunability of monoclinic BZN (reproduced from **[37]).**

Figure 2.14(a) and (b) shows the dielectric tunability of a cubic and monoclinic phase BZN thin film at 77K, respectively. For the cubic pyrochlore BZN, the large dielectric constant (125) which is associated with ionic polarization comes from the $O' - Bi - O'$ bond **[37].** A large applied electric field allows the source of polarization to be clamped out. This provides the dielectric tunability for cubic BZN

thin film. According to figure 2.14(a), the measured dielectric constant decreases from 125 to 70 under a tuning electric field of 3MV/cm. In contrast, monoclinic (β phase) $Bi_{2.0}Zn_{2/3}Nb_{4/3}O_7$ has a smaller dielectric constant of ε_r = 75 compared to cubic phase BZN and is barely tunable [37] under a tuning electric field of 3MV/cm. Therefore, pure monoclinic BZN material cannot be used to implement tunable microwave devices.

2.3.4 Improvements on dielectric properties of BZN

As mentioned earlier, the dielectric properties of cubic pyrochlore BZN is relatively independent of the strain caused by lattice mismatch of the substrates. Therefore, the most effective way of improving BZN dielectric properties is ion doping which can substitute into the A or B site of the pyrochlore structure.

B site substitution by Ti ions

In cubic pyrcohlore BZN, the A site of this crystal is occupied by Bi^{3+} with a larger radius of 1.11 Å and the B site is usually occupied by the smaller atom Nb with 0.64 Å. Due to the medium radius of the Zn^{2+} ion (0.75 Å) [48] , Zn^{2+} was unevenly distributed in both the A and B site of the pyrochlore material with a preference for the B site [48]. The doping of "Ti" ion into cubic BZN can co-substitute Zn^{2+}or Nb^{5+}at the B site of the crystal [49]. Therefore, the atoms in B sites of the crystal are Ti^{4+}, Nb^{5+} and Zn^{2+}. Because the origin of high dielectric constant is associated with BO_6 – octehedras [49], the correlation between octahedras of TiO6 and NbO6 have very high polarization which leads to higher dielectric constant [49]. So far, several papers [50, 51, 52] on Ti doped BZN films have shown an improvement in dielectric constant at various frequencies. On the other hand, the doping of Ti ions in the B site of BZN crystal can also affect the hopping of Bi and Zn atoms which are

associated with the activation energy of dielectric relaxation **[50].** This may provide the mechanism for reducing the dielectric loss of BZN thin film.

A site substitution by Ti ions

As mentioned above, cubic (α phase) BZN has greater dielectric loss than monoclinic (β phase) BZN caused by the appearance of frequency relaxation in cubic BZN. Since pure monoclinic BZN only exists in a narrow region of $Bi_{2.0}Zn_{2/3}Nb_{4/3}O_{7.0}$ **[48],** the doping of $Ca^{2+}(1.12\dot{A})$ ion in the A site of BZN may lead to a phase transition from cubic to monoclinic BZN **[48].** This could lead to the formation of a mixture of cubic and monoclinic BZN which has lower dielectric loss and still has relatively high dielectric tunability with respect to the tuning electric field.

In 2006 and 2007, *Hong Wang* **[45]** and *Meiling Zhang* **[48]** had reported independently on Ca doped BZN ceramics with different compositions. Both of the works suggested an increase in material quality factors compared to the undoped BZN. In particular, *Hong Wang* and her colleagues have shown that an increase in quality factor from 1755 to 3989 can be obtained with Ca doping.

To study the dielectric properties of BZN thin films, undoped cubic pyrochlore $Bi_{1.5}Zn_{1.0}Nb_{1.5}O_7$thin films were synthesized by using chemical solution deposition (CSD) method. The microwave dielectric properties of the thin films were measured using both the MIM capacitors and CPW techniques. The relationship between the crystallization phase and microwave properties of the material is of particular interest in this work. The fabrication and microwave characterization of BST and BZN thin films are given in chapters 5 and 6.

2.4 Summary

There has been a great deal of effort by numerous researchers to develop microwave tunable devices based on BST thin films. The dependence of the dielectric properties of BST on its composition is particularly attractive for implementing microwave devices. Since ferroelectric BST is associated with large dielectric loss, it is more attractive to use the paraelectric phase in the microwave devices. Although bulk BST has greater dielectric constant and lower dielectric loss than thin films of BST, bulk material requires a very large tuning electric field to tune its capacitance. It is also known that bulk BST has a dielectric peak around the *Curie* temperature and so the dielectric properties of bulk BST are more temperature dependent than thin film BST. In practice, BST thin films are much more attractive for applications in microwave devices. However, the dielectric properties of BST thin films are heavily influenced by the substrates, strain, compositions and deposition process parameters. This thesis focuses on the modification of the dielectric properties of BST thin films by Li and Co ion doping and the relationship between the crystal structure and dielectric properties.

In this work, an alternative tunable material (pyrochlore BZN) has been proposed to replace the traditional BST. Cubic pyrochlore BZN thin film has very small dielectric loss, relatively high dielectric constant (120) and very small TTC. According to figure 2.15(a), thin film BZN's dielectric relaxation peak is at very low temperature (<100K) and so the dielectric loss of this material is very low at room temperature. In addition, the dielectric properties of BZN thin film are independent of the strain induced by the substrate which allows the material to be easily integrated into MMIC.

In this thesis, the crystal and microstructures of BZN and BST thin films are characterized by using instruments such as XPS, XRD, EDX, AFM and SEM. The elemental compositions of the thin films were studied by XPS and EDX techniques,

respectively. A coplanar waveguide (CPW) and metal insulated metal (MIM) capacitor method have been employed to measure the microwave dielectric properties of the thin films. The film synthesis methods and microwave characterization methods are presented in chapters 3 and 5.

References:

[1] J. M. Vega, *Dielectric materials for electrical engineering*, John Wiley & Son, 3-6, 2010.

[2] K. J. Uchino, *Piezoelectric actuators and ultrasonic motors*, Kluwer Academic,13, 2000.

[3] J. H. Koh, *Processing and properties of ferroelectric Ag(Ta,Nb)O3 thin films (thesis)*, Royal Institute of Technology, Sweden, 2002.

[4] J. K. West and L. L. Hench, *Principles of electronic ceramics*, John Wiley & Sons, 193-245, 1989.

[5] L.A.A. Warnes, *Electronic materials*, Macmillan Education, 209-218, 1990.

[6] C. K. Ong L.F Chen, *Microwave electronics measurement and materials characterization*, John Wiley & Sons, 12-384, 2004.

[7] T. J. Jackson, P. Bao, X. Wang and M. J. Lancaster, "Barium Strontium Titanate thin film varactors for room-temperautre microwave device applications," *J. Phys. D: Appl. Phys* ,vol. 41 ,6, 063001, 2008.

[8] D. Damjanovic, "Ferroelectric, dielectric and piezoelectric properties of ferroelectric thin films and ceramics," *Rep. Prog. Phys* ,vol.61 ,9, 1267-1324, 1998.

[9] V.O. Sherman, A. K. Tagantsev, K. F. Astafiev, *et al*, "Ferroelectric materials for microwave tunable applications," *Journal of Electroceramics* ,vol. 11, 5-66, 2003.

[10] H. L. Wang, *Strucutre and dielectric properties of perovskite Barium Strontium Titanate ($BaTiO_3$) (thesis)* , San Jose State University, United Sates of America, 2002.

[11] E. K. Hollmann, O. G. Vendik, A. B. Kozyrev, and A. M. Prudan, "Ferroelectric tuning of planar and bulk microwave devices," *Journal of Superconductivity* ,vol. 12 ,2, 325-338, 1999.

[12] S. S. Gevorgian and E. Ludvig, "Do we really need ferroelectrics in paraelectric phase only in electrically controlled microwave devices," *IEEE Trans Microwave Theory and Techniques* , vol.49 , 11, 2117-2124, 2001.

[13] Z. Suo T. M Shaw, M. Huang, E. Liniger, *et al*, "The effect of stress on the dielectric properties of Barium Strontium Titanate thin films," *Applied Physics Letters* , vol. 75 ,14, 2129-2131, 1999.

[14] J. Kub, D. Rafaja, D. Simek, J. Lindner and J. Petzelt, "Microstructure of $Ba_xSr_{1-x}TiO_3$ thin films grown on sapphire substrates," *Thin Solid Films* ,vol. 422 ,1, 8-13, 2002.

[15] C. L. Canedy, H. Li, S. P. Alpay, "Dielectric properties in heteroepitaxial $Ba_{0.6}Sr_{0.4}TiO_3$ thin films: effect of internal stress and dislocation-type defects," *Applied Physics Letters* ,vol. 77 ,11, 1695-1697, 2000.

[16] S. G. Lu, X. H. ZHu, C. L. Mak and K. H. Wang, "Compositionally graded $Ba_xSr_{1-x}TiO_3$ thin films for tunable microwave applications," *Materials Chemistry and Physics* ,vol. 79, 2-3, 157-160, 2003.

[17] S. E. Moon, S. J. Lee, H. C. Ryu. *et al*, "Microwave properties of compositionally graded $(Ba,Sr)TiO_3$ thin films according to the direction of the composition gradient for tunable microwave applicants," *Applied Physics Letters* ,vol. 82, 13, 2133-2135, 2003.

[18] P. Rundqvist, A. Vorobiev, K. Khamachane, and S. Gevorgian, "Microwave loss mechanisms in $Ba_{0.25}Sr_{0.75}TiO_3$ thin film varactors," *J. Appl. Phys*, vol. 96 ,8, 4642-4649, 2004.

[19] P.C. Joshi, M.W. Cole, *et al*, "The influence of Mg doping on the materials properties of $Ba_xSr_{1-x}TiO_3$ thin films for tunable device applications," *Thin solid films* ,vol. 374 ,1, 34-41, 2000.

[20] P.C. Joshi, E. Ngo, *et al.*, "Electrophoretic deposition of pure and MgO-modified $Ba_{0.6}Sr_{0.4}TiO_3$ thick films for tunable microwave devices," *Applied Physics Letters* , vol.79 ,2 , 248-250, 2001.

[21] L. Wu, S. Wu, F.C Chang, Y. T. Shen *et al,* "DC field dependence of dielectric constant andloss factor of Al_2O_3- doped barium strontium titanate for application in phased array antennas," *Journal of Materials Science*, vol. 35 ,23, 5945-5950, 2000.

[22] M. Y. Fan and S. L. Jiang, "Influence of La-Mn-Al Co-doping on dielectric properties and structure of BST thick film," *Journal of Electronic Science and Technology of China, vol.* 7, 3 , 281-285, 2009.

[23] B. L Cheng, S.Y Wang, "Dielectric properties of Co-doped $Ba_{0.5}Sr_{0.5}TiO_3$ thin films fabricated by pulse laser deposition," *Journal of Crystal Growth,* vol. 259 ,1-2, 137-143, 2003.

[24] G. Vélu, A. Khalfallaoui, L. Burgnies, J. C. Carru, "Characterization of doped BST thin films deposited by sol-gel for tunable microwave devices," *IEEE Trans Ultrason Ferroelectr Freq Control.* vol.57 ,5, 295-298, 2010.

[25] M. S. Guo, S. X. Wang, *et al*, "Effect of K-doping on the dielectric and tunable properties of $Ba_{0.6}Sr_{0.4}TiO_3$ thin films prepared by RF magnetron sputtering"," *Journal of Crystal Growth* , vol. 306 ,1, 22-26, 2007.

[26] C. R. Yang, W. L. Zhang and W. C. Hu, "Fabrication and characteristics of La, Cd and Sn doped BST thin films by sol-gel method," *J Mater Sci: Mater Electron* ,vol. **19** ,12, 1197-1201, 2008.

[27] B. L. Zhu, X. H. Sun, T. Liu, M. Y. Li and X. Z. Zhao, "Dielectric and tunable properties of K-doped $Ba_{0.6}Sr_{0.4}TiO_3$ thin films fabricated by sol-gel method," *J. Appl. Phys*, *vol.* 99, 8, 084103, 2006.

[28] P. C. Joshi, M. W. Cole, and M. H. Ervin, "La doped $Ba_xSr_{1-x}TiO_3$ thin films for tunable device applications," *J. Appl. Phys*, vol. 89, 11, 6336-6340, 2001.

[29] S. H. Kim and J. H. Koh, "Li-doped $(Ba,Sr)TiO_3$ thick film interdigital capacitors for microwave applications," *Microelectronic Engineering* , vol. 86 ,1, 59-62, 2002.

[30] S. H. Kim, "The microwave properties of Li doped 0.7 $(Ba,Sr)TiO_3$ – 0.3MgO thick film interdigital capacitors on the alumina substrates", *Microwave Engineering* ,vol. 87 ,1, 79-92, 2010.

[31] C. S. Liang and J. M. Wu, "Electrical properties of W-doped $(Ba_{0.5}Sr_{0.5}TiO_3)$ thin films," *Journal of Crystal Growth*, vol. 274 ,1-2, 173-177, 2005.

[32] J. Zhu, W. F. Qin, J. Xiong, *et al*, "Electrical behaviour of Y-doped $Ba_{0.6}Sr_{0.4}TiO_3$ thin films," *J Mater Sci: Mater Electron* , vol. 18 , 12, 1217-1220, 2007.

[33] K. T. Kim and C. I. Kim, "The effect of Cr doping on the microstructural and dielectric properties of $(Ba_{0.6}Sr_{0.4})TiO_3$ thin films," *Thin Solid Films*, vol. 472 ,1-2, 26-30, 2005.

[34] M. Ouaddari, S. Delprat, F. Vidal, *et al*, "Voltage and frequency dependent dielectric properties of BST thin films on alumina substrate," *IEEE Trans Microwave and Wireless Components Letters, vol.* 13 , 6, 211-213, 2003.

[35] Q. X. Jia, X. D. Wu and A. T . Findikoglu, "High temperature superconductors (HTS) material tunable and adaptive bandpass filter using a nonlinear dielectric thin film of $SrTiO_3$," *Applied Physics Letters*, vol. 68, 12, 1651, 1996.

[36] G. Subramanyam, F. W. Van Keuls and F. A. Miranda, "Design and development of ferroelectric tunable microwave components for Ku- and K- band Satellite Communication Systems," *IEEE Trans Microwave Theory and techniques* , vol. 48 ,7, 1181-1189, 2000.

[37] C. A. Randall , S. T. Mckinstry and R.L. Thayer, "Medium permittivity bismuth zinc niobate thin film capacitor," *J. Appl. Phys, vol.* 94, 3, 1941-1947, 2003.

[38] H. Funakubo and S. Okaura, "Low strain sensitivity of the dielectric property of pyrochlore Bi-Zn-Nb-O films," *Applied Physics Letters,* vol, 92 ,18, 182901 ,2008.

[39] S. M. Zanetti, *et al,* "Synthesis and Characterization of Bismuth Zinc Niobate Pyrochlore Nanopoweder," *Materials Research*, vol. 10, 3, 261-266, 2007.

[40] S. H. Young, P. Hong, H. Y. Lee, *et al*, "Voltage tunable dielectric properties of rf sputtered $Bi_2O_3 - ZnO - Nb_2O_3$ pyrochlore thin films," *Thin Solid Films*, vol. 419 , 1-2, 183-188, 2002.

[41] B. Jiang, S.W Jiang, X. Z. Liu and Y. R. Li, "Laser deposition and dielectric properties of cubic pyrochlore Bismuth Zinc Niobate thin films," *J.Vac.Sci.Technol, vol.* 24, 261-263, 2006.

[42] J. W. Lu and S. Stemmer, "Low loss, tunable Bismuth Zinc Niobate films deposited by rf magnetron sputtering," *Applied Physics Letters*, vol. 83, 12, 2411-2413, 2003.

[43] T. G. Amos I. Levin, J. C. Nino, T. A. Vanderah, C. A. Randall, and M. T. Lanagan, "Strucutre study of unusual cubic pyrochlore $Bi_{1.5}Zn_{0.92}Nb_{1.5}O_{6.92}$," *Journal of Solid State Chemcistry,* vol. 168, 1, 69-75, 2002.

[44] S. T. Mckinstry, R. Wei, C. A. Randal and R. Thomas, "Bismuth Zinc Niobate pyrochlore dielectric thin films for capacitive applications," *J. Appl. Phys*, vol. 89, 1, 767-773, 2001.

[45] S. Kamba, H. Wang, M. L. Zhang and X. Yao, "Microwave and infrared dielectric response of monoclinic Bismuth Zinc Niobate based pyrochlore ceramics with ion substitution in A site," *J. Appl. Phys*, vol. 100, 3, 034109, 2006.

[46] M. T. Lanagan, J. C. Nino, C. A. Randall and S. Kamba, "Anomalous broad dielectric relaxationin $Bi_{1.5}Zn_{1.0}Nb_{1.5}O_7$ *Pyrochlore," Physics Review. B , vol.* 66, 5, 054106, 2002.

[47] J. C. Nino, M.L. lanagan, C.A. Randall, *et al,* "Correlation between infrared phonon modes and dielectric relaxation in $Bi_2O_3 - ZnO - Nb_2O_3$ cubic pyrochlore," *Applied Physics Letters,* vol. 81, 23, 4404-4406, 2002.

[48] H. Wang, X. Yao, M. L. Zhang, "Effect of Ca substitution on structure and dielectric properties of Bismuth-based microwave ceramics," *J Electroceram, vol.* 21,1-4, 461-464, 2008.

[49] H. L. Du and X. Yao, "Dielectric relaxation characteristics of Bismuth Zinc Niobate pyrochlores containing titanium," *Physica B Condensed Matter,* vol. 324 1-4, 121-126, 2002.

[50] S. Kamba and H. Wang, "Microwave dielectric relaxation in cubic Bismuth based pyrochlores containing titanium," , *J. Appl. Phys*, vol. 100, 1, 014105, 2006.

[51] K. Sudheendran and K. Chinnayya and J. Raju, "Microwave dielectric properties of Ti-substituted $Bi_2(Zn_{2/3}Nb_{4/3})O_7$ pyrochlores at cryogenic temperature," *J.Am. Ceram. Soc, vol.* 92, 6, 1268-1271, 2009.

[52] Y. Zhang, S. T. Zhang, M. H. Lu, *et al*, "Structure and dielectric properties of $Bi_{1.5}Zn_{1.0}Nb_{1.5-x}Ti_xO_7$ (x = 0, 0.05, and 0.10) thin films," *Applied Physics Letters*, vol. 90, 4, 042903, 2007.

Chapter 3: Thin film synthesis and characterizations

This chapter discusses the synthesizing and characterization methods of the BST and BZN thin films. In section 3.1, different types of thin films deposition methods are compared and the justifications for using chemical solution deposition (CSD) method are also presented. The details of the thin film deposition procedure are presented in sections 3.1, 3.2, 3.3 and 3.4. Finally, the characterization methods for determining the crystal and microstructures of the thin films are discussed in section 3.5.

3.1 Thin film deposition techniques

Thin films can be synthesized by three different techniques: chemical solution deposition (CSD), physical vapour-deposition (PVD) and chemical vapour-deposition (CVD). All deposition techniques have their advantages and drawbacks. The choice of using the CSD method for thin film deposition was decided by the requirements, cost, film thickness and manufacturability. In this work, the chemical solution deposition (CSD) technique has been employed to fabricate BST and BZN thin films. In the following section, the advantages and disadvantages of each deposition technique will be discussed. Sections 3.3 and 3.4 provide the detailed procedures used to synthesise BST and BZN thin films.

3.1.1 Physical vapour deposition (PVD)

Physical vapour deposition (PVD) is a technique which deposits a thin film on the surface of a solid substrate by condensation from the vapour phase [1]. Therefore,

only physical effects are involved in PVD. The deposition is usually achieved by the following three steps **[1]**.

(a) The material to be deposited is converted into a gas phase (Vapour) by different vaporization methods.

(b) The emitted particles are transferred from the source material to the substrate through the gas phase.

(c) The vapour is condensed on the substrate to form a solid thin film layer by nucleation and diffusion.

DC sputtering

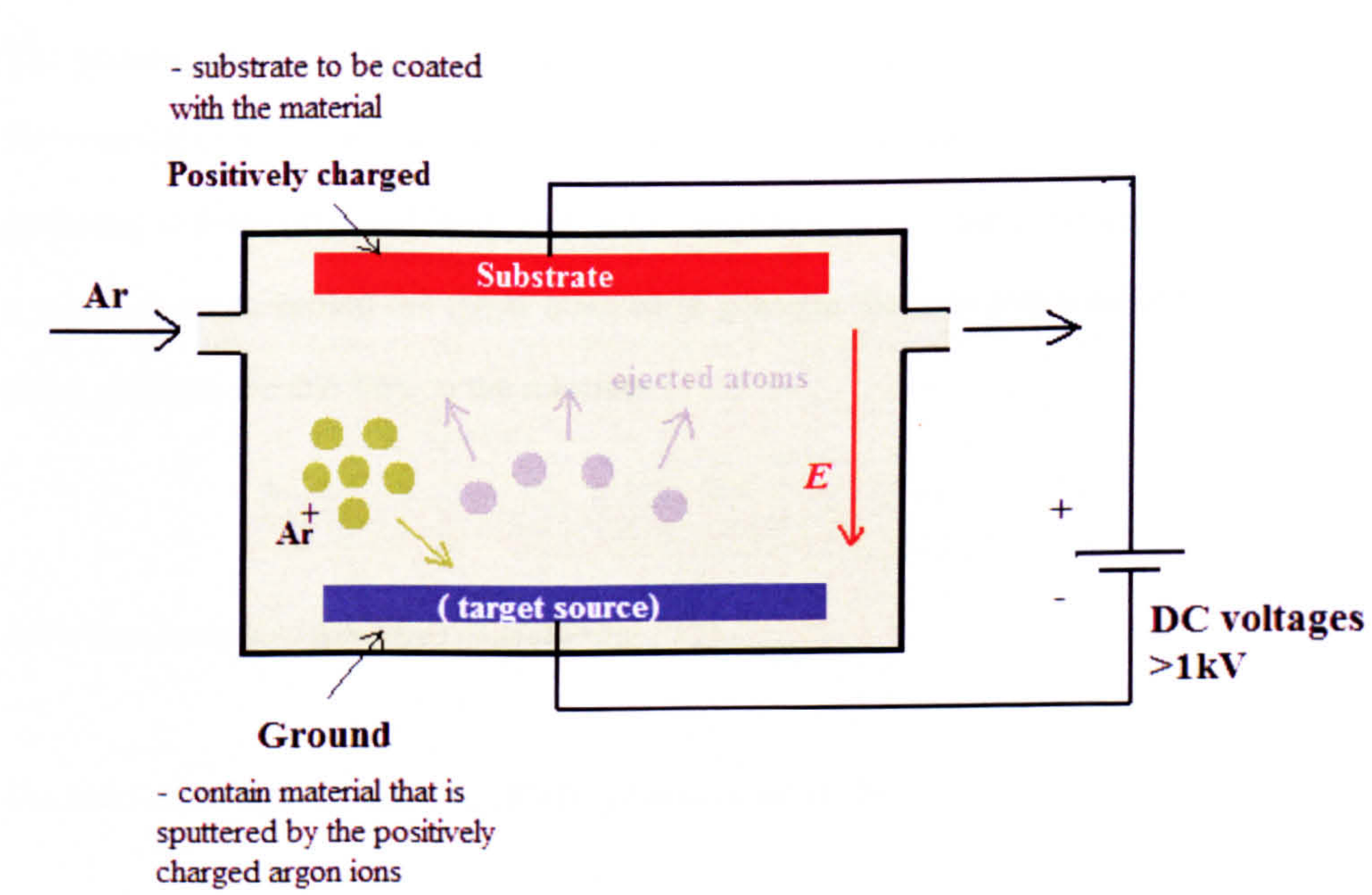

Figure 3.1 shows the working principle of DC sputtering system (reproduced from **[2]**)

Sputtering is a grouping of different deposition techniques including DC-sputtering, RF-sputtering, Plasma sputtering, Magnetron-sputtering, etc. The most commonly

used process is DC-sputtering (figure 3.1). In DC-sputtering, positive ions such as argon are used to strike the surface of the target material. The whole process is carried out in a vacuum chamber which contains both the substrate and target material. As shown in figure 3.1, the target is connected to a ground and the substrate is connected to a positive voltage supply (>1kV). Therefore, a strong electric field (E) is created inside the chamber. The positively charged argon ions (Ar^+) are accelerated towards the negatively charged target material, striking the target with a very high velocity which removes part of the target material. As the argon ions collide with the target, the atoms of the target material are ejected towards the substrate **[3]**. At last, the ejected atoms stay onto the surface of the substrate.

RF sputtering

The process described above is usually used to fabricate conductive thin films **[1]**. For depositing insulator materials (with high dielectric constant) such as BST, RF sputtering is frequently used **[4-6]**. Unlike DC-sputtering, a RF potential is applied to a metal electrode behind the target material to generate the ions that bombard the target and form the thin film on the substrate.

Advantages and disadvantages of sputtering PVD

The main advantages of sputtering PVD techniques are **[1, 7]**:

(a) Dense and uniform thin film

(b) Good adhesion to the substrate

(c) Better reproducibility

(d) Simple film thickness control

The main disadvantage of sputtering is the manufacturing cost, since the sputtering process and all other PVD processes are carried out in vacuum conditions and require very high operation voltages.

3.1.2 Chemical vapour deposition (CVD)

The chemical vapour deposition (CVD) technique is also a common method of fabricating ferroelectric thin films **[8-10].** For chemical vapour deposition (CVD), a mixture of vapour species enters the deposition chamber, which contains the heated substrate, and undergoes heterogeneous gas phase reactions to form a layer of solid film onto the heated substrate surface **[11]**.

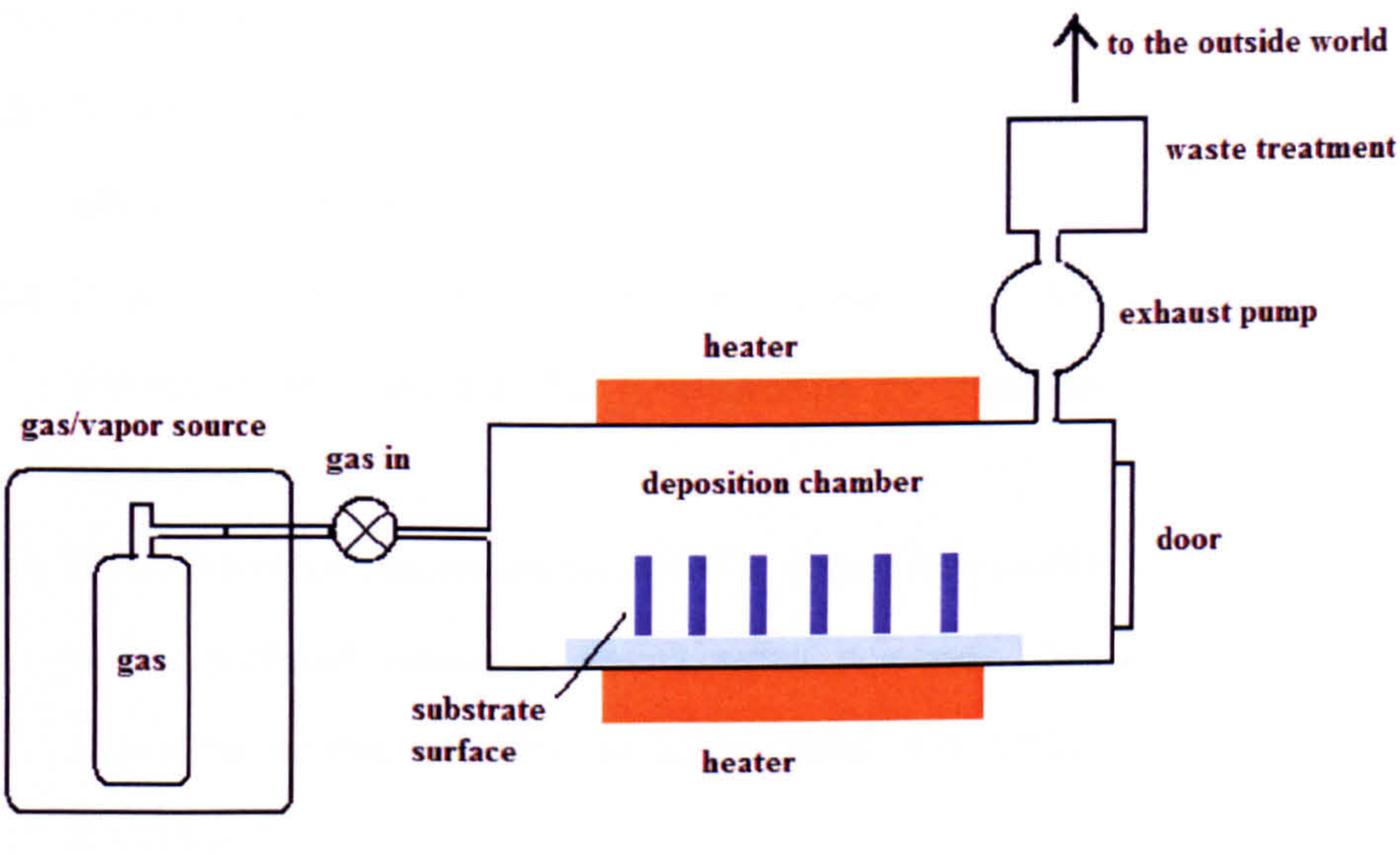

Figure 3.2 shows the instrument set up of a CVD system (reproduced from **[12]** and **[13]**).

The above figure shows the working principle of a basic CVD system. As shown, a mixture of gas phase chemical vapour enters into a tube furnace like deposition chamber through the gas inlet. The sample substrates are placed inside the deposition

chamber and heated to a high temperature. A vacuum pump is used to keep the deposition chamber at low pressure or under vacuum conditions. At the same time, the chemical waste is pumped out of the chamber to the outside. The deposition involves homogeneous gas phase reactions and heterogeneous chemical reactions near the vicinity of the heated substrate surface **[11].** These reactions lead to the formation of solid thin films on the surface of the substrates. The substrates coated with thin films can be moved away from the chamber through the door.

Advantages and disadvantages

The CVD technique offers many distinct advantages over other methods **[11].**

(a) It Produces high quality and pure crystal materials

(b) It produces a uniformly coated thin film with very good adhesion with the substrate

(c) It provides the ability to control the crystal phase and microstructures of the thin film by controlling the deposition parameters.

(d) It uses deposition temperature below 600°C which is compatible with commercial microchip manufacturing processes. This allows the tunable thin films to be integrated with MMIC microchips.

The CVD method also has disadvantages including :

(a) The chemicals used for deposition are usually toxic, corrosive and flammable gases **[11].**

(b) It's difficult to form a multicomponent material with desired stoichiometry.

(c) The use of sophisticated reaction chamber and vacuum systems.

3.1.3 Chemical solution deposition (CSD)

The chemical solution deposition technique (CSD) **[14-16]** is a non-vacuum thin film deposition process which has been widely used in the fabrication of tunable thin films. A common feature **[17]**of this method is that the as-deposited film is transformed into the desired crystal phase through an amorphous intermediate.

Deposition process

The CSD deposition technique can be divided into five basic steps:

(a) Synthesis of the organic precursor solution,

(b) Deposition by wet chemical methods such as: spin coating or dip-coating processes.

(c) Formation of an amorphous film by drying the organic species and solvent on a hotplate at 300-400°C.

(d) Repeat previous steps (b) and (c) in order to obtain the required film thickness,

(e) High-temperature annealing (typically around 600–1100°C) to crystallize the amorphous film into the desired crystal phase.

Figure 3.3 shows a flow diagram of the CSD process.

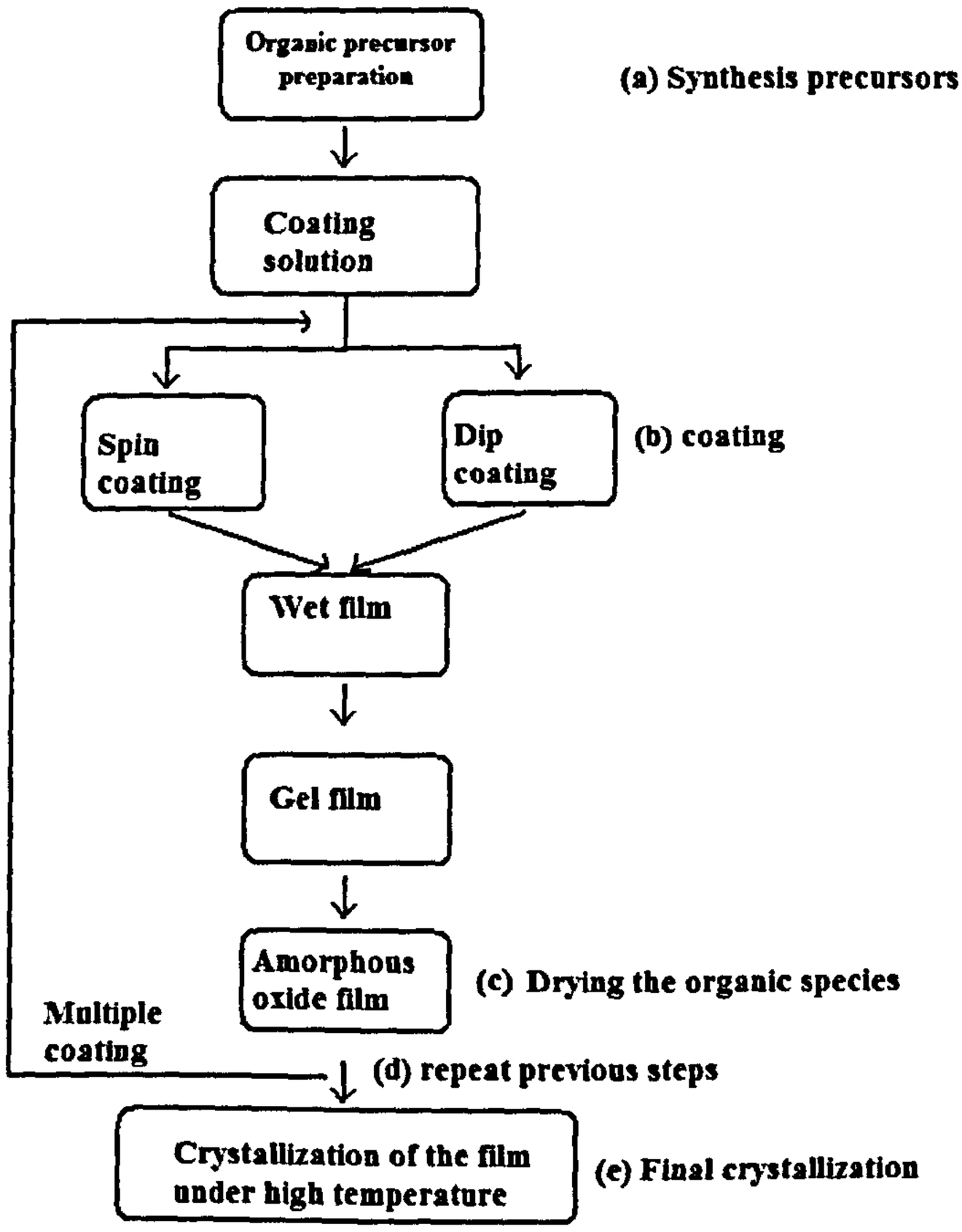

Figure 3.3 Process of Chemical solution deposition (CSD) (reproduced from [18])

Advantages and disadvantages of CSD

The CSD technique offers several advantages including **[17]**:

(a) Precise control of the composition of the material,

(b) Cost effectiveness,

(c) Fabrication process that can be carried out in air without vacuum condition,

(d) Quick prototyping which allows a new material to be produced in short time.

However, thin films deposited by the CSD method can also have problems such as poor uniformity, cracking and lack of phase purity **[17]**. Another major challenge of the CSD technique is the problem of repeatability, since the chemical precursors are prepared manually and the chemical solution degrades as time passes.

3.1.4 Why use the Chemical Solution Deposition (CSD) method?

In general, all of the deposition techniques (CVD, PVD and CSD) have their advantages and disadvantages. As mentioned earlier, the choice of which deposition technique to use is decided by the requirement and specification of the task. In this work, the desired thin film deposition technique must have the following features:

(a) Safe to be used and cost effective

(b) Simple equipment

(c) Precise control of the material's stoichiometry

(d) Quick prototyping

According to section 3.11 and 3.12, both CVD and PVD techniques offer the advantages of high purity crystal thin films. In particular, thin films can be crystallized at a lower processing temperature in CVD which allows it to be integrated with a MMIC microchip. However, both techniques involve the use of sophisticated reactor and/ or vacuum systems. In CVD, flammable and toxic chemical precursors are often used to produce the thin films. Furthermore, it is difficult to synthesize the multicomponent material with well-controlled stoichiometry using the CVD technique. In comparison with the CVD and PVD techniques, the CSD

technique offers the advantages of easy composition control, low cost, quick prototyping, and depending on the precursors used it can be performed in air. These features meet with our requirements. As a result, both BST and BZN thin films were synthesized by the CSD method.

3.2 CSD deposition

3.2.1 Organic precursor synthesis

Depending on the chemical preparation routes of the solution and the chemical compounds used in solution synthesis, the chemical solution deposition (CSD) techniques can be categorised into three main categories **[18].**

a) *Metal organic deposition (MOD):* In metal organic deposition (MOD), the metal-organic compounds are dissolved into a single organic solvent. This approach is very simple but it still poses one major disadvantage: large cracks can occur on the surface of the thin film **[18].** This is attributed to the excessive weight loss and shrinkage that occur in the solvent that coated on the surface of substrate. These cracks will significantly lower the dielectric properties of the thin films. Therefore, this synthesis method was discounted.

b) *Sol-gel*: The sol-gel process involves the generation of "sol" and the subsequent conversion to gels and hence to solid materials. In a typical sol-gel process, metal alkoxide has been used to form chemical species with *metal–oxygen–metal (M–O–M) bonds* by a two step reactions involving hydrolysis and condensation. At first, a hydrolysis reaction takes place **[17]:**

$$M(OR)_x + H_2O \rightarrow M(OR)_{x-1}(OH) + ROH$$

After hydrolysis, the formed precursor undergoes a condensation process [17] either by water elimination;

$$2M(OR)_{x-1}(OH) \rightarrow M_2O(OR)_{2x-2} + H_2O$$

or by alcohol elimination:

$$2M(OR)_x\text{-}OH \rightarrow M_2O(OR)_{2x-3}(OH) + ROH$$

At the same time as the above process is occurring, the alcohol-exchange reaction in the precursor also occurs, which results in a decrease in the hydrolysis sensitivity. Hence, it slows down the speed of hydrolysis [17].

$$M(OR)x + xR'OH \rightarrow M(OR')x + 2ROH$$

where OR′ is a less reactive 2-methoxyethoxy group and OR is the ractive alkoxy group [17].

In practice, the chemical solution is commonly prepared by mixing alkoxide compounds and metal acetate with 2-methoxyethanol. A major drawback of sol-gel is that the use of 2-methoxyethanol, which is a known teratogen that has safety issues [17]. To overcome this problem, a modified sol-gel synthesis (chelation) method has been proposed.

c) *Chelation process*: Chelation is a modified Sol-gel process. This process is called chelation because the chelation reaction is the key for defining the quality of the organic precursor [17, 18]. This process is also referred to as 'hybrid' because it uses both carboxylate and alkoxide precursors, and the B-site alkoxides react with the carboxylic acid to form chemical species with metal–oxygen-metal (M-O-M) bonds [18]. This is shown by the following:

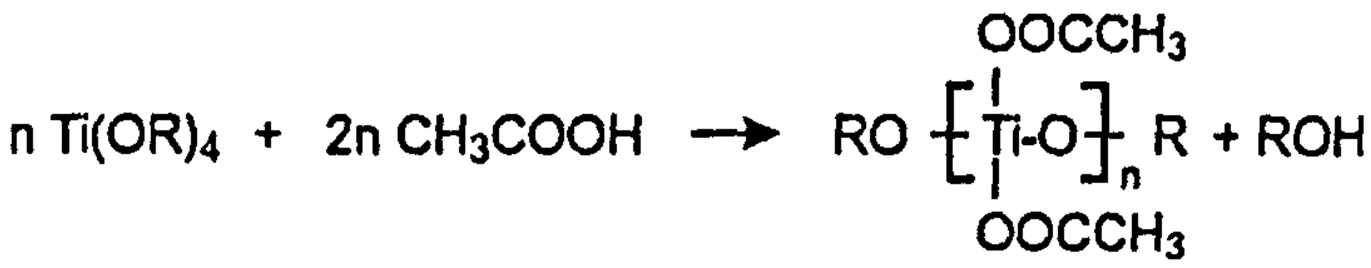

Figure 3.4 Chelation or "hybrid" reaction **[18].**

In practice, a carboxylic acid, such as acetic acid, and acetylacetone are used as solvents to dissolve the metal organic precursors instead of 2-methoxyethanol. The chelation process overcomes the safety problem posed by 2-methoxyethanol but still provides very high quality of thin films. However, the chelation process involves very complicated reactions such as chelation, esterfication, polymerization and hydrolysis **[17].** This makes it difficult to control the properties of the precursor and leads to a poor yield of the deposited thin film. In addition, the precursor is under constant attack by water, causing the precursor to degrade as time passes **[17].** Despite these drawbacks, the advantages of the chelation method, i.e. safe and quick, far outweigh its drawbacks.

3.2.2 Spin coating process

Once the organic precursor has been synthesized by the chelation process, the precursors can be applied to the surface of the substrate by a spin coating process. The surface of the substrate is fully covered with the chemical solution (*figure 3.5(a) and (b)*) and then accelerated to several thousand rpm for 10 seconds or more (*figure 3.5(c)*).

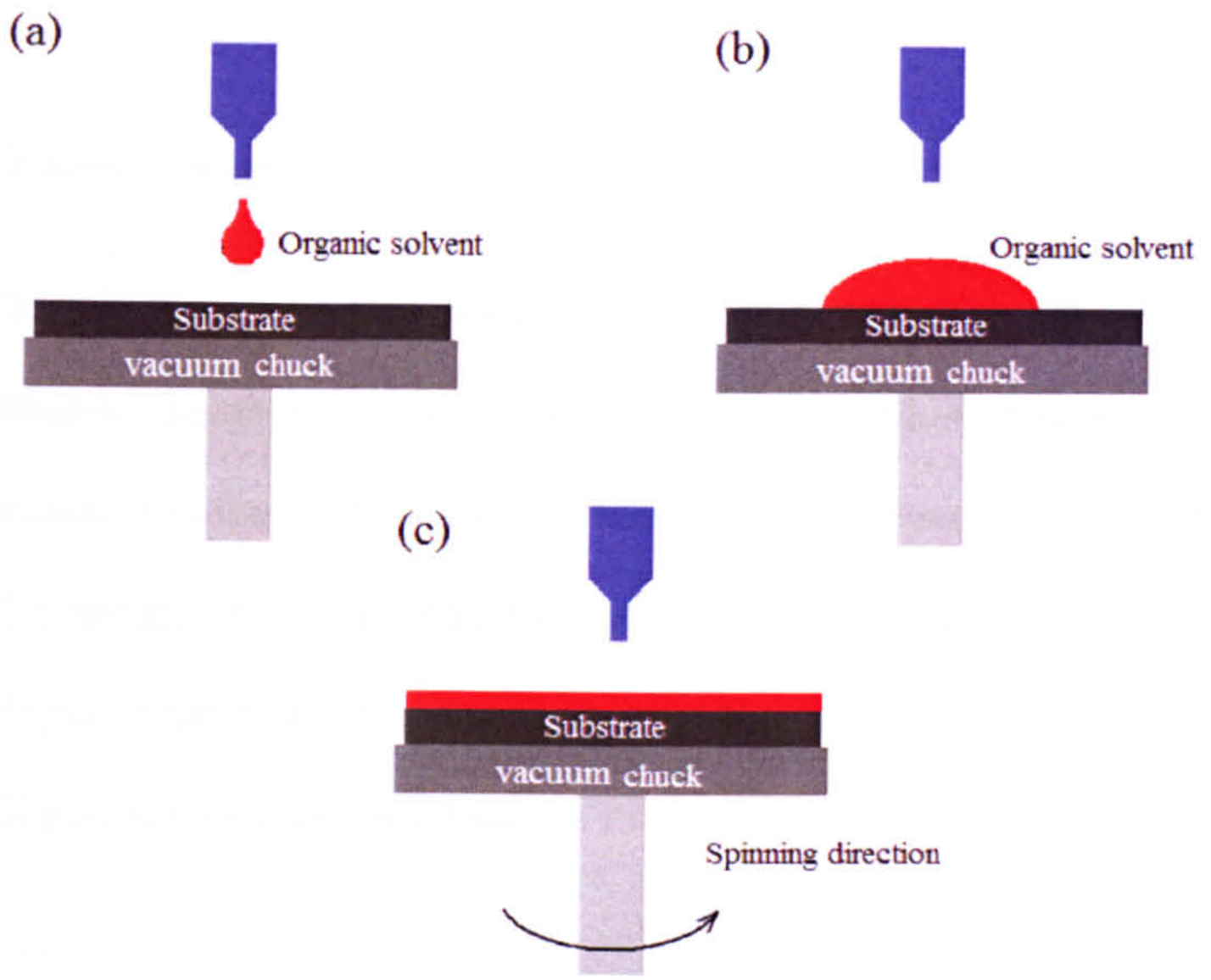

Figure 3.5 (a) dropping the organic precursor onto the substrate, (b) before the spinning of the chemical precursor, (c) after the spinning of the chemical precursor

After the precursor was coated onto the substrate, the sample is baked on a hotplate at 400°C to remove the organic residues. Then the sample is annealed at very high temperatures (e.g. between 600°C and 800°C) for crystallization. Consequently, a layer of thin film is deposited onto the substrate. In this work, the spin coating process has been repeated 6, 9 or 12 times to achieve the desired thickness (between 180nm and 300nm). The thickness of the film can be controlled by either changing the angular velocity, spin time or the number of spin coating cycles.

3.3 BST thin film synthesis process

In the present work, BST thin films with a composition of $Ba_{0.5}Sr_{0.5}TiO_{3.0}$ were doped by two different types of acceptor ions: (a) Co ions with concentrations of 0 mol% 0.25mol%, 0.5mol% and 1.0mol%; (b) Li ions with concentrations of 0 mol% 1mol%, 2mol% and 4mol%.

Organic precursor synthesis

The thin film deposition process involved three key steps: (1) solution synthesis, (2) substrate cleaning and (3) spin coating and annealing. As discussed in section 3.2, the organic solution of the BST thin film was synthesized using the chelation process. The starting precursors were barium acetate (99% Sigma Aldrich), strontium acetate (Sigma Aldrich 99%), titanium isopropoxide (Sigma Aldrich 97%), lithium acetate (Sigma Aldrich) and cobalt acetate (Sigma Aldrich).

The impurity in barium acetate is mainly Strontium (Sr) (2000mg/kg) which is also one of the elements in Barium Strontium Titanate Oxide material. (Deleted, since the impurity (Sr) of Ba is part of the BST material) Therefore, it does not invalid the effects of Li and Co doping. However, the increase of Sr concentration lowers the *Curie* temperature of the BST thin films. This results in a reduction of dielectric constant of BST thin films.

In contrast, titanium isopropoxide contains 3% of impurity including the metal oxides, which can affect the properties of BST thin films. However metal oxides can not react with acetic acid to form Oxide-Metal-Oxide chains in the synthesized organic solution. The metal oxide impurity in the synthesized organic precursor was removed by a filter.

The first step of synthesizing the organic solution is to add strontium acetate into a mixture of acetic acid (40ml Sigma Aldrich 99%) and ethylene glycol (20ml Sigma Aldrich) at 2:1 ratio (in volume). Here ethylene glycol was used as an addictive to change the viscosity of the organic solution in order to avoid the appearance of cracks on the thin films **[19]**.

To completely dissolve strontium acetate, it was necessary to heat the solution to 120°C for >10 min until the solution was transparent and clear. The equipment set up for this process is shown in figure 3.6(a) and (b).

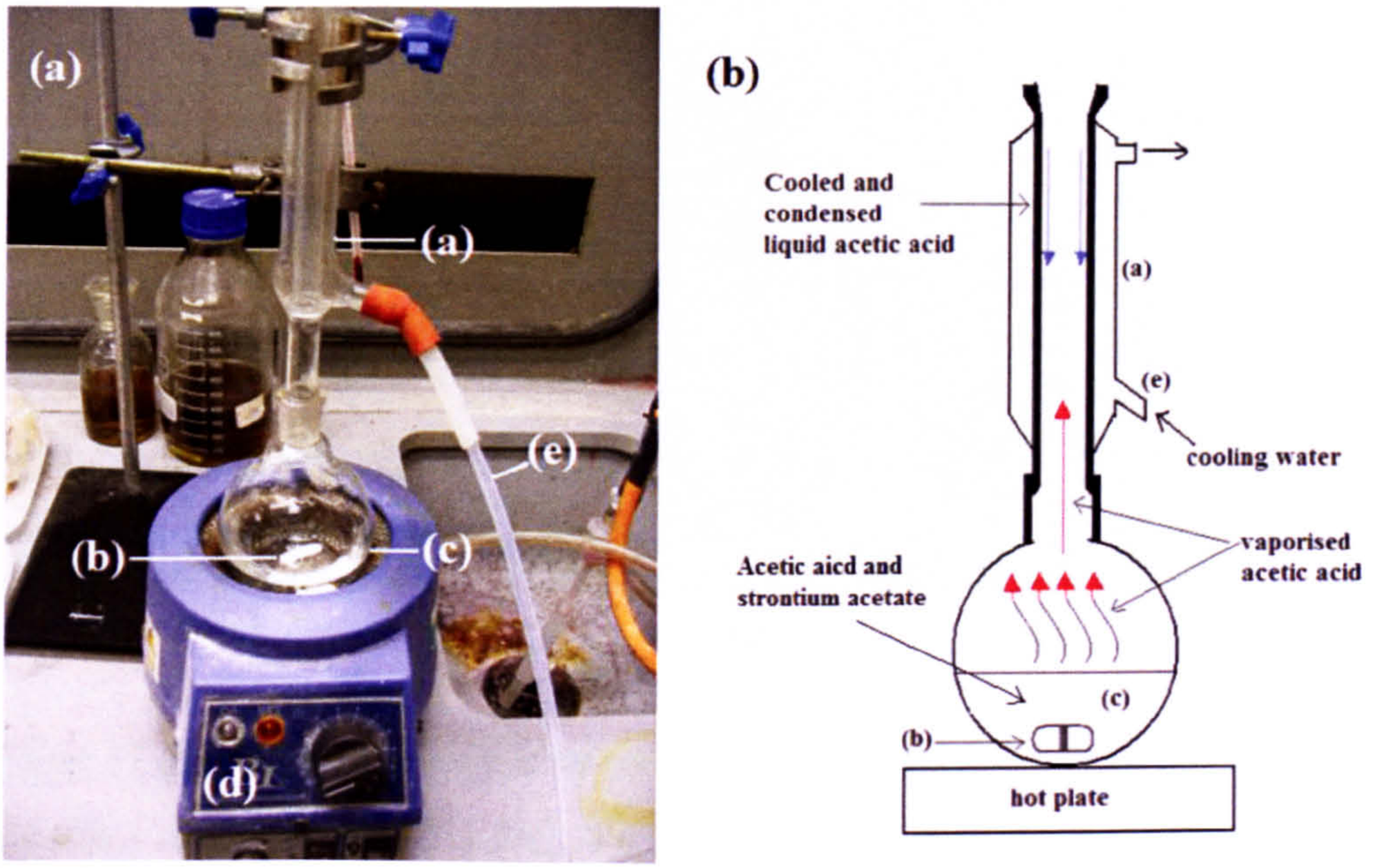

(a) condenser (b) stirrer (c) clean solution (strontium acetate and acetic acid) (d) heater and (e) cooling water tube

Figure 3.6 (a) The apparatus used for the chemical synthesis of the precursor and (b) a schematic of the working principle of distilling

Once the strontium acetate was completely dissolved, barium acetate was mixed with 30ml of acetic acid at 60°C for 5 min until it was completely dissolved. Both precursors were then mixed with each other at room temperature. Then titanium isopropoxide (Sigma Aldrich 99%) was carefully added into 10ml of acetylacetone (Sigma Aldrich). A magnetic stirrer was used to aid the process. The titanium isopropoxide solution was added into the mixed Ba/Sr solution to form a clean and transparent solution (BST precursor). In this work, some of the BST thin films were also doped by different concentrations of Li or Co ions. To achieve this doping, Li or Co acetate was dissolved into acetic acid and added to the BST precursor to form the final organic solution for spin coating. For health and safety reasons, all chemical

synthesis processes were carried out in a fume cupboard. The following figure shows the organic precursors with different concentration of Co ions.

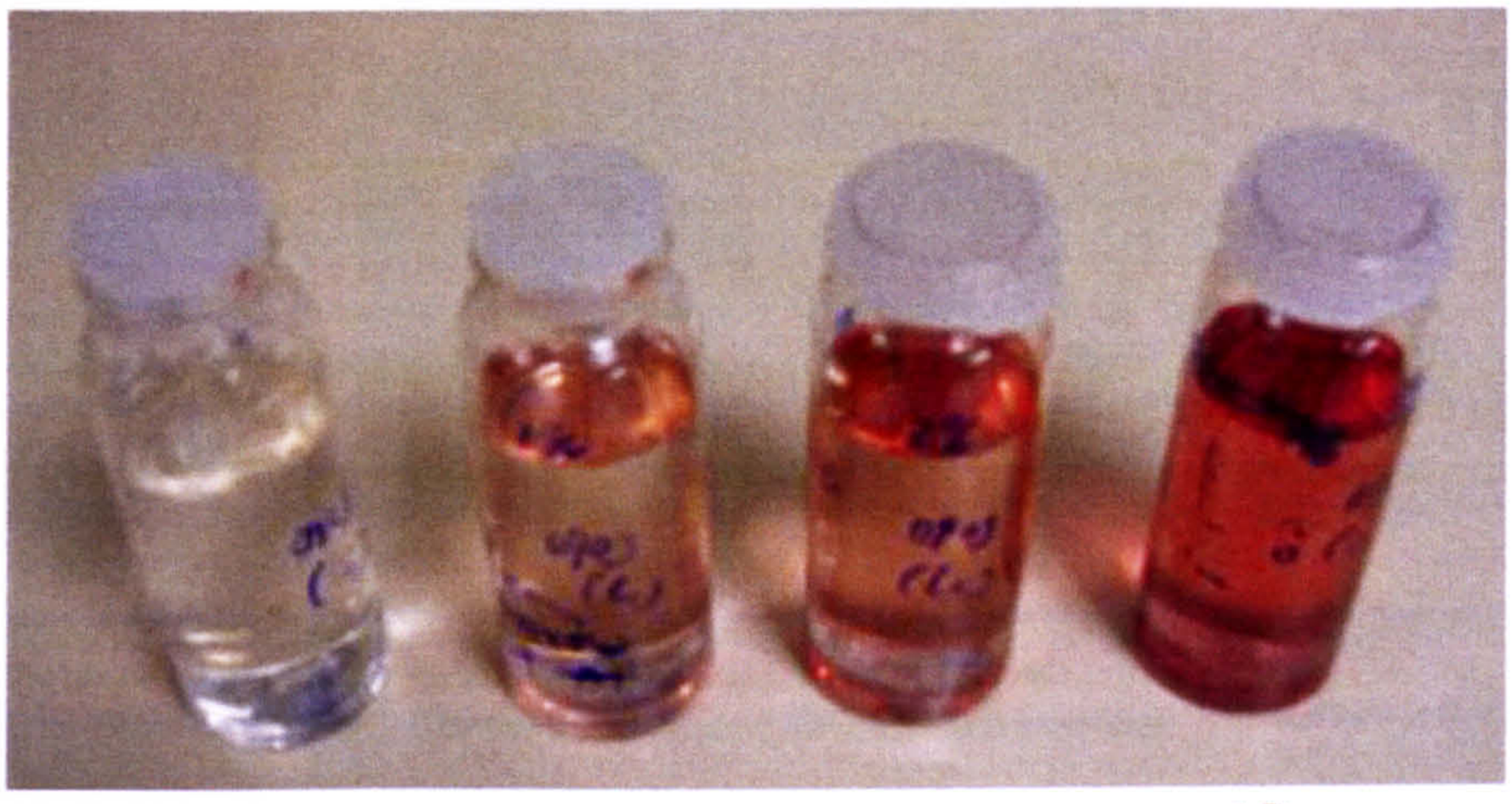

Figure 3.7 Different concentrations of the synthesized organic precursors for the BST deposition (a) 0mol%, (b) 0.25mol%, (c) 0.5mol%, and (d) 1.0mol% of Co doped $Ba_{0.5}Sr_{0.5}TiO_{3.0}$.

Substrate cleaning process

Prior to the spin coating process, the substrates needed to undergo a three step cleaning process where the sample substrates are immersed into methanol, acetone and propan-2-ol, in an ultrasonic bath (*figure 3.8*), for 3 minutes each. The substrate was then immersed into de-ionised water and dried using nitrogen gas. Finally, the substrates were baked at 160°C for 3 min to remove the organic residues. The cleaning process was carried out in a class 100 clean room (under laminar flow cabinet).

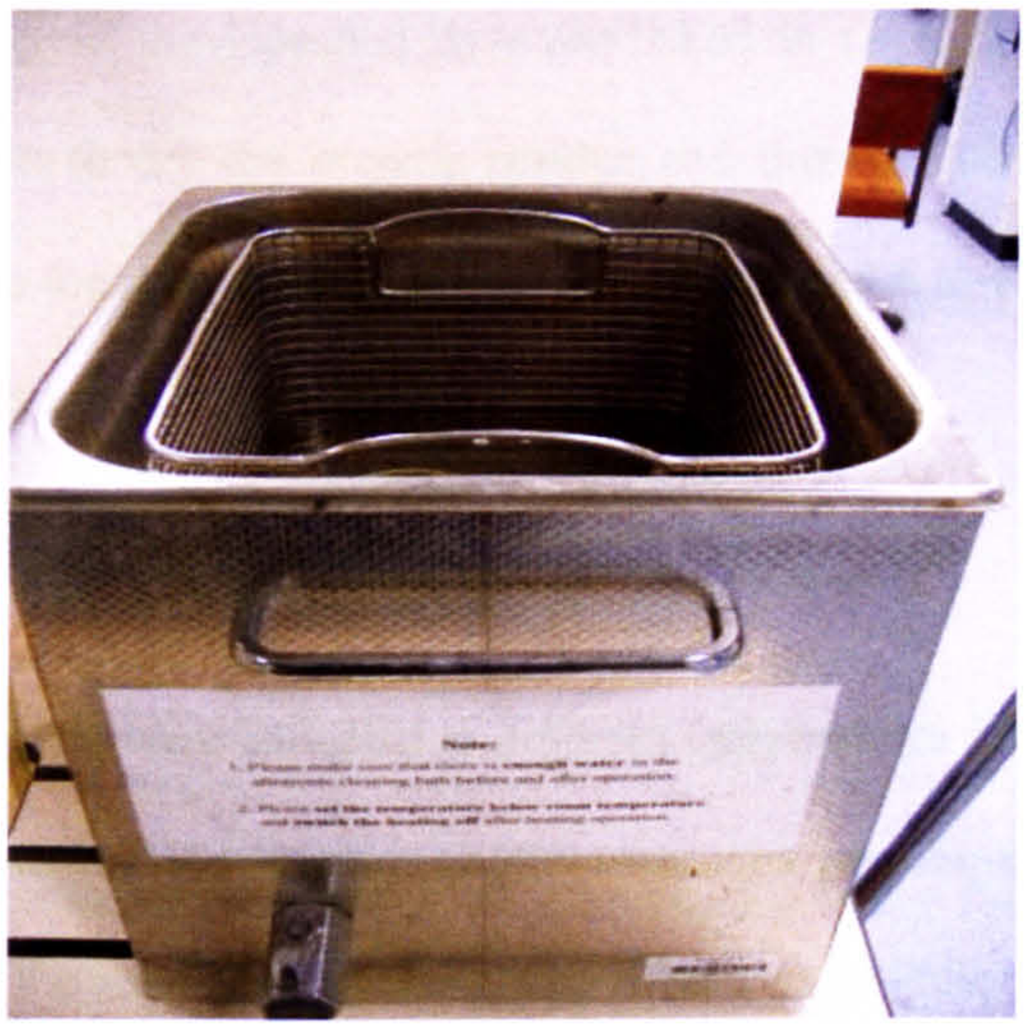

Figure 3.8 Ultrasonic bath used for substrate cleaning

Spin coating process

The BST thin films were coated onto the substrates by using a *Model 100* (provided by cost effective instrument or CEE) spin coater as shown in figure 3.9. The substrate was held onto the chuck of the spin coater by a vacuum. The prepared organic solution was dropped onto the substrate by using a pipette. Once the substrate was fully covered by precursor, it was accelerated to 4000 rpm for 10 seconds.

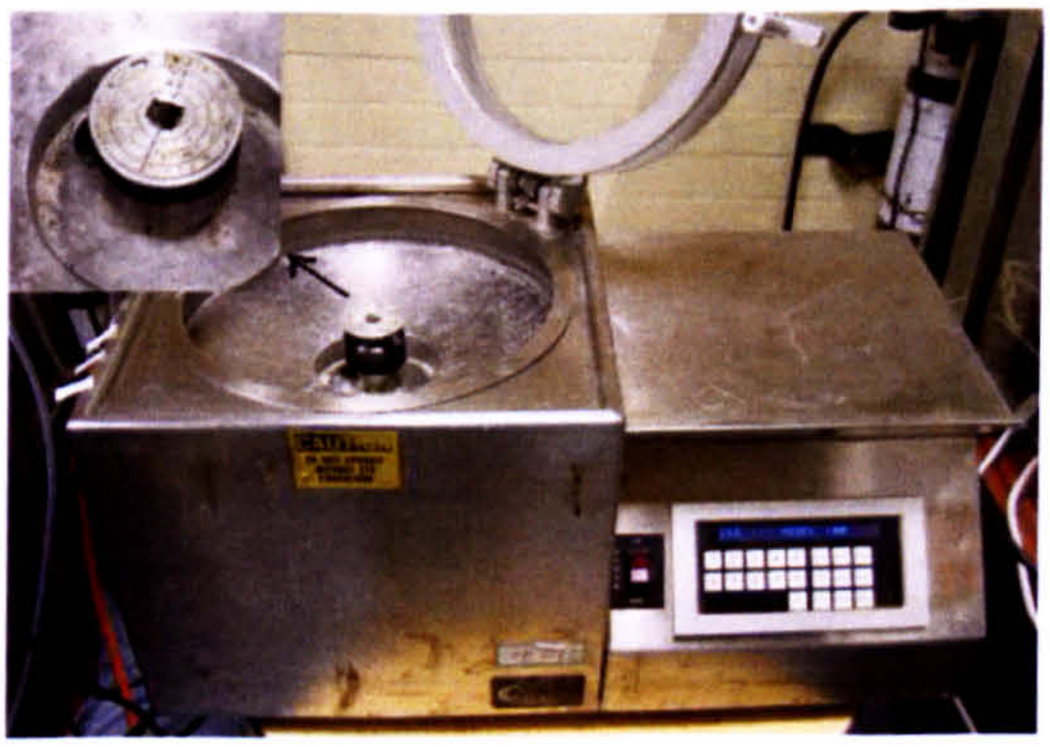

Figure 3.9 Photograph of the spin coater and a zoomed in photo of the vacuum chuck with substrate

After each spinning cycle, the deposited layer was baked on a hotplate (*Tenway 1000*) at 400°C for 3 min to dry the organic residue and then at 700°C for 5 min to crystallize the film to the right phase. This cycle was repeated 6 to 12 times until the desired thickness was achieved.

The completed thin films were annealed at different temperatures (600°C, 700°C and 800°C) for 2 hours. An X-ray diffraction (XRD) technique was employed to analyses the crystallization of the annealed thin films. The X-ray results indicated that the BST thin film annealed at 800°C is well crystallized. In the present work, all BST thin films underwent a final crystallization anneal at 800°C for 2 hours in an open furnace.

Figure 3.10 shows the furnace used. The choice of the temperature and time were dependent on which kind of device was to be fabricated. For making a CPW, the thin film was annealed at 800°C for 2hrs. However, for making a MIM capacitor, the BST film was annealed at 700°C for just 10min, since the capacitor's substrate was made of gold which can be damaged by high temperature annealing. The exact parameters of sample annealing (time and temperature) are given in chapters 6 and 7.

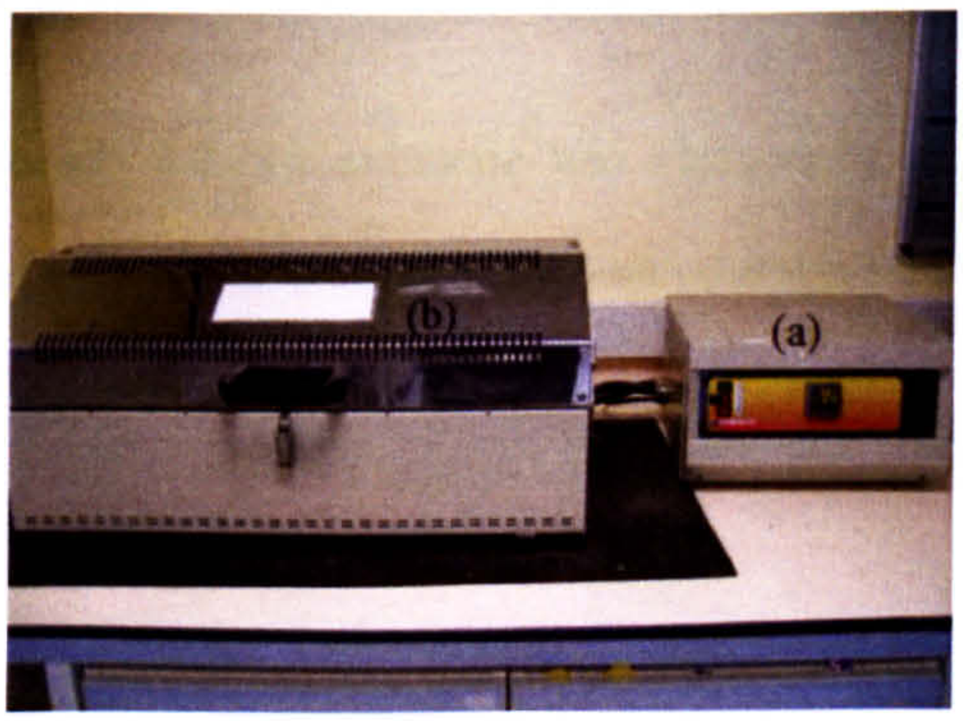

Figure 3.10 CARBOLITE furnace (a) temperature controller for the furnace (b) furnace chamber

3.4 BZN thin film Synthesis process

In this work, BZN thin films with compositions of $Bi_{1.5}Zn_{1.0}Nb_{1.5}O_7$ were fabricated. The BZN thin film deposition process also involved three key steps: (1) solution synthesis, (2) substrate cleaning and (3) spin coating and annealing.

Organic solution synthesis

The BZN thin films were also synthesized by using the Chemical Solution Deposition method (CSD) as mentioned in section 3.3. In this case, the starting precursors were bismuth acetate, zinc acetate and niobium ethoxide. At first, bismuth acetate was dissolved into acetic acid at 60°C for >10min on a hot plate. At the same time, the zinc acetate was mixed with absolute ethanol (Sigma Aldrich) in an ultrasonic bath at >55°C for 10 min. The two precursors were mixed in one beaker to form a clean and transparent solution. Niobium ethoxide was dissolved into acetic acid at room temperature and then added into the Bi/Zn solution to form a clean and transparent precursor for spin coating.

Substrate cleaning process

As mentioned in section 3.3, the substrate was cleaned by a three step cleaning process before the organic precursor was coated onto the substrate.

Spin coating process

The BZN precursor was coated onto the substrate by using the same spin coating process described in section 3.3. At first, the substrate was fully covered by the precursor and then accelerated to 4000 rpm for 10sec. The sample was baked at 400°C on a hotplate to remove the organic residue and then pre-annealed at 700 °C for 5 min. The spin coating cycle was repeated for a number of times to achieve the desired film

thickness. For making the CPW, the BZN thin film was annealed at 800°C for 2hrs. Because the bottom electrode of the MIM capacitor was made of a very thin layer of gold, which can be damaged by high temperature annealing, the BZN thin film in the MIM capacitor was annealed at a lower temperature of 700°C for just 10min.

3.5 Thin film structure characterization

The microstructure and crystal structure of the tunable thin films such as BST and BZN are strongly influenced by their compositions. Thus, the elemental composition in the films is investigated first by using two different techniques: Energy dispersive X-ray (EDX) analysis and X-ray photoelectron spectroscopy (XPS). Once the compositions of the thin films are obtained, the crystal phases present in the thin film can be identified by X-ray diffraction (XRD). The recorded X-ray data also provides information on the crystal phase and lattice parameters. Scanning electron microscopy (SEM) and atomic force microscopy (AFM) were used to study the surface morphology and microstructures of the crystallized thin films. In this work, AFM images are used to determine the grain size and surface roughness of the thin film while the quality of the crystallized films is studied by SEM. In this chapter, the principles of these characterization techniques have been discussed.

3.5.1 X-ray diffraction (XRD)

X-ray diffraction (XRD) is a well known technique for identifying the crystal structure of a solid material which has a regular array of atoms with inter atomic spacing (*d*). Therefore, when the material is illuminated by an X-ray with a fixed wavelength which is comparable to the inter atomic space (*d*) of the material; a diffraction of X-ray pattern is created. The crystal phase of the material is mathematically related to the X-ray diffraction pattern by the "Bragg" equation **[20, 21]**.

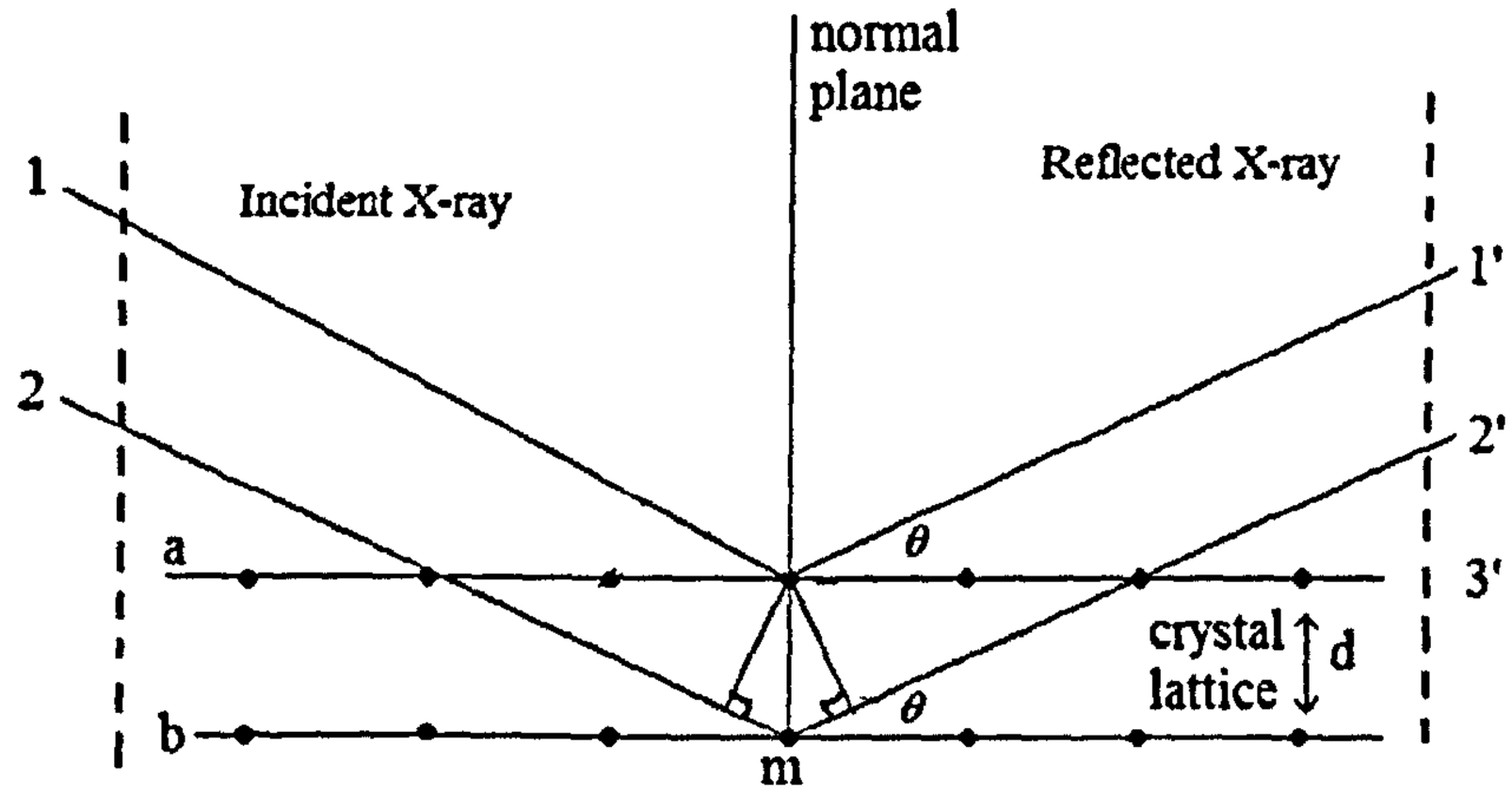

Figure 3.11 Diffraction of X-ray by a single crystal material **[20]**

Figure 3.11 shows the basic principles of X-ray diffraction. In this figure, a parallel beam of X-rays strikes the crystal where the atoms are placed on two parallel planes (a and b) which are separated by a distance of *d* (inter atomic space). According to this figure, the parallel X-ray beams on the left strike onto the planes at an angle of θ and the atoms scatter the X-ray beams in all directions. If the detector is placed at an angle of θ on the right, then only when the path difference between the- two reflected beams 1' and 2' is an integral number of wavelengths, will the beam constructively interfere and the signal at the detector will be a maximum **[20]**. Mathematically this is expressed by the following equation **[20, 21]**:

$$n\lambda = 2\,d\sin\theta \qquad [3.1]$$

where λ is wavelength of the X-ray, θ is incident and detection angle, d is the atom space and n is the order of diffraction. This equation was first discovered by W. L. Bragg and so it has been called the "Bragg equation".

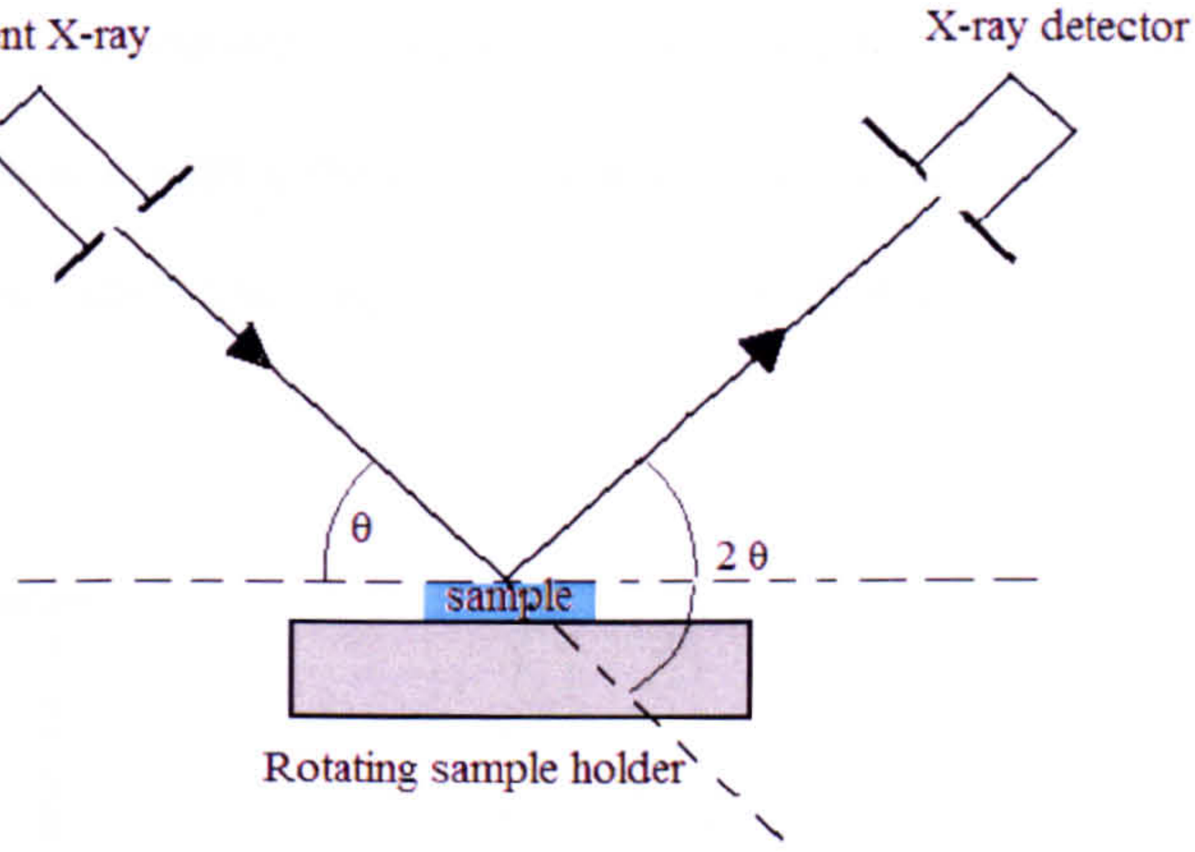

Figure 3.12 working principles of a XRD

Figure 3.12 shows the working principle of the XRD in practice. The crystallized film is placed onto a rotating sample holder inside the chamber of the diffractometer. The incoming X-ray beams strikes the rotating material from the left while keeping the X-ray source stationary. When the sample holder rotates to a particular angle so that "Bragg" equation has been satisfied, the X-ray receiver (on the right hand) receives a strong diffraction of X-ray beam. By rotating the material, a pattern of diffraction peaks can be obtained. The position and geometric shapes of these peaks are related to the crystal structures in the material. In this work, the crystal phases of the thin films are characterized by using a Siemens (Kristalloflex-D500) X-ray diffractometer. The XRD was operated at 40kV and 25mA which employs CuK_α radiation with a wavelength of 1.5402 Å. The X-ray data was collected over a range of 25^o and 95^o with a 0.05^o step size. Therefore, an X-ray diffraction pattern which consists of different diffraction peaks can be obtained. The crystal orientations corresponding to each of the diffraction peaks are also indicated. This provides the crystal phase and structure of the sample films.

Strain and stress

In addition, the stress and strain of the crystal thin film can also be obtained. According to the X-ray pattern in figure 3.13, the position of the diffraction peak is shifted to a higher angle ($2\theta'$), the crystal is believed to be under compressive strain since it has smaller lattice space (d) than the stress free crystal.

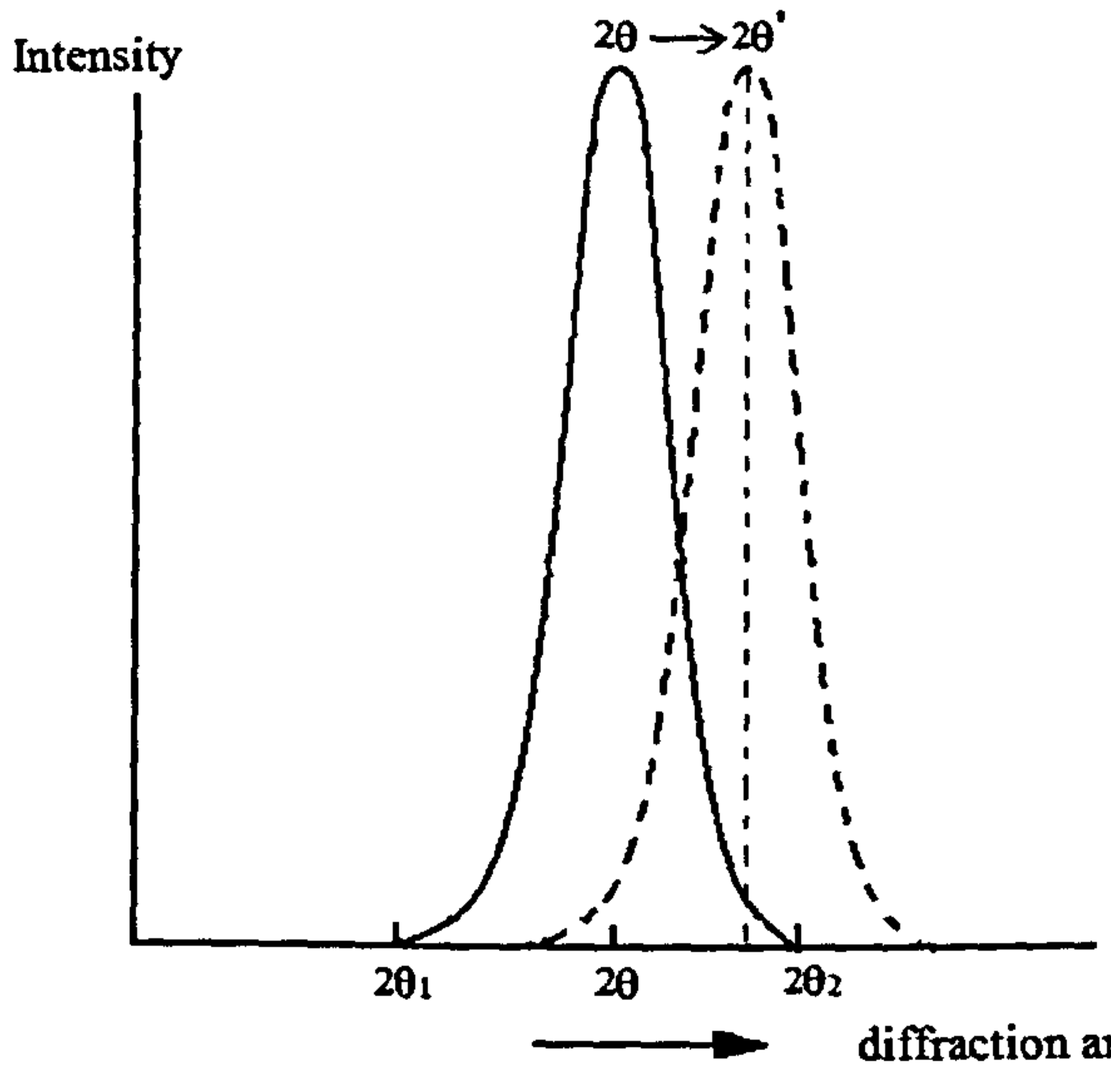

Figure 3.13, X-ray diffraction peak shifted towards an higher angle ($2\theta'$)

Grain size

The XRD pattern can also provide the information about the material's grain size. The grain size of a crystallized material is usually related with the width (B) of an X-ray diffraction peak (figure 3.14). The peak width (B) is measured from the diffraction peak where its intensity is at half of its maximum intensity [1]. Therefore, it is called the full width of half maximum (FWHM).

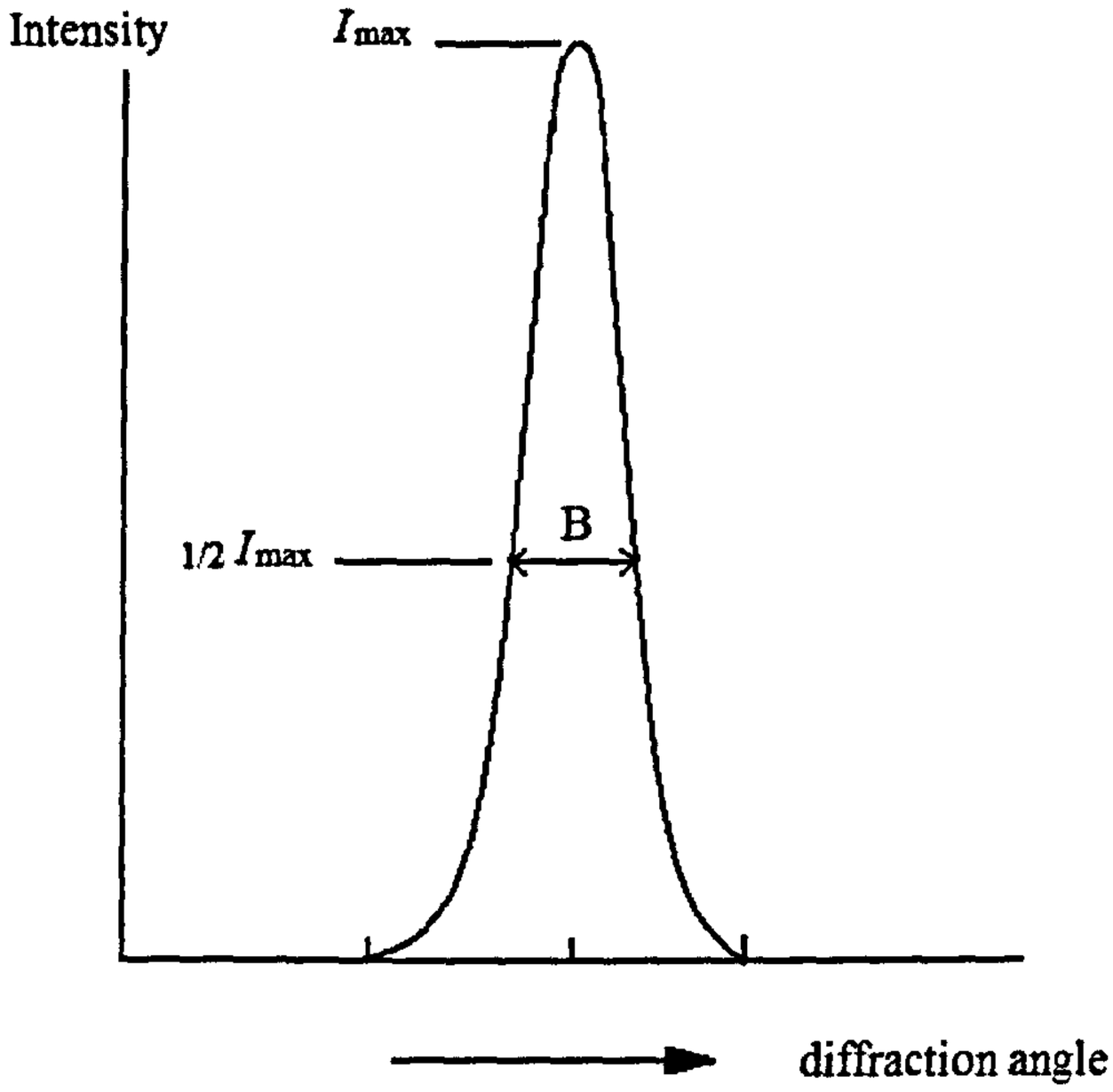

Figure 3.14 effects of grain size on X-ray diffraction peak

The measured FWHM can be mathematically converted to the grain size of the thin film by using "Scherrer" equation **[20]**.

$$t = \frac{K\lambda}{B\cos\theta_B} \tag{3.2}$$

Where t is the average grain size, λ is the wavelength of the incoming X-ray beam (1.5402 Å in this case), K is the dimensionless shape factor which has a typical value of 0.9, B is the width of the diffraction peak in radians, θ_B is the position of the diffraction peak.

3.5.2 Scanning Electron Microscope (SEM)

The Scanning Electron Microscope (SEM) produces a 2-D surface image of a material with exceptionally high resolution. Hence, SEM was widely used to study the microstructures of the thin film.

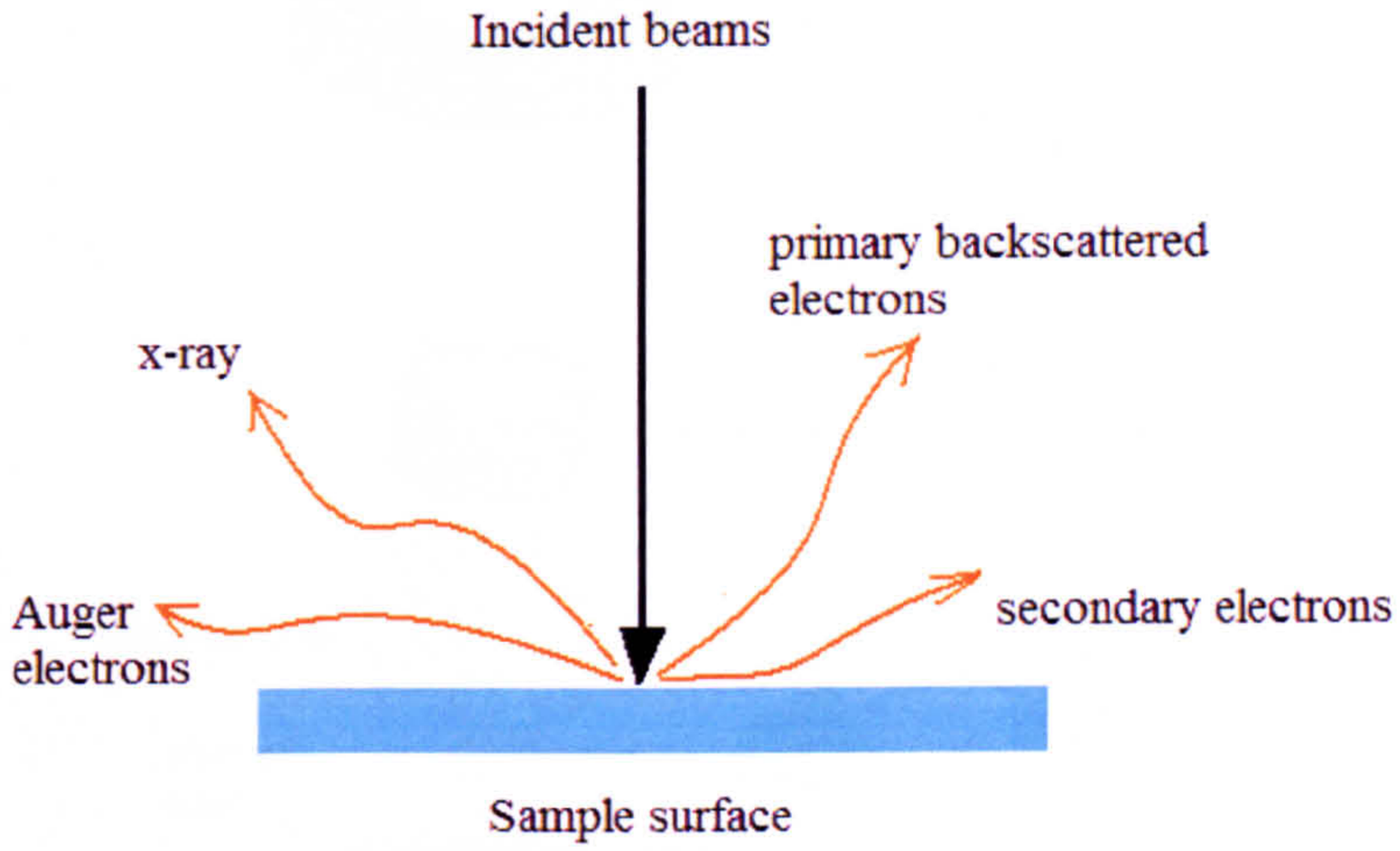

Figure 3.15 the emission of various particles including secondary electrons, X-ray, and backscattered electrons **[22]**

A high energy beam of electrons is focussed on to the surface of the sample and the interaction between the sample atoms and electron beam causes the emission of various particles including secondary electrons, X-ray, and backscattered electrons (figure 3.15). The electron beams are focused on the surface of the sample and scanned across the surface in a "roster" or parallel pattern **[23]**. The emitted "electrons" are collected as the position of the incident electron beam is scanned. The received electron current is amplified to produce the image of the sample surface. The following figure shows the working principles of a SEM.

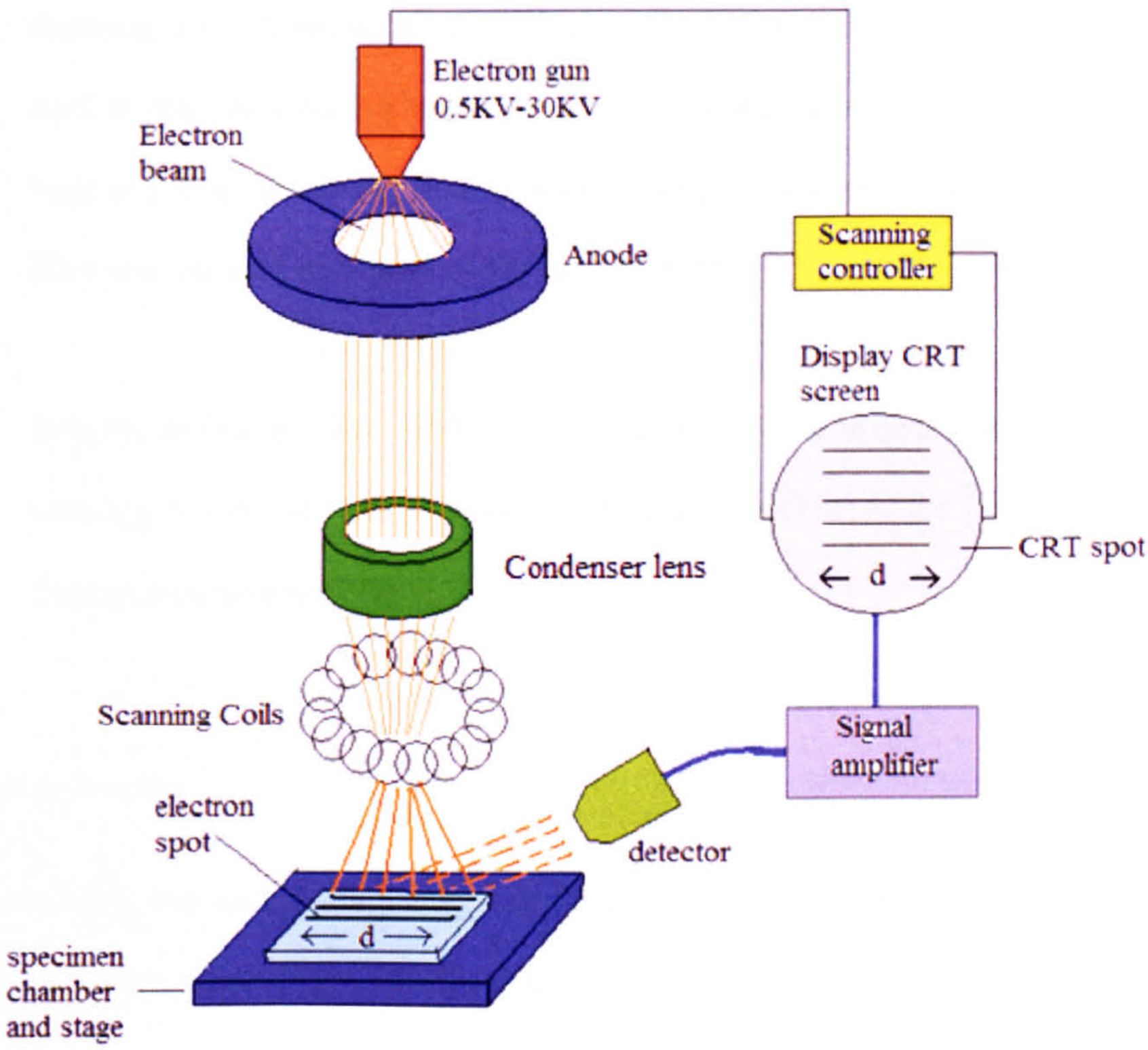

Figure 3.16 shows the working principle of a SEM (reproduced from **[23, 24]**).

1) *Electron gun:* The electron gun is located at the top of the SEM and consists of a tungsten thermionic filament and a triode arrangement of control plates. The filament is heated to very high temperature by passing a current through it. Electrons are emitted from the surface by thermionic emission and are accelerated away from the filament by the triode control plates. The electron gun usually produces a beam current of 250μA with energies between 1KeV and 30KeV **[23].**

2) *Condenser lens:* The emitted electrons are attracted through the anode and pass through the condenser lens. The condenser lens focuses the electron beams onto the surface of sample.

3) *Scanning coil:* A metal coil wire is placed within the object lens. This coil is used to produce a control magnetic field so that the electron beam is deflected back and forth as parallel lines to create a grid of rectangular lines or parallel lines over the area of interest on the sample **[25]**.

4) *Imaging technique:* The image of the scanned area is synchronized with the scanning coil of the SEM. Therefore, the relative position of the feature can be displayed on a screen **[25]**.

SEM in practice

In this work, the surface morphology of the samples is studied by using a Scanning Electron Microscope (SEM, Phillips XL30 ESEM-FEG). The SEM samples are attached to a sticky conducting carbon stab carrier and placed into the vacuum chamber of the SEM. To optimize the image resolution, the SEM is operated at 30kV. The images of the thin film surface have been collected at different magnifications. A scalar bar was displayed on each SEM image to measure the thickness and grain size of the thin film.

3.5.3 Electron dispersion X-ray (EDX)

Electron dispersion X-ray analysis is an analytical tool used to characterize the element composition of a given material. The material is bombarded by high energy electrons which "knocks" an electron from the inner electron shell of an atom in the material creating a vacancy in the electronic state of the atom **[7]**. This vacancy is then filled by another electron from the outer shell. Since conservation of energy must apply, a photon in the X-ray part of the spectrum is emitted. The energy of this X-ray photon is the energy difference between the inner and the outer shell electronic states. This energy depends on the atomic species and so this method can be used to

identify the atomic species in a material. An example transition is shown in figure 3.17.

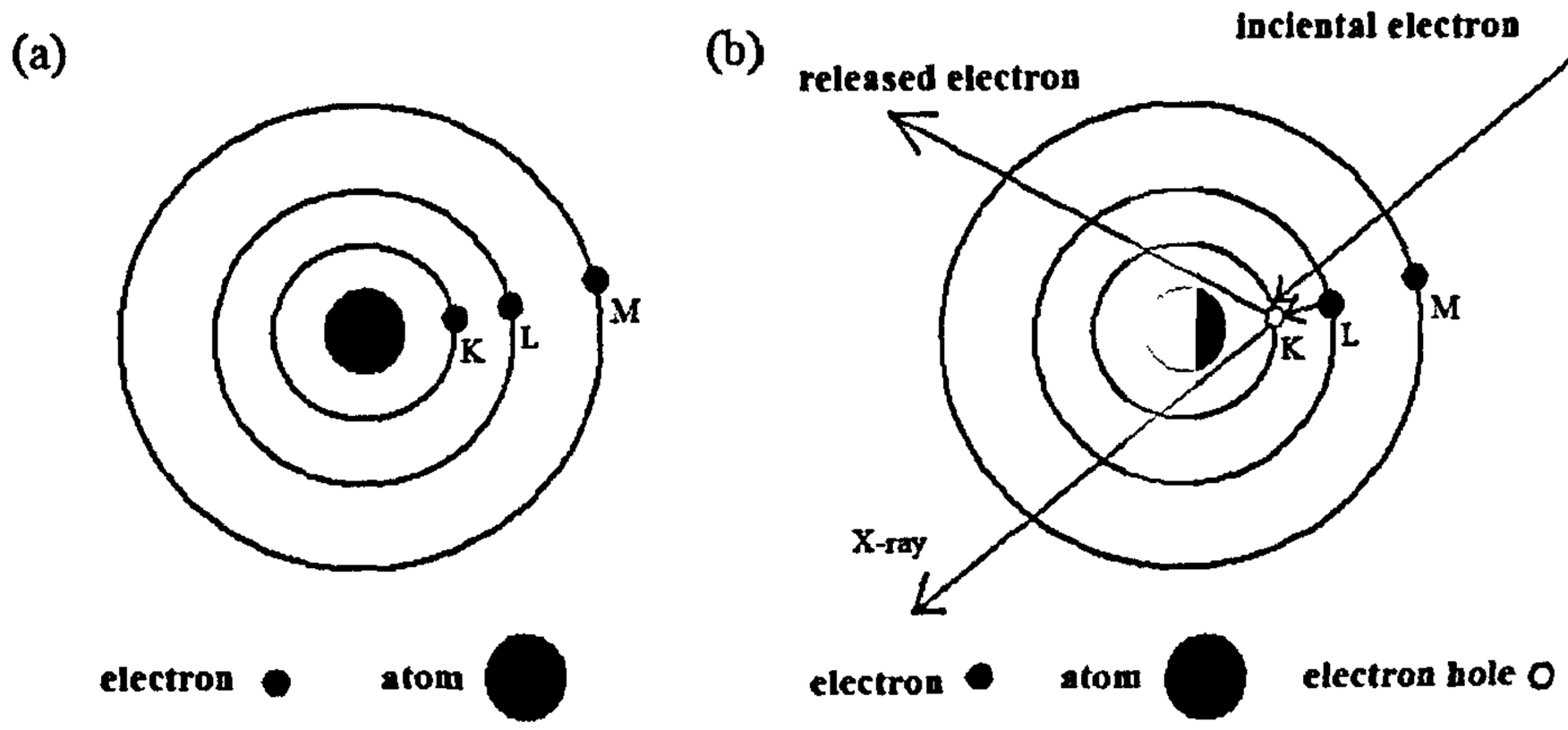

Figure 3.17 electron and energy transitions of an atom **[26]**

There are several distinct energy levels associated with the L shell of the atom, which means there will be multiple lines in the X-ray spectrum associated with the same element. This is shown in figure 3.18.

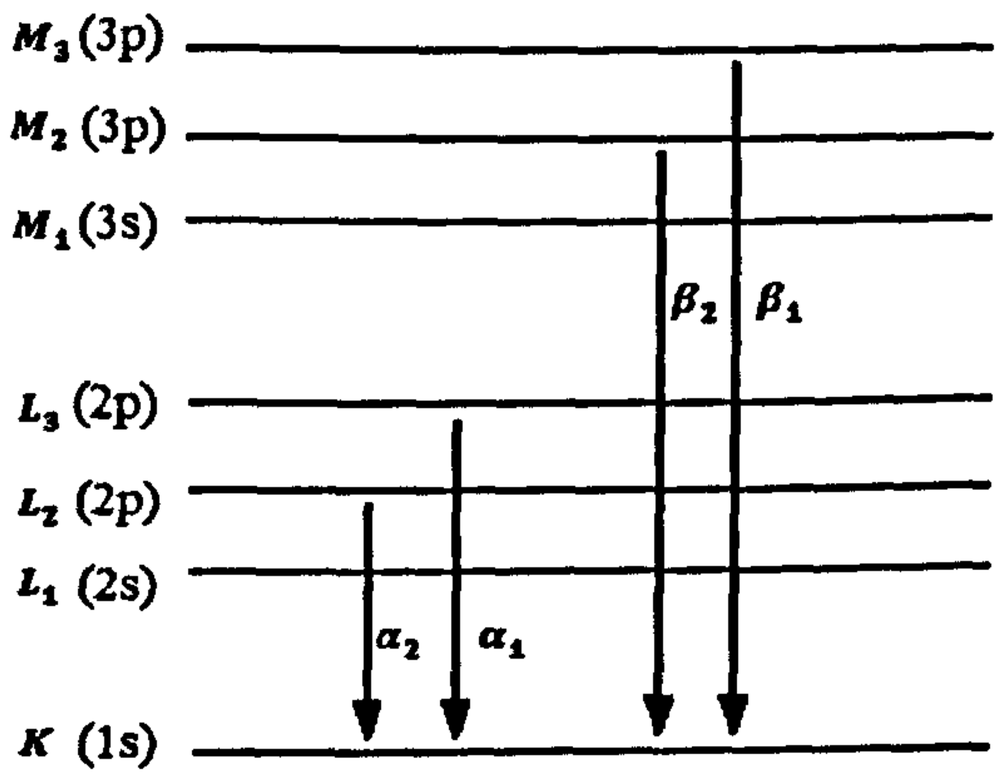

Figure 3.18 possible electron energy transition for the atom shown in figure 4.7 **[27]**.

EDX in practice

Since the measurement conditions for EDX are identical to those of the SEM, EDX is usually integrated into a normal Scanning Electron Microscope (SEM, XL30, Phillip). Here, the operating voltage and spot size were kept at 20keV and 3.0μm, respectively.

The collected data is displayed as an X-ray spectrum where the number of X-ray photons is plotted against their energy levels.

3.5.4 Photoelectron Spectroscopy (XPS)

The element compositions of the ferroelectric thin films can also analyzed by X-ray photoelectron spectroscopy (XPS) technique.

Basic principles and theory of XPS

In XPS, the surface of the specimen is radiated by a source of X-rays causing the photoionisation of atoms in the specimen. By measuring the number and energy of the escaped electrons the XPS spectra of the specimen can be obtained **[28]**. The photoionisation takes place at the surface of the sample. The escaped electrons (or photoelectrons) have a kinetic energy (K_E) which is mathematically related to the X-ray energy (hv) as follows **[28]**:

$$E_k = hv - E_b \tag{3.3}$$

This is illustrated in figure 3.19. Since each element has its own unique characteristic binding energy (BE) related to the energy of the electron states (e.g., 1s, 2s, 2p, 3s, etc), the peaks in the XPS spectrum can be used to identify the atoms on the surface of the sample.

In addition, atoms of a higher positive oxidation state exhibit a higher binding energy due to the extra coulombic interaction between the photo-emitted electron and the ion core [10]. This ability to distinguish between different oxidation states of the ion is the reason for employing the XPS technique in this work.

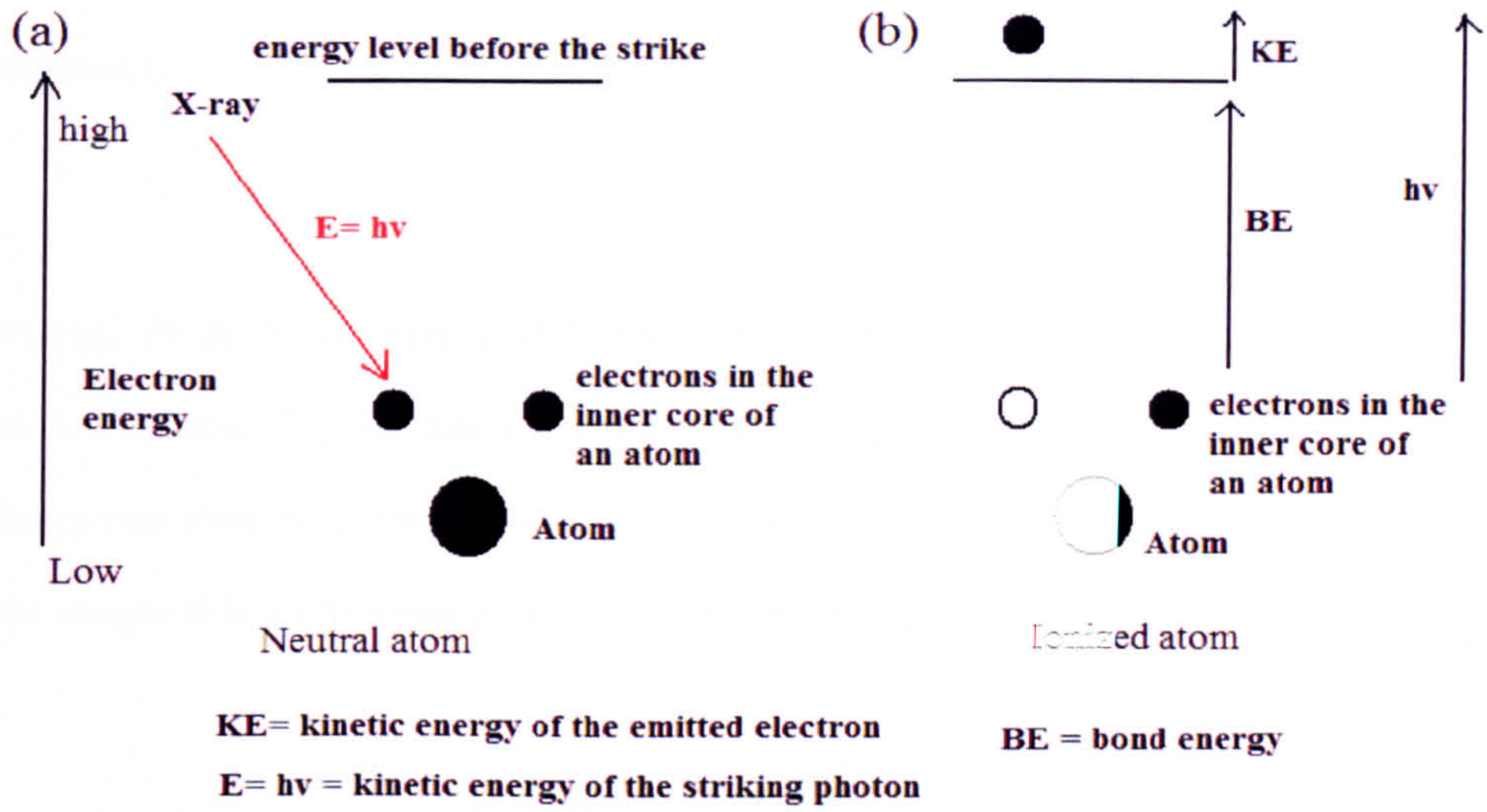

Figure 3.19 the transition of energy of an atom caused by an incident atom **[29]**

XPS in practice

XPS spectra were obtained using a VG Scientific, ESCALAB MARK 2 system and using the MgK_{α} radiation source (hv = 1253.6 eV.). Similar to EDX, XPS analysis can also provide the composition of the material. Unfortunately, the photoelectrons can only escape from the surface region of the sample (<10nm) and the total thickness of the BST thin film is greater than 100nm. Thus, the quantified composition results do not represent the whole film. Meanwhile, the accuracy of composition analysis varies depending on many other factors such as detector's sensitivity and sample cleanness.

3.5.5 Atomic Force Microscopy (AFM)

In our work, the synthesized films have an uneven surface and so the images of these thin film taken by SEM microscope does not provide any meaningful information about the grain size. Hence, the surface roughness and grain size of the thin film were

determined by Atomic Force Microscopy (AFM). AFM gives a very high resolution image of the surface and is an accurate way of measuring the surface of a sample at nanoscale.

Atomic Force Microscopic (AFM) technique is based on the measurement of different forces **[27]** between a moving tip and sample surface. By measuring the interaction force via a soft cantilever while the probe is scanning across the surface of the sample **[27]**, a 3-D image of the surface can be obtained.

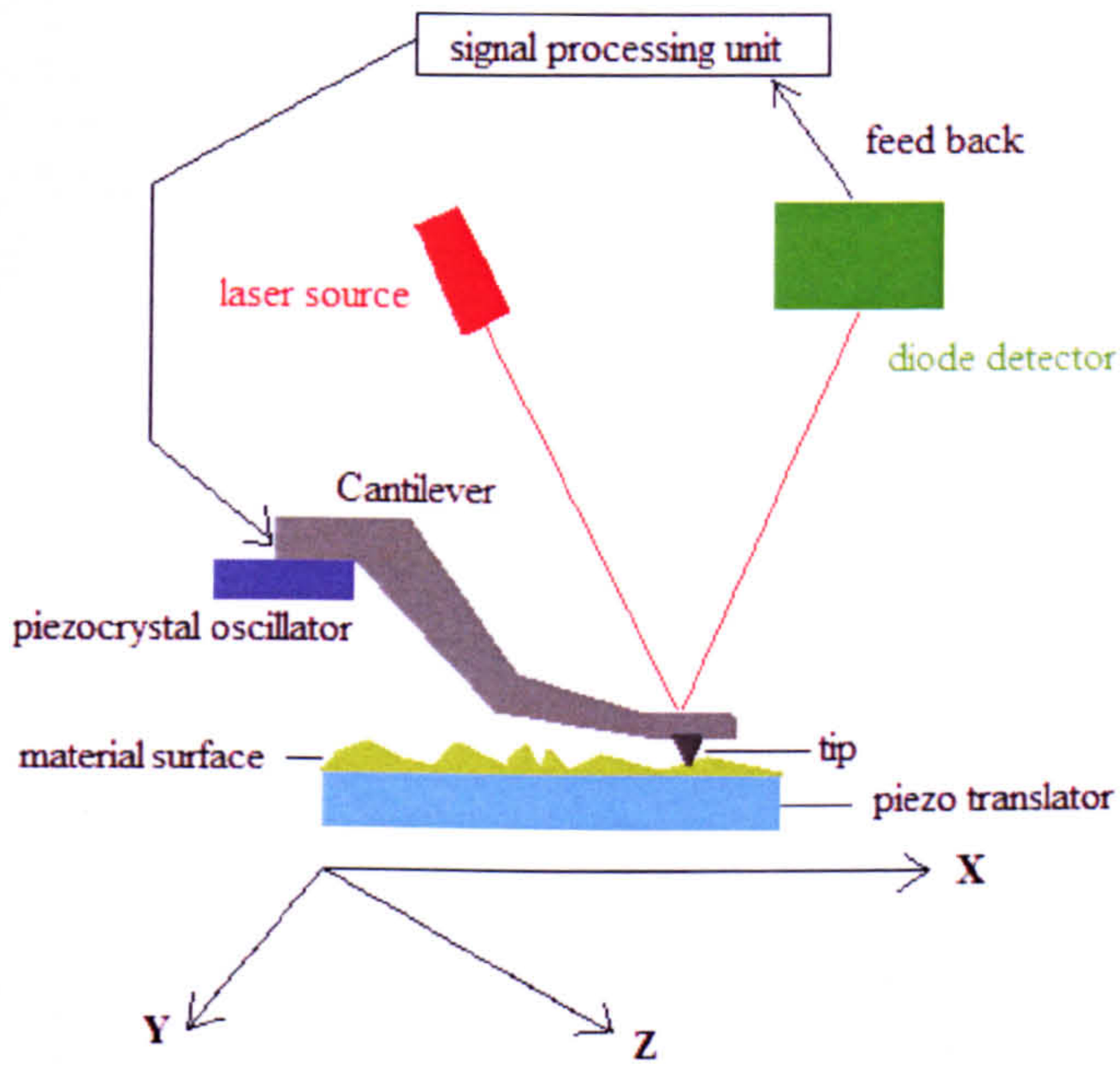

Figure 3.20, the working principles of the AFM (reproduced from **[30]**)

The basic set up of an AFM is shown in figure 3.20. A small tip at the front of the soft cantilever is used to scan the sample surface **[27].** The specimen's rough surface will force the tip to move echoing the specimen's terrain. The deflection of the cantilever is measured and the height of the tip above the sample surface is maintained by the use a laser diode feedback system and a vertical piezomicropositioning stage. In "contact mode", the tip is scanned across the sample

surface while the vertical displacement necessary to maintain a constant force on the tip is recorded. This results in a 3 D image of the topography of the sample surface.

AFM in practice

In this work, a "Veeco" AFM was employed to study the surface roughness of the thin film. The AFM was operated in contact mode with a scanning resolution of 256 ×256. The probing tip scans through the sample surface with a constant force (constant force mode).

References:

[1] B. Krause, *Thin films on glass*, Springer, 56-61, 2003.

[2] (Last access: 16/09/2010). *Sputtering Machine for thin film deposition.* Available: *http://www.getupanddiy.com/projects/thin-film-sputtering-machine/index.php*

[3] J. Du, "*Processing and characterization of functional multicomponent oxides by electrostatic spray assited vapour deposition (thesis),*" University of Nottingham, 2007.

[4] B. T. Lee. and. C. S. Huwang, "Influence of interfacial intrinsic low-dielectric layers on the dielectric properties of sputtered $Ba_{0.5}Sr_{0.5}TiO_3$ thin films," *Applied Physics Letters,* vol. 77, 124-126, 2000.

[5] A. Dhara, B. Pandaa, G.D. Nigamb, D. Bhattacharyab, and S.K. Rayb, "Optical properties of RF sputtered Strontium substituted Barium Titanate thin films," *Thin Solid Films,* vol. 332, 46-49, 1998.

[6] S. C. Sun, T. Y. Tseng and M. S. Tsai, "Effect of oxygen to argon ratio on properties of (Ba,Sr)TiO3 thin films prepared by radio-frequency magnetron sputtering," *J. Appl. Phys,* vol. 82, 3482-3487, 1997.

[7] J. Geoge, *Preparation of thin films*, Marcel Dekker, Inc, 41-226, 1992.

[8] H. J. Cho and Hyeong. Joon. Kim, "Improvement of dielectric properties of $(Ba,Sr)TiO_3$ thin films deposited by pulse injection chemical vapor deposition," *Applied Physics Letters,* vol. 72, 786-788, 1998.

[9] T. Aoyama and M. Kiyotosh, "Chemical vapour deposition of Ru and its applications in $(Ba,Sr)TiO_3$ capacitors for future dynamic random access memories," *Jpn. J. Appl. Phys,* vol. 38, 2194-2199, 1999.

[10] Y. Takeshima, *et al,* "Thickness dependence of characteristics for $(Ba,Sr)TiO_3$ thin films prepared by metalorganics chemical vapour deposition," *Jpn. J. Appl. Phys,* vol. 39, 5389-5392, 2000.

[11] K. L. Choy, "Chemical vapour deposition of coatings," *Progress in Materials Science,* vol. 48, 57-170, 2003.

[12] (Last access: 08/09/2010.). *Generic CVD reactor.* Available: *http://timedomaincvd.com/CVD_Fundamentals/introduction/generic_CVD_reactor.html*

[13] (Last access : 16/09/2010). *Deposition process.* Available: *http://www.mems-exchange.org/MEMS/processes/deposition.html*

[14] N. IIzawa and M. Yamada, *et al,* "Processing and Properties of Rare Earth Ion-Doped Bismuth Titanate Thin Films by Chemical Solution Deposition method," *Jpn. J. Appl. Phys,* vol. 42, 5222-5226, 2003.

[15] M. Jain, S. B. Majumder, A. Martinez, and R. S. Katiyara "Sol–gel derived grain oriented Barium Strontium Titanate thin films for phase shifter applications," *J of Appl. Phys.* vol. 90, 896-903, 2001.

[16] R. W. Schwartz, "Chemical solution deposition of perovskite thin films," *Chem Mater,* vol. 9, 2325-2340, 1997.

[17] M. Paranthaman, K. Salama and M. S. Bhuiyan, "Solution-derived textured oxide thin films—a review," *Supercond. Sci. Technol,* vol. 19, R1-R25, 2006.

[18] Theodor. Schneller and Robert. Schwartz, *et al,* "Chemical solution deposition of electronic oxide films," *C. R. Chimie* vol. 7, 433-461, 2004.

[19] S. N.Jian, J.W.Zhai and X.Yao, "Investigation of Barium Strontium Titanate thin films for tunable micorwave applications", Journal of Ferroelectrics, vol. 388, 1, 67-73,2009.

[20] B. D. Cullty and S.R.Stock, *Elements of X-ray diffraction* 3rd ed, Pearson education, 92-170, 2001.

[21] M. F. Ladd. and R. A. Palmer, *Structure determination by X-ray crystallography*, Newyork: Plenum press, 134-137, 1994.

[22] (Access date: 10/10/2010). *SEM setup.* Available: *http://mse.iastate.edu/microscopy/beaminteractions.html.*

[23] I. M. Watt, *The principles and practice of electron microscopy*, Press syndicate of the University of Cambridge, 1989.

[24] (Last access: 13/04/2010). *Scanning electron microscope*. Available: *http://www.purdue.edu/rem/rs/sem.htm* .

[25] (Last access, 02/04/2010). *Electron microscopy*. Available: *http://encyclopedia.jrank.org/articles/pages/1129/Electron-Microscopy.html.*

[26] (Last access: 09/09/2010), *Energy disperson X-ray analysis*, Available: *http://www.concrete.cv.ic.ac.uk/durability/research%20techniques%20sem%20edx.htm.*

[27] H. Bubert and H. Jenett, *Surface and thin film analysis*, Wiley-VcH, 195-280, 2002.

[28] J. M. Walls, *Methods of surface analysis*, Cambridge University, 128, 1992.

[29] *(Last access: 06/09/2010), Photoelectron Spectroscopy.* Available: *http://chem.qmul.ac.uk/surfaces/scc/scat5_3.htm.*

[30] (Last access: 01/09/2010) *Atomic Force Microscopy,* Available: *http://www.npl.co.uk/nanoscience/surface-nanoanalysis/research/atomic-force-microscopy.*

Chapter 4: Device fabrication

As mentioned in section 2.2.7, two types of microwave devices, coplanar waveguide (CPW) and metal insulated metal capacitors (MIM), have been fabricated to characterize the dielectric properties of the thin films. The CPW is a two layer transmission line with two ground planes on each side of a centre conductor **[1-3].** On the other hand, the MIM capacitor is a three layer device with the tunable thin film between the top and bottom electrodes **[4].** The 3D configurations of these devices are shown in figure 4.1(a) and (b). Both devices are too small to be manufactured by a conventional mechanical process. Instead, these devices are made by a micro-fabrication process called photo lithography.

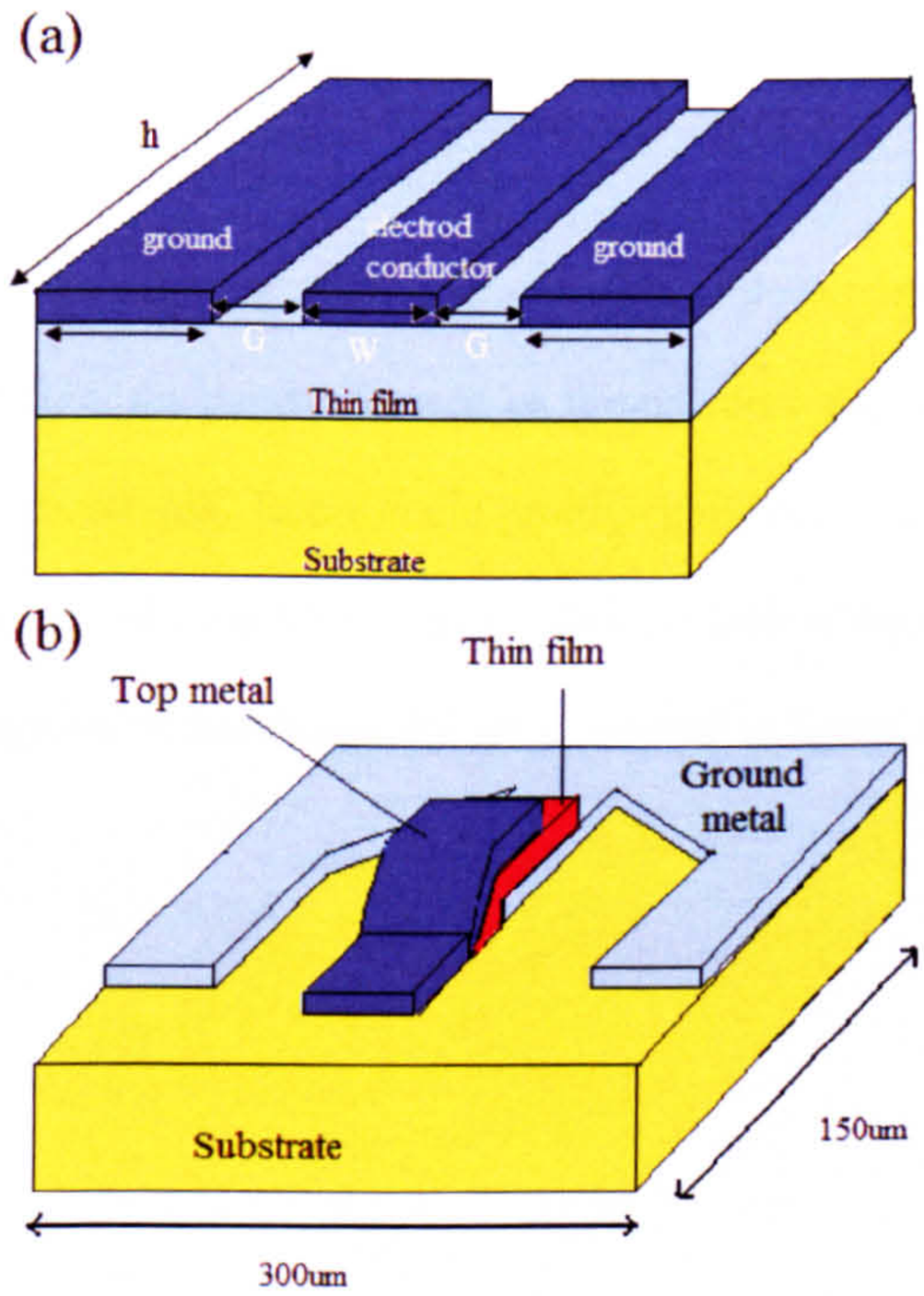

Figure 4.1(a) Coplanar waveguide (CPW) (b) Metal Insulated Metal (MIM) capacitor.

Photo lithography is a process of transferring a geometric pattern from a photomask onto a layer of photoresist which is highly sensitive to ultra violet (UV) radiation **[5, 6].** Today, most of the lithography equipment use optical radiation sources. Optical

lithography has two different methods of transferring the geometric pattern onto the photoresist. They are commonly known as shadow printing and projection printing. Shadow printing puts the wafer and mask in direct contact and so offers much greater resolution over the projection printing. The contact between the wafer and mask inevitably increases the chance of breaking the photomask. However, the number of steps in fabricating devices such as CPW and MIM capacitor is small and so the chance of breaking the photomask using contact printing is relatively small. In this work, contact printing has been used to transfer the patterns onto the photoresist.

Figure 4.2 shows the general process of photolithography. Positive photoresist is soluble in the developer when it is exposed to UV light. Consequently, the pattern in the photoresist will be exactly the same as the pattern on the photomask.

On the other hand, the negative resist is less soluble in developer when it is exposed to UV light. Therefore, the pattern formed on the negative photoresist is opposite to the pattern on the photomask. Because the positive photoresist is readily available in our lab, positive photoresist has been used to fabricate both of the devices. The results of positive and negative photolithography are compared in figure 4.2.

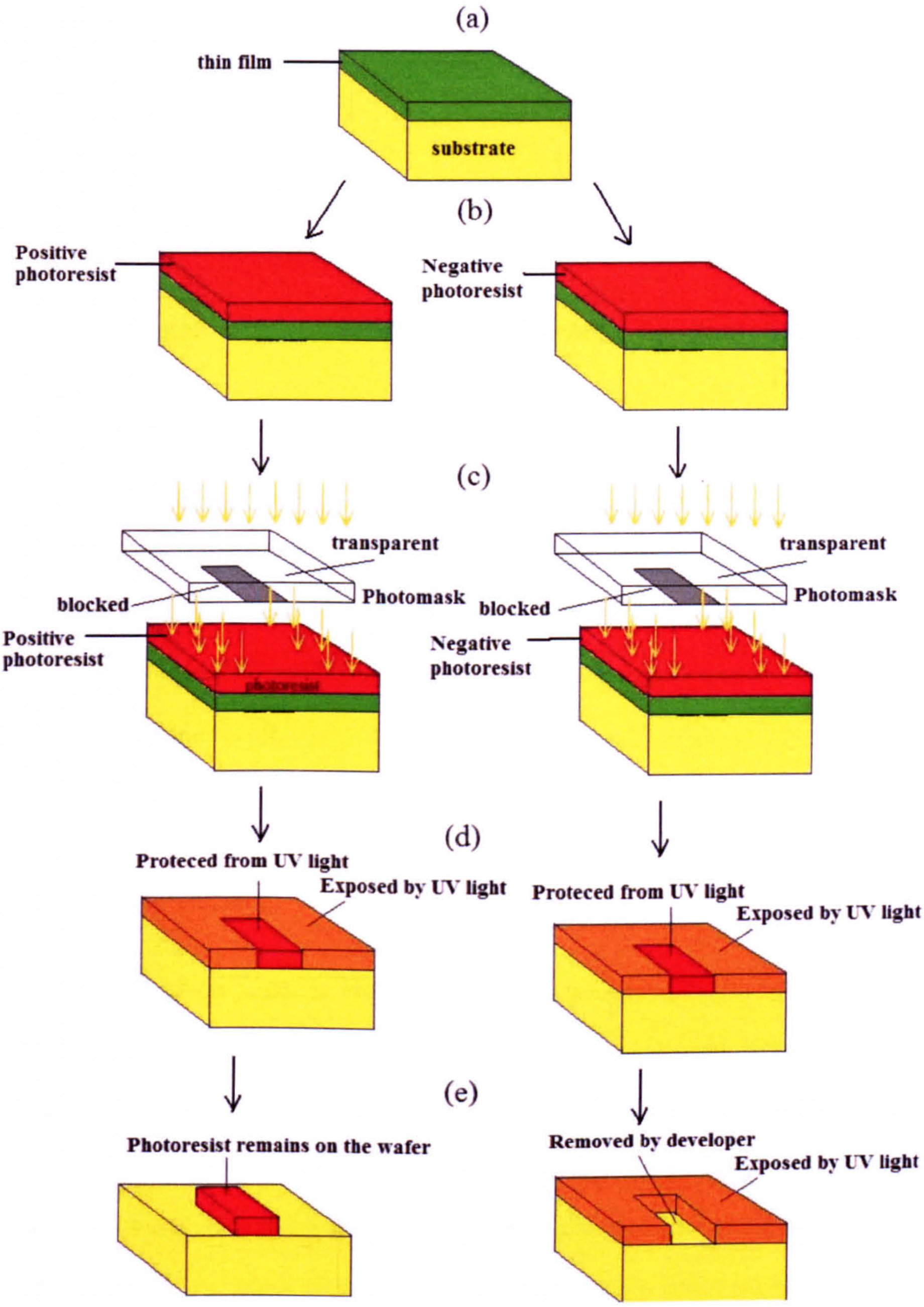

Figure 4.2 Photolithographic processes using positive and negative photoresist.

The steps involved in conventional photolithographic process are: wafer cleaning, photoresist coating, soft baking, mask alignment, exposure and developing. The following is a step by step description of fabricating CPW by photolithography

technique. In section 4.2, we will give a detail discussion on the fabrication of MIM capacitor using a combination of photolithography and etching techniques.

4.1 Coplanar waveguide (CPW) fabricated by photolithography process

CPW is a planar microwave device which contains only one layer of metal pattern on top of the wafer (figure 4.1). This pattern can be coated onto the surface of wafer by a positive photolithography process. The steps involved in this process are wafer cleaning: photoresist, coating, soft baking, mask alignment/exposure, developing, metallization and lift off.

Step1: wafer cleaning

The surface of the wafer is cleaned by organic chemical solvents to remove the contaminants that include dust, particles, chemical residue and metal ions. The organic solvents used for cleaning are methanol (ACS reagent, ≥99.8%, Sigma Aldrich), acetone (99.9%, Sigma Aldrich) and propanol-2ol (ACS reagent, ≥99.0%, Sigma-Aldrich). At first, the substrate is immersed into each kind of the solvent in an ultrasonic bath for 3mins (figure 4.3(a)) and subsequently immersed in de-ionized *water (DIW) (18MΩ)* to remove the organic residue. To completely remove the DIW, the wafers are baked on a hotplate at 150 degrees for 3min (figure 4.3(b)).

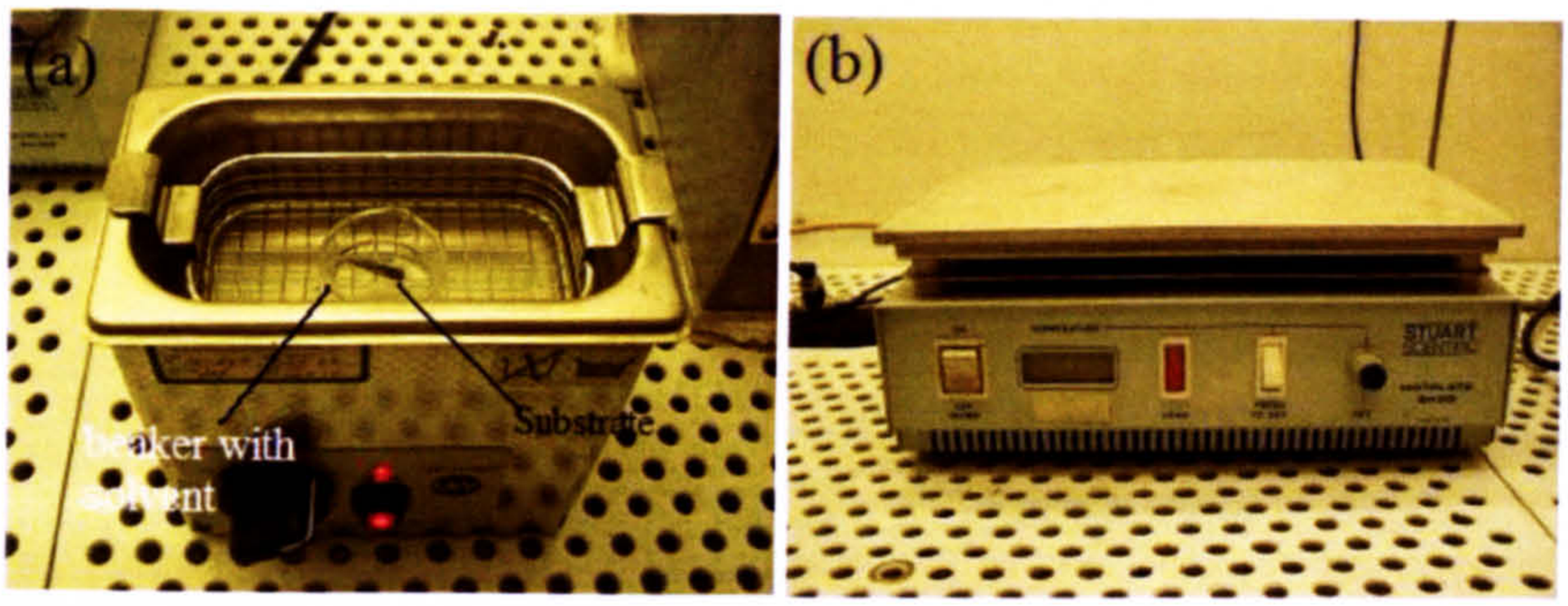

Figure 4.3(a) wafer in ultrasonic bath (b) hotplate used for baking

Step2: Photoresist deposition

After cleaning, a thin layer of positive photoresist (AZ1512HS) is spin coated onto the surface of the wafers by a spin coater (figure 4.4(a)). The wafer is held on the spinner chuck by vacuum (figure 4.4(b)).

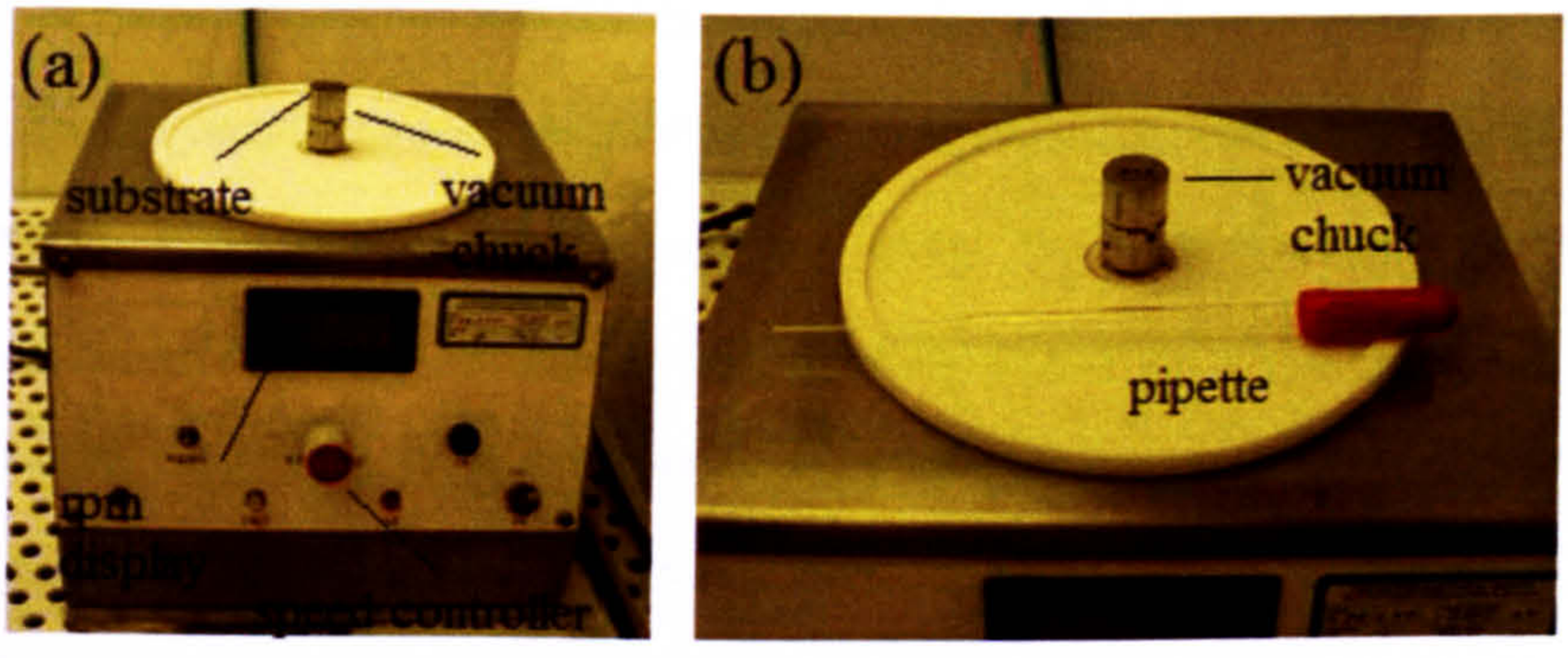

Figure 4.4(a) Spin coater (b) A close look of the vacuum chuck of the spin coater

Using a pipette, the liquid photoresist is dropped on the surface of wafer. By spinning the substrate at 4000rpm for 45sec, the photoresist is coated onto the wafer with a uniform thickness of approximately 1.2um. Figure 4.5 shows a typical set up for spin coating.

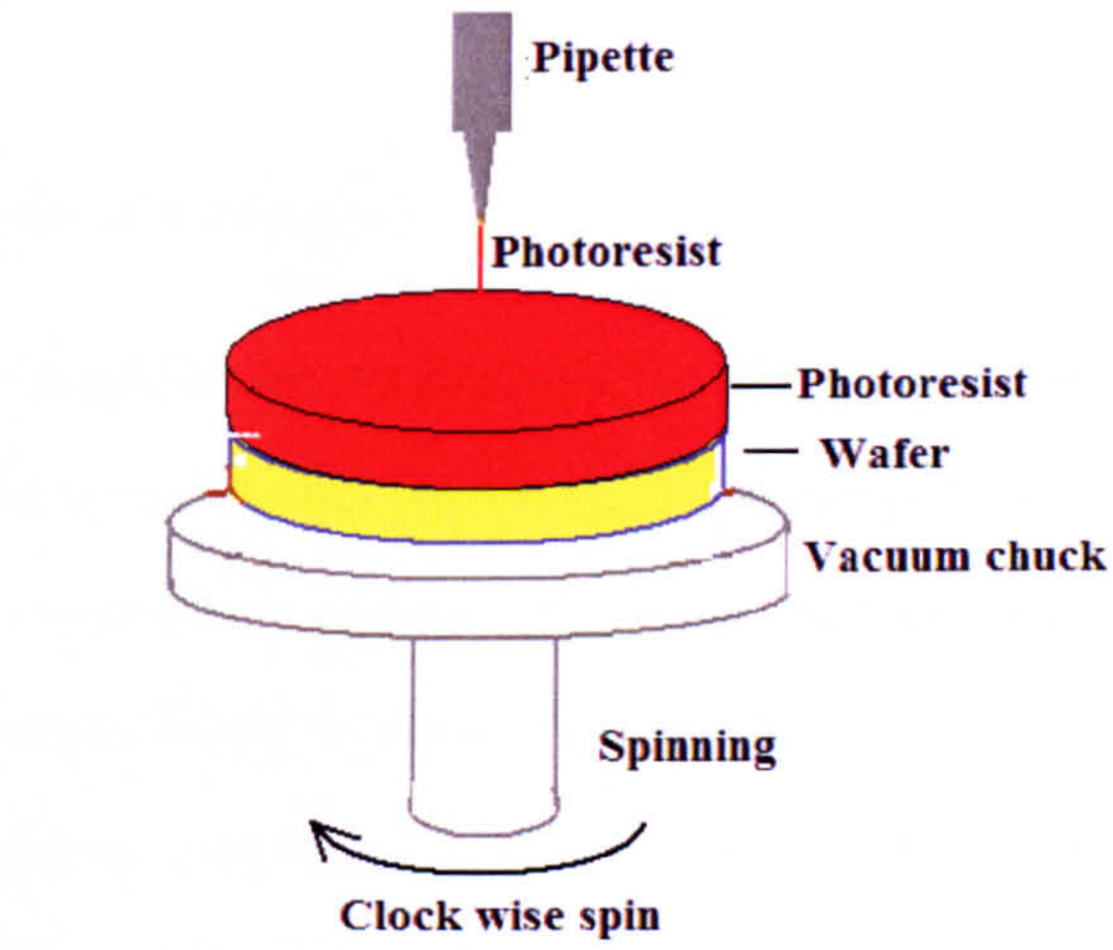

Figure 4.5 a typical set up for spin coating

Step 3: soft baking

Once the photoresist has been coated onto the wafer, a soft-baking or prebake process is used to densify the photoresist. This process is important because the photoresist only becomes sensitive to UV light after soft baking. The length of the baking time is critical. If it's too long, the resist is over baked and its sensitivity to UV light will be reduced. On the other hand, the exposure and developing processes will be affected if the developing time is too short. In this work, the wafer covered by photoresist is placed on a hotplate at 100 degrees for 50 sec. The setup of the soft baking is shown in figure 4.6 and figure 4.3(b) shows the picture of the hotplate.

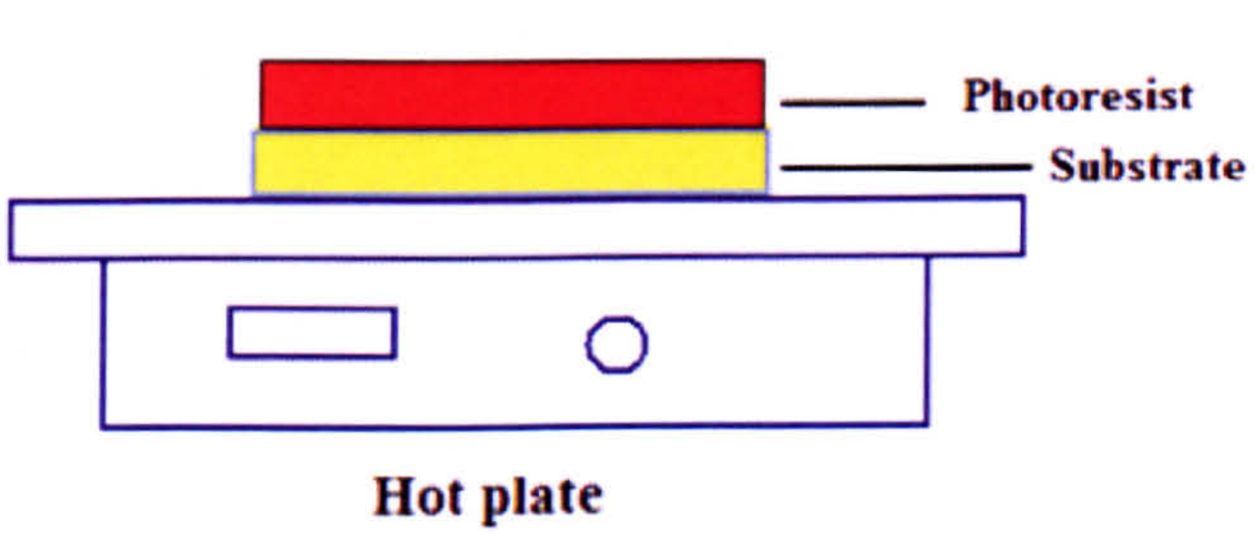

Figure 4.6 Set up of soft baking

Step 4: Exposure and alignment

Exposure and alignment are important in photolithography because the geometric pattern is actually transferred onto the surface of photoresist in this process. For making CPW, we are only interested in exposure because CPW is a planar device, which contains only one layer of metal pattern on the surface of the wafer, and so there is no need to align this pattern with another photomask. An overview of exposure is given so that we can understand its principles.

An overview of exposure

Exposure is carried out using a manual contact aligner where the substrate is held on a sample holder and the UV source is above it (figure 4.7(a)). The aligner puts the wafer in contact with the photomask which is transparent in some areas and blocked in the others (figure 4.7(b)). Once the UV light is turned on, the UV light is blocked in some areas and passes through in others. In the transparent areas, the UV light can pass though to the wafer causing a change of chemical structure in the photoresist (figure 4.7(c) and 4.7(d)). The photoresist exposed by the UV light is soluble in a chemical developer and so it can be removed.

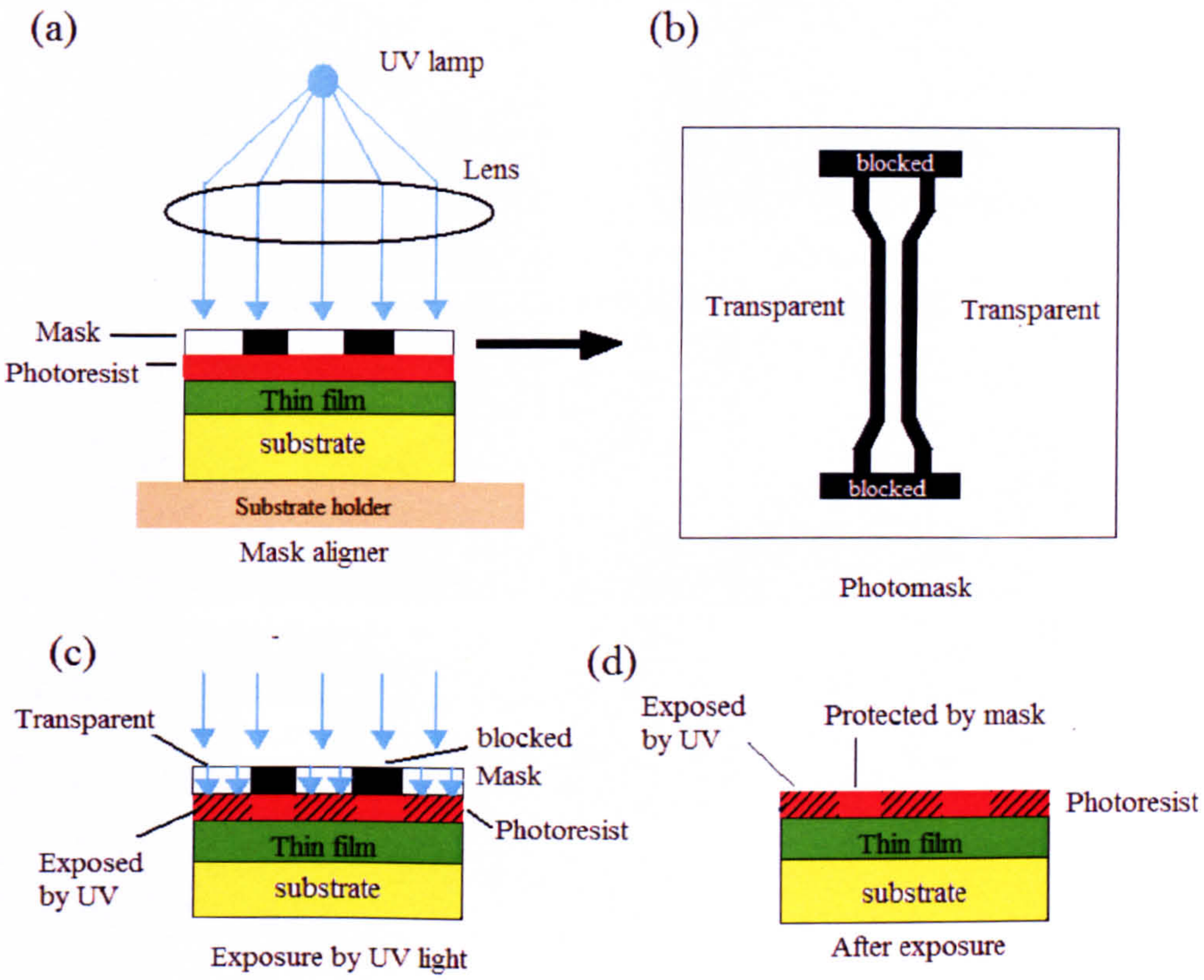

Figure 4.7(a) Set up of contact printing. (b) CPW photomask (c) Exposure (d) after exposure.

Equipments used in exposure

In practice, the exposure is carried out using a Karl Suss MJB3 manual mask aligner (figure 4.8(a)) where the photomask is held on a vacuum chuck above the wafer (figure 4.8(b) and (c)). A picture of the CPW pattern on the photomask is shown in figure 4.8(b). By moving a control slot on the left of the mask aligner, the whole assembly rises up towards the photomask (figure 4.8(d)). Once, the contact indicator is on, the mask is in contact with the wafer (figure 4.8(e)). The exposure time is controlled by the buttons on the right hand side of the aligner. In this work, the photoresist is exposed to 8mW UV light for 13.5 sec.

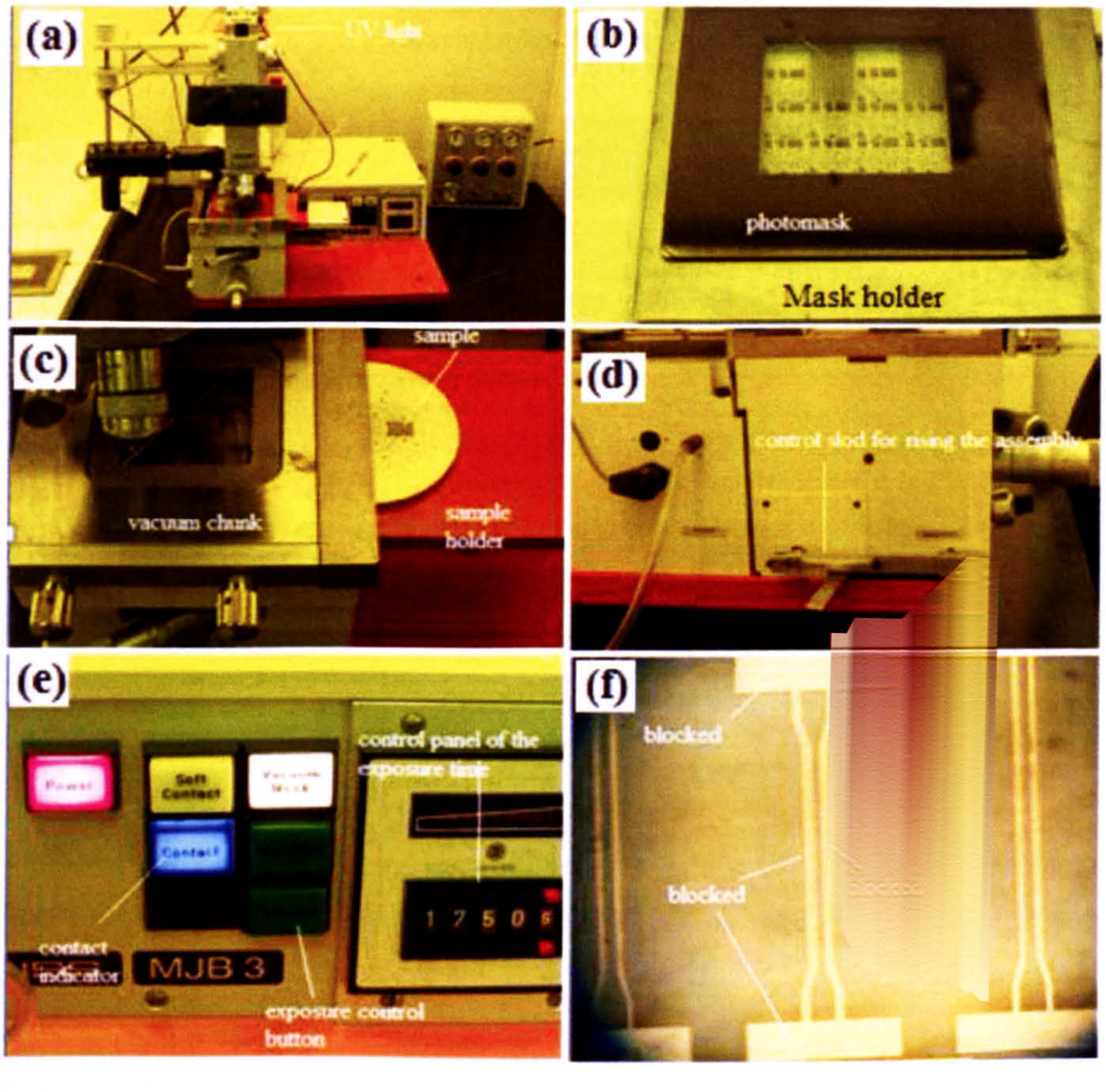

Figure 4.8 (a) Karl Suss Mask aligner. (b) photomask on the vacuum chuck (c) photomask placed opposite to the wafer (d) control slot for rising the assembly (e) control panel for the exposure and alignment (f) CPW pattern on the wafer

Step 5: developing

The last step of photolithography process is developing which removes the exposed photoresist to form a CPW pattern in the photoresist on the wafer. Since the photoresist exposed to UV light is soluble in the developer, immersing the wafer into developer removes the photoresist exposed by UV light. Figure 4.9(a) and (b) show the geometric patterns of the photoresist on the wafer after the developing process.

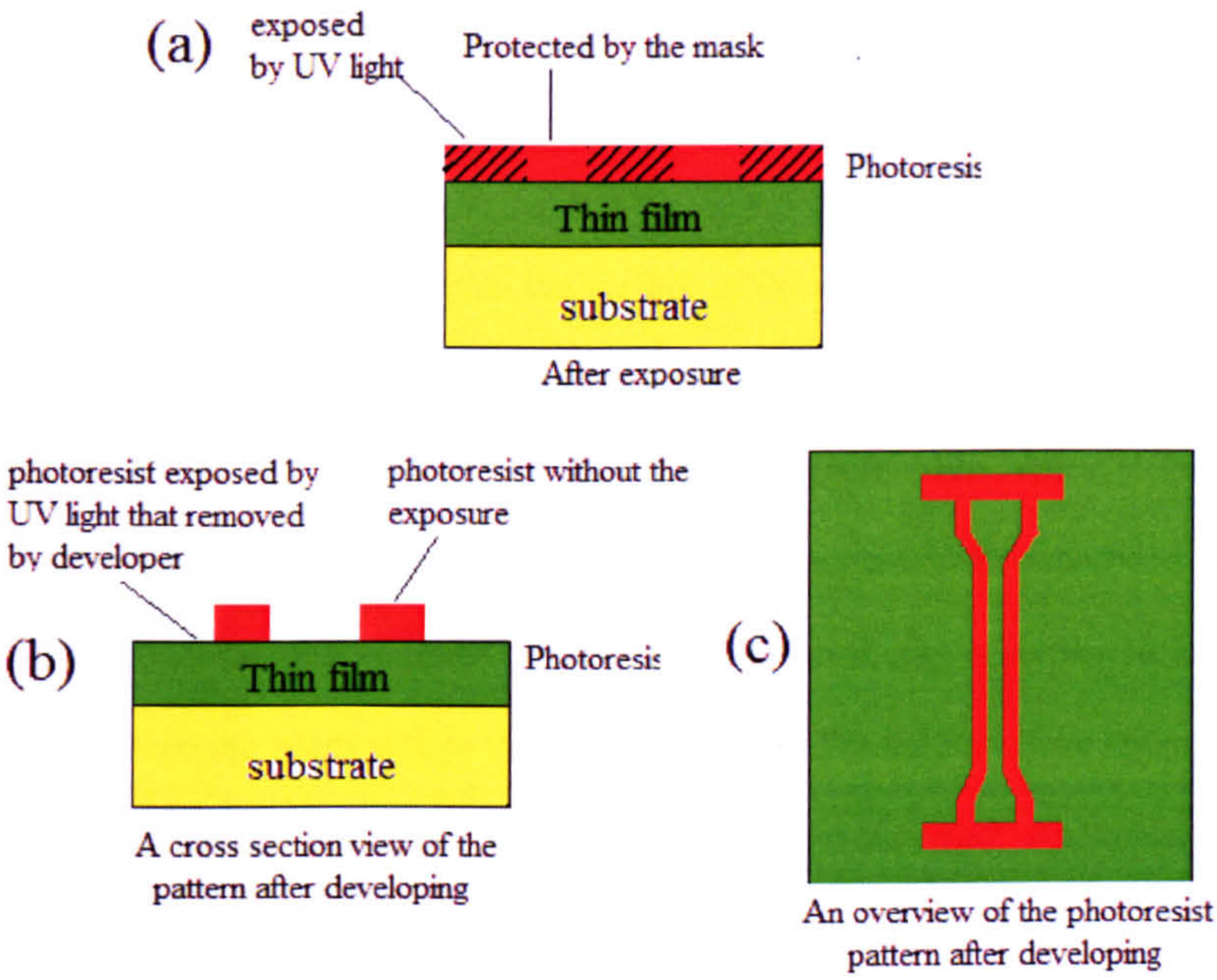

Figure 4.9 (a) after exposure (b) developing (c) an overview of the photoresist pattern on the wafer after developing

In practice, this developer is formed by a mixture of de-ionized water and AZ400 developer in a 1:1 ratio. The wafer coated with photoresist is immersed into a beaker of the developer for 20 seconds and subsequently cleaned in deionised water to stop this process. Figure 4.10(a) shows a picture of a photoresist pattern on the wafer after developing. Figure 4.10(a) and (b) compare the CPW patterns on the photomask and photoresist.

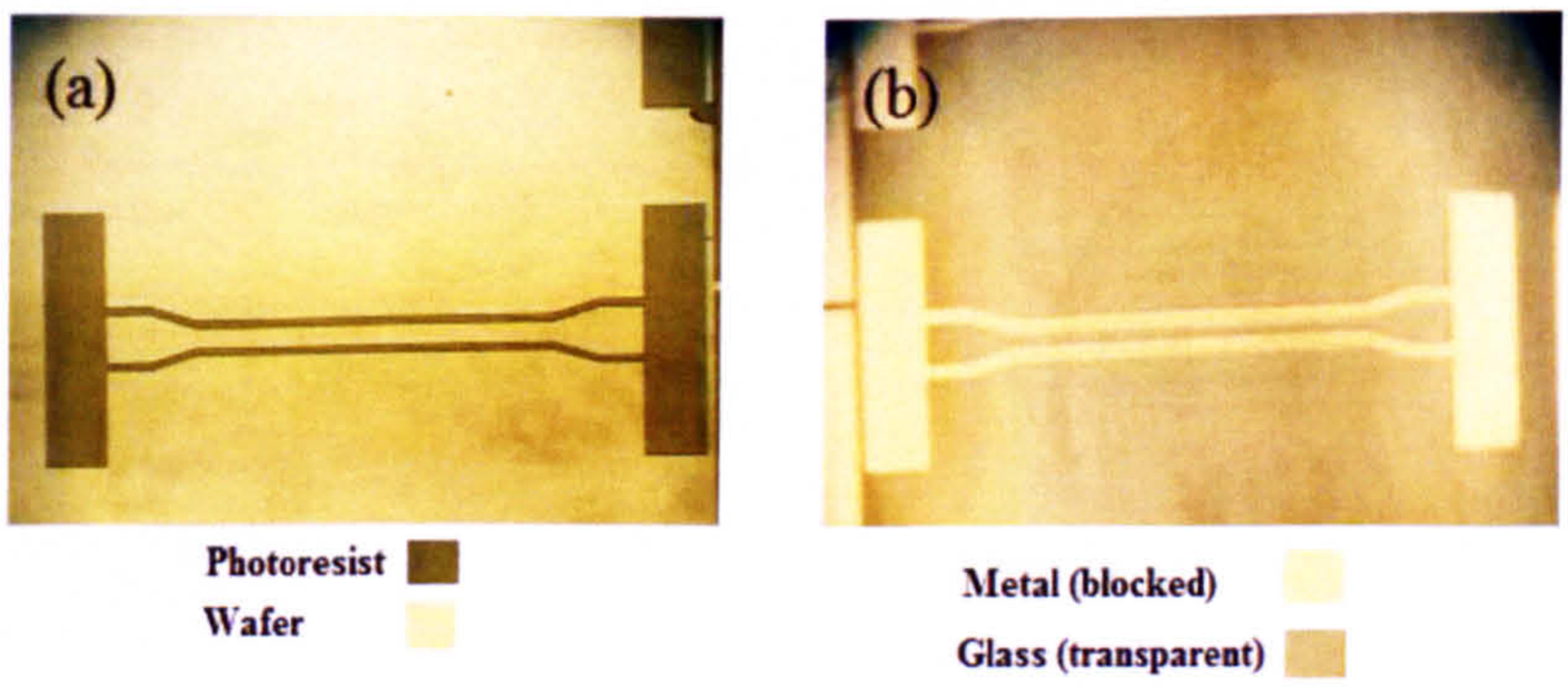

Figure 4.10(a) a picture of the CPW photoresist pattern on the wafer (b) a picture of the CPW pattern on the photomask.

Step 6: Metallization and metal lift off

The metal pattern is coated onto the surface of the wafer by electron beam (E-beam) vaporization method. The principle of E-beam is similar to that of cathode ray tube. A tungsten filament is heated to incandescence in vacuum which emits electron. These free electrons can be accelerated by an anode. The generated electron beam is focused on an ingot of the desired metal. Most of the electron energy is converted into thermal energy when the beam strikes the ingot increasing the ingot surface temperature. As the temperature is increased, some of the atoms in the ingot evaporate. Since the sample is in a vacuum, the evaporated atom travels in a straight line until it hits the cold surface of the sample where it condenses.

To achieve a layer of uniformly coated metal, the substrate is rotated during the deposition. As figure 4.11 shows, the surface of the wafer is completely covered by a layer of metal. However the edges of the photoresist are still free of metal (figure 4.11(b)). The photoresist below the metal layer is soluble in acetone (figure 4.11(c)). Therefore, the metal on top of the photoresist can be removed by acetone. The cross section and top view of the wafer after lift-off is shown in figure 4.11(d) and 4.11(e).

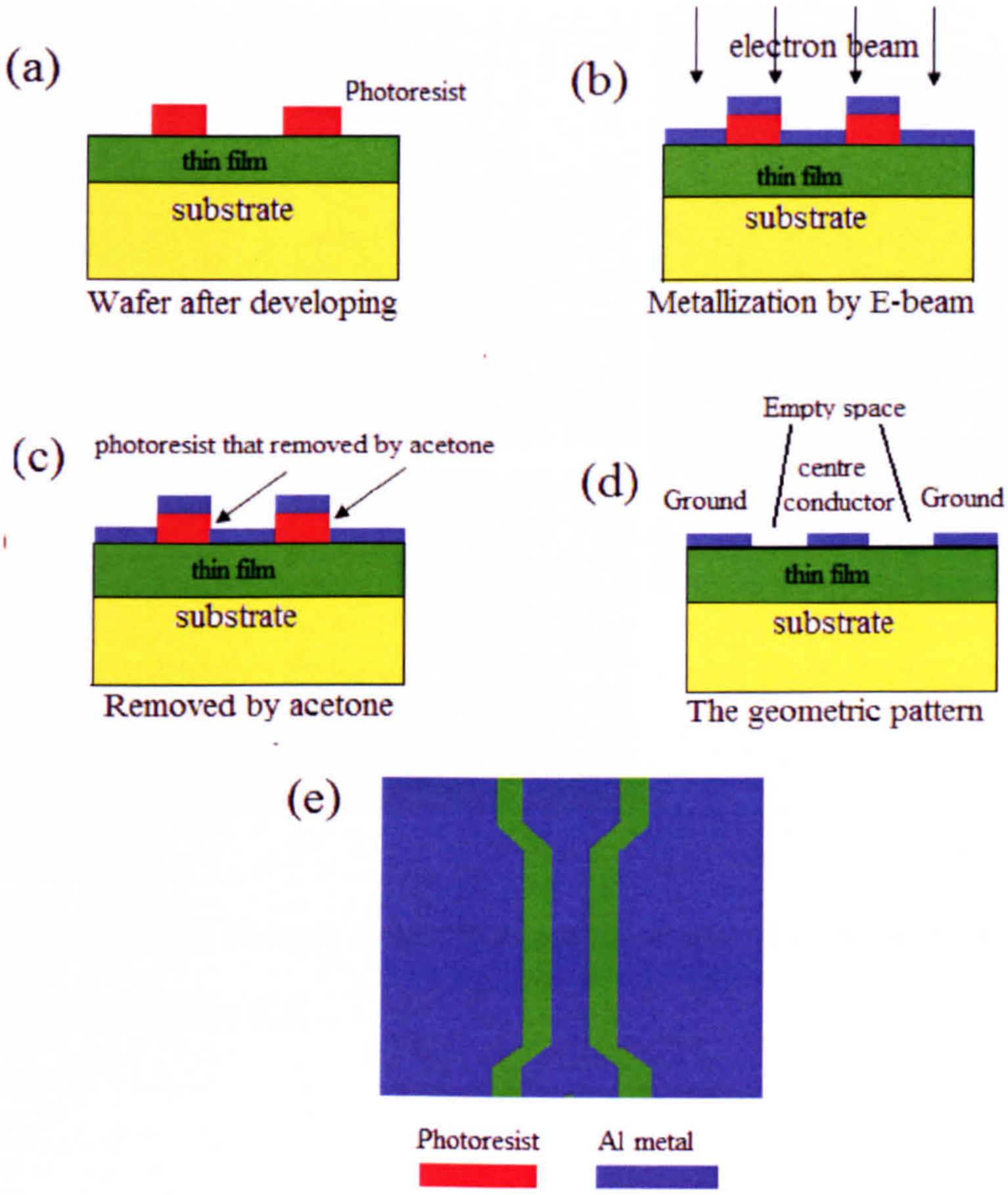

Figure 4.11, (a) developed substrate (b) Metallization by E-beam (c) Photoresist removed in acetone (d) CPW metal pattern on wafer

Equipments and practical solutions

In practice, the wafer is coated with metal using an Edwards E610 electron beam (figure 4.12 (a)). The wafer is held onto the glass slide by photoresist (figure 4.12(c)) and placed inside the vacuum chamber of the E-beam (figure 4.12(b)). In this work, the wafer is coated with a layer of aluminium (140nm). Aluminium is a low cost and high conductance metal which lowers the conductor attenuation of the CPW.

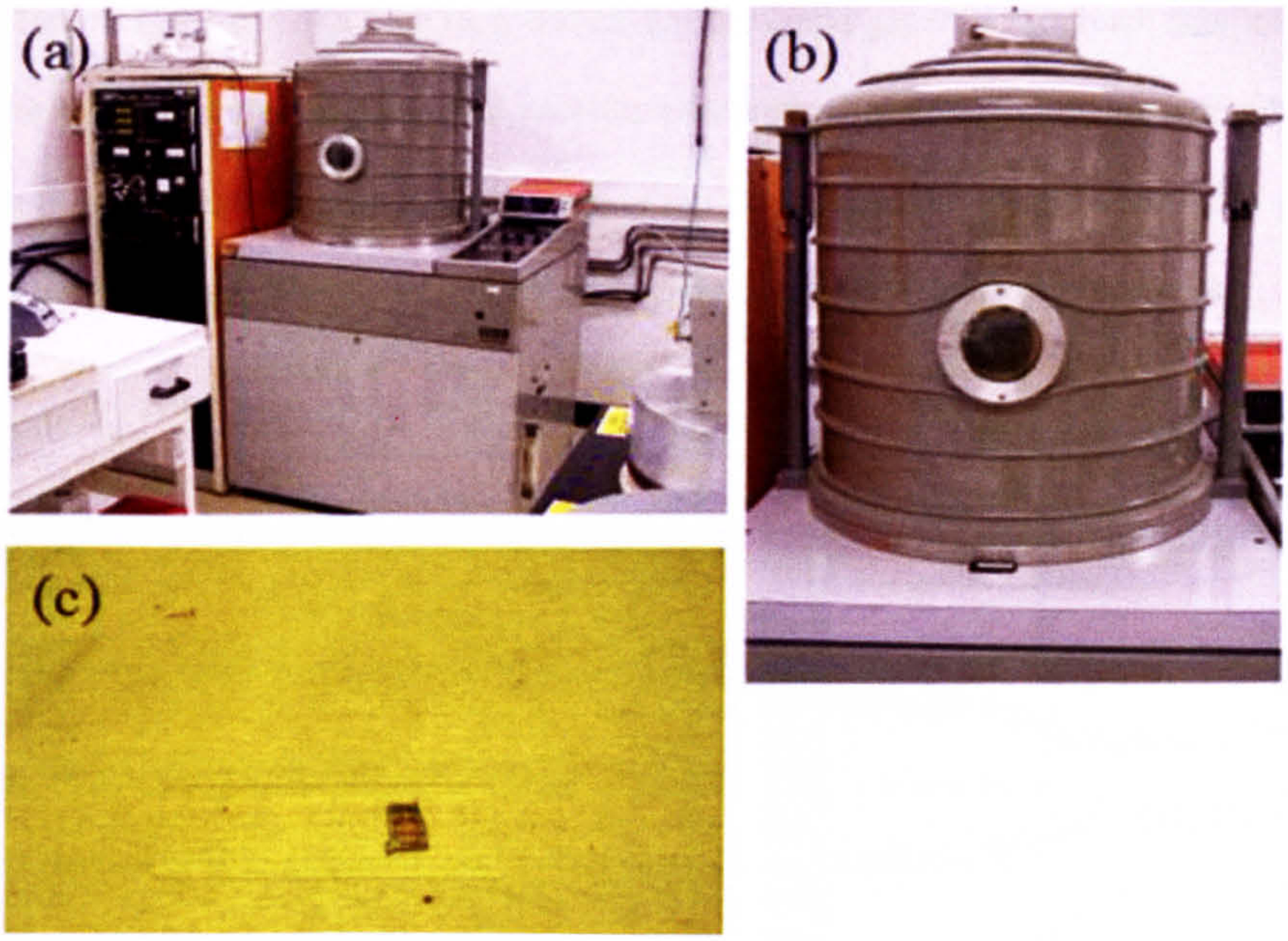

Figure 4.12(a) Electron beam (E-beam) evaporator (b) Chamber of E-beam (c) Substrate on glass slide

To lift off the metal, the wafer coated with metal is immersed into the acetone solvent and gently agitated. Eventually, the metal on top of the photoresist becomes detached from the wafer leaving behind the required pattern in the metal. To remove the acetone from the sample, the wafer is immersed into deionised water. The picture of the completely fabricated CPW is shown in figure 4.13 (a) and (b).

Because the deposition of the thin film was carried out in an uncontrolled environment, dust has fallen onto the surface of the substrates. To avoid the dust, the deposition of the thin film should be carried out in a clean room. In this work, a high temperature furnace has been employed to crystallize the thin films. The furnace can not be moved into a clean room, because there is not enough space to accommodate the furnace.

Moreover, the use of a high temperature furnace could generate too much heat inside the small clean room. The other problem encountered in this work is the difficulties in lifting off the metal to form the gaps of the CPW, since the length of the CPW gap is over 1500um. This leads to a very low yield of the CPW fabrication process.

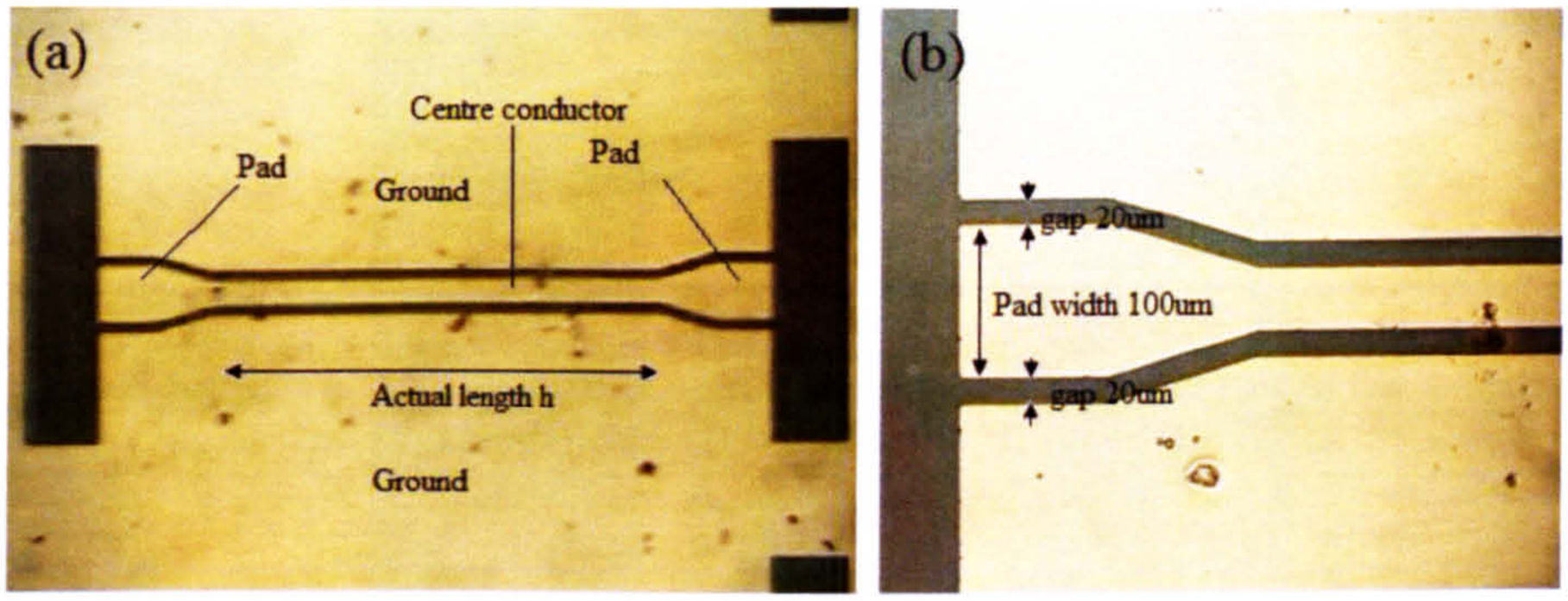

Figure 4.13(a) A picture of the CPW (b) A picture of the probing pad

4.2 Metal insulated metal capacitor (MIM) fabrication

The metal insulated metal (MIM) capacitor (figure 4.14 (a) and (b)) consists of three main components: bottom electrode, tunable thin film and top electrode. The capacitor is fabricated by a combination of photolithography and etching processes. In the following sections, a step by step description of the MIM capacitor fabrication process is presented.

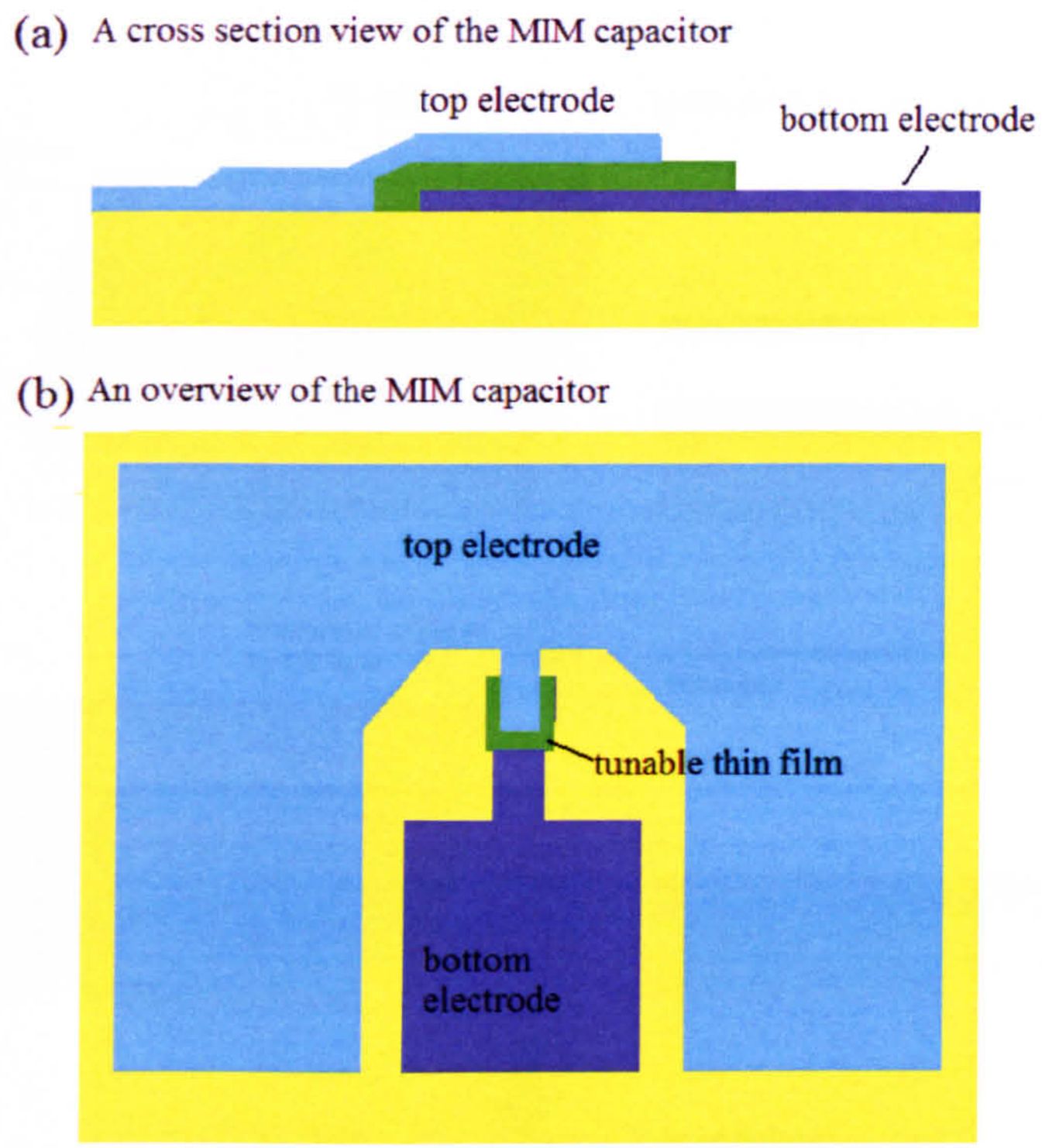

Figure 4.14 (a) a cross section image of the MIM capacitor (b) A top view of MIM capacitor.

Step 1: Ground metal pattern fabrication

The bottom electrode is made by the same positive photolithography process that was used to make the CPW. Since the principle of photolithography has already been discussed in section 4.1, it will not be discussed again. Figure 4.15 illustrates the procedures for making the bottom electrode of MIM capacitor. The thickness of the gold layer was 140nm.

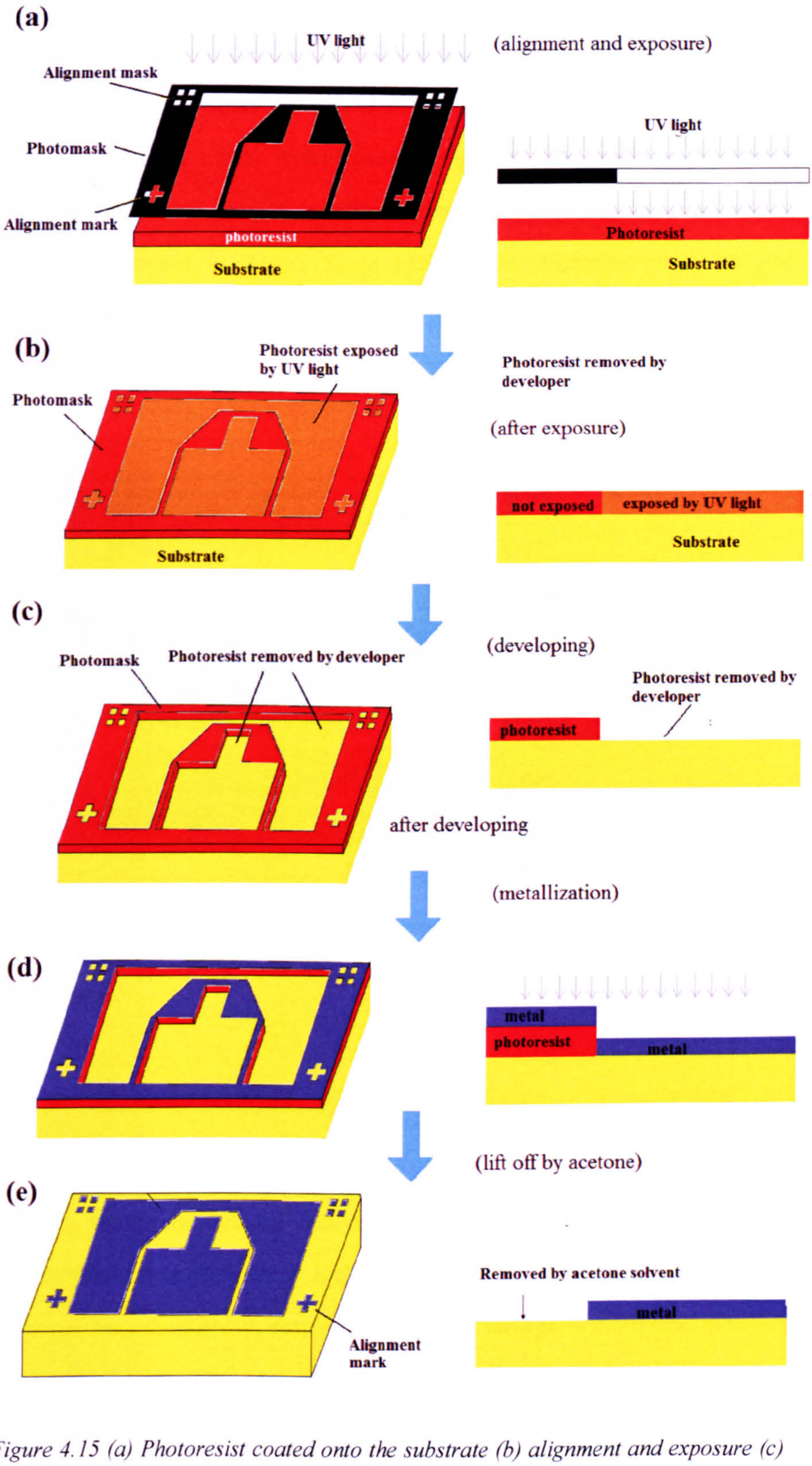

Figure 4.15 (a) Photoresist coated onto the substrate (b) alignment and exposure (c) after exposure (d) developing (e)metallization (f) lift off in acetone

The photomask used for exposure and the fabricated bottom electrode are shown in figures 4.16 (a) and figure 4.16 (b). Gold was chosen over Al because it has a much higher melting temperature and should be able to withstand the high temperature annealing necessary for the crystallization of thin film. The mask contains twelve different patterns, ten are used for different device sizes and two for de-embedding purposes (discussed in chapter 5). In addition, two alignment marks are also fabricated onto the wafer. They are used to align with the top layer photomask.

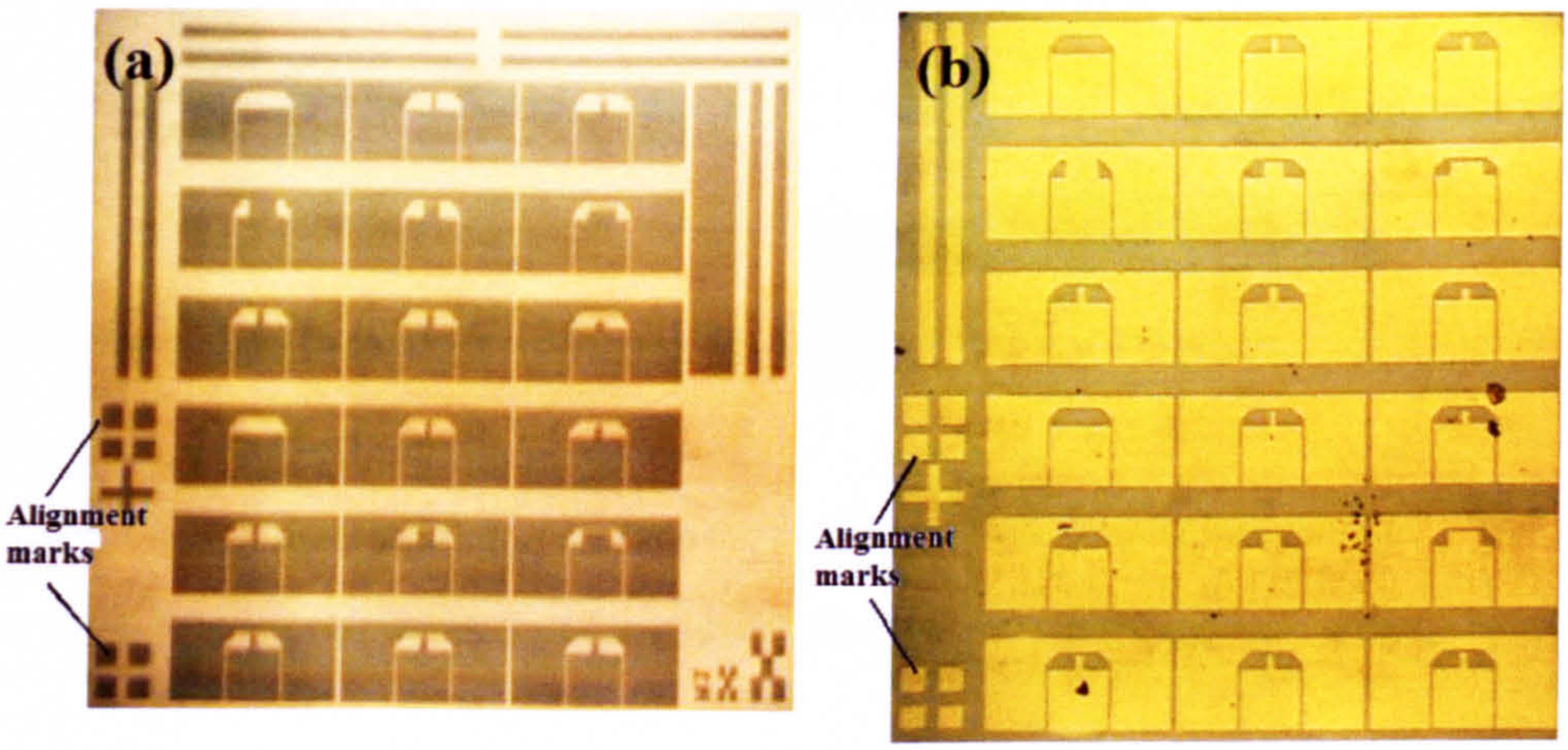

4.16(a) Photomask for bottom electrode (b) Bottom electrode of the MIM capacitor made of gold

Step 2: Thin film deposition

Once the bottom electrode has been defined, the tunable thin film can be deposited and subsequently crystallized at high temperature. The process of depositing thin films has been discussed in chapter 3. To prevent damage to the bottom electrode from the high temperature annealing process, the crystallization temperature has been kept below 700°C. This temperature was reported by many of the previous works **[7-9]** which involved the fabrication of MIM capacitors. A cross section and a top view of the wafer coated with the thin film are shown in figure 4.17. Although the entire

surface of the wafer has been covered by the crystallized thin film, only a small rectangular part of the thin film is need for the fabrication of the MIM capacitor. This rectangular shaped thin film is directly above the bottom electrode.

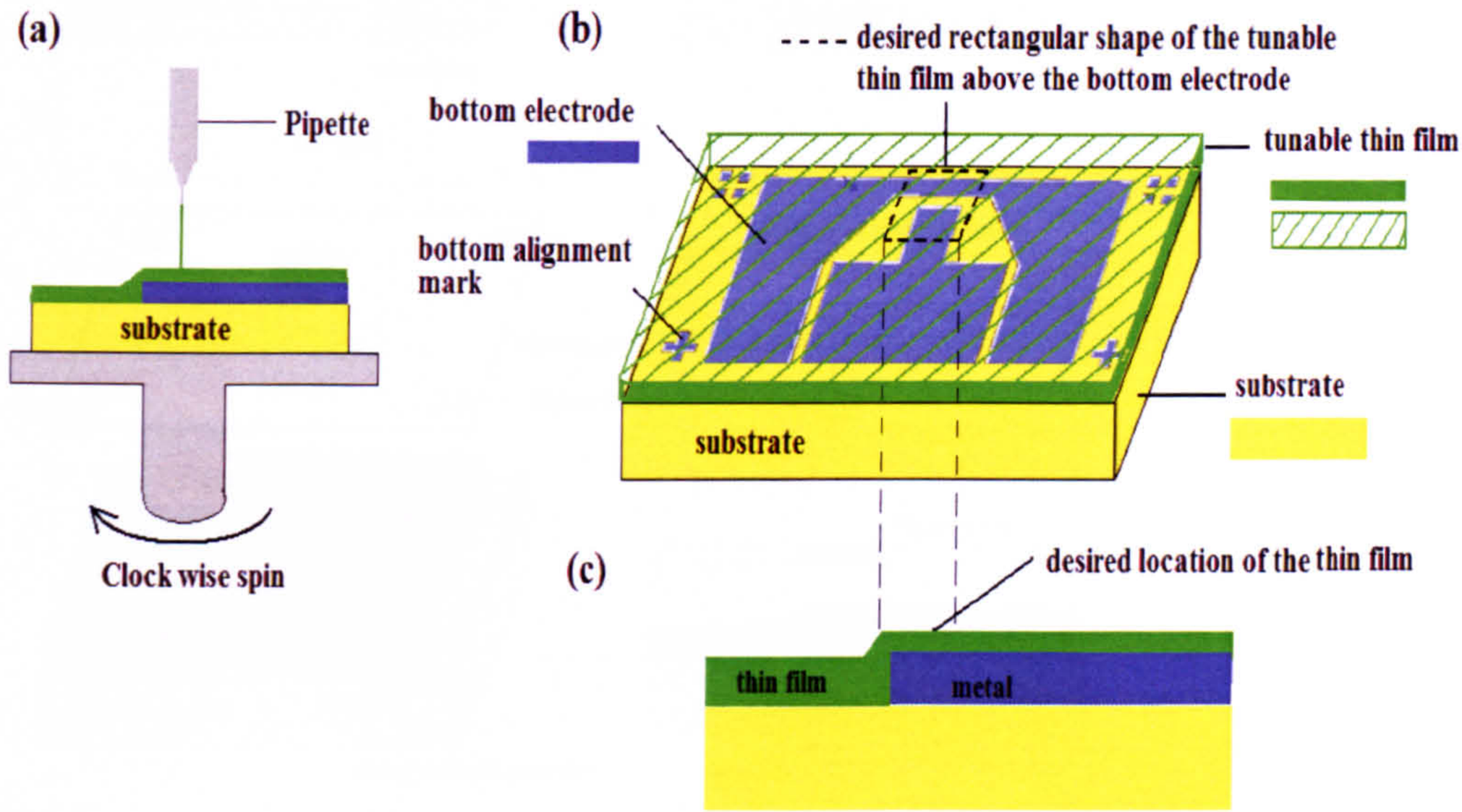

Figure 4.17 (a) spin coating process (b) a top view of the wafer coated with thin film (c) a cross section view of the wafer coated with thin film

Step 3: Thin film etching and alignment

In step 2, the entire surface of the wafer was covered by the tunable thin film. However, the MIM capacitor only contains a rectangular shaped film that is above the bottom electrode. Hence a chemical etching process is used to remove the unwanted part of the film using hydrofluoric acid (HF). To create a rectangular shaped thin film on the wafer, a layer of rectangular shaped photoresist is coated on top of the electrode, which prevents the etching of the thin film by the HF. Figure 4.18 shows the procedures of thin film etching.

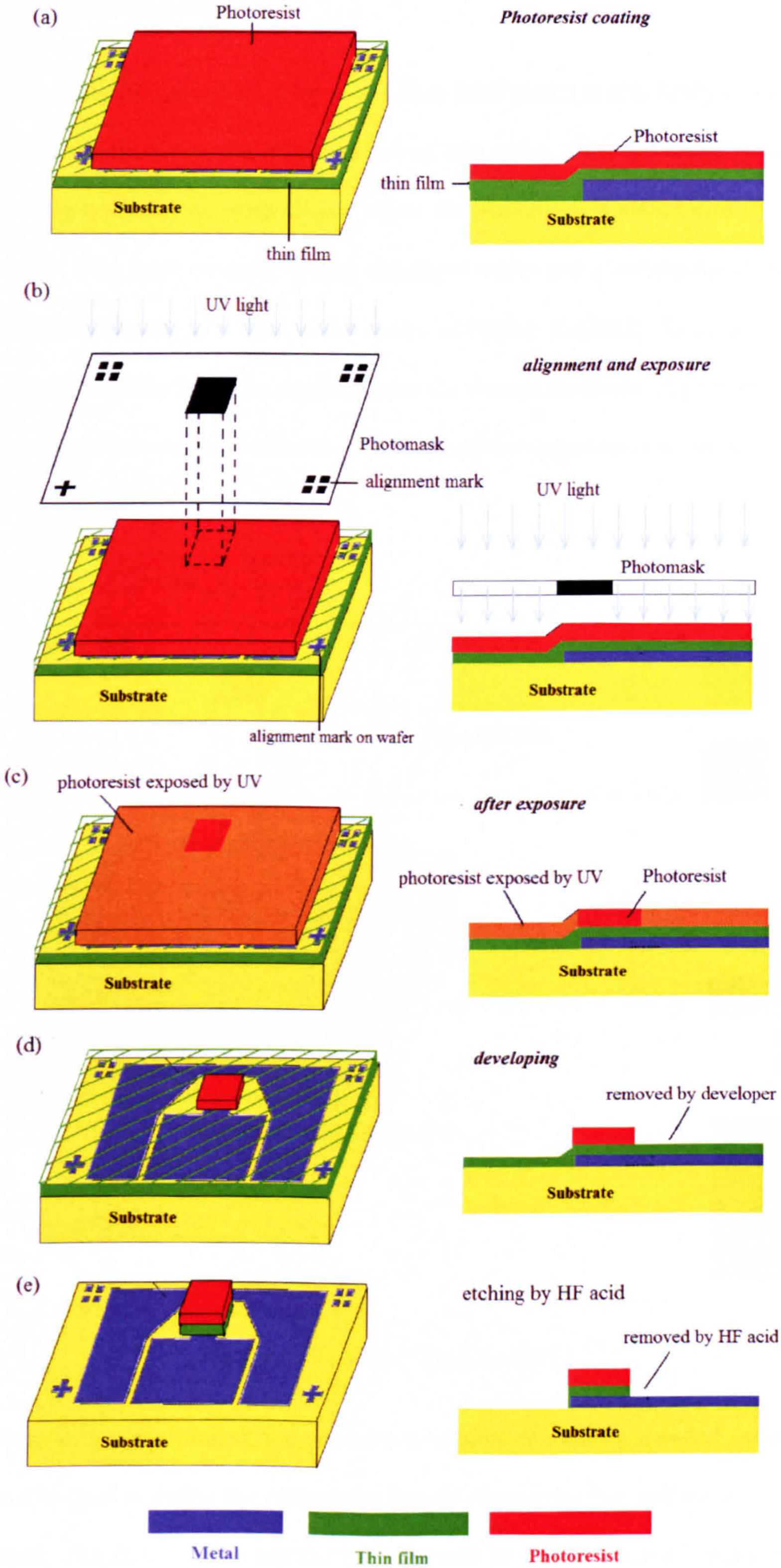

Figure 4.18 (a) photoresist coating (b) alignment and exposure (c) after exposure (d) developing (e) etching in HF acid (f) photoresist washed away by acetone

Procedures of etching

According to figure 4.18, a layer of 1.2μm thick photoresist is firstly coated onto the wafer which covers the entire surface of the wafer. Then the wafer is placed on a sample holder in the mask aligner where the photomask is placed directly above this wafer. This mask contains several alignment marks and a rectangular shaped pattern which blocks the UV light in the centre of bottom electrode. Since the rectangular shaped thin film has to be created above the bottom electrode, alignment marks have been included on the photomask. The set up of the alignment is shown in figure 4.19.

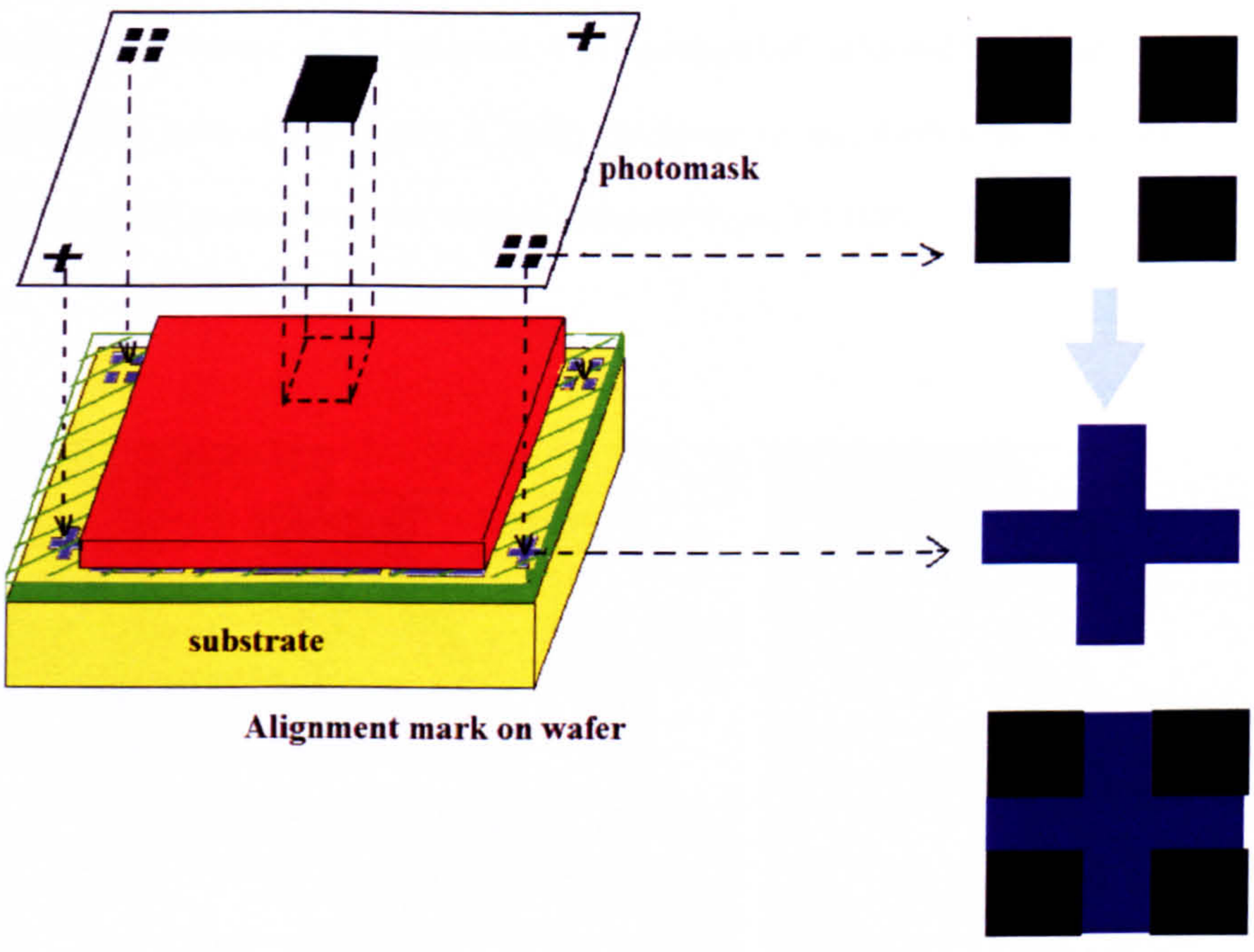

Figure 4.19 set up of the alignment

Once they were aligned, the photolithographical procedures detailed in section 4.1 can be used to define the rectangular shaped photoresist that will be used as an etch mask. The film that that has not been covered by the photoresist is removed by HF (figure 4.19 (e)). In contrast, the film covered by the rectangular shaped photoresist will not react with the HF acid, leaving a rectangular shaped thin film on the wafer. Finally, the photoresist on top of the film is washed away in acetone solvent.

Alignment in practice

In practice, the alignment mark on the wafer is aligned with the mark on the photomask by adjusting the X-Y positions of the sample holder. The control rods for adjusting the positions of sample holder are indicated in figure 4.20. The one at the front of the wafer holder controls the movement of wafer in Y direction and the other one control the movement of the mask in X direction. By carefully adjusting these rods, the alignment marks on the photomask can be manually aligned with another mark on the photomask. Once the photomask and the wafer are aligned, the wafer holder is moved upwards to the photomask and therefore, a good contact between the wafer and photmask can be achieved. The movement of wafer holder is controlled by turning the control rod (figure 4.20(b)) clockwise or anti clockwise. A picture of photomask in contact with the wafer is shown in figure 4.21(d).

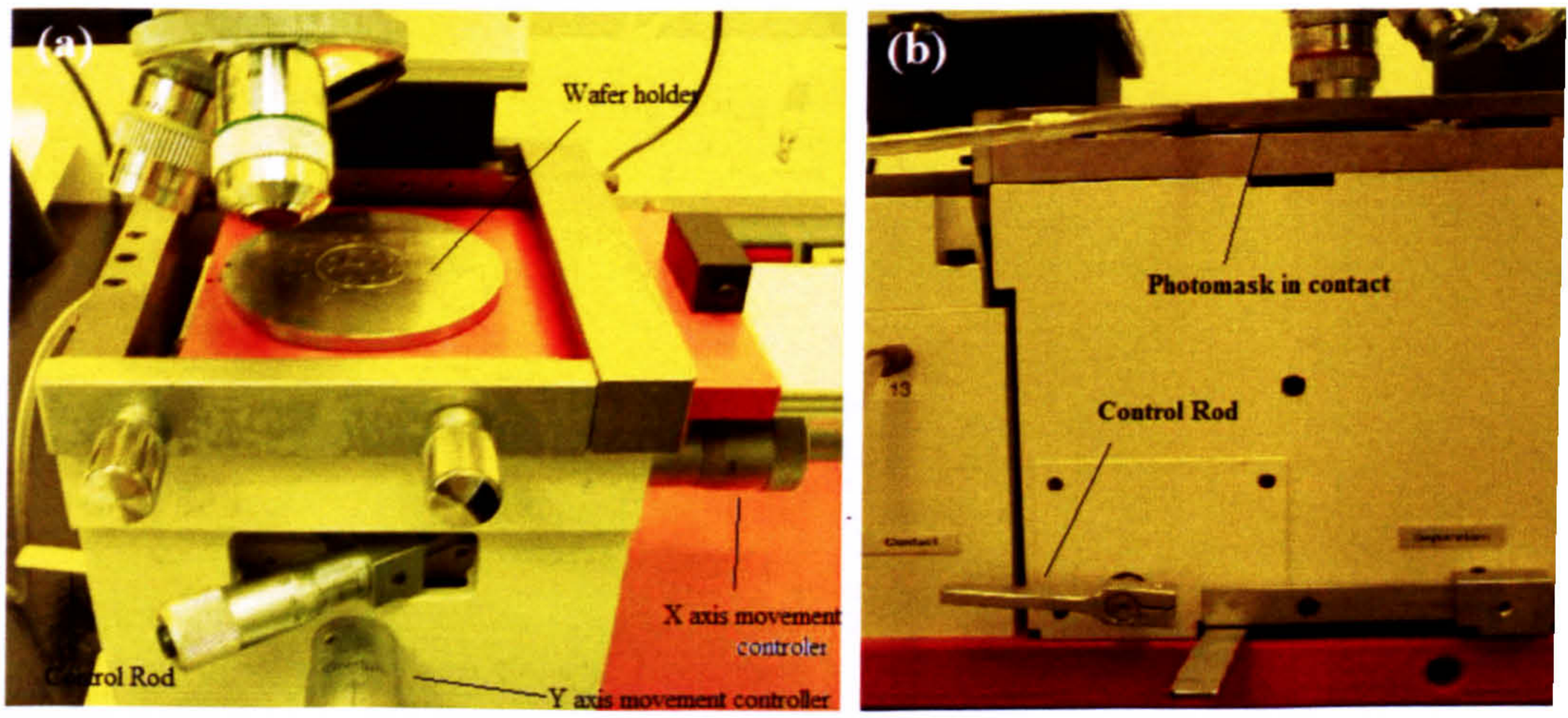

Figure 4.20 (a) a top view of mask aligner (b) an side view of the mask aligner (in contact)

Figure 4.21(a) shows a picture of the photomask used for etching the thin film. The alignment marks on the wafer and photomask are shown in figure 4.21 (b) and (c),

respectively. Figure 4.21(d) shows the alignment between the photomask and wafer. Although, the alignment mark on the photomask is not perfectly aligned with the alignment mark on the wafer, the rectangular shaped pattern is above the bottom electrode and covers the whole bottom electrode. Therefore, the imperfect alignment does not affect the capacitance of the device.

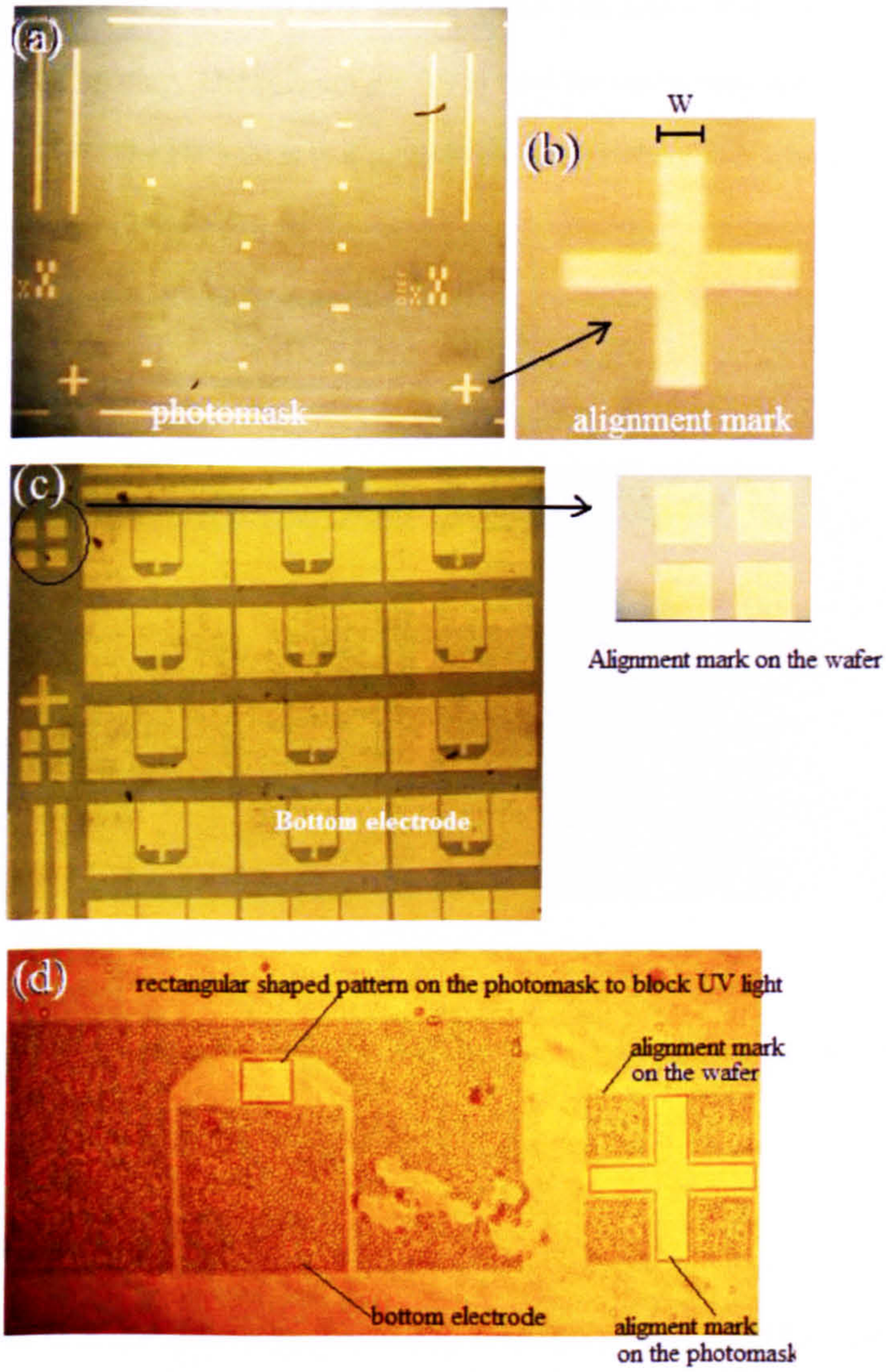

Figure 4.21 (a) a picture of the photomask (b) alignment mark on photomask (c) the bottom electrode of MIM capacitor on the wafer with alignment marks (d) Photomask aligned with the bottom electrode on the wafer

Etching in practice

Etching with HF is a very dangerous process and can be lethal. Therefore, this process was carried out in great care and closely following detailed protocols. Figure 4.22 (a) is a photograph of the arrangement used in the etching process. The stop watch (a) is used for counting the etching time. The deionised water in (b) and (f) are used to stop the etching process and cleaning the containers that are made of polyethylene after etching. The calcium gel (d) is used for emergency aid if skin has been exposed to HF. The HF acid is in a ceramic beaker (e) where the etching process takes place.

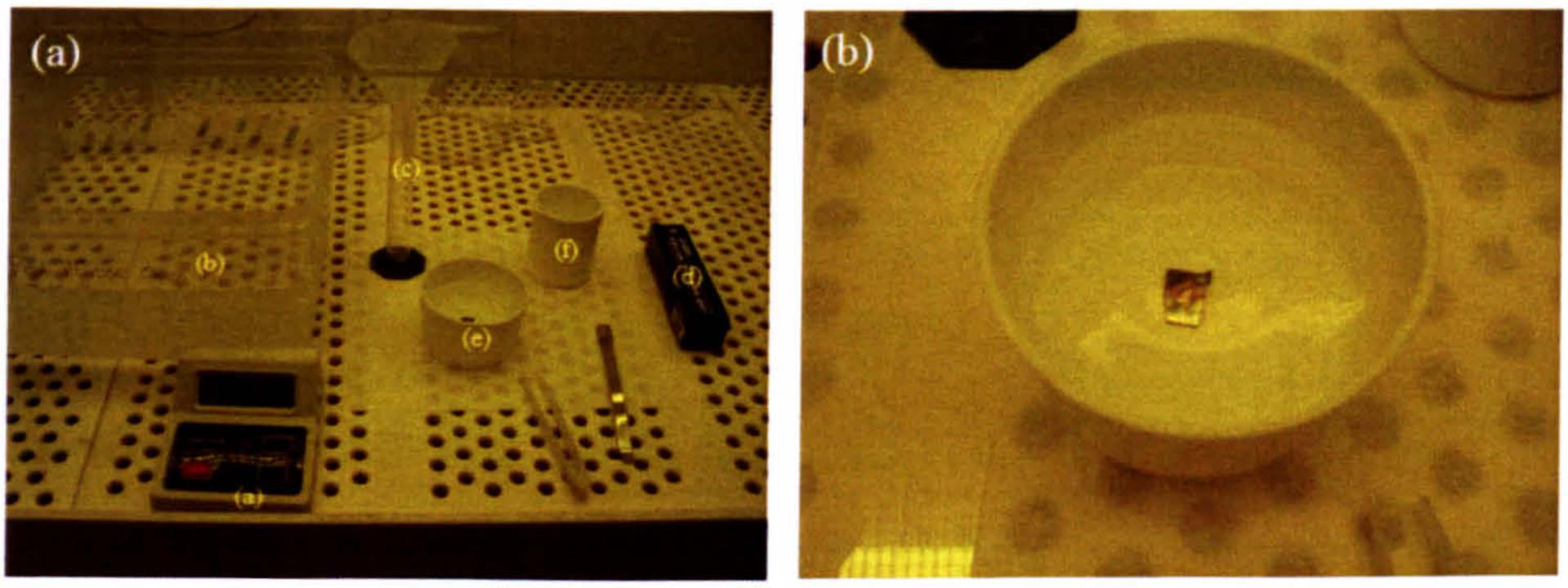

Figure 4.22 (a) the equipment used for etching (b) a real picture of etching in progress

To etch the thin film, the wafer is immersed into a mixture solution with HF acid and deionised water at a ratio of 1:10 for 30sec and then washed in deionised (DIW) to stop the etching process. As result of this etching process, a rectangular shaped thin film is created above the bottom electrode and the rest of the film is removed. Figure 4.23 shows a photograph of the wafer with the square shaped thin film above the bottom electrode. Because this picture was taken shortly after the etching process, the photoresist was not completely removed from the surface of the sample. The

remaining photoresist on the surface of the sample looks like "dust" which makes the quality of the device looks very poor. The remaining photoresist will be removed after the three step cleaning process that was discussed in section 3.2.

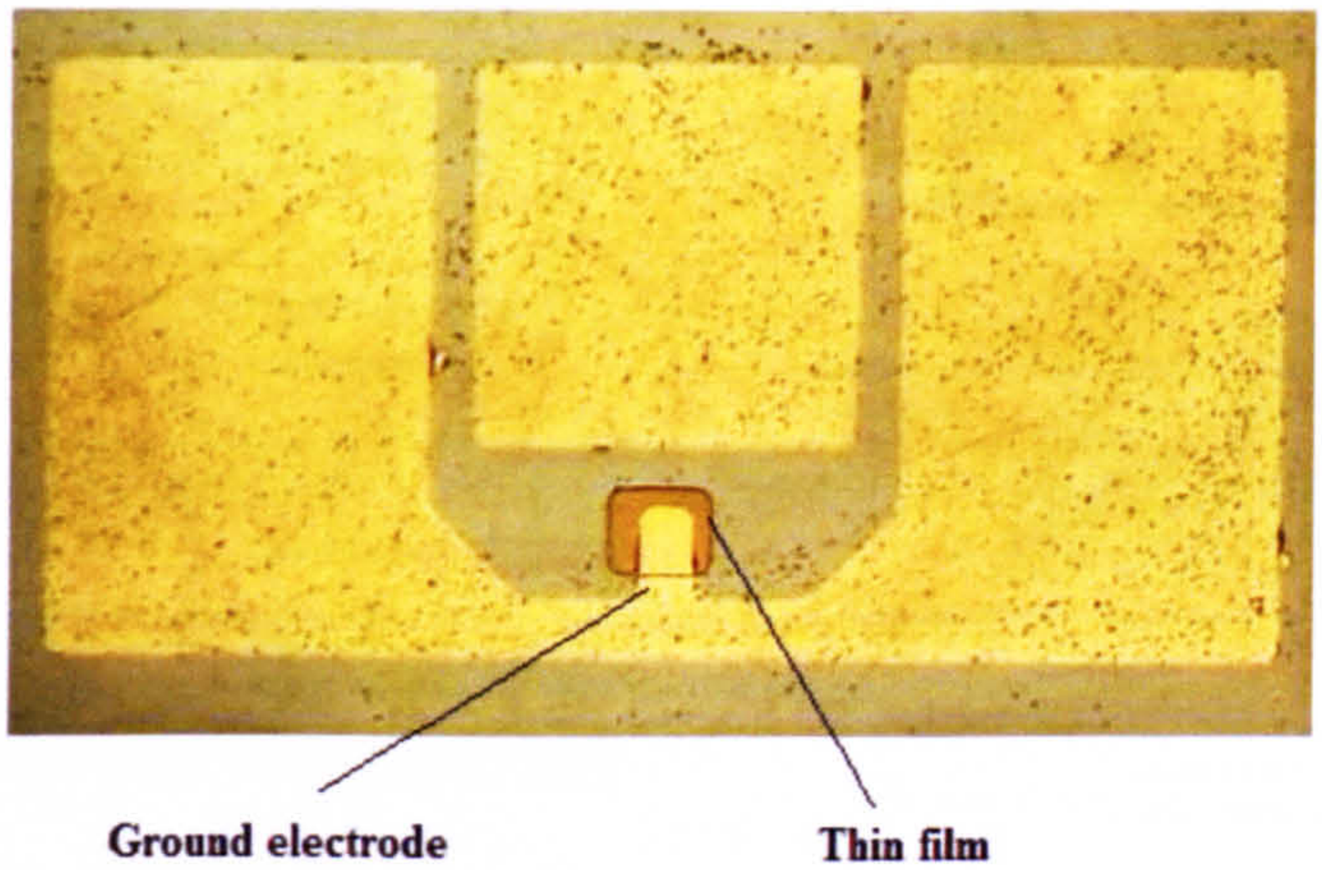

Figure 4.23 a top view picture of the tunable thin film on the bottom electrode.

Step 4: Top electrode deposition by photolithography

The top electrode of the MIM capacitor is also made by the lift off process discussed in step1. Figure 4.24 shows the detail procedures of making the top electrode of the MIM capacitor.

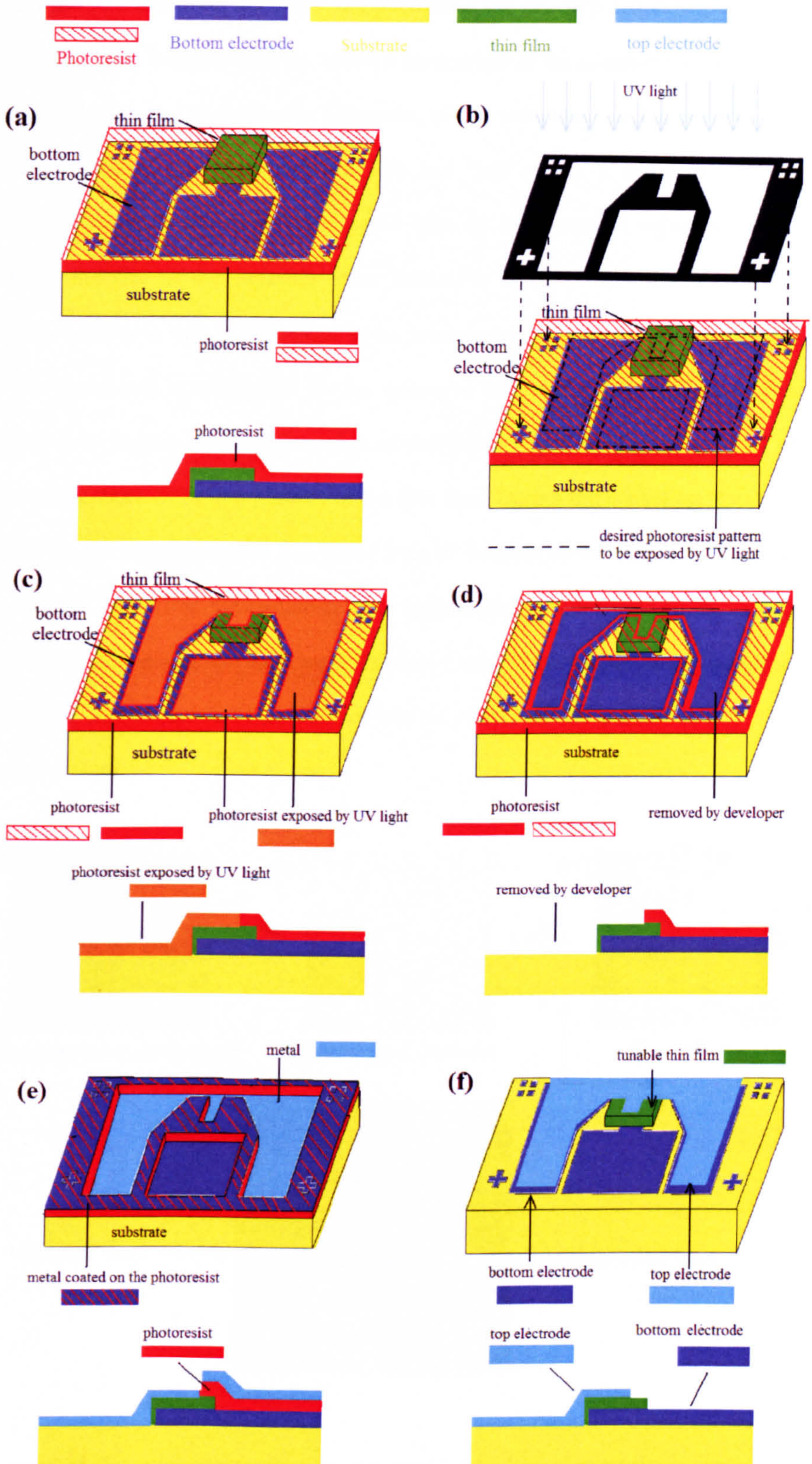

Figure 4.24 (a) photoresist coating (b) alignment and exposure (c) after exposure (d) developing (e) E-beam metallization (f) lift off by acetone.

The alignment marks on the wafer and photomask for this step are shown in figure 4.25 (a) and (b). In figure 4.25 (c), shows a photograph of the alignment marks on the finished device. As it shows the alignment of the photomask is not perfect. The misalignments of the photomark are 1μm and 2μm on the x and y-axis of the alignment mark on the wafer. This could form an asymmetrical capacitor, which changes the size of the capacitor from $100um^2$ to $70um^2$. The variations in the capacitor size also lead to large error in the measurement of capacitance. The effects of the photomask misalignment on the measured dielectric results will be further discussed in chapter 5. The appearance of bubbles in figure 4.25(c) is the result of high temperature annealing (700°C) of the thin film. During the annealing, the extra oxygen in the amorphous thin film could form air bubbles on the bottom of the gold electrode. Despite this, the formation of air bubbles was only observed on the surface of the alignment marks and there are no bubbles found on the surface of the capacitor. Therefore, the formation of air bubbles has no effects on the quality of the MIM capacitor at all.

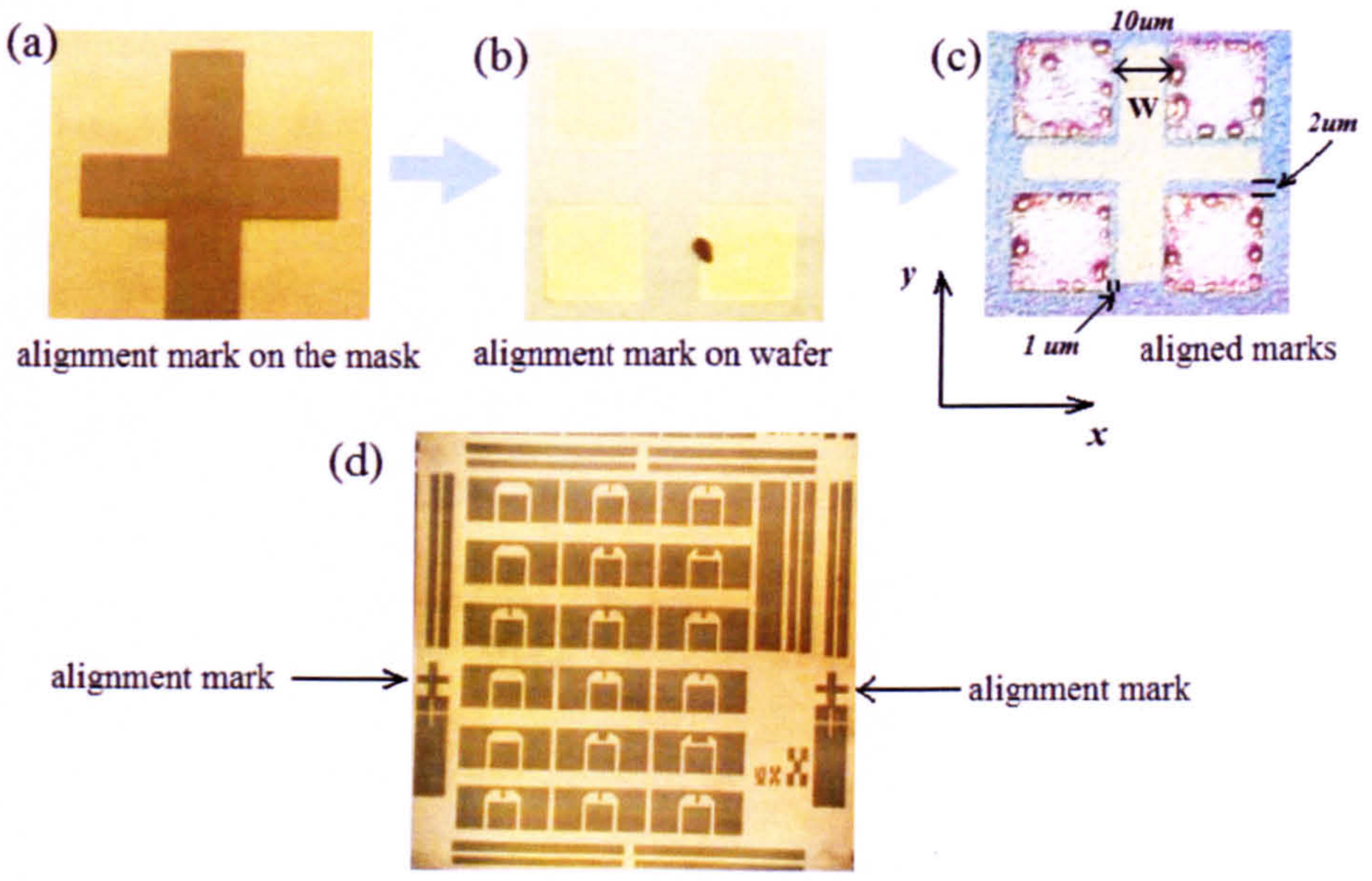

Figure 4.25 (a) alignment marks on the mask, (b) alignment mark on wafer (c) aligned marks (the errors of the alignment are indicated by the arrows) (d) a picture of the photomask

The MIM device is now complete and figure 4.26 gives a photograph of the completely fabricated MIM capacitor.

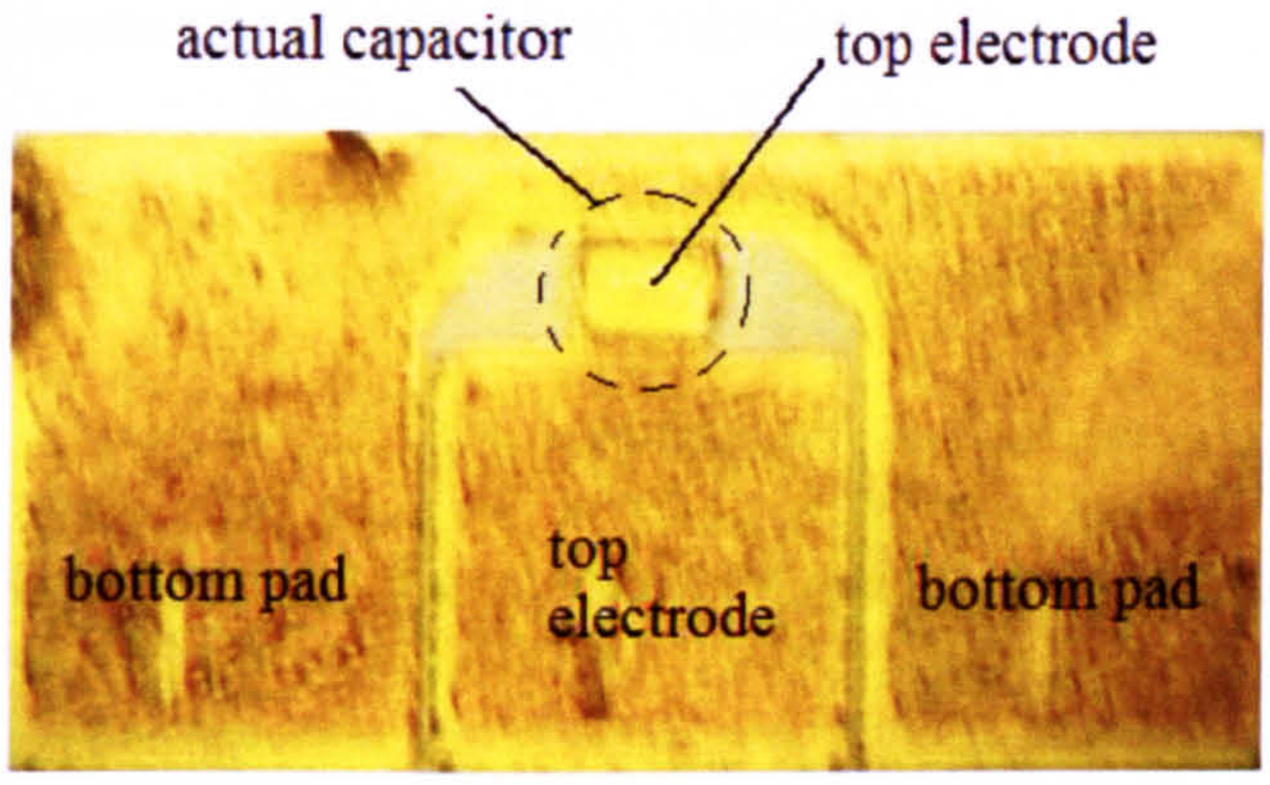

Figure 4.26 a picture of the completely fabricated Metal insulated metal (MIM) capacitor

References:

[1] J. Powell, A. Porch and M. J. Lancaster, "Thin-film ferroelectric microwave devices," *Supercond Sci. Technol,* vol. 11, 1323-1334, 1998.

[2] T. J. Jackson, M. J. Lancaster and P Bao, "Dielectric characterization of a ferroelectric film in the sub-GHz region," *J. Phys. D: Appl.Phys,* vol. 41, 185410, 2008.

[3] S. J. Lee, S. E. Moon, M. H. Kwak, *et al*, "High dielectric tunability of (Ba,Sr)TiO_3 thin films and their Coplanar waveguide phase shifter applications," *Jap.J of Applied Physics,* vol. 43, 6750-6754, 2004.

[4] J. Park, J. W. Lu, S. Stemmer and J Park, "Low loss, tunabe microwave capacitor using bismuth zinc niobate thin film," *14th IEEE International Symposium on Applications of Ferroelectrics*, 2004.

[5] W. Gardner and W. Julian, *et al*, *Microsensors MEMS and smart devices*, *Wiley,* 15. 2006.

[6] J. Du, *Processing and characterization of functional multicomponent oxides by electrostatic spray assited vapour deposition (thesis)*, University of Nottingham, 2007.

[7] P. C. Joshi and S. B. Krupanidhi, " Strontium Titanate thin films by rapid thermal processing", *Applied Physics Letters*, vol.61, 13, 1525-2527, 1992.

[8] G. Venkataramanan, *Barium Strontium Titanate films for tunable microwave and acousitc wave applications (thesis)*, University of South Florida, USA, 2007.

[9] J.W. Lu, Z.Q. Chen and S, Stemmer, "Composition control and dielectric properties of Bismuthc Zinc Niobate thin films synthesized by RF magnetron sputtering", *Journal of Vacuum Science and Technology A, vol.21, 5, 1745-1751, 2003.*

Chapter 5 Microwave characterization

As mentioned in section 2.2.7, the characterization of the dielectric properties of BST and BZN thin films was achieved by measuring the high frequency response of coplanar waveguide (CPW) and metal insulated metal (MIM) capacitors. In tunable microwave devices applications, three aspects of the material's dielectric properties are particularly interesting: (1) the real part of dielectric constant (ε')at 0V; (2) the dielectric loss tangent $tan\delta_{\varepsilon_r}$; (3) dielectric tunability. The definitions of the dielectric loss and dielectric tunability of the thin film are presented in sections 2.1.4 and 2.2.4.

In general, there are two different methods to characterize dielectric materials: non-resonant and resonant methods [1]. The non-resonant characterization method has been widely used to determine the dielectric properties of the thin films because of its simplicity. In the non-resonant method, the properties of the material are obtained by measuring the wave attenuation and phase constant of waves interacting with the material [1]. When an electro-magnetic wave passes through two different materials the attenuation and phase constant of the signal changes resulting in a reflection of the wave. The dielectric properties of the material can be determined from the magnitude and phase of the transmitted and reflected waves [1]. Hence, this particular type of non-resonant method is usually called "transmission/reflection" method.

The "transmission/reflection" method can be implemented using a transmission line such as a coplanar waveguide (CPW method) or by measuring the impedance of a

capacitor (capacitor method). The following section (5.1) provides the background information about the CPW characterization method. An example of the CPW characterization and the working principles of the MIM capacitor method are discussed in sections 5.2 and 5.3.

5.1 Background information for the coplanar waveguide (CPW) characterization method

In this work, the transmission/reflection characterization method is implemented by measuring the propagation coefficient of the TEM mode propagating along a coplanar waveguide (CPW) transmission line. The propagation constant of a transmission line describes the attenuation and phase shift of the microwave signal travelling through the transmission line. Thus, a brief discussion on transmission line theory is given in section 5.1.1. In section 5.1.2, the method of determining the dielectric properties of a thin film using a conformal mapping technique is presented.

To understand the measurements, the basic theory of microwave circuit characterization such as: impedance/admittance network theory and scattering parameters must be discussed first (sections 5.1.3, 5.1.4, 5.1.5 and 5.1.7). Because the response of CPW and MIM capacitor are measured from a vector network analyzer (VNA), a brief discussion on the working principles of the VNA is also presented in section 5.1.6.

5.1.1 Transmission line analysis using equivalent circuit model

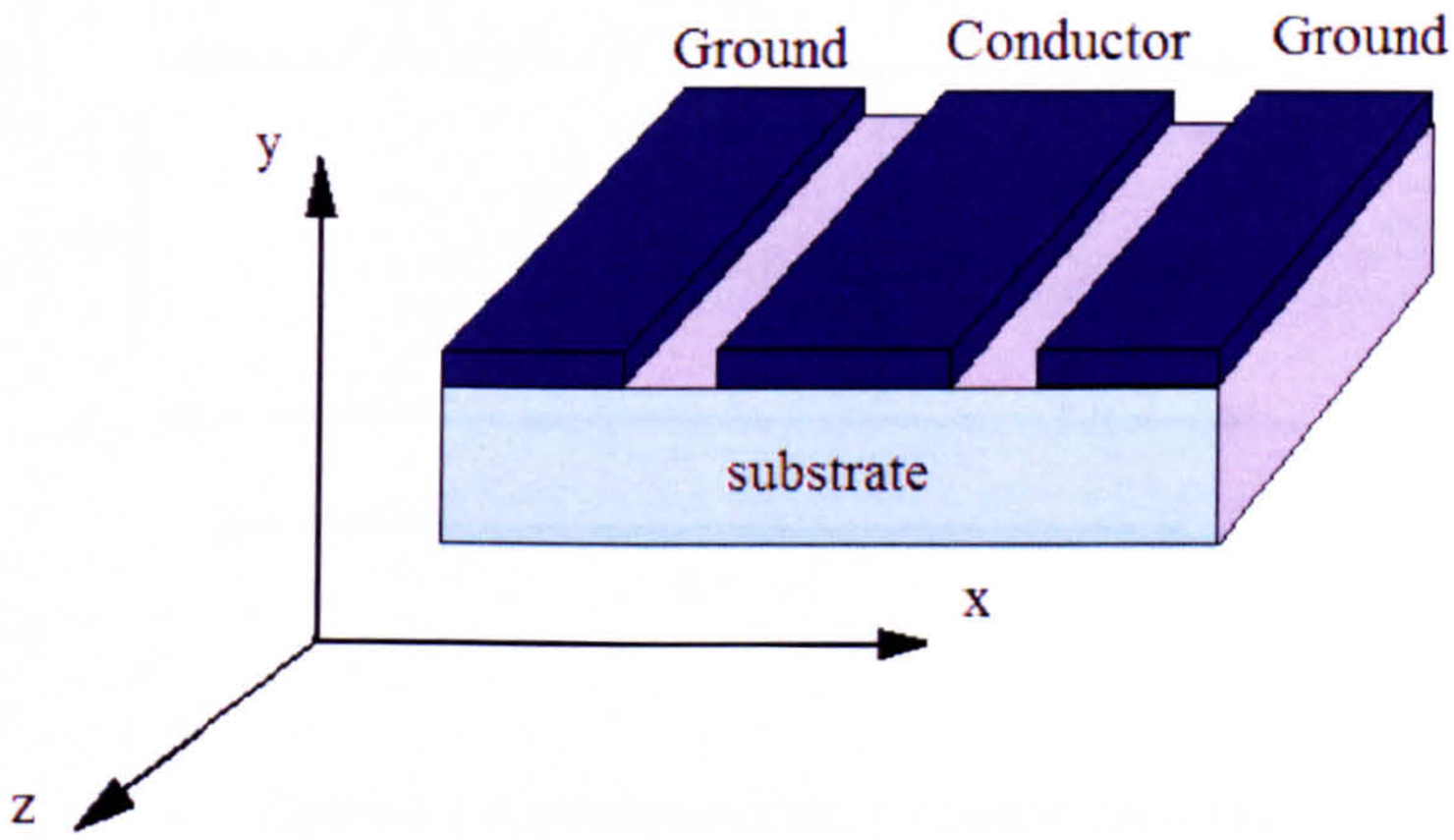

Figure 5.1 the 3-D image of a coplanar waveguide (CPW).

Figure 5.1 gives the 3-D schematic image of a TEM mode CPW transmission line, which like all TEM modes has a cut off frequency at 0Hz. The general theory of the propagation of electromagnetic (E/M) wave in this structure can be solved using "Maxwell" equations. "Maxwell" equations can provide the distribution of the microwave within a microwave structure (CPW). In the present work, we are only interested in the response of how the microwave structure (CPW) response to external microwave signals [1].

Therefore, the CPW is analyzed using an equivalent circuit model shown in figure 5.2. This model is based on the concept of equivalent voltage, current and impedance that are determined by the properties of the transmission line. In the equivalent circuit model, the transmission line is divided into several small sections of length Δz. Each section of the transmission line is represented by the passive circuit shown in figure

5.2 where R represents the ohmic loss of the conductor per unit length and G represents the loss associated with the dielectric per unit length. L and C are the inductance and capacitance per unit length.

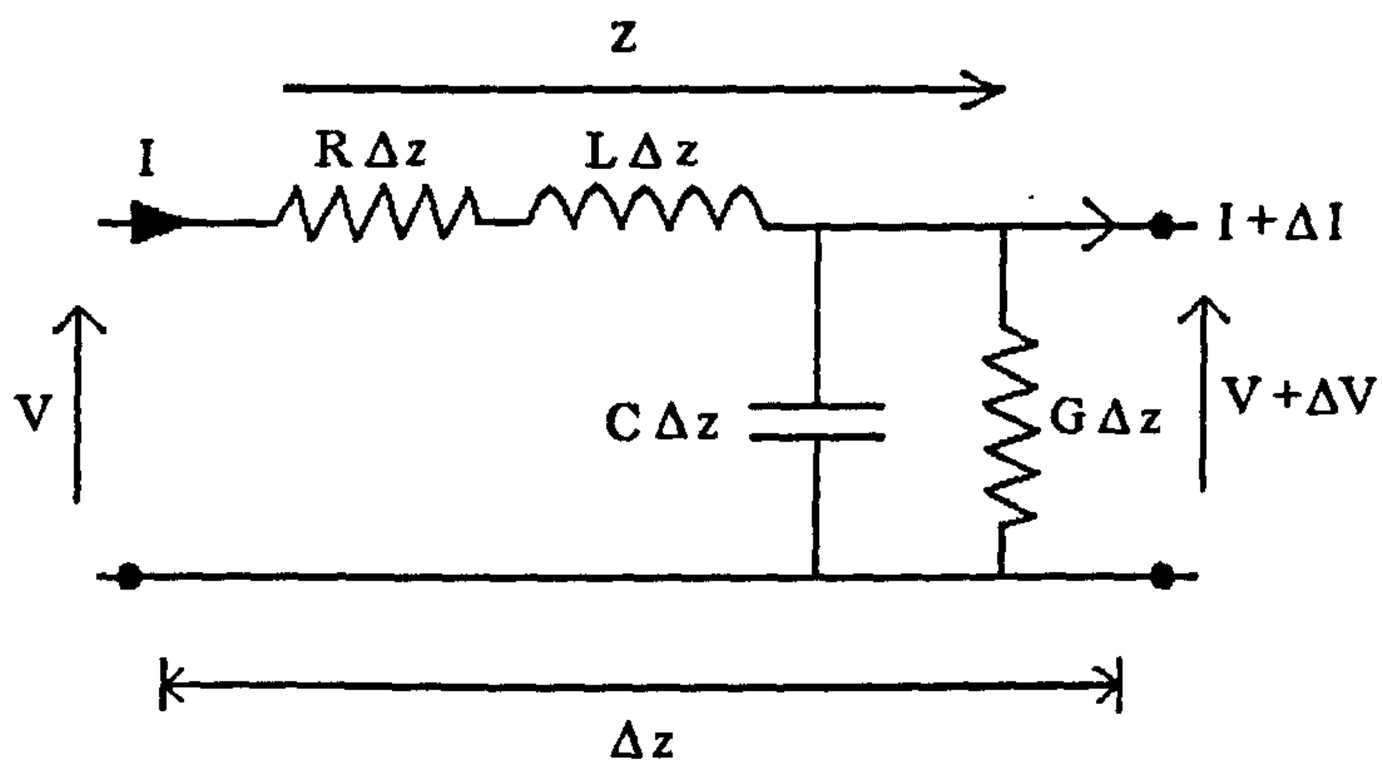

Figure 5.2 equivalent circuit of a transmission line

To measure the dielectric properties of the thin film, the important characteristic parameters of the transmission line are the characteristic impedance (Z_o) and the propagation constant (γ). The detailed mathematical calculation can be found in **[2, 3]** and so the results of the transmission line's characteristics are given in the following sections.

Characteristic impedance (Z_o)

It is well known that the unit length impedance and the unit length admittance of the transmission line are given by **[4]**

$$Z = R + jwL \tag{5.1}$$

$$Y = G + jwC \tag{5.2}$$

and the characteristic impedance of the transmission line is given by

$$Z_o = \sqrt{\frac{Z}{Y}} = \sqrt{\frac{R+jwL}{G+jwC}} \tag{5.3}$$

For a lossless line, R = 0 and G =0 and so the characteristic impedance is real and equal to:

$$Z_o = \sqrt{\frac{jwL}{jwC}} = \sqrt{\frac{L}{C}} \qquad (5.4)$$

The characteristic impedance Z_o is independent of the transmission line length and the terminating impedance of the transmission line. It only depends on the geometry of the conductors and the dielectric properties of the substrate.

Propagation constant (Υ)

In transmission line theory, both the electric and magnetic fields vary in the z direction according to

$$exp\,(-\gamma z) \qquad (5.5)$$

where γ is a complex number called propagation constant which can be expressed as

$$\gamma = \alpha + \beta j \qquad (5.6)$$

where α is the attenuation per unit length of the transmission line and β is the phase constant per unit length.

The propagation constant can also be mathematically determined using the equivalent circuit model and is given by

$$\gamma = \sqrt{Y\,Z} = \sqrt{(R + j\omega L)(G + j\omega C)} = \sqrt{(RG - j\omega^2 LC) + j\,\omega(GL + RC)} \qquad (5.7)$$

where the Z and Y are determined from equations (5.1) and (5.2).

By using that $\frac{R}{\omega L} \ll 1$ and $\frac{G}{\omega C} \ll 1$, and applying binomial expansion the propagation constant can be shown to be equal to $\gamma = \alpha + \beta j$ where

$$\beta = jw\sqrt{LC} \tag{5.8}$$

$$\alpha = \frac{G}{2}\sqrt{\frac{L}{C}} + \frac{R}{2}\sqrt{\frac{C}{L}} \tag{5.9}$$

The dielectric loss tangent and dielectric constant of the thin film are mathematically determined from α and β of the coplanar waveguide as will be described in section 5.1.2 **[1, 5]**. The determination of the dielectric constant of the thin film is not straight forward. The dielectric constant of the thin film can not be directly obtained from the CPW phase constant (β) of the CPW. Instead, the phase constant is first converted into the effective dielectric constant (ε_{eff}) of the CPW. Then a conformal mapping technique is used to calculate the dielectric constant of the thin film from the effective dielectric constant (ε_{eff}). The following section provides the mathematical relationship between the effective dielectric constant (ε_{eff}) of the CPW and the thin film dielectric constant.

5.1.2 Determination of the dielectric properties of thin film by using conformal mapping technique

The CPW transmission line consist of a centre conductor strip with two ground planes located in parallel with the conductor. Figure 5.3 shows the cross section of a two-layer CPW **[6]**. In this study, the centre conductor width S = 2a = 40um and the gap width W = 20um. The metal thickness (t) of the conductor is 140nm. The substrate and thin film dielectric constant of the CPW are represented by $\varepsilon_{r\,Sub}$ and ε_{rTF}, respectively. Meanwhile, h_s(500um) and h_{TF}(180nm to 300nm) indicate the thickness of the thin film and substrate.

Coplanar waveguide (CPW)

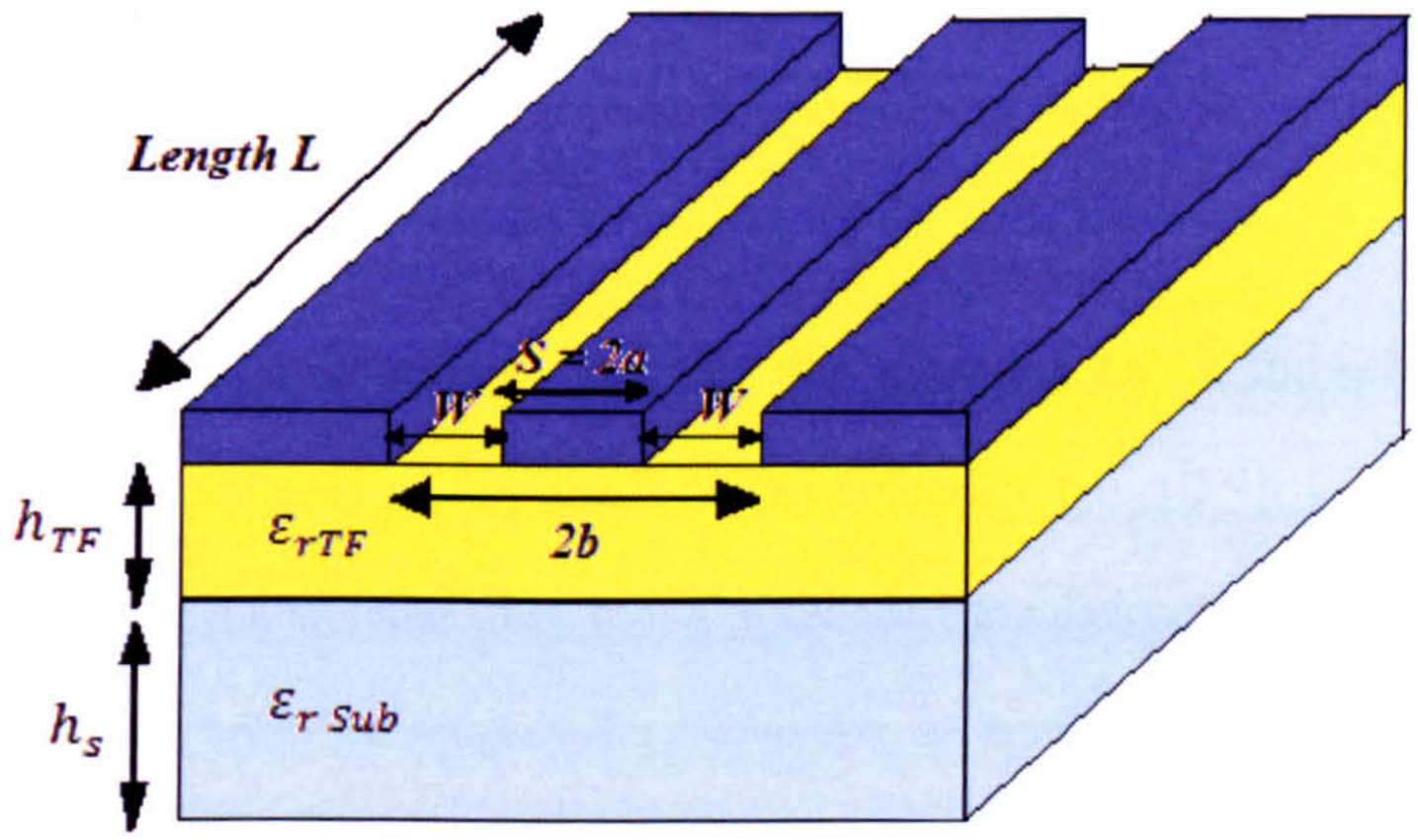

Figure 5.3 a schematic view of the two layers CPW with top and bottom metal separated.

The effective dielectric constant (ε_{eff}) of the CPW can be mathematically determined from the capacitance of each CPW section using "conformal mapping techniques". The mathematical relationship between the effective dielectric constant (ε_{eff}), dielectric constant of the thin film (ε_{r2}) and the substrate dielectric constant (ε_{r1}) can be expressed as: **[6, 7]**

$$\varepsilon_{eff} = 1 + q_1(\varepsilon_{r1} - 1) + q_2(\varepsilon_{r2} - \varepsilon_{r1}) \qquad (5.10)$$

The dielectric filling factors for the thin film (q_2) and substrate (q_1) are given by

$$q_1 = \frac{1}{2}\left(\frac{K(K_1)}{K(K_1')} + \frac{K(K_0)}{K(K_0')}\right) \quad , q_2 = \frac{1}{2}\left(\frac{K(K_2)}{K(K_2')} + \frac{K(K_0)}{K(K_0')}\right) \qquad (5.11)$$

where K is the complete elliptic integral of the first kind with

$$K_2 = \frac{\sinh(\pi S/2h_2)}{sinh\{[\pi(S+2W)]/2h_2\}} \qquad (5.12)$$

$$K_1 = \frac{\sinh(\pi S/2h_1)}{sinh\{[\pi(S+2W)]/2h_1\}} \tag{5.13}$$

$$K_0 = \frac{s}{s+2W} \tag{5.14}$$

$$k_i' = \sqrt{1-k_i'}(i = 1,2,3,4) \tag{5.15}$$

In this work, the ratio between the thin film thickness ($h_2 = 300nm$) and the substrate ($h_1 = 500um$) is very small (300nm/500um = 0.6×10^{-3}). Computational difficulties were encountered when trying to calculate the dielectric filling factor (q_2) for the thin film layer. To simplify the calculation, an empirical mathematical model was used to obtain the value of q_2 **[6, 7]**.

$$q_2 = \frac{\pi}{(\ln(16)+g\pi/h_2)} \frac{K(K_o')}{K(K_o)} \tag{5.16}$$

Determination of the dielectric constant of thin film from phase constant

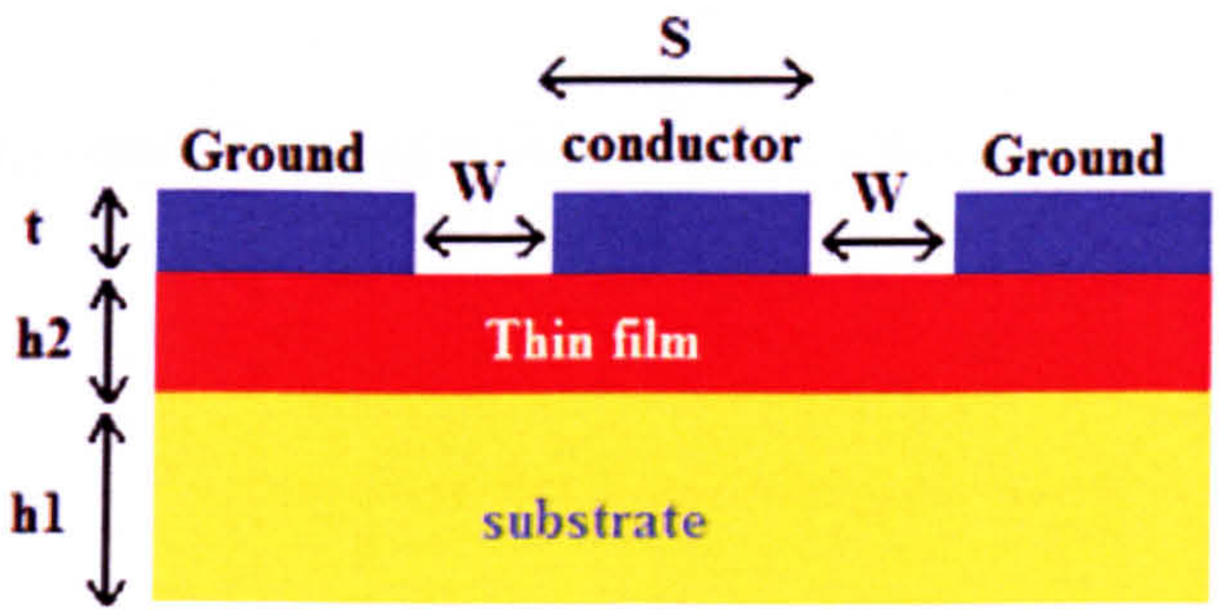

Figure 5.4 cross section view of the CPW used to characterize the thin film's dielectric properties.

In practice, it is not possible to obtain (ε_{eff}) from equation 5.10, since the dielectric constant of the thin film is unknown. As discussed earlier, the CPW effective

dielectric constant (ε_{eff}) is actually obtained from the measured phase constant (β) of CPW. The phase constant (β) which is the imaginary part of the propagation constant ($\gamma = \alpha + \beta j$) is mathematically related to the effective wavelength (λ) of CPW by

$$\beta = \frac{2\pi}{\lambda} \tag{5.17}$$

where λ is related to the free space wavelength (λ_o) via the effective dielectric constant (ε_{eff}) of CPW and is given by

$$\lambda = \lambda_o \frac{1}{\sqrt{\varepsilon_{eff}}} = \frac{C_o}{freq \cdot \sqrt{\varepsilon_{eff}}} \tag{5.18}$$

where C_o is the velocity of light in vacuum.

By substituting equation 5.18 in to equation 5.17, an expression relating the effective dielectric constant (ε_{eff}) to the propagation constant can be found:

$$\beta = \frac{2\pi f\sqrt{\varepsilon_{eff}}}{C_o} \tag{5.19}$$

By rearranging equation 5.19, an expression for the effective dielectric constant can be obtained.

$$\sqrt{\varepsilon_{eff}} = \frac{\beta C_o}{2\pi f} \tag{5.20a}$$

$$\text{or} \quad \varepsilon_{eff} = \left(\frac{\beta C_o}{2\pi f}\right)^2 \tag{5.21b}$$

Once the effective dielectric constant (ε_{eff}) of the CPW is obtained from equation 5.21b, ε_{eff} and ε_{r1}(substrate dielectric constant) can be substituted into equation

5.10 and the dielectric constant of the thin film (ε_{r2}) is determined from the following equation.

$$\varepsilon_{r2} = ((\varepsilon_{eff} - 1) - q_1(\varepsilon_{r1} - 1))/q_2 + 1 \qquad (5.22)$$

q_1, q_2 = filling factors of the substrate and thin film of the CPW

ε_{r1}= dielectric constant of the substrate

ε_{r2} = dielectric constant of the thin film

ε_{eff}= CPW effective dielectric constant

According to ref [8], the relative error for ε_{eff} calculated from the conformal mapping technique is below 5% between 10GHz and 15GHz.

Determination of the dielectric loss tangent of the thin film from CPW attenuation loss

The dielectric loss tangent ($tan\delta_2$) of the thin film can be deduced from the measured attenuation loss (α_{cpw}) of CPW which is the real part of propagation constant ($\gamma = \alpha + \beta j$). The CPW attenuation consists of the conductor attenuation (α_c), effective dielectric attenuation (α_d) and substrate leakage current loss (α_{leak}).

$$\alpha_{cpw} = \alpha_c + \alpha_d + \alpha_{leak} \qquad (5.23)$$

To minimize the attenuation due to substrate leakage current, the BZN thin films are usually deposited on the highly insulated materials such as: sapphire, quartz, LAO and MgO with resistivity larger than 10,000Ohm/cm. In this case, the leakage current loss (α_{leak}) of the substrate can be neglected and so equation 5.23 can be simplified to

$$\alpha_{cpw} = \alpha_c + \alpha_d \tag{5.24}$$

In equation (5.24), the conductor attenuation (α_c) is mathematically determined from the following equation **[7, 9]**.

$$\alpha_c = \frac{8.68R_S}{16Z_o K^2(k)(b^2-a^2)}\left[\frac{1}{a} ln\left(\frac{2a}{\Delta}\frac{b-a}{b+a}\right) + \frac{1}{b}\left(\frac{2b}{\Delta}\frac{b-a}{b+a}\right)\right] \tag{5.25}$$

where $a = S/2$, $b = (S + 2W)/2$ and $\Delta = \frac{t}{4\pi e^{\pi}}$.

The (R_s) is the surface resistance of the metal conductor caused by skin effect and is given by $R_s = \sqrt{\mu_o \pi . f . \rho}$ **[10]** where ρ is the resistivity of aluminium ($\rho = 2.82 \times 10^{-8}$ Ω·m). The calculated surface resistance (in Ω/m) against the frequency (in GHz) is shown in figure 5.5.

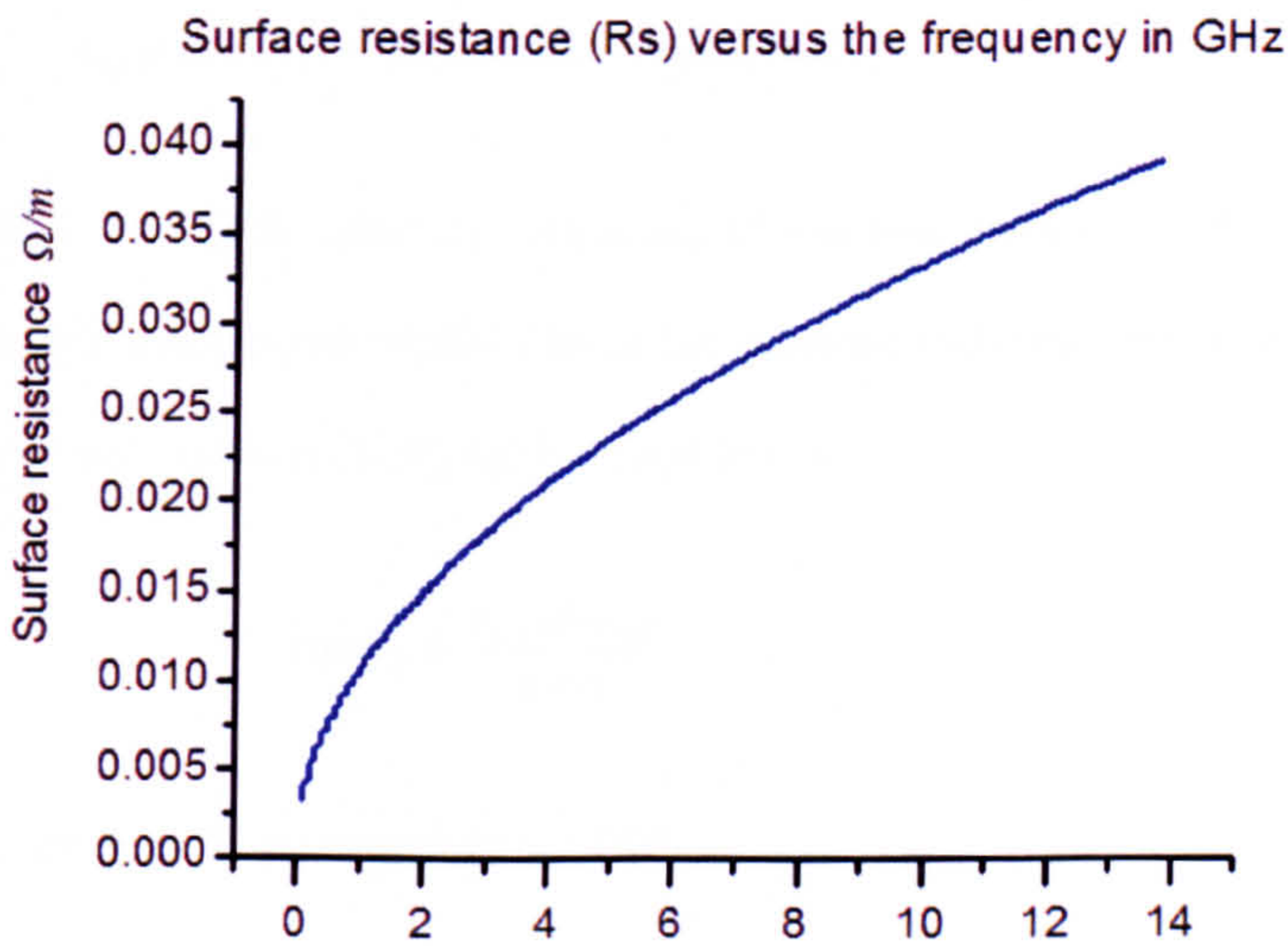

Figure 5.5 Surface resistance (R_s) as a function of frequency from 0GHzto 14GHz

By substituting the surface resistanceR_s, a, b, Δ and characteristic impedance Z_o into equation (5.25), the conductor attenuation α_c (dB/m) will be determined. Therefore, the effective dielectric attenuation (α_d) can be obtained from

$$\alpha_d = \alpha_{cpw} - \alpha_c \tag{5.26}$$

The effective dielectric attenuation (α_d) is mathematically related to the effective dielectric loss tangent as **[1]**

$$\tan(\delta_{eff}) = \frac{\alpha_d C_o}{1.89\, L\, \pi f \sqrt{\varepsilon_{eff}}} \tag{5.27}$$

where the effective dielectric loss tangent is $\tan(\delta_{eff})$, CPW length is L ,effective permittivity of the CPW = ε_{eff} and effective dielectric attenuation = α_d(dB/m).

For a two-layer CPW, the effective dielectric loss $\tan(\delta_{eff})$ consists of the substrate dielectric loss ($tan\delta_1$) and thin film dielectric loss ($tan\delta_2$). By using the conformal mapping technique, the thin film dielectric loss can be obtained from equation **[7, 10]**.

$$\varepsilon_{eff} tan\delta_{eff} = q_1 \varepsilon_{r1} tan\delta_1 + q_2 \varepsilon_{r2} tan\delta_2 \tag{5.28}$$

As we know, the CPW substrates are made of low loss materials such as sapphire with dielectric loss tangent <0.001. Hence the substrate dielectric loss tangent ($tan\delta_1$) is neglected and equation (5.28) can be simplified to

$$tan\delta_2 = \frac{\varepsilon_{eff} tan\delta_{eff}}{q_2 \varepsilon_{r2}} \tag{5.29}$$

q_1 and q_2 are the filling factors of the CPW .

$\varepsilon_{r2}$is the dielectric constant of the thin film determined from equation (5.22) .

ε_{eff} is the effective dielectric constant of CPW.

$tan\delta_{eff}$ is the effective dielectric loss tangent.

5.1.3 Microwave network analysis using network theory

The phase constant (β) and attenuation (α_{cpw}) are obtained from the scattering parameters of the CPW. The measurement of scattering parameters is based on network theory. The details of this theory are discussed in the following sections. A microwave device with a given number of output/input terminals can be analyzed using network theories. The responses between each of the points or "ports" are described using an impedance or admittance matrix.

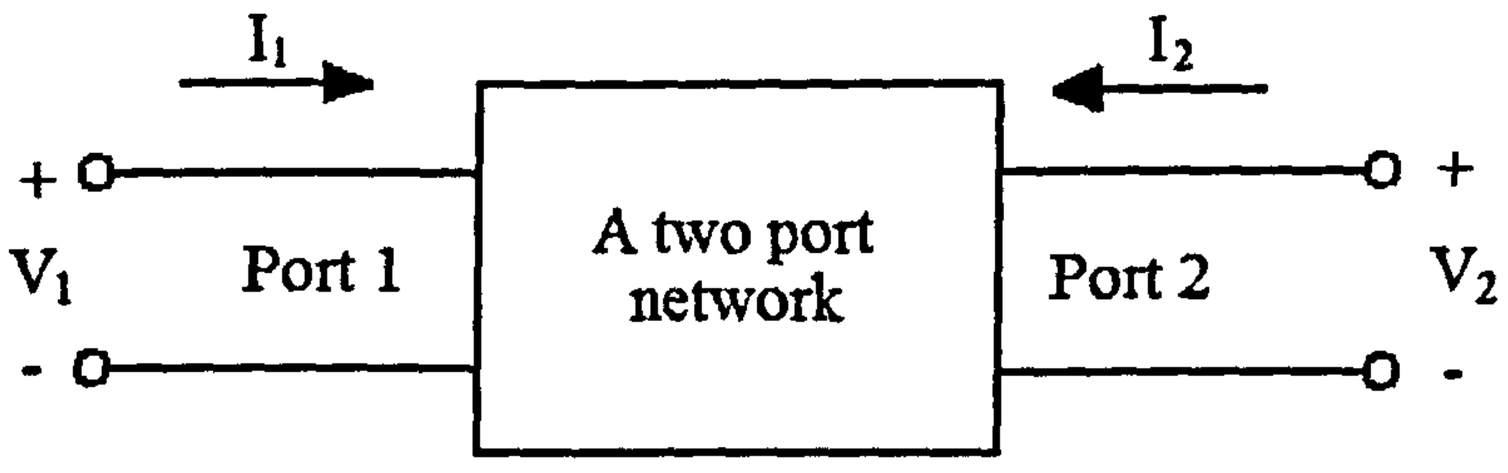

Figure 5.6: an arbitrary 2-port network

Figure 5.6 is a 2-port network representing the terminals of a circuit. This graph can be expanded to an n-port network. The general solutions for the impedance matrices [Z] of the 2-port network are: **[1]**

$$\begin{bmatrix} V_1 \\ V_2 \end{bmatrix} = \begin{bmatrix} Z_{11} & Z_{12} \\ Z_{21} & Z_{22} \end{bmatrix} \begin{bmatrix} I_1 \\ I_2 \end{bmatrix}$$

$$\text{where } Z_{11} = \left[\frac{V_1}{I_1}\right]_{i_2=0} Z_{12} = \left[\frac{V_1}{I_2}\right]_{i_1=0} Z_{21} = \left[\frac{V_2}{I_1}\right]_{i_2=0} Z_{22} = \left[\frac{V_2}{I_2}\right]_{i_1=0} \qquad (5.30)$$

The admittance matrix [Y] is expressed in another way **[1]**:

$$\begin{bmatrix} I_1 \\ I_2 \end{bmatrix} = \begin{bmatrix} Y_{11} & Y_{12} \\ Y_{21} & Y_{22} \end{bmatrix} \begin{bmatrix} V_1 \\ V_2 \end{bmatrix} \tag{5.31}$$

The relationship between [Z] and [Y] is [Z] [Y] = 1.

5.1.4 Scattering parameters

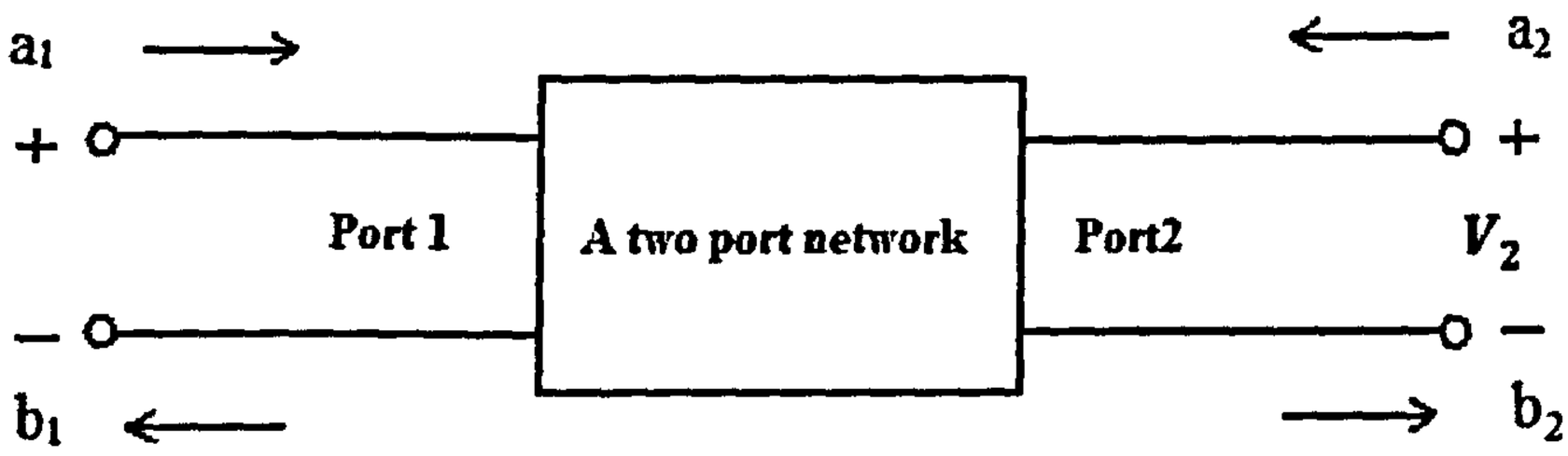

Figure 5.7 a diagram of two port network

In section 5.1.3, we have discussed the basic concept of analyzing transmission lines using impedance/admittance networks. In practice, the response of a network to another network is usually described by the input/output waves rather than the actual incident voltages or current. Figure 5.7 shows a two port transmission line with input waves a_1 and a_2 and output wave b_1 and b_2. These parameters can be considered as voltages or current. The reflected and incident waves of a_n and b_n are defined as:

$$a_n = \frac{V_n^+}{\sqrt{Z_o}} \; ; \; b_n = \frac{V_n^-}{\sqrt{Z_o}} \tag{5.32}$$

The S-parameters of the two-port network can be defined as **[1]**:

$$S_{11} = \frac{b_1}{a_1}\Big|_{a_2=0}, \; S_{12} = \frac{b_1}{a_2}\Big|_{a_1=0}, \; S_{21} = \frac{b_2}{a_1}\Big|_{a_2=0}, \; S_{22} = \frac{b_2}{a_2}\Big|_{a_1=0} \tag{5.33}$$

The expression of an S-parameters matrix for a two-port network is defined as:

$$\begin{bmatrix} b_1 \\ b_2 \end{bmatrix} = \begin{bmatrix} S_{11} & S_{12} \\ S_{21} & S_{22} \end{bmatrix} \begin{bmatrix} a_1 \\ a_2 \end{bmatrix} \tag{5.34}$$

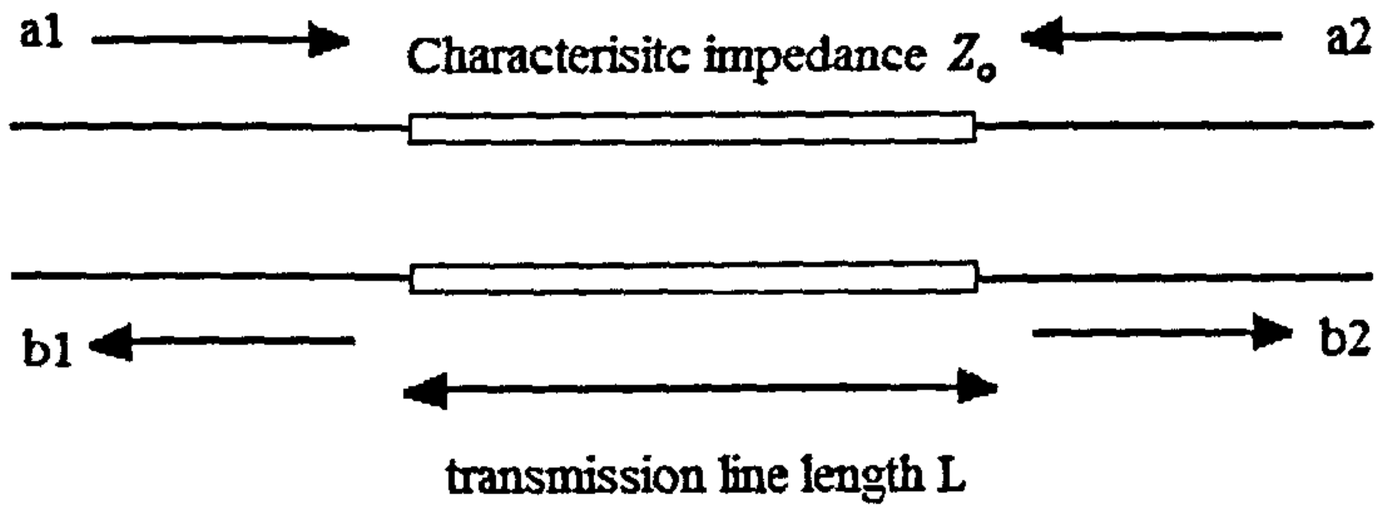

Figure 5.8 a two port transmission line with length L and uniform properties

For a two port lossless transmission line (assuming the attenuation (α) is zero) with length L and uniform dielectric properties (figure 5.8), the expression of its S-parameter matrix is given by

$$\begin{bmatrix} S11 & S12 \\ S21 & S22 \end{bmatrix} = \begin{bmatrix} 0 & exp^{-\gamma l} \\ exp^{\gamma l} & 0 \end{bmatrix} \tag{5.35}$$

5.1.5 The transmission line (ABCD) matrix

The impedance (Z), admittance (Y) and S-parameters matrix of network theories described in sections 5.1.3 and 5.1.4 can be used to characterize a microwave network with a given number of ports. However, most microwave circuits are made of a cascade of 2-port network systems.

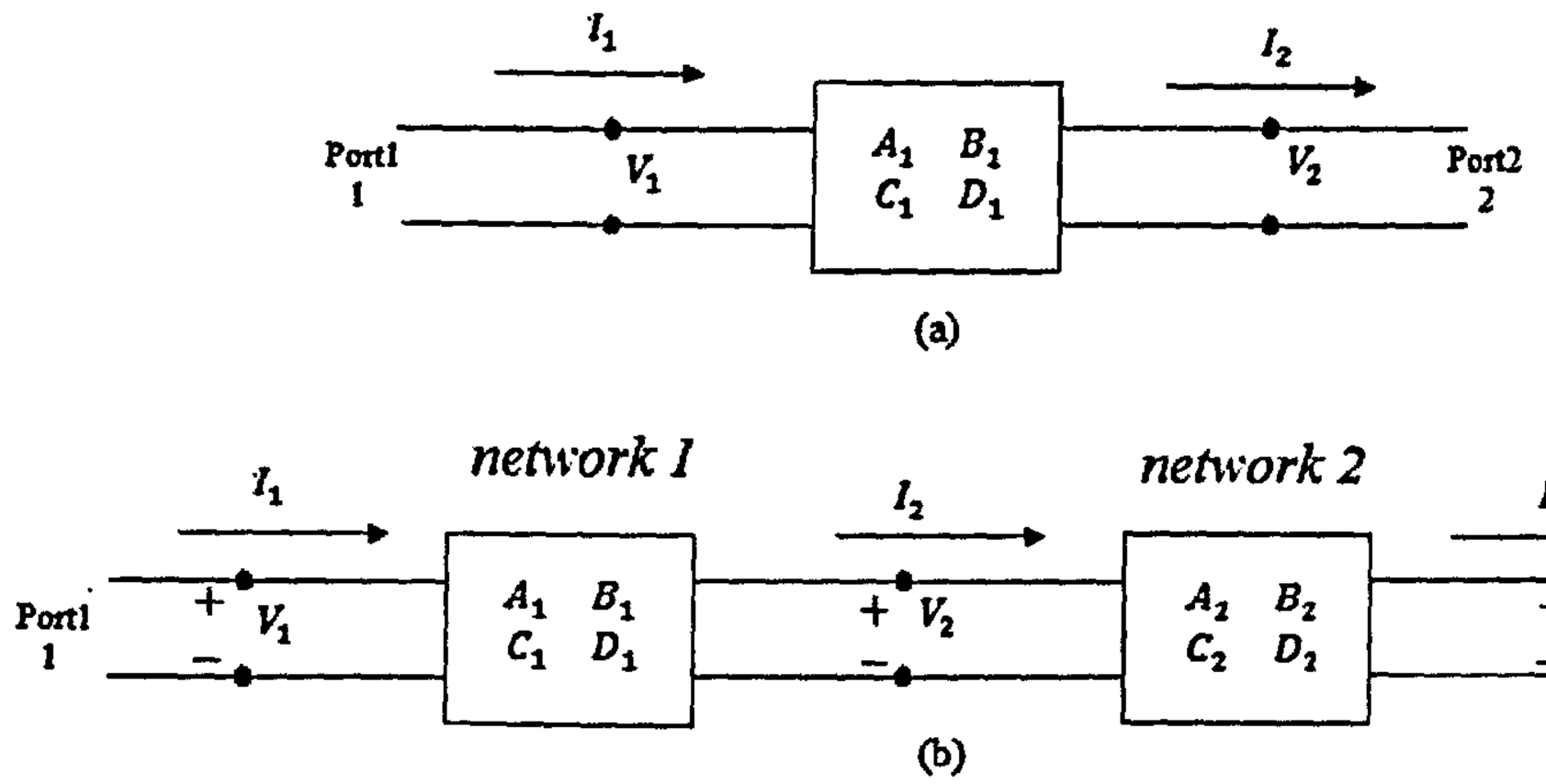

Figure 5.9 (a) two port ABCD network, (b) a cascade of such two port networks **[11].**

For a cascaded microwave networks (figure 5.9(b)), it is easier to use a 2×2 ABCD matrix transmission for each two port network. The advantages of using an ABCD network is that a cascade of simple two port ABCD matrices can be used to build up and form a complicated microwave network. The overall ABCD matrix of a network can be easily obtained by multiplying two ABCD matrices of the individual two-ports.

For a 2-port network, the ABCD matrix is defined as: **[11]**

$$\begin{bmatrix} V_1 \\ I_1 \end{bmatrix} = \begin{bmatrix} A & B \\ C & D \end{bmatrix} \begin{bmatrix} V_2 \\ I_2 \end{bmatrix}$$

where $A = \left.\frac{V_1}{V_2}\right|_{I_2=0}$, $B = \left.\frac{V_1}{I_2}\right|_{V_1=0}$, $C = \left.\frac{I_1}{V_2}\right|_{I_2=0}$, $A = \left.\frac{I_1}{I_2}\right|_{V_2=0}$ (5.36)

In ABCD matrix form, the networks shown in figure 5.9(a) can be written as: **[11]**

$$\begin{bmatrix} V_1 \\ I_1 \end{bmatrix} = \begin{bmatrix} A_1 & B_1 \\ C_1 & D_1 \end{bmatrix} \begin{bmatrix} V_2 \\ I_2 \end{bmatrix} \qquad (5.37)$$

According to figure 5.9 (b) (a cascade connection of two-port networks), I_2 is the output current from network 1 and it is identical to the input current of network 2. Therefore, the ABCD matrices of the cascaded network (figure 5.9(b)) can be expressed as: **[11]**

$$\begin{bmatrix} V_1 \\ I_1 \end{bmatrix} = \begin{bmatrix} A_1 & B_1 \\ C_1 & D_1 \end{bmatrix} \begin{bmatrix} A_2 & B_2 \\ C_2 & D_2 \end{bmatrix} = \begin{bmatrix} V_3 \\ I_3 \end{bmatrix} \qquad (5.38)$$

where the ABCD matrices of the two networks on each side of figure 5.9(b) are identical with each other. The obtained ABCD matrix can also be related to the impedance matrix and scattering matrix **[1, 11]**

$$\begin{bmatrix} A & B \\ C & D \end{bmatrix} = \begin{bmatrix} \frac{Z_{11}}{Z_{21}} & \frac{Z_{11}Z_{22}-Z_{12}Z_{21}}{Z_{21}} \\ \frac{1}{Z_{21}} & \frac{Z_{22}}{Z_{21}} \end{bmatrix}$$

$$\begin{bmatrix} A & B \\ C & D \end{bmatrix} = \begin{bmatrix} \frac{(1+S_{11})(1-S_{22})+S_{12}S_{21}}{2S_{21}} & Z_o\frac{(1+S_{11})(1+S_{22})-S_{12}S_{21}}{2S_{21}} \\ \frac{1}{Z_o}\frac{(1-S_{11})(1-S_{22})-S_{12}S_{21}}{2S_{21}} & \frac{(1-S_{11})(1+S_{22})+S_{12}S_{21}}{2S_{21}} \end{bmatrix} \qquad (5.39)$$

5.1.6 Vector Network Analyzer (VNA) and calibration

A network vector analyzer (VNA) is an important tool in the characterization of analogue microwave circuits. The equipment allows the measurement of the amplitude and phase of the reflected and transmitted signals with respect to the input signals allowing the four S-parameters of an analogue circuit (S_{11}, S_{22} S_{12} S_{21}) to be measured.

Measurement Equipment set up

In this study, an "Antritsu ME7808B" lightning network analyzer has been used to measure the S-parameters of the CPW and MIM capacitor with different applied DC voltages. The device under test (DUT) is connected with the VNA by a pair of RF cables and Ground Signal Ground (GSG) probes. The tuning DC voltages are applied to the device though the VNA's internal DC block. A schematic view of the test bench is shown in figure 5.10.

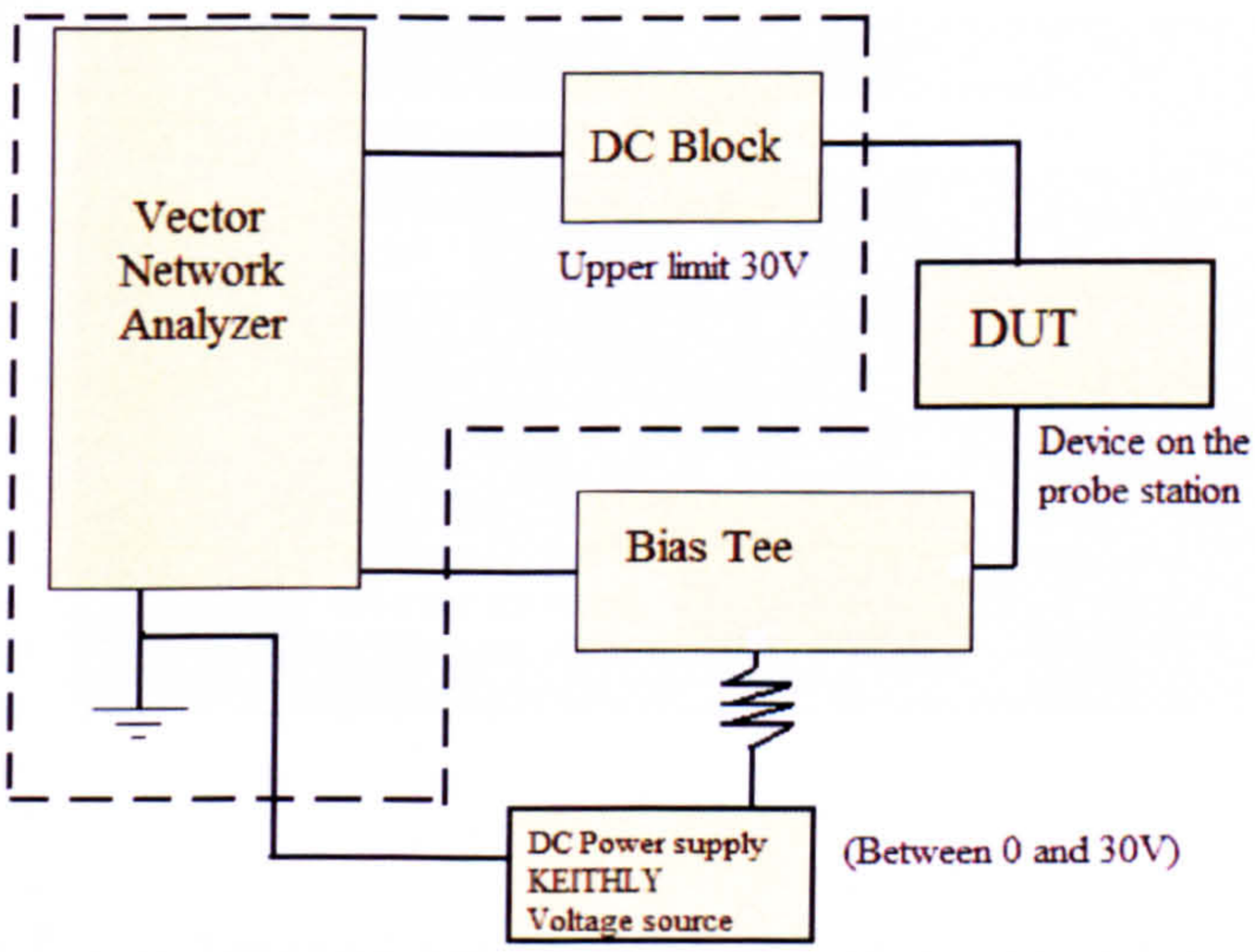

Figure 5.10 Schematic of the measurement set up

A photograph of the experimental system is shown in figure 5.11(a) and includes a Network analyzer, the RF cable, RF probes and the optical microscopes (Olympus).

(a)

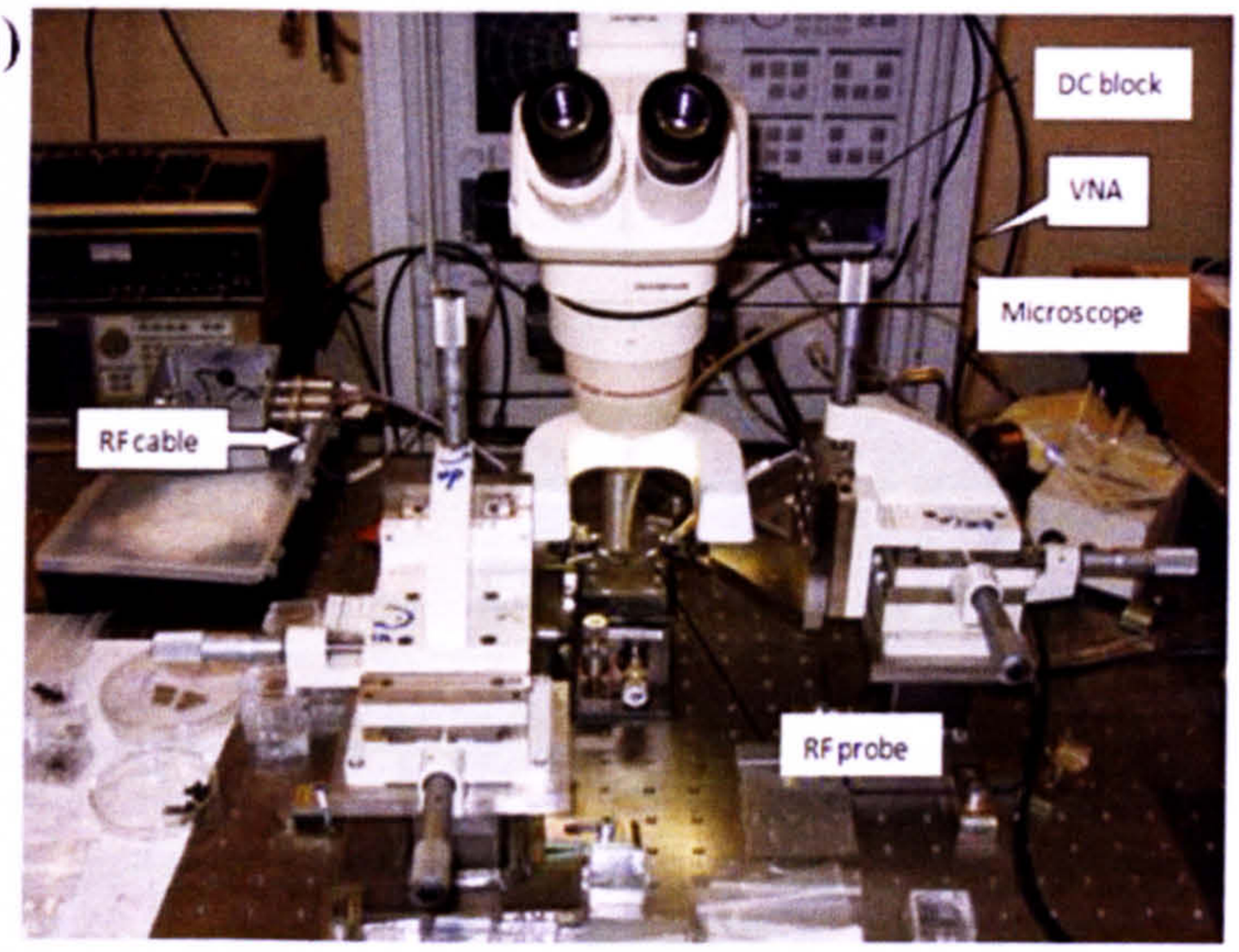

(b)

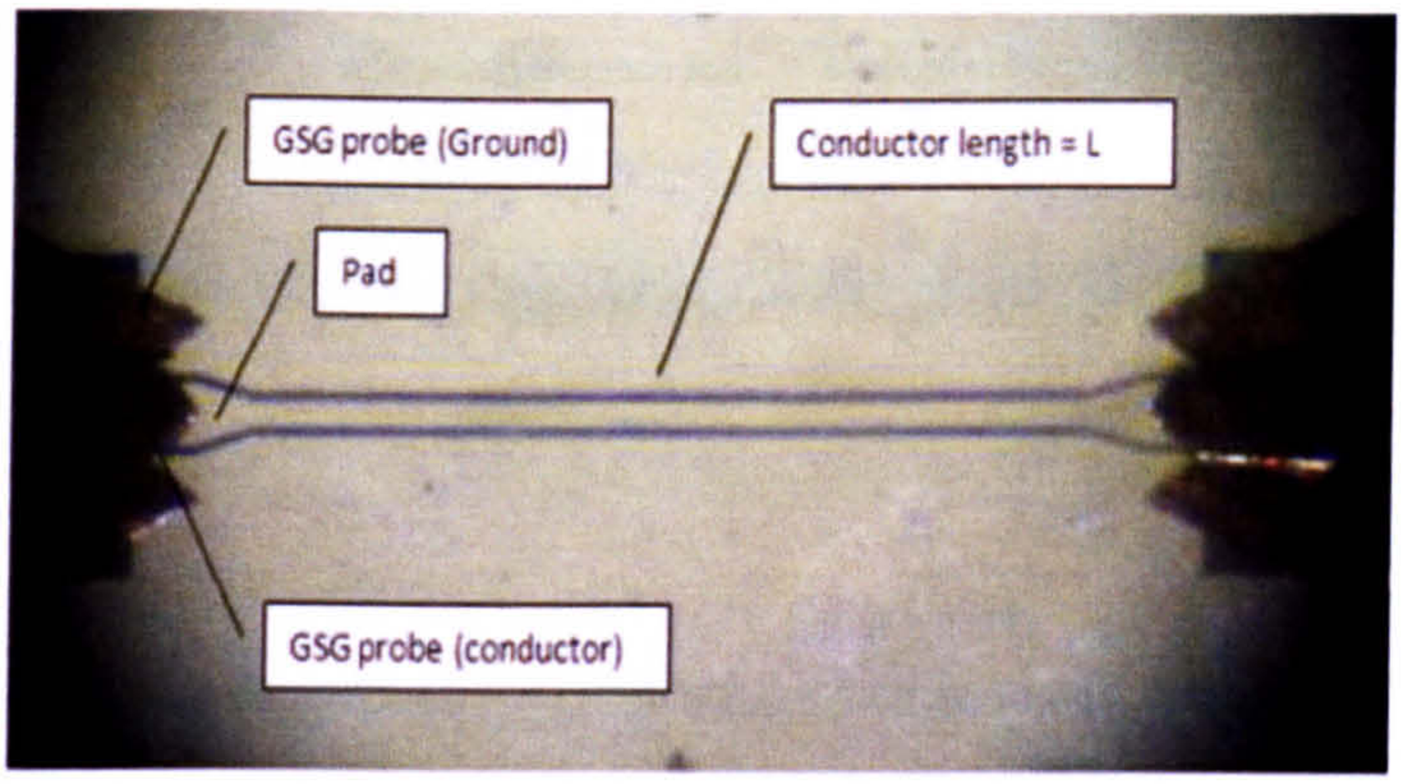

Figure 5.11 (a) Test bench and equipment set up (b) a close look of the CPW under measurement

A photograph (taken through the optical microscope) of a CPW under measurement is shown in figure 5.11(b). As it can be seen, the Ground Signal Ground (GSG) RF probe consists of a central conductor tip and two ground tips are in the contact with the ground metal and conductor pad of the CPW.

Measurement reference plane and Calibration

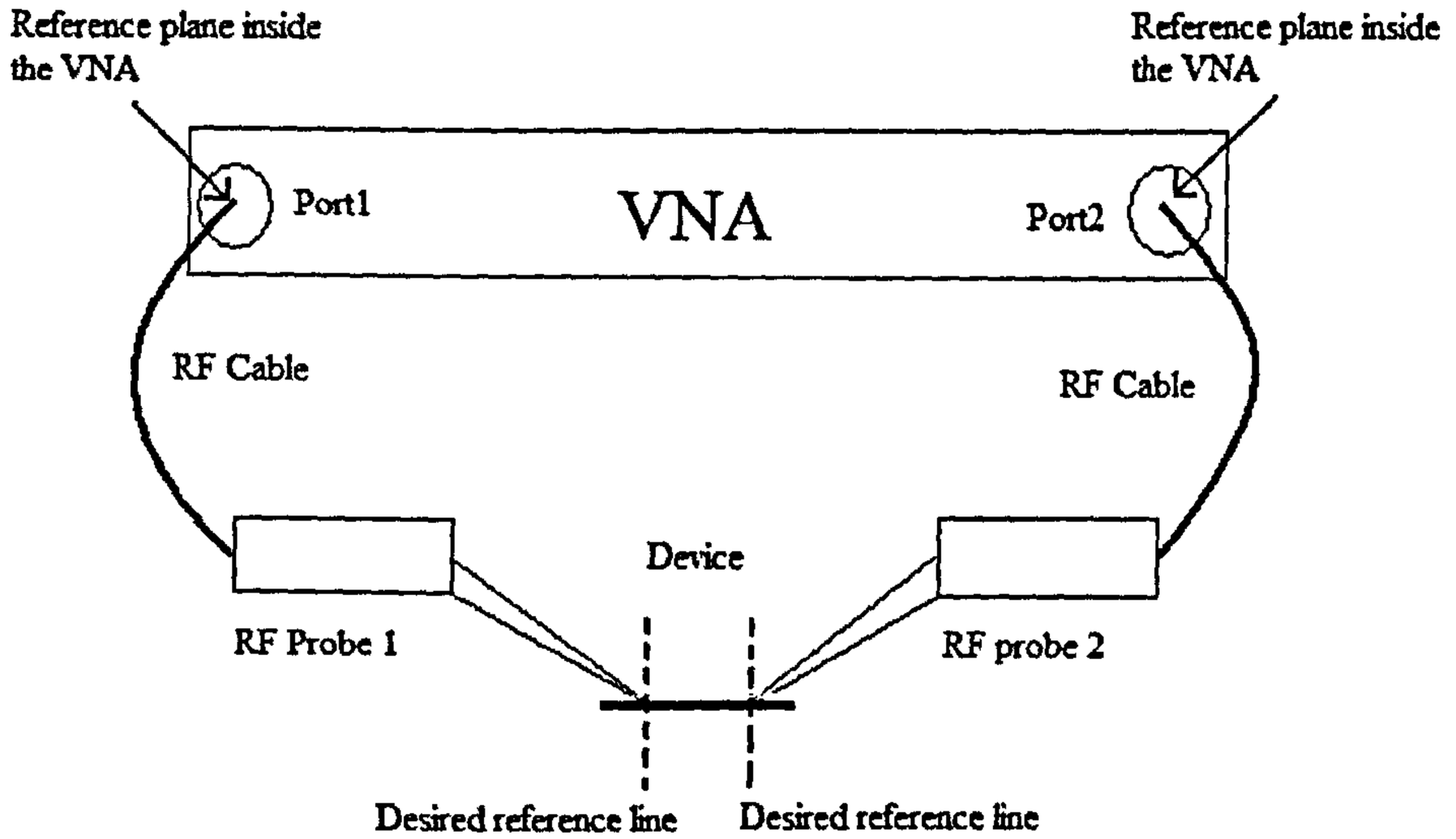

Figure 5.12 a schematic view of the probing station.

The vector network analyzer (VNA) collects the data (S-parameters) at the reference planes. Hence the exact position of the reference plane needs to be known. As it shown in figure 5.12, the measurement reference plane is inside the VNA. This plane is not appropriate because the measured S-parameters are also affected by the RF probes, cables and pads (figure 5.13). In this work, we are only interested in the propagation constant (γ) of the CPW's transmission line with length *L*. According to figure 5.13, the most appropriate reference plane is at the edge of each probe pad (desired reference plane).

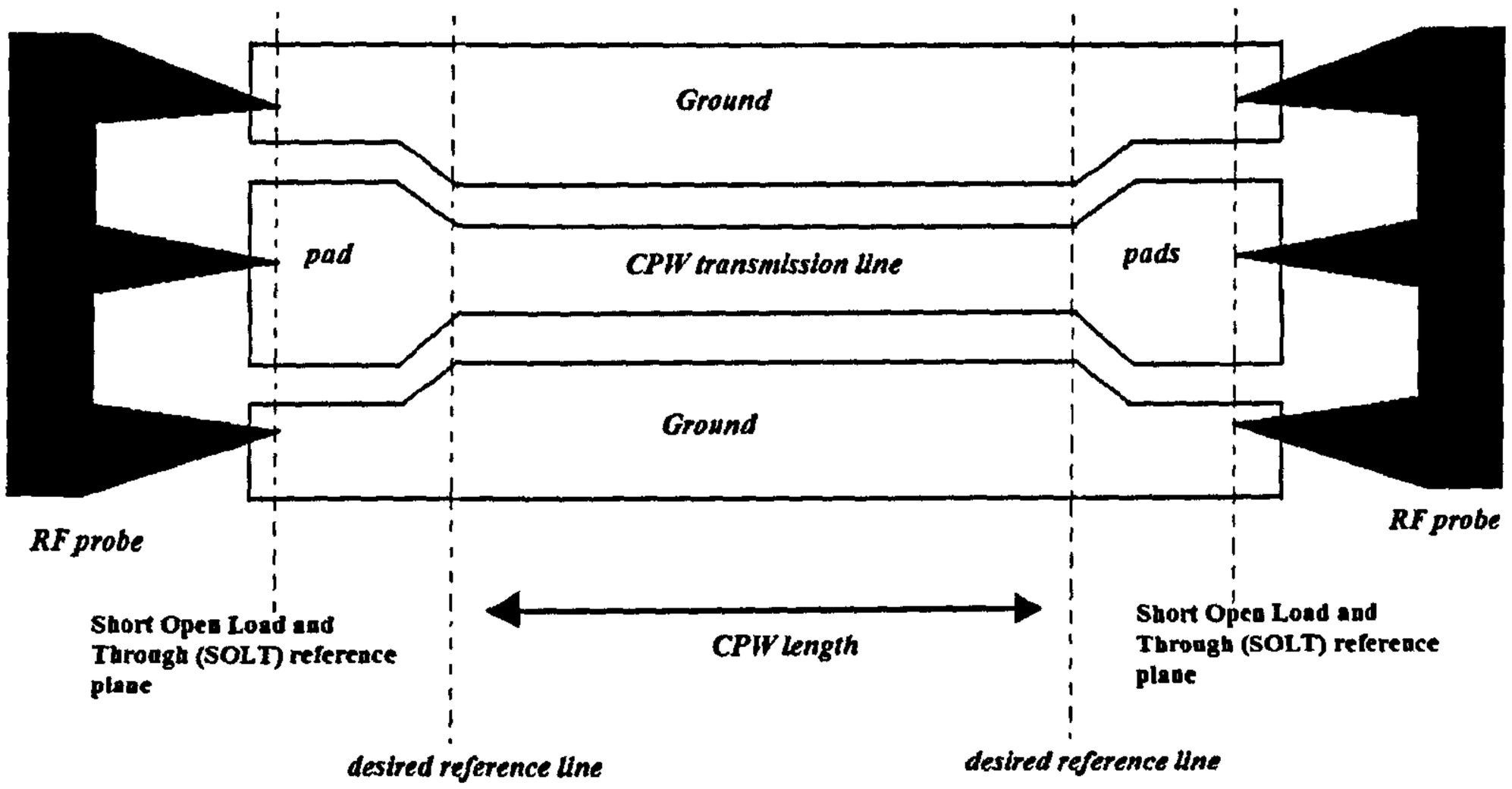

Figure 5.13 a close look of the measured CPW by a pair of RF probes

To move the reference planes to the desired position requires calibration. Ideally, this can be achieved by a simple on wafer TRL (*Thru, Reflect* and *Line*) calibration process. However, in the present work, the TRL calibration process is not embedded into the VNA. A computer program based on "Matlab" software was used to perform the calibration. Unfortunately, this program has a "phase ambiguous" problem [1] due to VNA's data recording method. The problem is illustrated in figure 5.14. As it shown, the measured phase shifts θ (between VNA's internal reference plane and RF probe tip) varies between $+\pi$ ($+180^o$) and $-\pi$ (-180^o). However, the actual phase shift is equal to $2n\pi + \theta$. This is called the "phase-wrapping" effect. The "Matlab" program is unable to solve this problem. As a result, TRL calibration cannot be directly applied to calibration of CPW lines.

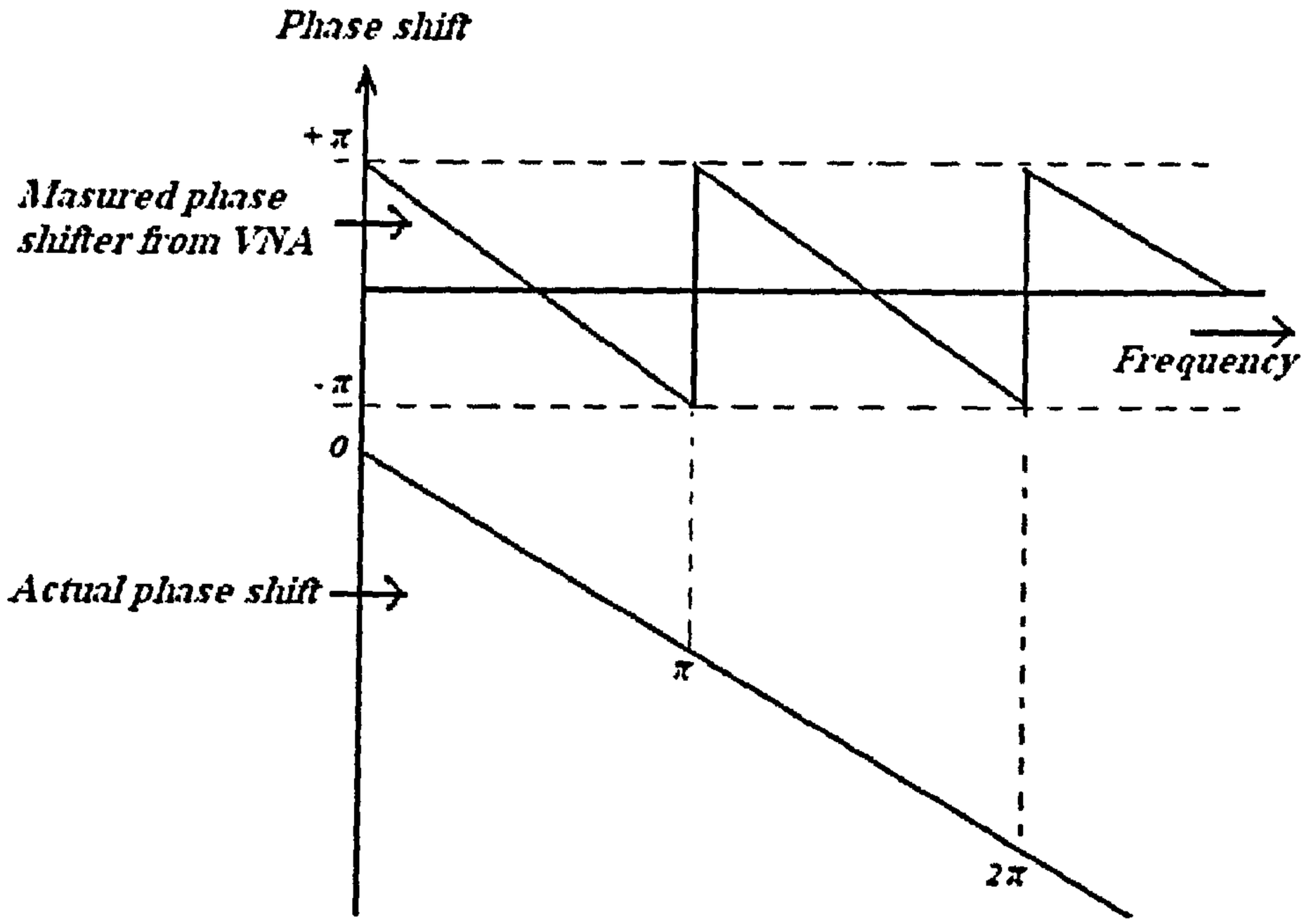

Figure 5.14 a comparison of measured and actual phase shift between the VNA and RF probe (reproduced from **[1]**).

Instead, a two step calibration process involving SOLT and TRL calibration has been used. First, a SOLT (*Short, Open, Line* and *Thru)* calibration process was used to move the reference plane from VNA's internal detector to the tip of RF probe (*SOLT reference plane*). Since the calibration program has been embedded into the VNA, this process was performed by the VNA itself, and is capable of resolving "phase-wrapping" effect. Because the distance between *SOLT references plane*s at port1 and port2 is very short (<3000μm), the measured phase shift (θ) after SOLT calibration is relatively small (between 0° and $-\pi$ (180°)) and so there is no problem of phase ambiguity caused by "phase-wrapping" effect. However, the measured results after SOLT calibrated are still corrupted due to the parasitic capacitance and impedances of the pads at port 1 and 2. A second "TRL" (*Thru, reflect* and *Line*) calibration process has been used to remove the errors caused by the probing pads. After the TRL calibration, the reference plane is moved from *SOLT reference planes* to the

*desired reference plan*e. The working principle of the SOLT calibration is discussed in the following section.

Basics of SOLT calibration

The directly measured S-parameters are influenced by the effects of the RF cables and the RF pads, these can be modelled using a simple 2 port terminal (figure 5.15). In figure 5.15, [2] these effects are shown as a12-term error model and a 2-port DUT (Device under test) is between the two desired reference lines.

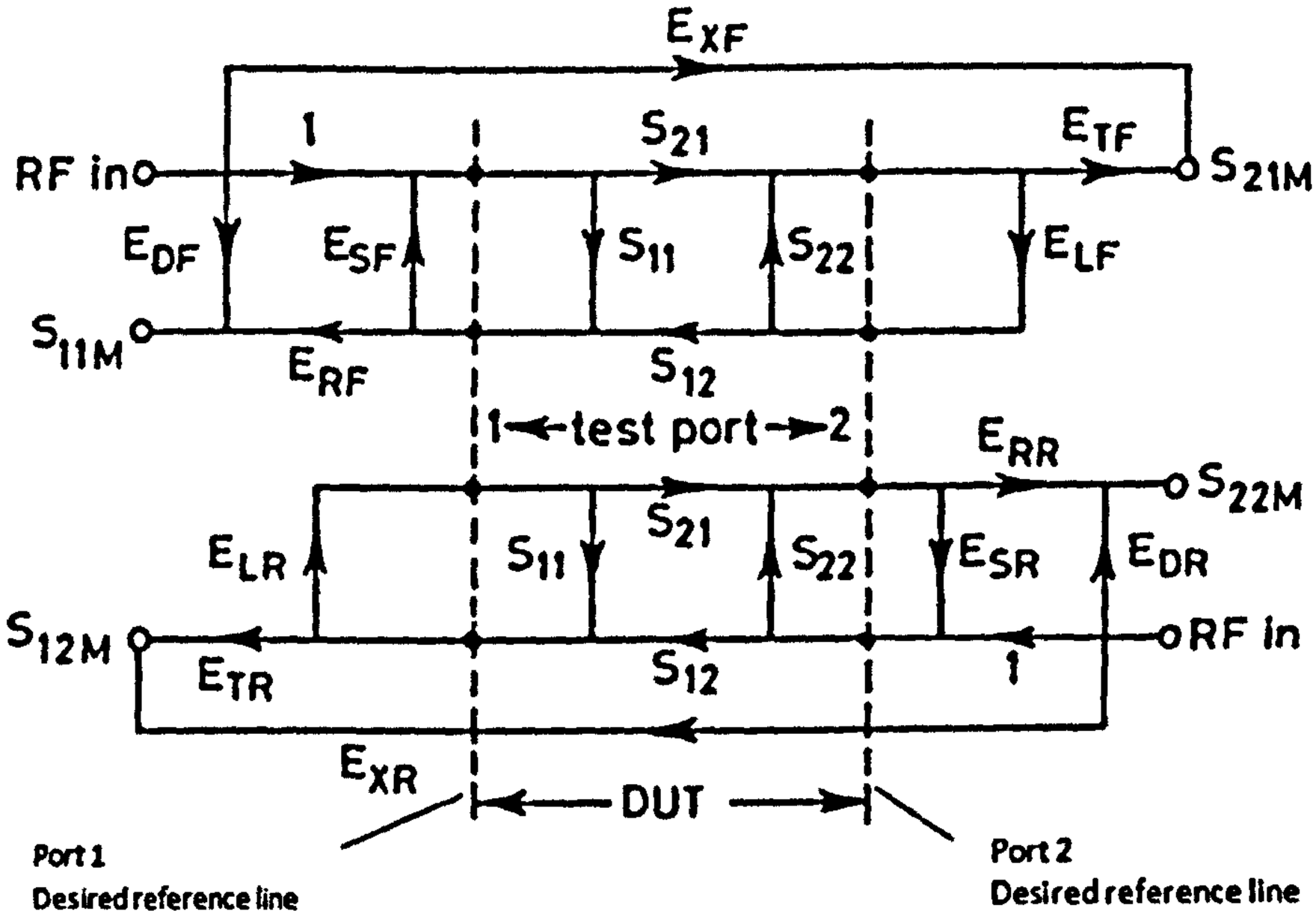

Figure 5.15 a 12-term error model used to perform the SOLT calibration (reproduced from [2])

To obtain the actual S-parameters of the DUT (device under test) the 12 different errors have to be measured by a self calibration process. These errors can be removed by substituting the DUT (device under test) with known standards (reflection and transmission). Their equivalent flow graphics are shown in figure 5.16(a) and 5.16(b) [2]. For the reflection calibration, the standards are implemented by a perfectly

matched 50Ω load, a short or an open connection. For transmission calibration, the standard is implemented by a "through" connection and an isolation measurement with no connections to either port. In this work, the standard calibration circuits (CS-5 calibration kit) were used. They are fabricated on an alumina wafer with gold electrode.

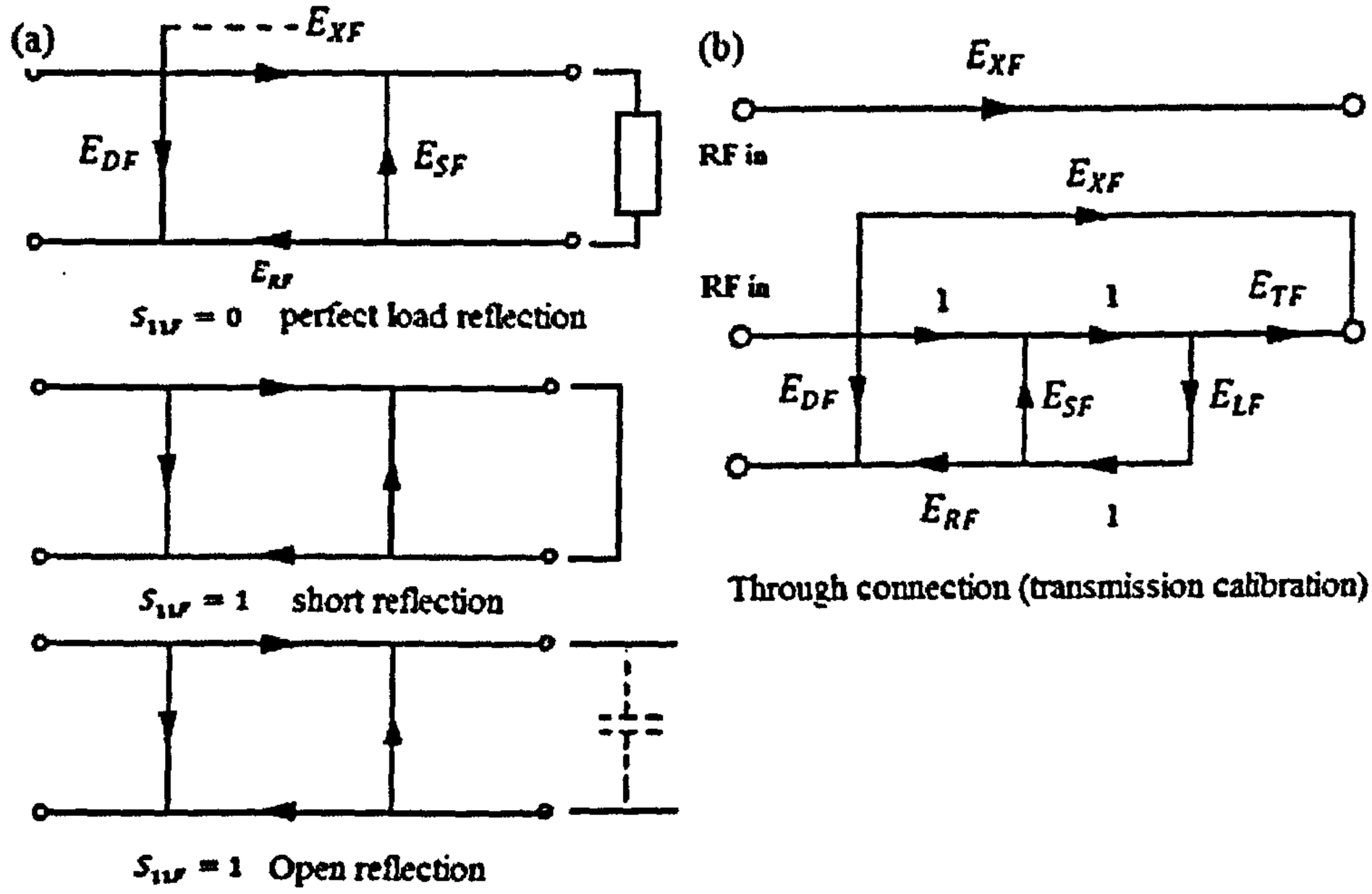

Figure 5.16 (a) perfect load reflection, short reflection, Open reflection connections (isolation) and (b) transmission connection (through) (reproduced from [2])

According to figure 5.16(a), the errors includingE_{DF}, E_{RF} and E_{SF} are obtained from the three measured reflection coefficients ($S_{11\,load}$ $S_{11\,short}$ $S_{11\,Open}$). The crosstalk E_{XF} error is obtained from an "isolation" measurement with no connection to either port. Meanwhile, the load match error $E_{LF}$and reflection error E_{TF} can be solved from the obtained reflection and transmission errors (E_{DF}, E_{RF}, E_{SF} and E_{XF}). Since the calibration procedure (SOLT) will be automatically performed, the mathematical process used in the calibration is not presented in this work.

5.1.7 On wafer TRL error calibration

As mentioned in previous sections (5.1.5 and 5.1.6), the SOLT calibration only moves the reference plane to the tips of RF probes (SOLT reference plane). A second calibration process (TRL) has to be used to move the reference plane to the desired position. This problem is further illustrated in figure 5.17 **[11]** by using the notation of ABCD block where it is intended to measure the "*actual*" propagation constant ($\gamma = \alpha + \beta$) of the CPW line between the desired reference planes.

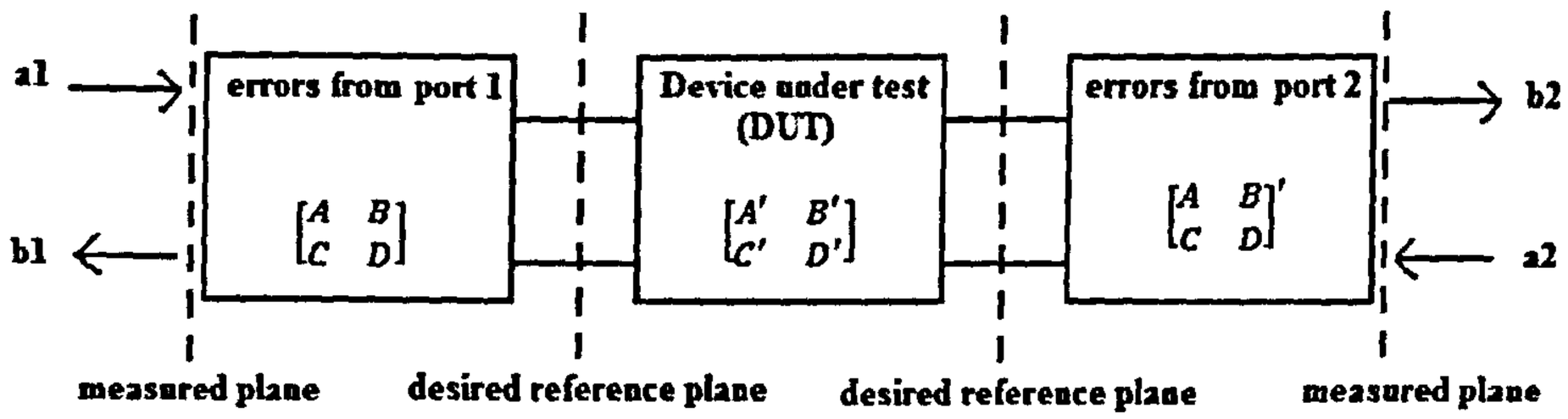

Figure 5.17 a block diagram of a network analyzer measurement (reproduced from **[11]**)

TRL calibration requires the measurement of three different circuits including a *line, a through* and a pair of *open reflection* pads. These calibration devices are shown in figure 5.18 (a), (b) and (c). The "*through*" is made of a made of a direct connection between the two ports. The line is made of a 1500um CPW line connecting ports1 and 2. For the reflection measurement, the probing pads are connected with a discontinuity in the CPW, which in this work is the reflection from an open circuit (figure 5.18(c)).

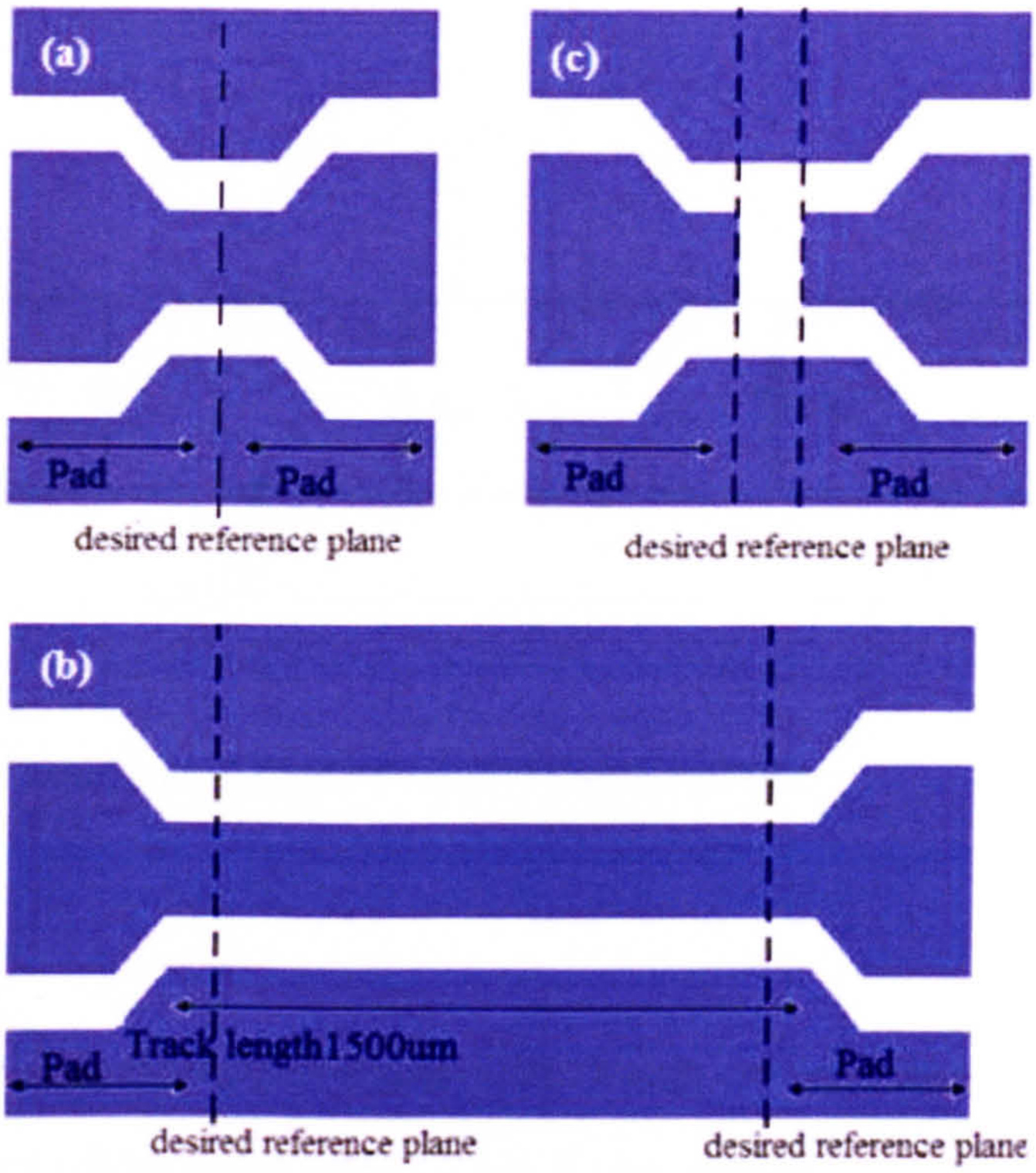

Figure 5.18 Configuration of the TRL calibration lines (a) through line (b) 1500 um line and (c) Open reflection pad

From figure 5.18, the probing pads at port 1 and 2 are designed to have gradual transition lines to smooth the transition between the probing pads and conductor track. The width and gaps of the CPW conductor track are 40m and 20um respectively. The S-parameters for the error boxes and CPW's propagation constant (γ) are found by using signal flow graphs of "line", "through" and "reflection" connections (shown in figures 5.19, 5.20 and 5.21). Since the physical dimensions of port 1 and 2 are identical, we assume that the error boxes of both ports are identical. In addition, we also assume that the forward reflection coefficient error $e_{21} = e_{12}$ for both ports. To distinguish the measured S-parameters of though, Reflection and lines connections, we will use T, R and L for each of these connections. The detailed mathematical procedures of TRL calibration is reported by *David M. Pozar* **[11].** This process is presented in the following sections.

(1) Measurement of through connection

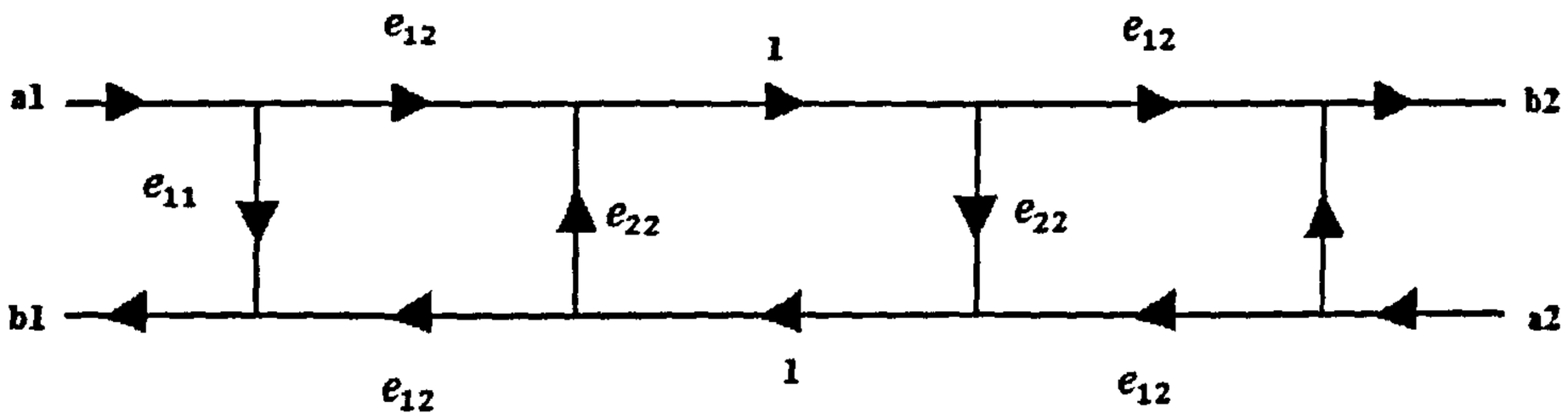

Figure 5.19 error flow graph of a through connection ([11]).

Figure 5.19 shows the signal flow graph of the through connection where the forward and backward reflection coefficients S_{21}^T and S_{12}^T are identical.

Therefore, the measured S-parameters of this connection can be expressed as:

$$S_{11}^T = \frac{b_1}{a_1}(a_2 = 0) = e_{11} + \frac{e_{22}e_{12}^2}{1-e_{22}^2} \tag{5.40}$$

$$S_{12}^T = \frac{b_1}{a_2}(a_1 = 0) = \frac{e_{12}^2}{1-e_{22}^2} \tag{5.41}$$

Since the dimensions of port1 and port 2 are identical, the measured S_{12}^T is also identical with S_{21}^T.

(2) The measurements of open reflection

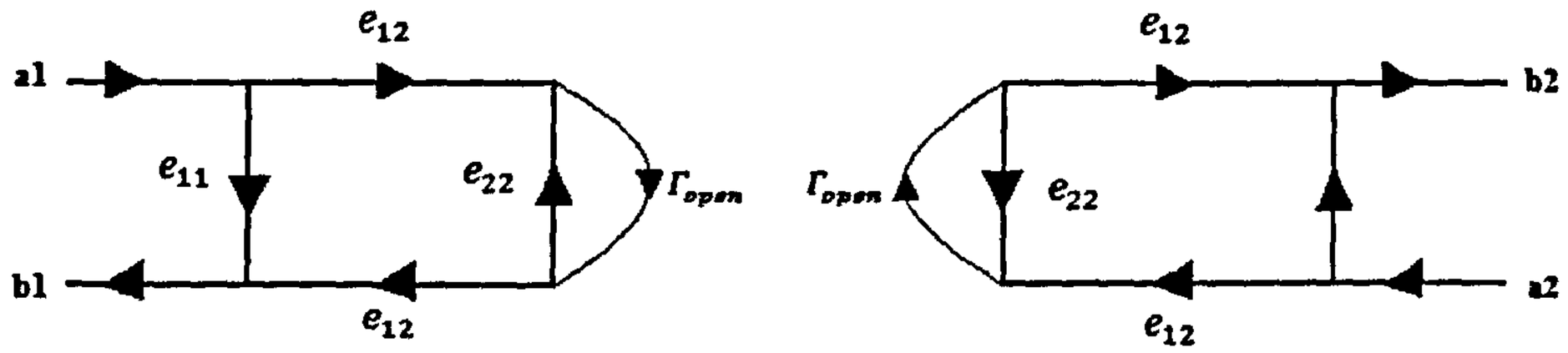

Figure 5.20 Error flow graph of an Open reflection connection (reproduced from **[11]**).

Figure 5.20 gives the signal flow graph of an open reflection connection. Since the two ports are disconnected, the measured forward reflection coefficients $S_{21}^R = S_{12}^R$ are zero. The measured reflection is nearly perfect. Again, we assume that $S_{11}^R = S_{22}^R$ or port1 and 2.

$$S_{11}^R = \frac{b_1}{a_1}(a_2 = 0) = e_{11} + \frac{e_{12}^2 \Gamma_L}{1 - e_{22} \Gamma_L} \tag{5.42}$$

(3) the measurement of line connection

The signal flow graph of the line connection is given in figure 5.21. The forward reflection coefficients of the line (1500um) connected between port1 and 2 are expressed as $exp^{-\gamma l}$.

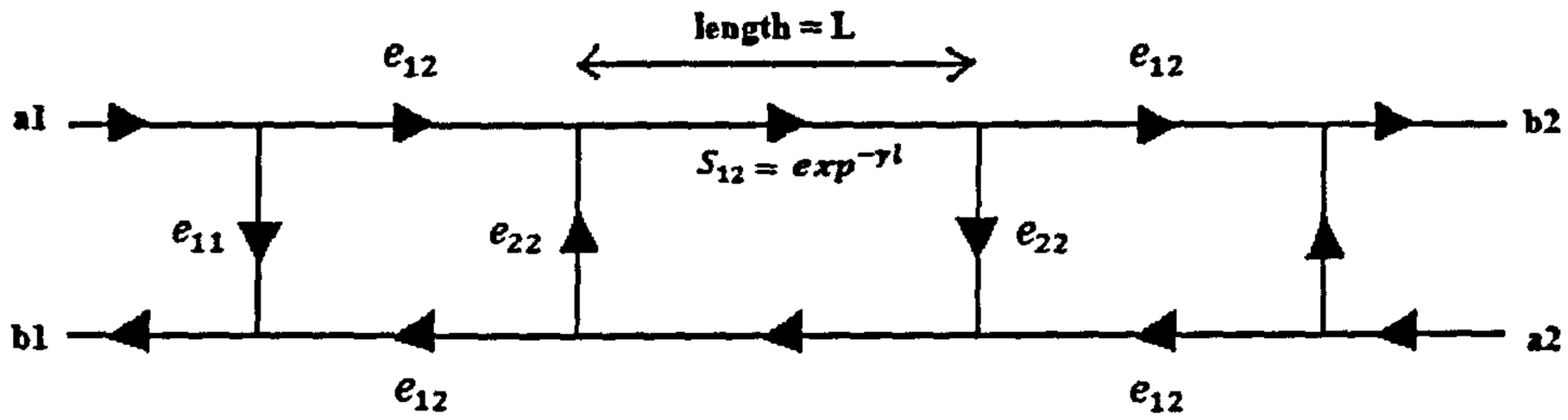

Figure 5.21 error flow graph of a line connection (reproduced from **[11]**).

The measured S-parameters of this connection are:

$$S_{11}^{L} = \frac{b_1}{a_1}(a_2 = 0) = e_{11} + \frac{e_{22}e_{12}^2 exp^{-2\gamma l}}{1 - e_{22}^2 exp^{-2\gamma l}} \tag{5.43}$$

$$S_{12}^{L} = \frac{b_1}{a_2}(a_1 = 0) = \frac{e_{12}^2 exp^{-\gamma l}}{1 - e_{22}^2 exp^{-2\gamma l}} \tag{5.44}$$

Where $S_{11}^{L} = S_{22}^{L}$ and $S_{12}^{L} = S_{21}^{L}$

So far we have five equations (4.40, 4.41, 4.42, 4.43 and 4.44) for 5 unknown parameters $e_{11}, e_{22}, e_{12}, e_{21}$ and $exp^{-\gamma l}$.The first step of the elimination process is to eliminate e_{12} from equation 5.40 and 6.41. Then e_{11} can be eliminated from equations 5.40, 5.41 and 5.42. Thus we have two equations left to solve the unknown e_{22} and $exp^{-\gamma l}$. According to *D.M Pozar* **[11]**, the mathematical process is straight forward, but time consuming. Thus, only the results for solving $exp^{-\gamma l}$ are given.

$$S_{12}^{L} exp^{-2\gamma l} - S_{12}^{L} e_{22}^2 = S_{12}^{T} exp^{-\gamma l} - S_{12}^{T} e_{22}^2 exp^{-\gamma l} \tag{5.45}$$

$$exp^{-2\gamma l}(S_{11}^{T} - e_{22}\, S_{12}^{T}) - S_{11}^{T} e_{22}^2 = S_{11}^{L}(exp^{-2\gamma l} e_{22}^2) - e_{22} S_{11}^{T} \tag{5.46}$$

Equation 5.45 can be rearranged so that e_{22} is solved as:

$$e_{22} = \sqrt{(S_{12}^{L} exp^{-2\gamma l} - S_{12}^{T} exp^{-\gamma l})/(S_{12}^{L} - S_{12}^{T} exp^{-\gamma l})} \qquad (5.47)$$

By substituting this equation into equation 5.46, we have the following quadratic equation for the propagation coefficient (γ) where $\gamma = \alpha + \beta j$.

$$exp^{-\gamma l} = \frac{S_{12}^{L\,2} + S_{12}^{T\,2} - (S_{12}^{T} - S_{12}^{L})^2 \pm \sqrt{S_{12}^{L\,2} + S_{12}^{T\,2} (S_{12}^{T} - S_{12}^{L})^2 4 S_{12}^{L\,2} S_{12}^{T\,2}}}{2 S_{12}^{T} S_{12}^{L}} \qquad (5.48)$$

As it shown equation 5.48 gives a choice of positive (+) or negative (-). The choice is depending on the requirement of real (α) and imaginary (β) part of γ to be positive or negative. In this case we choose both of α and β to be positive.

Although there has no analysis on the errors of the TRL calibration, it has been widely accepted that [10, 11] the accuracy of the TRL calibration depends on the phase difference of the measured transmission line. When the phase shift difference through the CPW lines is one quarter of its wavelength (90 degrees), the most accurate calibration results will be obtained and so it's common to keep the transmission line's phase shift between 20^{o} and 160^{o} [10, 11].

5.2 An example of characterizing ferroelectric BST thin film by CPW method

To demonstrate how the dielectric properties are obtained, an example of characterizing ferroelectric thin film (BST) using the CPW method is presented in this part of the thesis. The characterized results are also provided as a benchmark for other materials. The thickness of the thin film is 180nm determined from the SEM image (figure 5.22).

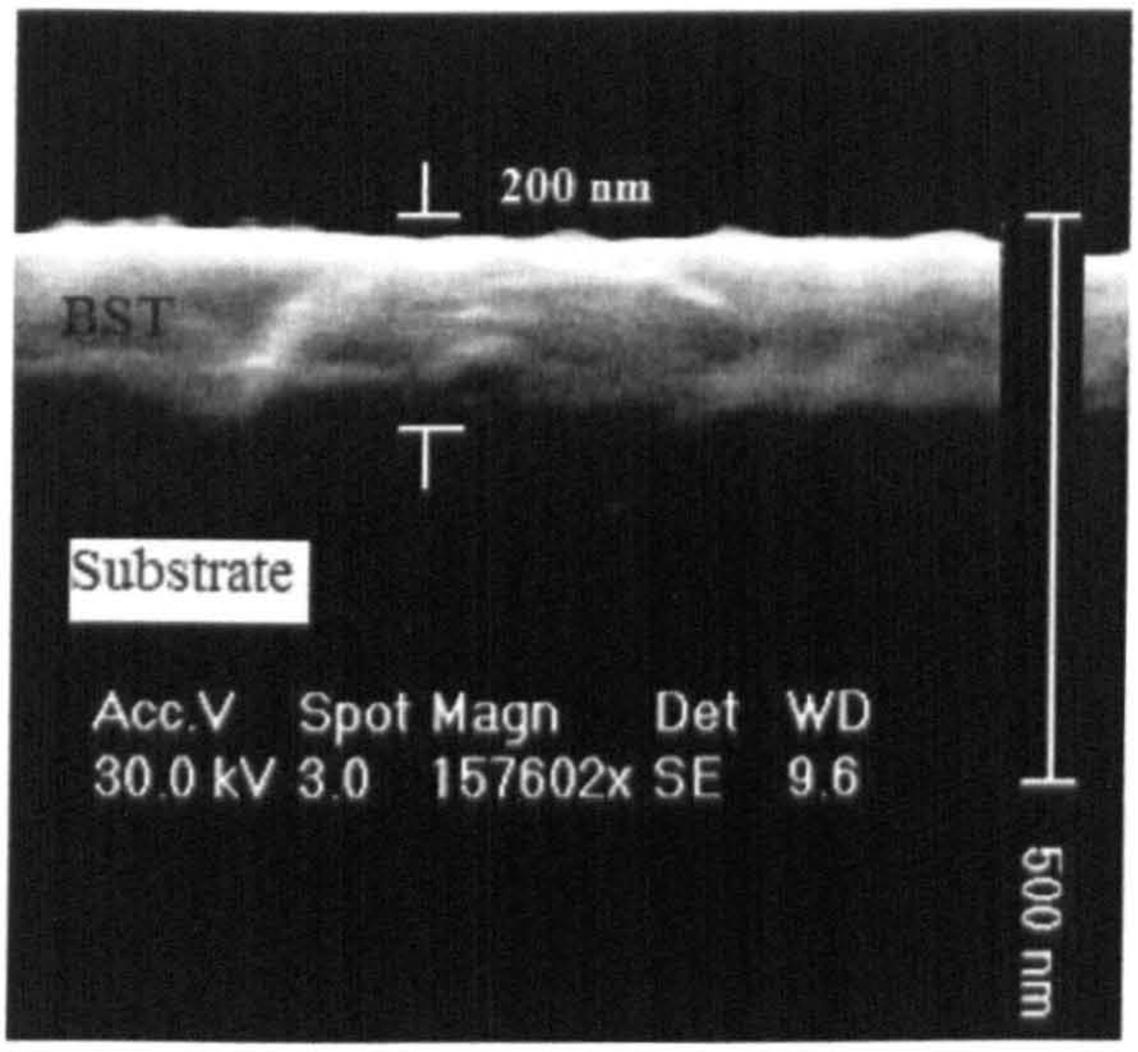

Figure 5.22 image of BST thin film cross section

Calibration devices configuration

The CPW patterns shown in figure 5.23 were fabricated using the simple photolithographic method described in chapter 4. The configurations of the *line*, *through* and *reflection* connections are shown in figure 5.23(a), (b) and (c). The width and gap of the CPW waveguide used in this work are 40um and 20um respectively. All three connections are fabricated on the same sapphire wafer.

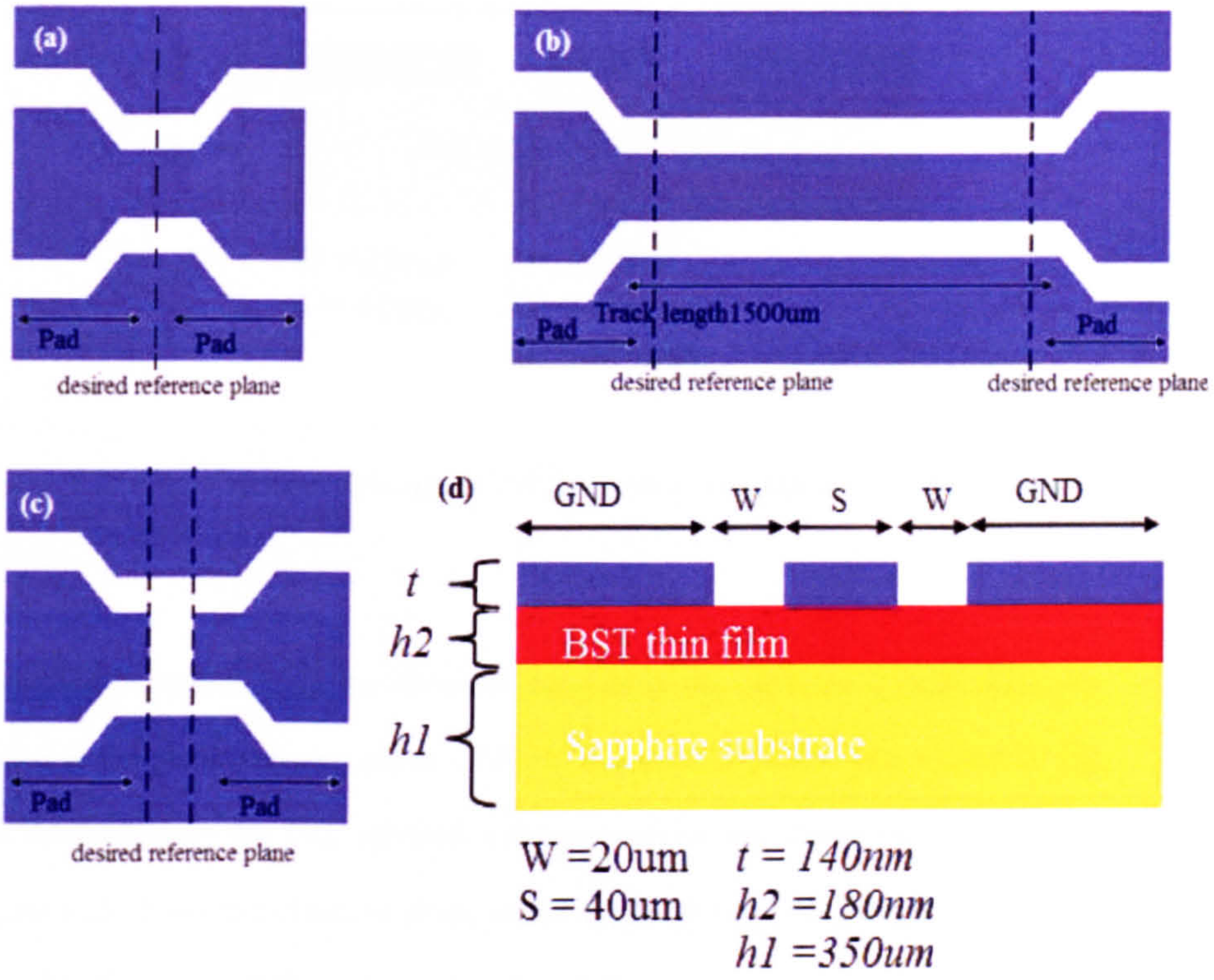

Figure 5.23 configuration and dimension of the CPW for characterization

There are three steps to obtaining the dielectric constant and loss tangent of the thin film from the measured CPW propagation constant (γ). These are 1) Determine the dielectric properties of CPW substrate (sapphire), 2) Determine the dielectric constant (ε_r) of BST thin film from the CPW phase constant (β) and 3) Determine the dielectric loss of thin film from the CPW attenuation (α). The detailed measurement processes are given in the following sections.

STEP 1: Determine sapphire substrate dielectric constant

To determine the dielectric properties of the substrate, CPW lines were fabricated on the surface of sapphire wafer without the BST thin film (figure 5.24). Since sapphire's dielectric loss tangent is below 0.001, its effect is negligible. Therefore, we are only interested in the measurement of the dielectric constant of sapphire substrate.

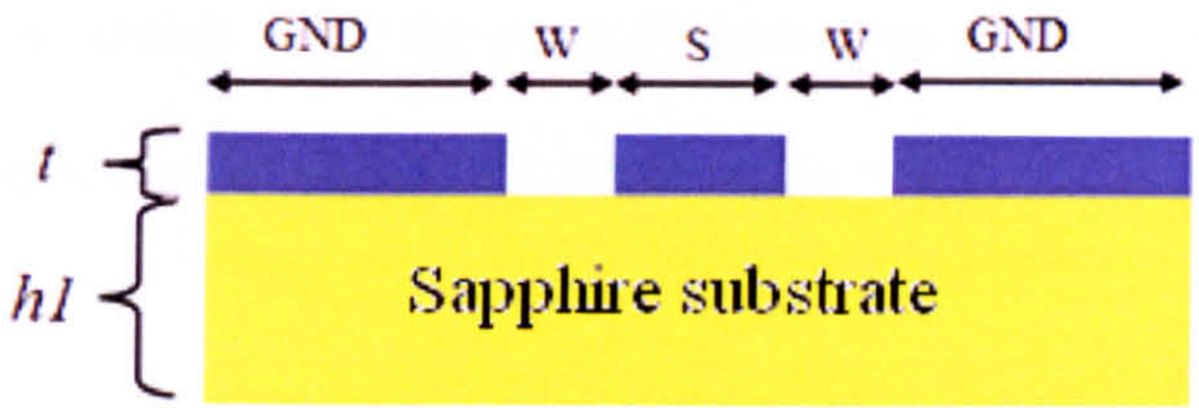

W =20um t = *140nm*
S = 40um *h2* =*180nm*
h1 =*350um*

Figure 5.24 Cross section view of a CPW patterned on sapphire substrate without BST film

According to section 5.1.2, the dielectric constant of the substrate is mathematically related to the phase constant (β) of CPW. In this case, the CPW phase constant (β) was determined by the TRL calibration process, which was discussed in part 5.1.7. Figure 5.25 shows the obtained phase constant (β) of the CPW (in radians) and its corresponding phase shift (in degrees) of the CPW.

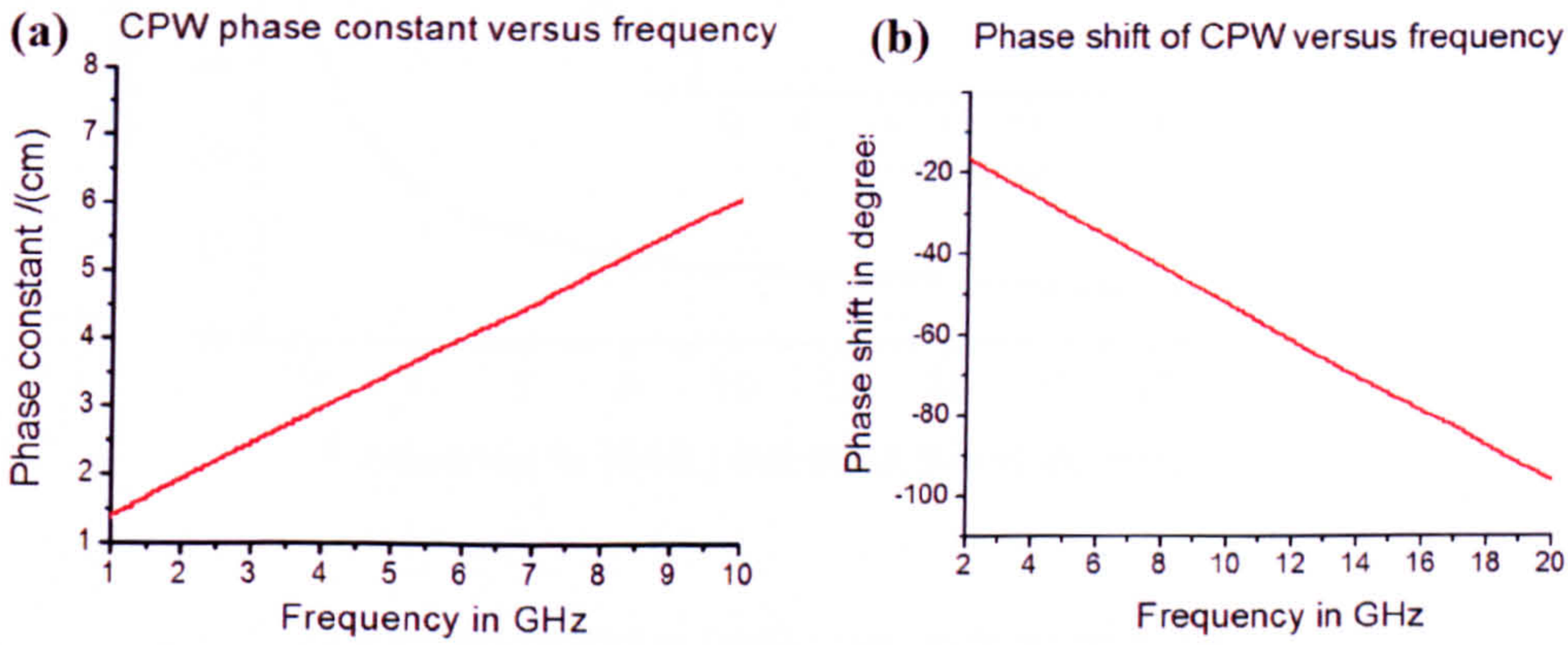

Figure 5.25 (a) the phase constant (β) of CPW obtained from TRL calibration between 1GHz and 10GHz (b) corresponding phase shift of the CPW

As discussed in section 5.1.2, the obtained phase constant (β) is related to the effective dielectric constant ($\varepsilon_{r,eff}$) of CPW as : $\varepsilon_{r,eff} = \frac{\beta C_o}{2\pi f}$.

With known effective dielectric constant ($\varepsilon_{r,eff}$) from equation $\varepsilon_{r,eff} = \frac{\beta C_o}{2\pi f}$, the dielectric constant of sapphire (ε_{r1}) can be solved by equation $\varepsilon_{eff} = 1 + q_1(\varepsilon_{r1} - 1) + q_2(\varepsilon_{r2} - \varepsilon_{r1})$, where q_1 is mathematically determined from equation 5.10 and q_2 is neglected, since the BST thin film was not coated onto the substrate. The mathematically obtained sapphire substrate dielectric constant is shown in figure 5.26.

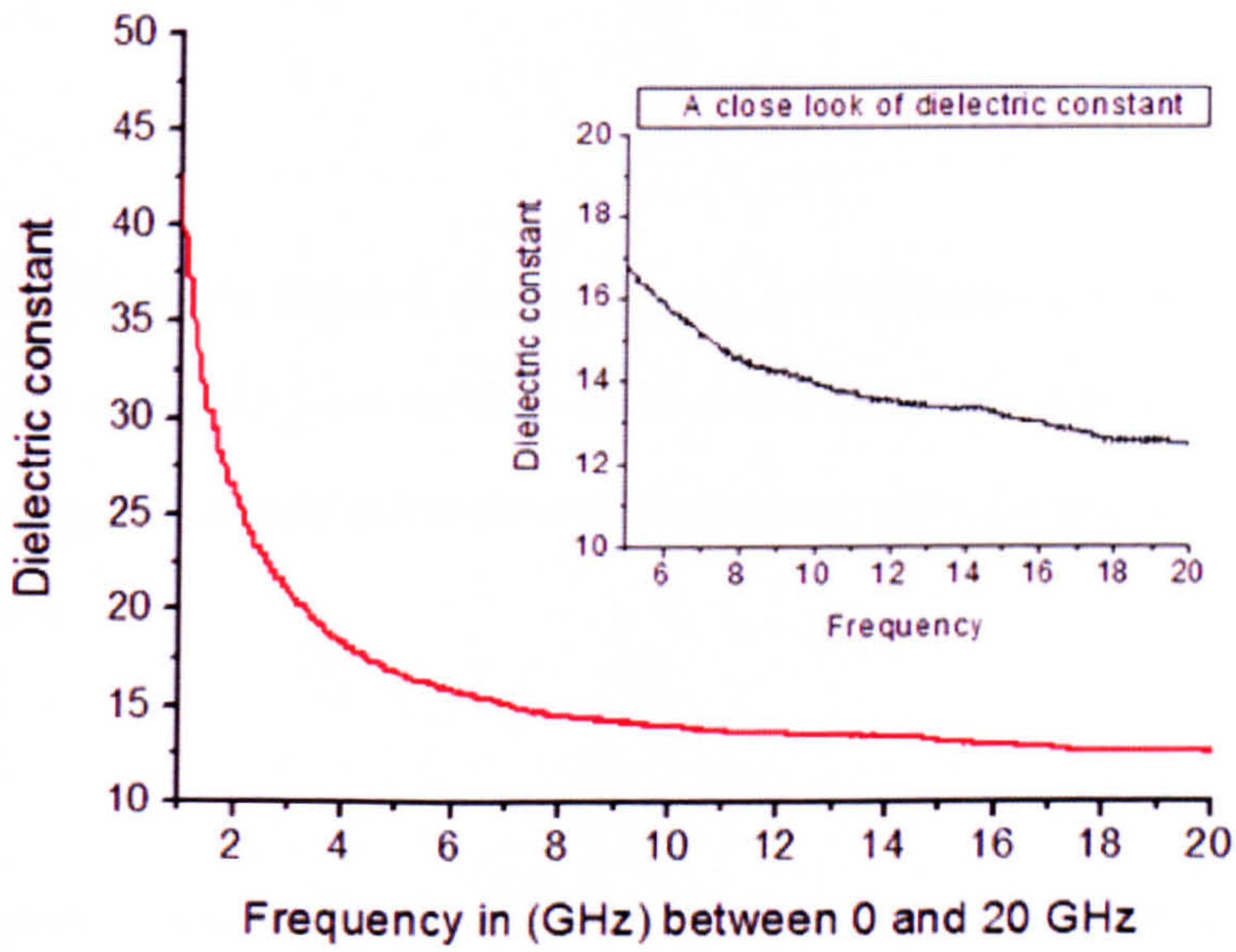

Figure 5.26 Dielectric constant of sapphire substrate versus frequency

As figure 5.26 shows, there is a fast relaxation of loss tangent at low GHz (<4GHz). This could be attributed to the frequency relaxation of dielectric materials where the real part of dielectric constant decreases as frequency increases. The same effect has already been reported by *Hang-Ting Lue's* **[10]** work. According to their suggestions,

the unexpected high dielectric constant at low GHz frequencies is caused by the errors of TRL calibration near zero GHz. When the phase shift of CPW is below 20^o, the accuracy of TRL calibration worsened. When the phase shift difference through the CPW lines is one quarter of its wavelength (90 degrees), the most accurate calibration results will be obtained **[10]**.

In figure 5.26, the CPW phase shift reaches 90 degrees at 19GHz, the measured substrate dielectric constant is ε_{r1}=12.57. The measured value is higher than the specified sapphire dielectric constant ($\varepsilon_{sapphire}$=10.154) **[13]**. The overestimation of dielectric constant is probably caused by the relatively low dielectric constant of sapphire.

In this work, lower dielectric constant ($\varepsilon_{sapphire}$=10.154) leads to smaller effective dielectric constant (ε_{eff}) of the CPW and so smaller phase shift. A small error in the measured phase constant (β) (or phase shift) can greatly affect the measured dielectric constant.

The errors in the measured phase shift (β) are caused by three factors (1): the interference of the probe station. Because the measured microwave signal by the vector network analyzer is very weak, a small vibration in the probe station could lead to large errors in the measured dielectric results. This type of interference occurs randomly and therefore, it can not be removed by the calibration; (2) the relative errors for ε_{eff} calculated from the conformal mapping technique is below 5% between 10GHz and 15GHz **[8]**; (3): the TRL calibration error at 90 degrees. Although the most accurate calibration results can be obtained when the phase shift

of the CPW is 90 degrees, the measurement error at 90 degrees is unknown. So far there has no report on the TRL calibration error at 90 degrees.

A simple way of estimating the error in the dielectric constant is to compare the measured dielectric constant of sapphire ($\varepsilon_{r(measured)}$) with the known dielectric constant of sapphire ($\varepsilon_{r(known)}$). The error (in %) in the measured dielectric constant is estimated as:

$$\text{Error} = (\varepsilon_{r(measured)} - \varepsilon_{r(known)}) / \varepsilon_{r(known)} \times 100\% = 24\% \quad (5.49)$$

This estimated error (24%) is too high for the measured dielectric results of the BST thin film, because BST has much higher dielectric constant than sapphire, which leads to greater phase shift. Hence a small variation of the measured phase shift (β) would not affect the measured dielectric results of the BST thin film. In this work the estimated error (24%) is used as a guideline for comparison.

STEP 2: Determine the dielectric constant of BST thin film

Once the substrate dielectric constant is determined, the dielectric constant of the BST thin film can be measured using the method that was described in section 5.1.2. In this case, an 180nm BST thin film was coated onto the sapphire substrate and the CPW lines were also fabricated by the photolithographic technique. Again using the TRL calibration method, the effects of parasitic capacitance from the probing pads have been removed and so the CPW's actual phase constant (β) is determined. The obtained phase constants of the CPW at 0V and 30V are shown in figure 5.27 (a) and (b).

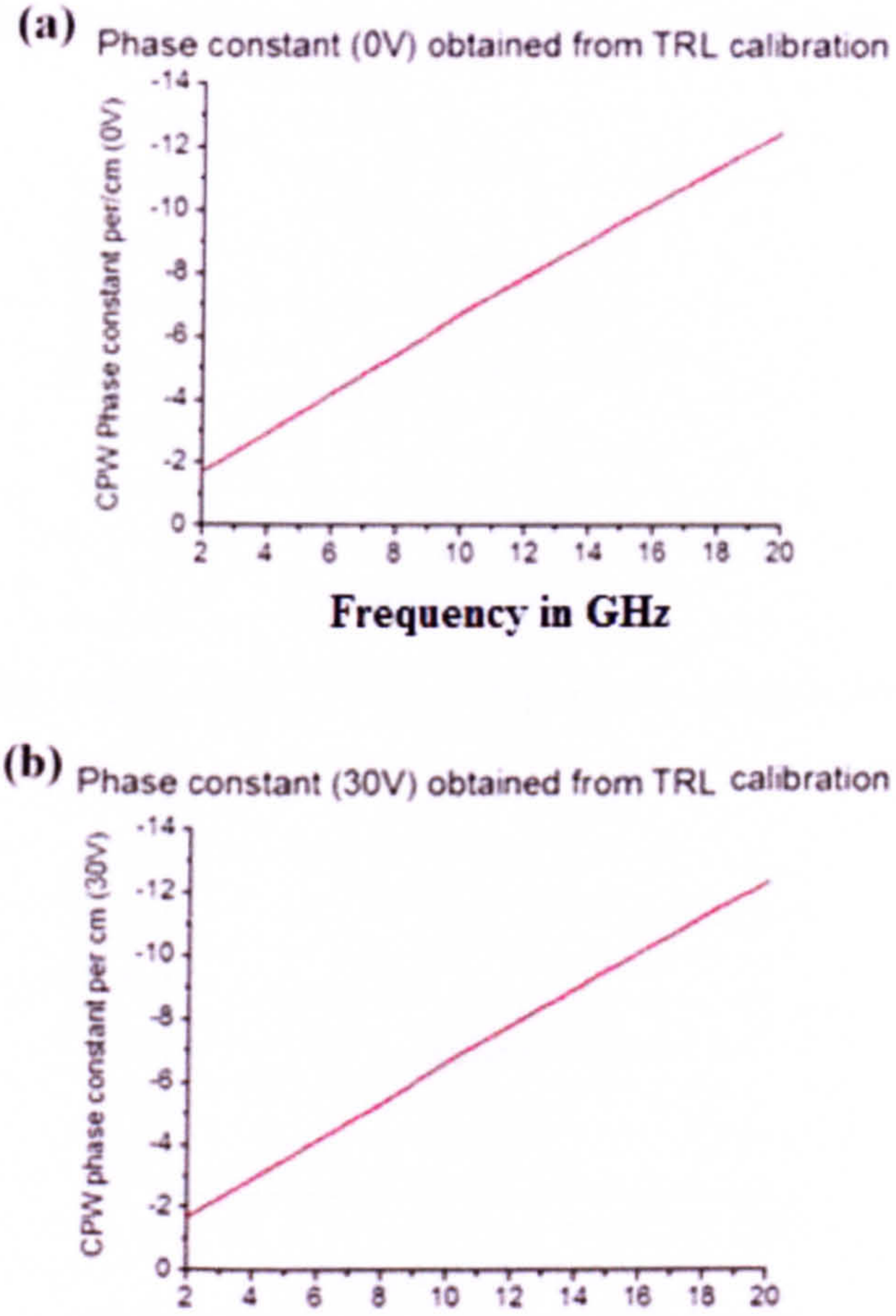

Figure 5.27 Phase constant (β) of the two layered CPW (1500um) under 0 and 30V (15KV/cm=30kV/20um)

Meanwhile, the corresponding CPW phase shifts at 0V and 30V are also given by figure 5.28(a) and (b).

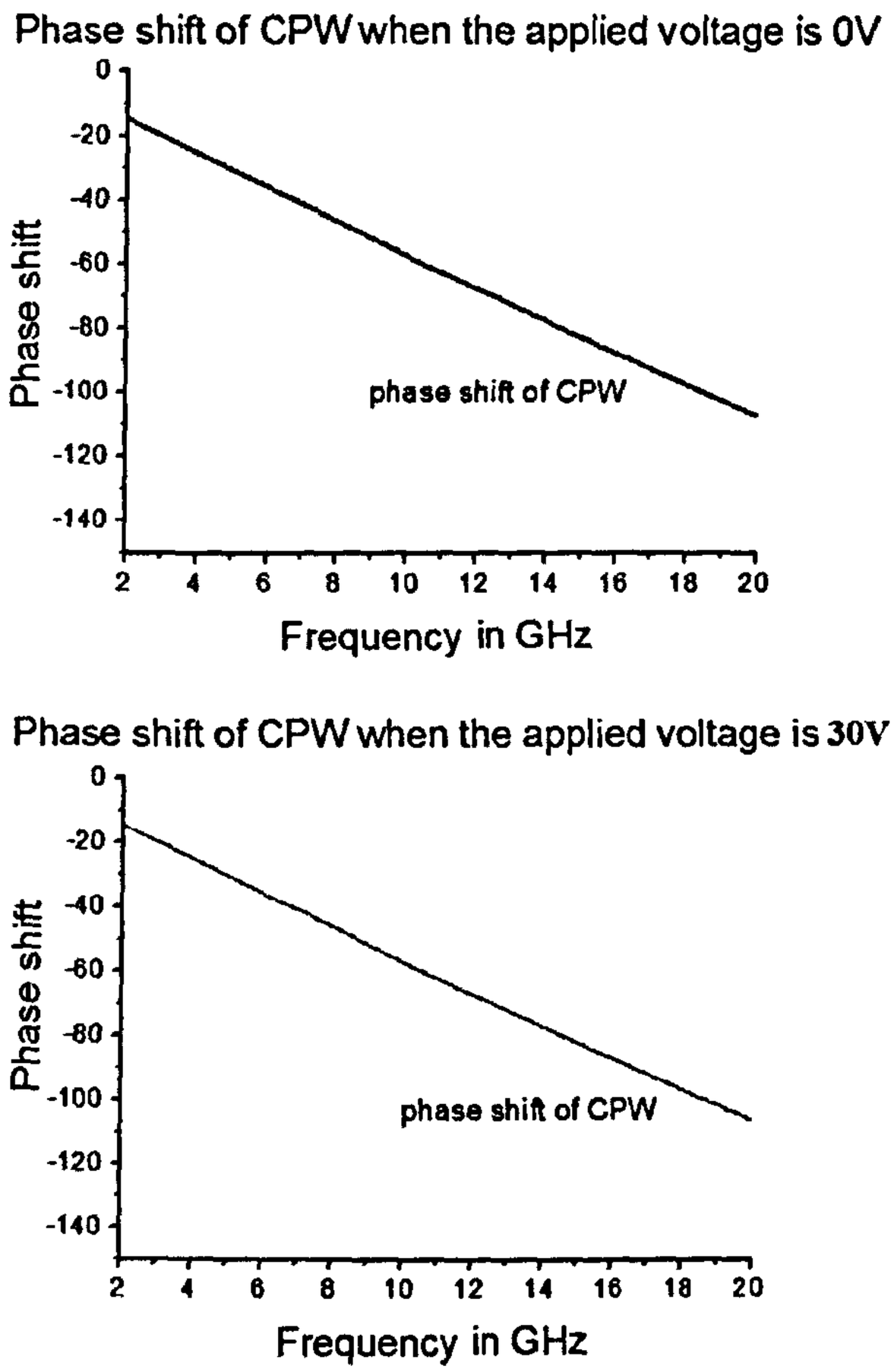

Figure 5.28 Corresponding phase shifts of the two layered CPW (1500um) under (a) 0V and (b)30V (15KV/cm=30kV/20um)

As mentioned in step 1, the effective dielectric constants ($\varepsilon_{r,eff}$) of the CPW with 0 and 30V are determined from equation $\varepsilon_{r,eff} = \frac{\beta C_0}{2\pi f}$, where β is from figure 5.27.

With known effective dielectric constants $\varepsilon_{r,eff}$, substrate dielectric constant (determined from step 1), q_1 (determined from equation 5.11) and q_2 = 0.01183 (obtained from the simplified mathematical equation 5.15) the dielectric constant of the BST thin film can be determined from equation $\varepsilon_{r2} = ((\varepsilon_{eff} - 1) - q_1(\varepsilon_{r1} - 1))/q_2 + 1$. The BST thin film's dielectric constants under 0V and 30V are shown in figure 5.29.

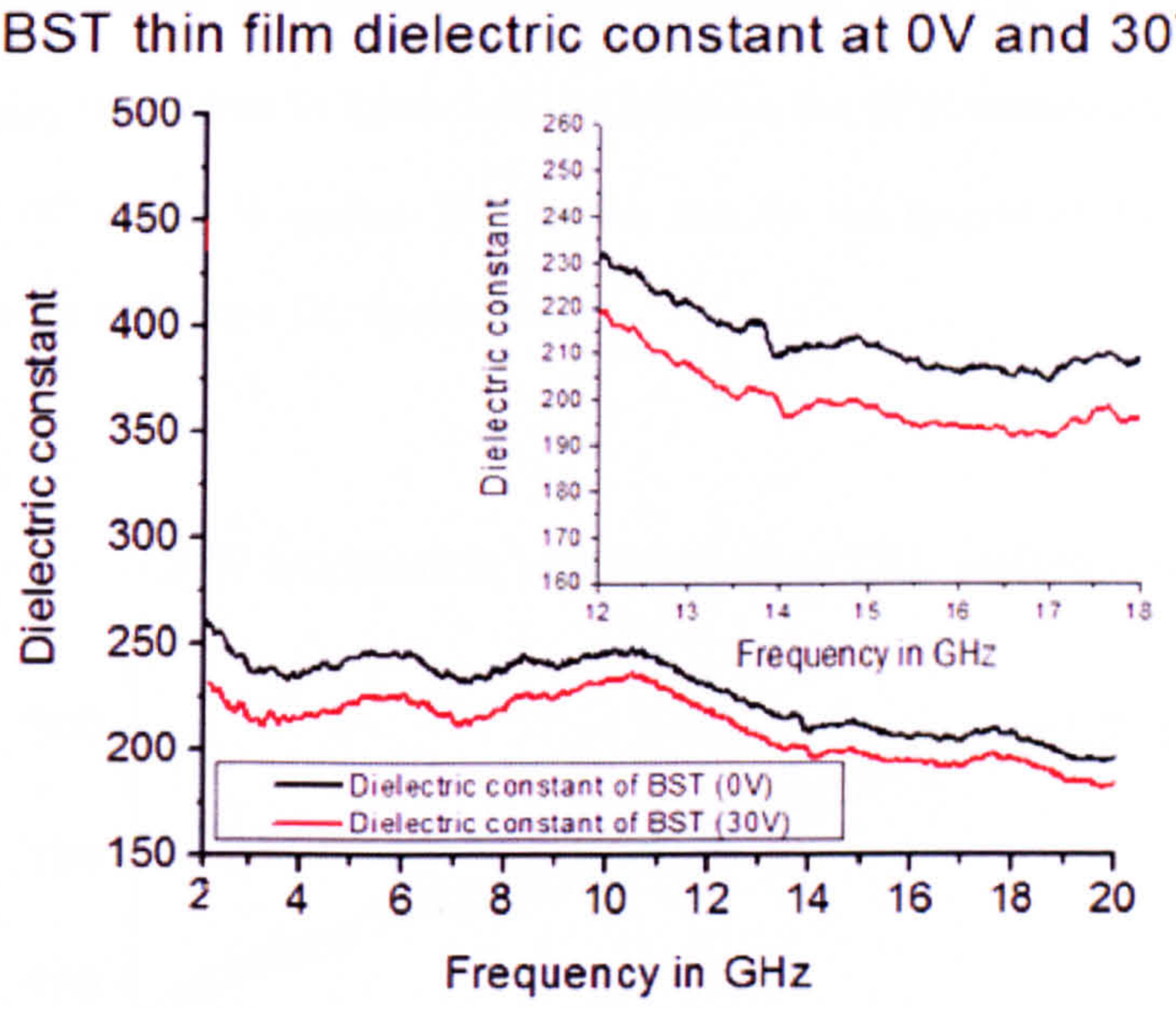

Figure 5.29 Dielectric constant of the BST thin film between 0 and 20GHz under 0 and 30V

As it can be seen, the measured dielectric constant of the thin film varies significantly. This is caused by the errors in the TRL calibration. As the measuring frequency increases to 16 GHz (90^o), the calculated dielectric constant of BST ferroelectric are 210 and 195 respectively, for a DC tuning voltage of 0V and 30V (15kV/cm). In other words, a dielectric tunability of 7.2% has been achieved at 16GHz by applying an electric field of 15kV/cm. Here the tunability is defined as $\frac{\varepsilon_{r(0V)}-\varepsilon_{r(30V)}}{\varepsilon_{r(0V)}}$. According to the error analysis in step (1), the estimated error in the measured dielectric constant is 24%.

STEP 3: Determination of the dielectric loss tangent of BST thin film

To determine the dielectric loss of the thin film, the total attenuation (α_{cpw}) of the CPW must be determined. The total CPW attenuation (α_{cpw}) is obtained from the real part of the propagation constant ($\gamma = \alpha + \beta j$) of the CPW by using theTRL

calibration method. The magnitude of the attenuations at 0V ($\alpha_{cpw(0V)}$) and 30V ($\alpha_{cpw(30V)}$) are shown in figure 5.30. As it shown, the CPW attenuation is reduced when a DC voltage is applied. This implies that the loss tangent of BST thin film decreases by applying a DC electric field.

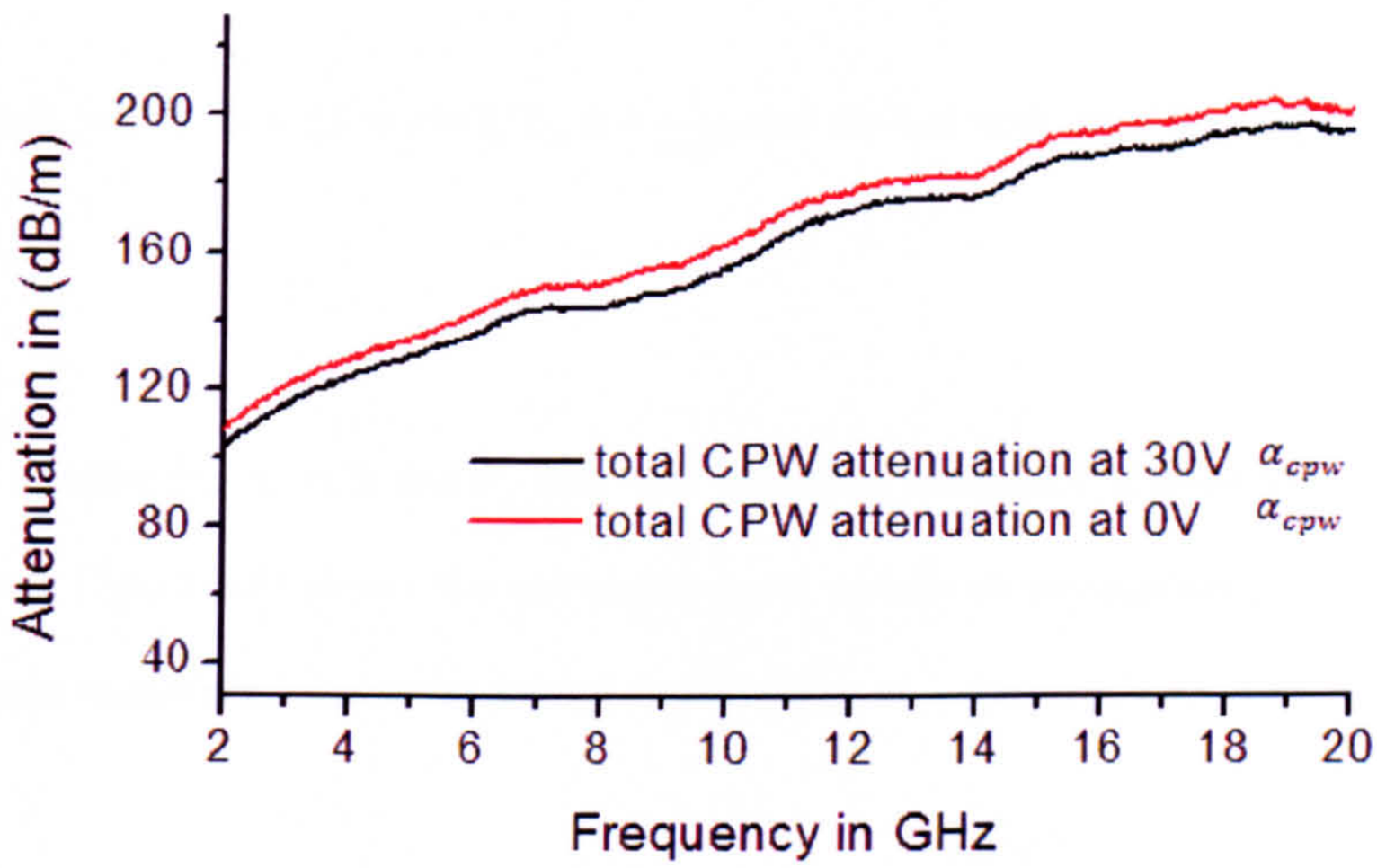

Figure 5.30: the CPW attenuation (α_{cpw}) under 0V and 30V or 15KV/cm

Once, the CPW attenuation (α_{cpw}) is determined, the effective dielectric attenuation (α_d) of the thin film can be mathematically obtained by

$$\alpha_d = \alpha_{cpw} - \alpha_c. \qquad [5.26]$$

where α_{cpw} is determined by using TRL calibration and α_c is the conductor attenuation. As mentioned in section 5.1.2, the conductor attenuation is caused by the skin effect where the magnitude of the electric current is stronger at the surface of the sample than inside of the conductor. The reduction in current is described by the term

of skin depth. Skin depth is the distance over which the current falls to $^1/_{exp}$ of its origin. The skin depth of aluminium is 0.8 μm at 10 GHz.

The conductor loss (α_c) due to skin effect is defined as **[7, 9]:**

$$\alpha_c = \frac{8.68R_S}{16Z_oK^2(k)(b^2-a^2)}\left[\frac{1}{a}ln\left(\frac{2a}{\Delta}\frac{b-a}{b+a}\right)+\frac{1}{b}\left(\frac{2b}{\Delta}\frac{b-a}{b+a}\right)\right] \quad (5.25)$$

with $a = S/2, b = (S + 2W)/2$, $\Delta = \frac{t}{4\pi e^{\pi}}$ and surface resistance ($R_s = \sqrt{\mu_o \pi . f . \rho}$)

By substituting a, b, Δ and R_s into this equation, conductor attenuation α_c can be found. Figure 5.31 shows the calculated metal conductor attenuation (in dB/m) with respect to metal thickness between 0 and 20 GHz.

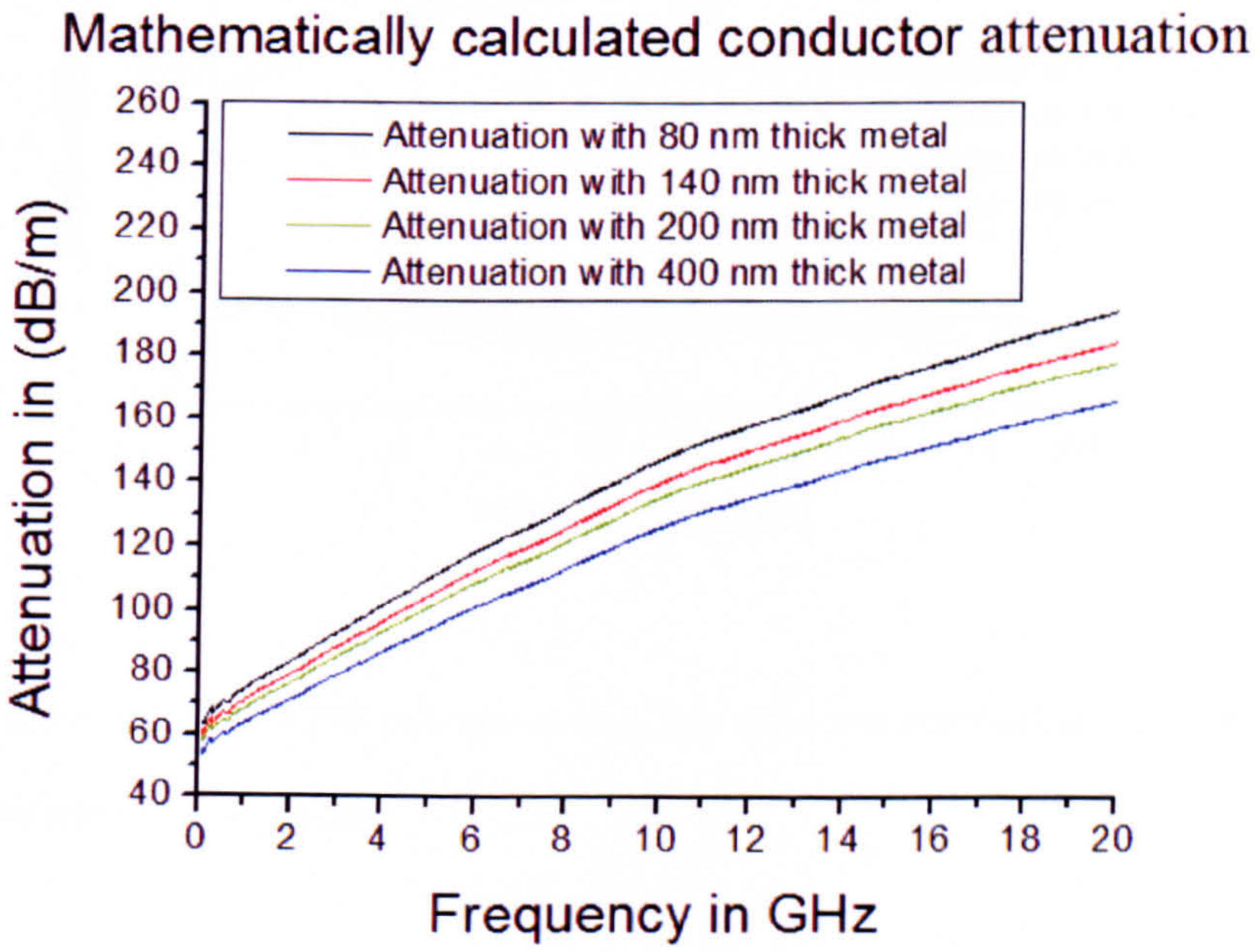

Figure 5.31 Mathematical calculated metal conductor attenuation in dB/m from 80nm to 400nm

As it can be seen, the conductor attenuation (α_c) decreases as the thickness of the conductor increases from 80nm to 400nm. At 16 GHz, the 140nm thick aluminium metal results in a conductor attenuation (α_c) of 170dB/m or 1.7dB/cm. With known α_{cpw} and calculated conductor attenuation(α_c), the effective dielectric attenuation (in dB/m) can be obtained by subtracting $\alpha_{cpw}$with α_c.

$$\alpha_d = \alpha_{cpw} - \alpha_c \quad (5.26)$$

The effective dielectric attenuation ($\alpha_d = \alpha_{cpw} - \alpha_c$) and the total CPW attenuation (α_{cpw}) of the CPW under 0V and 30V bias are shown in figure 5.32.

A comparison between CPW attenuation (α_{cpw}) and dielectric attenuation (α_d) at different tuning voltage

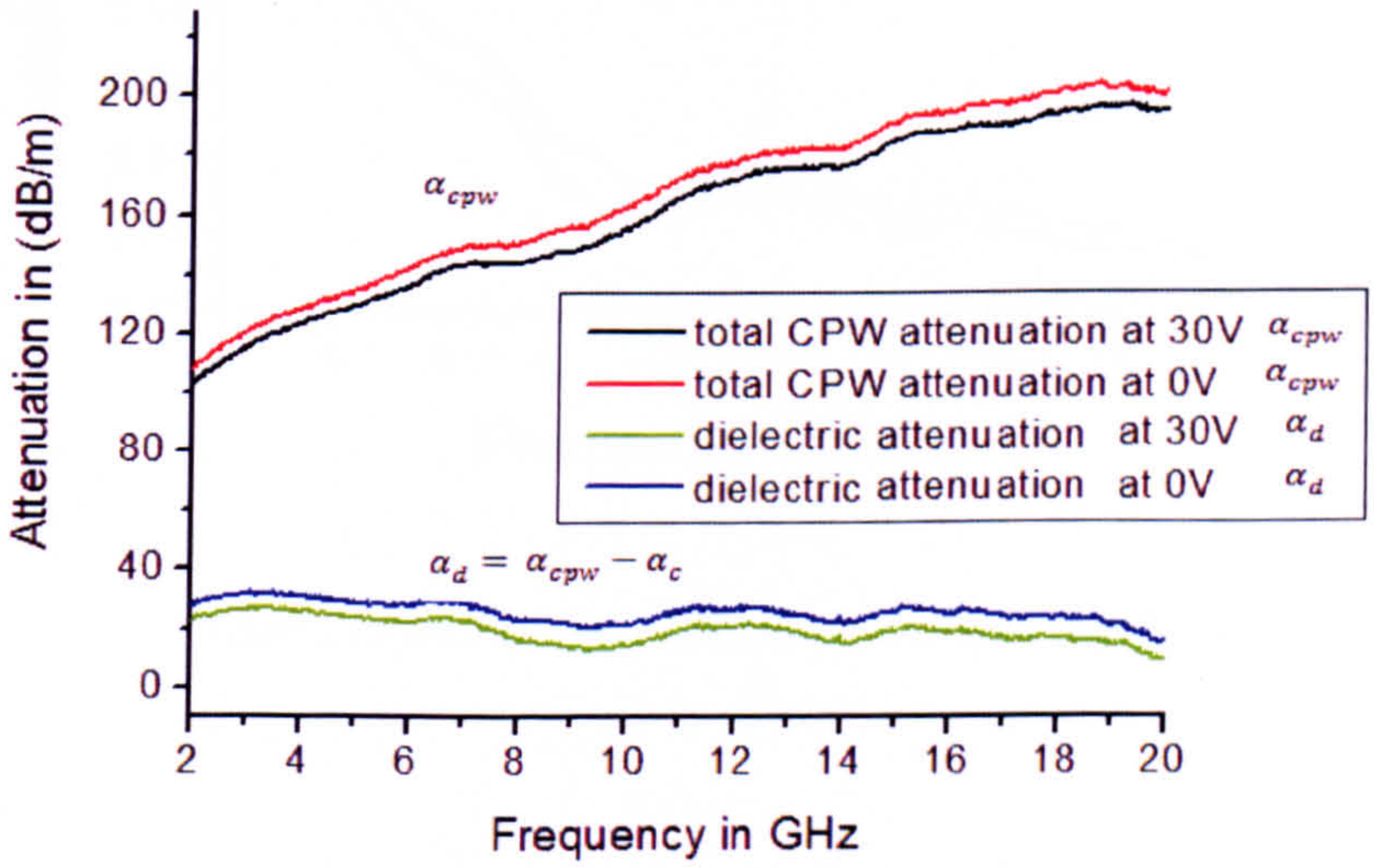

Figure 5.32 Total CPW attenuation (α_{cpw}) in dB/m and attenuation due to effective dielectric loss (α_d) dB/m

According to section 5.1.2, the effective dielectric loss tangent $\tan(\delta_{eff})$ can be mathematically determined from the effective dielectric attenuation (α_d) as: **[1]**

$$\tan(\delta_{eff}) = \frac{\alpha_d C_o}{1.89 L \pi f \sqrt{\varepsilon_{eff}}} \qquad (5.27)$$

By solving this equation, effective dielectric loss tangent of the CPW at 0 and 30V can be determined. The results of $\tan(\delta_{eff})$ are shown in figure 5.33.

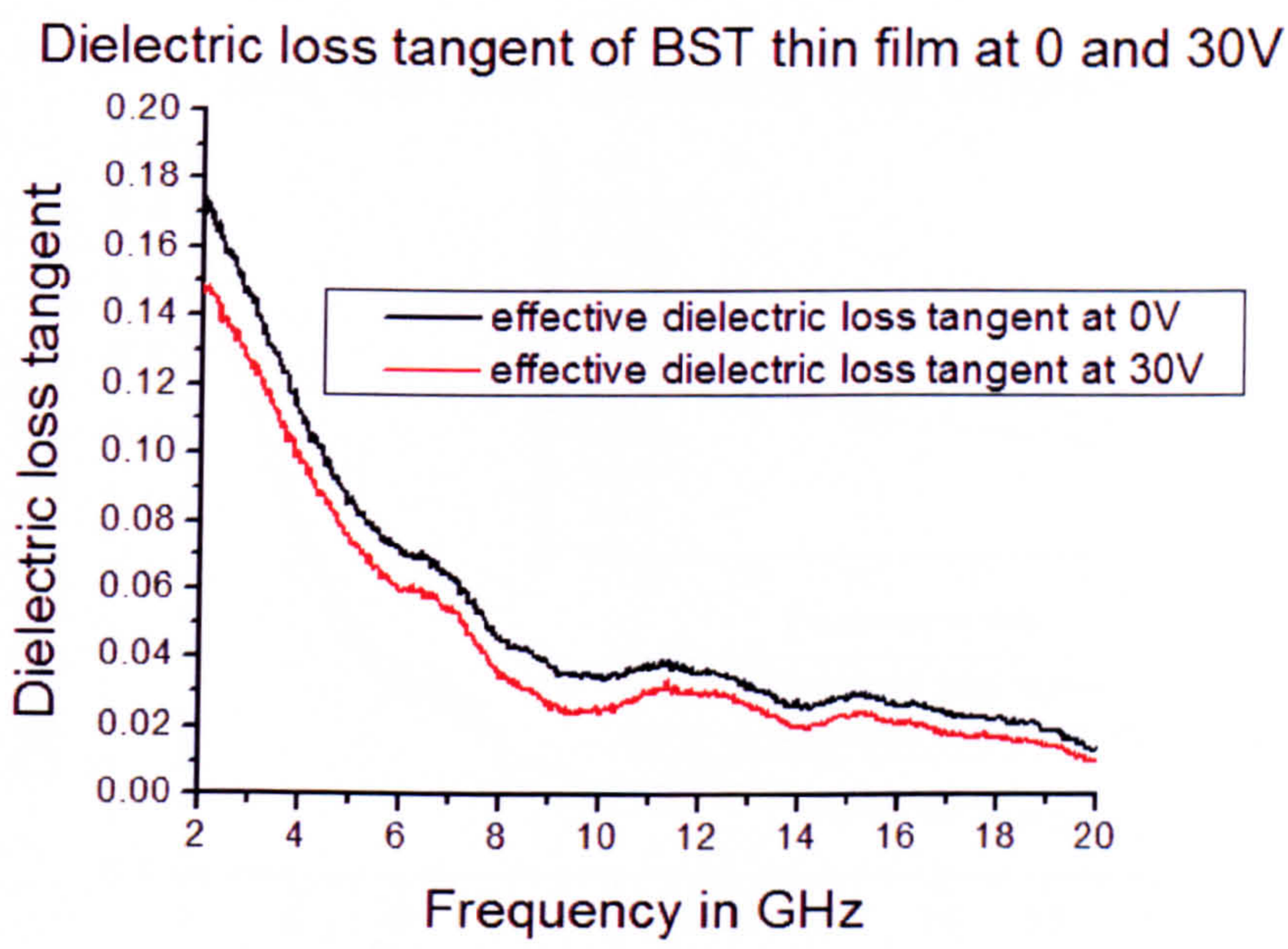

Figure 5.33 total effective dielectric loss tangent ($tan\delta_{eff}$)

With known substrate dielectric constant (ε_{r1}), thin film dielectric constant (ε_{r2}) and CPW effective dielectric loss tangent ($tan\delta_{eff}$), the dielectric loss tangent of the BST thin films can be determined as:

$$\tan(\delta_{\varepsilon_{r2}}) = \frac{\varepsilon_{eff} tan\delta_{eff}}{q_2 \varepsilon_{r2}} \qquad (5.29)$$

with q_2=0.01183 and ε_{r2} (thin film dielectric constant) obtained from step2.

Figure 5.34 gives the dielectric loss tangent of BST thin films between 2GHz and 20GHz under the DC tuning voltages of 0V and 30V. As mentioned previously, the most accurate calibration results are obtained when the phase shift of the CPW is 90 degrees. In this case the phase shift is 90 degrees when the measured frequency is 16GHz. The dielectric loss tangent of the BST thin film is reduced from 0.10 to 0.08 (at 16.0 GHz) when a 30V (15kV/cm) DC electric field is applied.

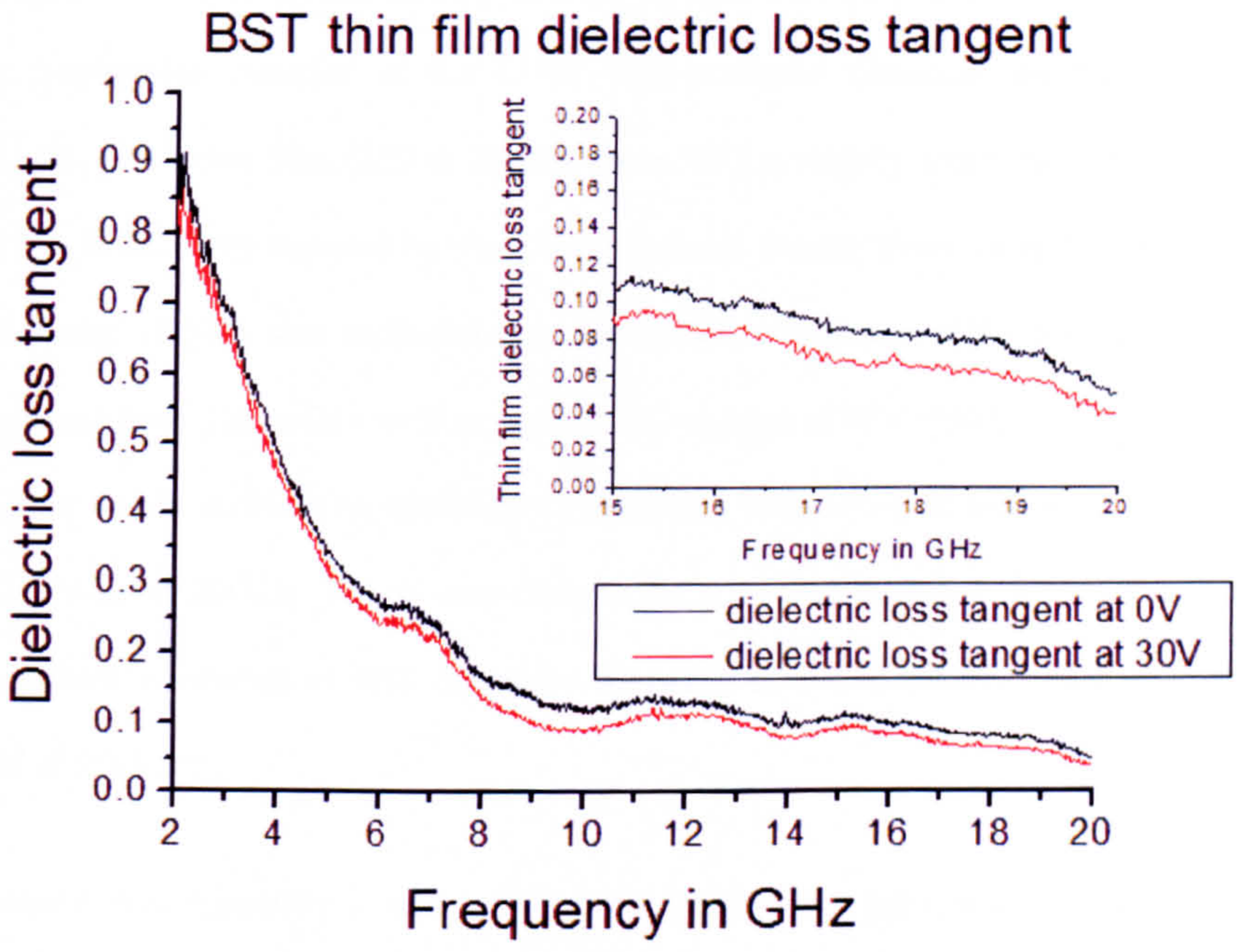

Figure 5.34 BST thin film loss tangent ($tan\delta_2$) with 30V and without applying voltage

As mentioned in section 5.12, the error in the measured dielectric constant of BST is determined by comparing the known dielectric constant of the sapphire with the measured dielectric constant of the sapphire. The error in the measured dielectric loss of BST thin film can not be estimated by this way, since the dielectric loss of the sapphire (<0.001) is too small to be measured and has been neglected (discussed in section 5.1.2). In figure 5.34, the dielectric loss of the thin film varies between 15GHz and 20GHz, a straight forward way to estimate the measurement error is to

record the minimum and maximum dielectric loss between 15GHz and 20GHz. The estimated error in the dielectric loss is between the measured minimum and maximum dielectric loss.

Conclusion of the CPW characterization

The principles of CPW characterization method have been discussed in section 5.1. Using this method, the dielectric properties of BST thin film were determined from the propagation constant of the CPW. The measured dielectric constant of the $Ba_{0.5}Sr_{0.5}TiO_3$ thin film (210 at 20GHz under 0V) is slightly lower than the values (225 at 20GHz 0V) reported by Hang-Ting *Lue* and Tseung-Yuen *Tseng10* **[10]**. *Lue* and *Tseng 10* **[10]** also indicated that the dielectric constant of the BST thin film decreased from 225 to 211 with an applied DC voltage of 40V (20kV/cm) at 20GHz. In other words, a dielectric tunability of 6.2% had been achieved with a tuning field of 20kV/cm at 20GHz. This is very close to the measured results in this work where the dielectric constant of BST decreased from 210 to 195 at 20GHz under a tuning field of 15kV/cm.

However, this tunability is not sufficient for commercial applications. This is the result of the small filling factor of q_2. A simple way to enhance the tunability is to increasing the filling factor by either increasing the film thickness or increase the line width. However, the reduction of line width will lead to an increase of attenuation **[10]. Thus**, there is a trade-off between tunability and loss. On the other hand, the measured loss tangent of BST thin film (0.06 at 20GHz under 0V) is very close to result (0.05 at 0V at 20GHz) reported by *Lue's* at the same frequency 10 **[10]**. In general, the dielectric properties of BST thin film measured by using CPW method are accurate and comparable to a similar work given by *Lue* and his colleagues.

5.3 Capacitor method

A metal insulated metal (MIM) capacitor embedded with high permittivity thin film is one of the most extensively used microwave devices for ferroelectric thin films characterization **[13-16].** The structure of this capacitor is shown in figure 4.1. The dielectric properties of the thin film are obtained from the measured capacitance (C) and quality factors (Q) of this capacitor. As shown in figure 5.35, the intrinsic capacitance of the capacitor can be represented by a parallel RC circuit where C is the thin film capacitance and R is the equivalent resistance of the capacitor.

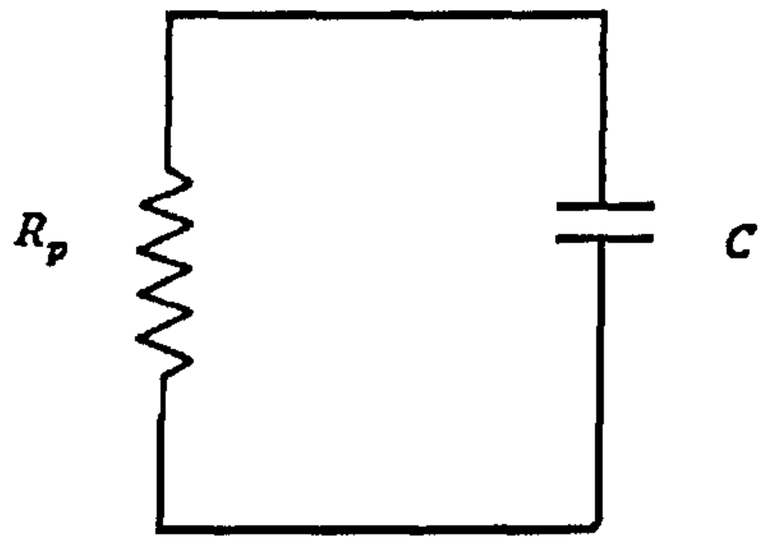

Figure 5.35 Equivalent circuit of a Metal Insulated Metal (MIM) capacitor **[1].**

The intrinsic capacitance between the bottom and top electrodes is related to the dielectric constant of the thin film as:

$$C_{int} = \frac{A\varepsilon_o\varepsilon_r}{d} \tag{5.50}$$

where d = Distance between the electrode , A = Actual capacitor area. ε_r= dielectric constant of the thin film

On the other hand, the quality factor of the actual capacitor is related to the capacitance and resistance of the thin film as

$$Q = \frac{1}{2\pi f C_{int} R_p} \tag{5.51}$$

where R_p= parallel resistance, f = operation frequency and Q = quality factor

The tunability of the thin film is measured by applying a DC electric field between the bottom and top electrode of the capacitor through the VNA's internal DC block. The tuning electric field on the MIM capacitor, defined as $E = \frac{V}{d}$ (d is the thickness of the thin film and V is the DC applied voltage), is greater than the tuning field that can be built up on a CPW due to the CPW's large gap (20μm). With a higher DC electric field, the same tunable material characterized by the capacitor method shows greater dielectric tunability than the CPW based characterization. In section 5.3.3, we will present the mathematical method of extracting the intrinsic impedance of the capacitor from the measured S-parameters and how to convert the intrinsic impedance to the dielectric properties of the thin film. Finally, results from a MIM capacitor embedded with BST thin film will be presented in section 5.3.4.

5.3.1 Capacitor configuration

Figure 5.36 shows the configuration of a typical MIM capacitor. The capacitor is made of three probing pads (in red) and a rectangular shaped capacitor (in blue). The three probing pads centre are separated by 100μm. Hence, a Ground Signal Ground probe with 100μm separation between its probing tips can be attached to the capacitor's pads. The top and bottom electrodes of the actual capacitor are connected with the signal and ground pads by short transmission lines. Because of the limits imposed by the photo resist, the capacitor pattern is made from a very thin layer of gold metal (140nm). To compare the measured results, the MIM capacitor with actual capacitance area of $100\mu m^2$was fabricated.

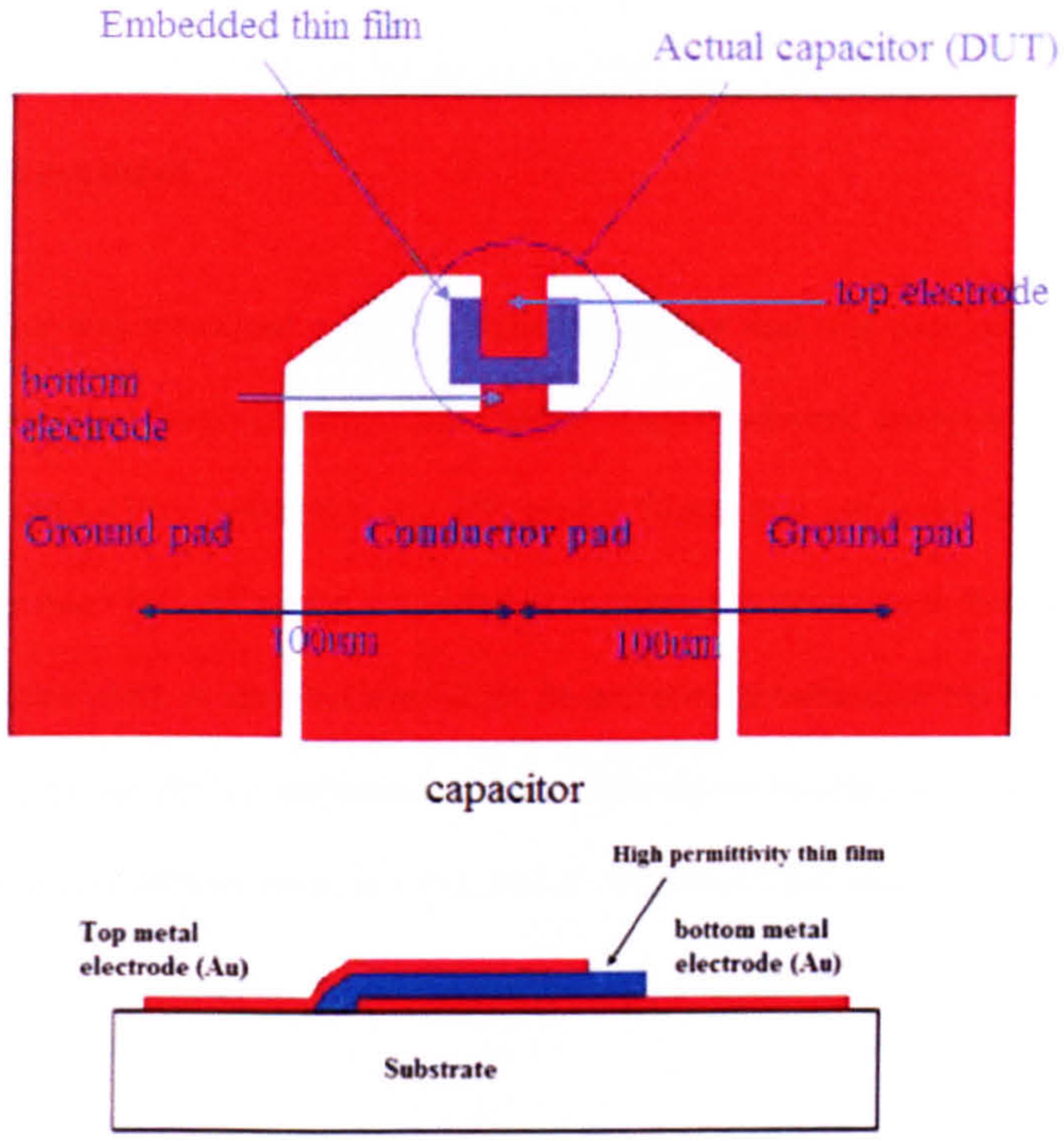

Figure 5.36 Configuration of a MIM capacitor

In figure 5.36, the size of the actual capacitor is relatively small compared with the pads. Because self-resonance occurs when the wavelength of the signal is close to the size of the device, the capacitor with smaller area has a smaller capacitance so that its self-resonant frequency is very high. This prevents the appearance of self-resonance of MIM capacitor at lower frequency.

However, using such a small capacitor results in an increase of Ohmic loss, which reduces its overall quality factor. In addition, the parasitic capacitance/resistance from the relatively large pads will strongly influence the measured capacitance (intrinsic). Hence, the directly measured data from the capacitor are corrupted and a de-embedding method is required to remove the unwanted parasitic capacitance and resistance from the pads and the short transmission lines that connect the actual capacitor.

5.3.2 Measurement

The capacitor was measured using the same equipment that was used to measure the CPW transmission lines: (Antritsu ME7808B) Vector network analyzer (VNA), RF cable and (40A-GSG_100EDP) one RF probe. Since this capacitor is a one-port device, only one GSG RF probe is needed to measure the device and therefore SOLT calibration was used. A simple Open-short de-embedding technique has been used to obtain the intrinsic device impedance (Zint). This de-embedding was accomplished by measuring two dummy pads, ie Open and Short pads on the same substrate.

The configurations of the two de-embedding devices are shown in figure 5.37. The configurations of the de-embedding pads in figure 5.37 are identical to the measured MIM capacitor. However, the open structures lacked the actual capacitor and left the pads open. The shorted devices connected the signal pad and ground pad together where the actual capacitor is located.

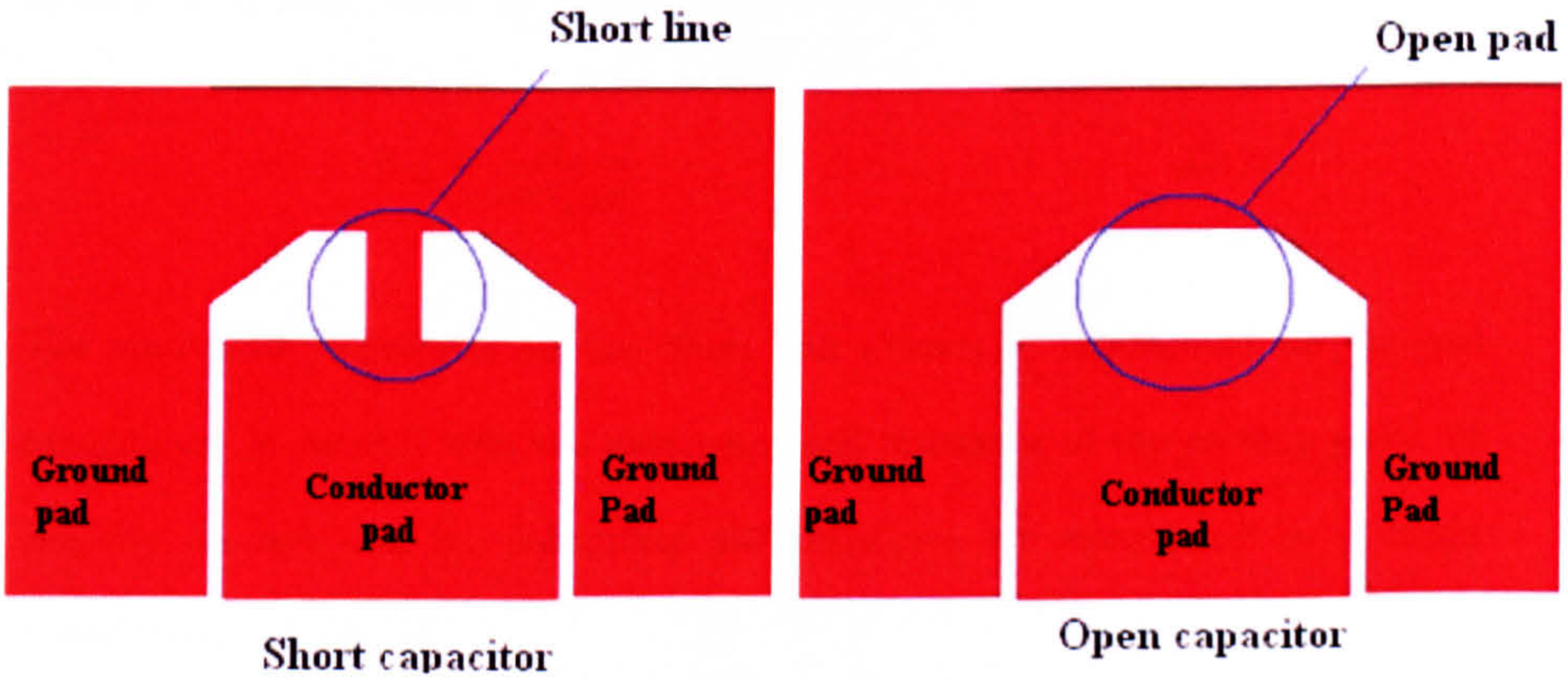

Figure 5.37 Configuration of the measured de-embedding circuits: Open and short pads

5.3.3 De-embedding

The equivalent circuits for the DUT and de-embedding pads are shown in figure 5.38. The lumped model of the DUT is modified from a two port equivalent circuit of the MIM capacitor [17].

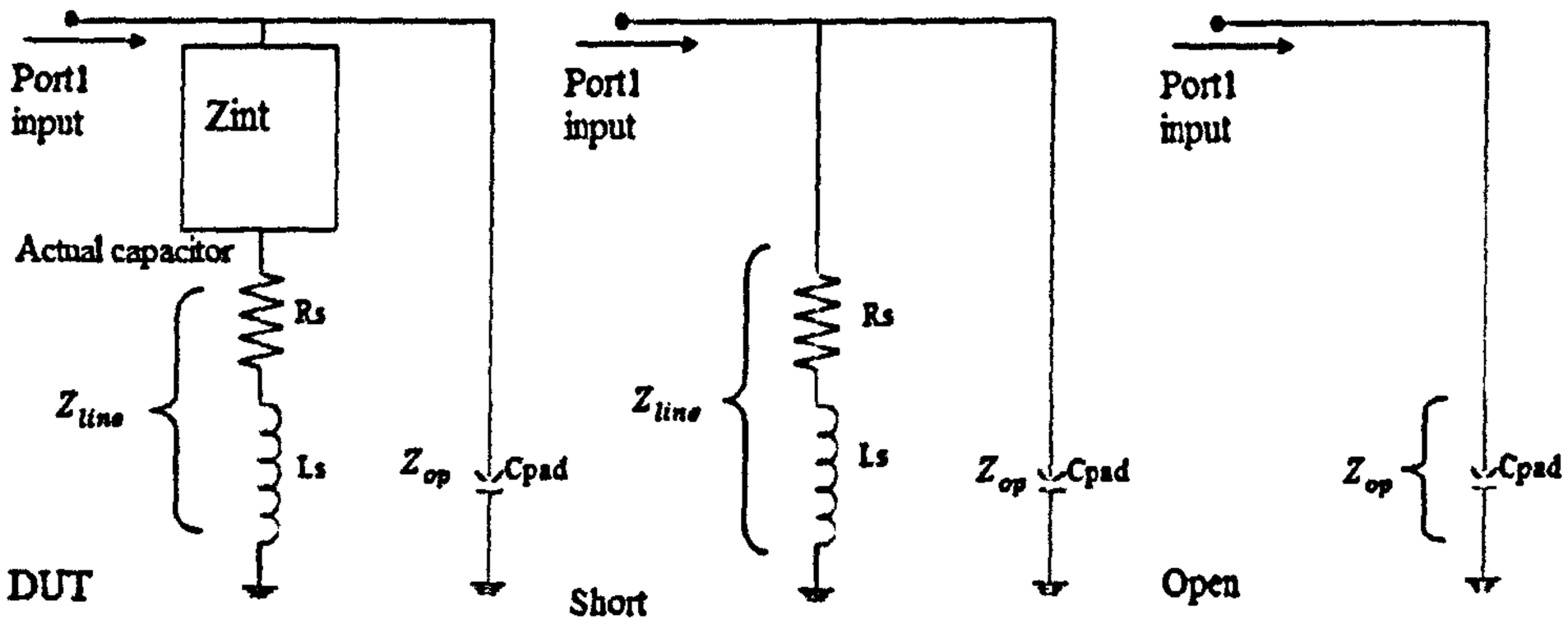

Figure 5.38 The equivalent lump circuits of the DUT, Short and Open pads (reproduced from [17])

According to this figure, R_s, L_s and C_{pad} represent the parasitic resistance, inductance and capacitance due to the probing pads, respectively. The measured impedance due to the probing pads (Open) is represented by a capacitor:

$$Z_{op} = \frac{1}{(j\omega C_{pad})} \tag{5.52}$$

The equivalent impedance of the Short pad (Short) is represented by the pad capacitance, in parallel with the inductance and resistance of the probing pads. To simplify the analysis, the inductance and resistance are represented by a single impedance block (Z_{line}).

$$Z_{line} = R_s + jwL_s \tag{5.53a}$$

$$Z_{sh} = \frac{Z_{op}Z_{line}}{Z_{op}+Z_{line}} \tag{5.53b}$$

The total impedance of DUT capacitor is modified from the equivalent short circuit by adding in an actual impedance blockZ_{int}.

$$Z_{dut} = \frac{Z_{op}(Z_{line}+Z_{int})}{Z_{int}+Z_{op}+Z_{line}} \tag{5.54}$$

The equivalent impedances include: Z_{DUT}, Z_{op} and Z_{sh} are mathematically obtained from the measured scattering parameters (S_{11}).

$$Z_{DUT} = Z_o \frac{(1+S_{11(dut)})}{(1-S_{11(dut)})} \tag{5.55}$$

$$Z_{op} = Z_o \frac{(1+S_{11(short)})}{(1-S_{11(short)})} \tag{5.56}$$

$$Z_{sh} = Z_o \frac{(1+S_{11(op)})}{(1-S_{11(op)})} \tag{5.57}$$

By substituting the equivalent impedances Z_{sh} , Z_{op} and Z_{DUT} into equations 5.55b and 5.56, we have two solutions (5.56 and 5.57) involving the two unknown parameters Z_{line} and Z_{int}.

$$Z_{sh} = \frac{Z_{op}Z_{line}}{Z_{op}+Z_{line}} \tag{5.58}$$

$$Z_{dut} = \frac{Z_{op}(Z_{line}+Z_{int})}{Z_{op}+Z_{int}+Z_{line}} \tag{5.59}$$

Equation 5.60and 5.61 can be rearranged as :

$$Z_{line} = \frac{Z_{op}Z_{sh}}{(Z_{op}-Z_{sh})} \tag{5.60}$$

$$Z_{int} = \frac{Z_{line}Z_{DUT}-Z_{line}Z_{op}+Z_{op}Z_{dut}}{(Z_{op}-Z_{DUT})} \tag{5.61}$$

By substituting equation for Z_{line} (5.620 into equation for Z_{int} (5.61), we have the final solution for the capacitor's intrinsic impedance.

$$Z_{int} = \frac{\left(\frac{Z_{op}Z_{sh}}{(Z_{op}-Z_{sh})}\right)Z_{dut} - \left(\frac{Z_{op}Z_{sh}}{(Z_{op}-Z_{sh})}\right)Z_{op} + Z_{op}Z_{dut}}{(Z_{op}-Z_{DUT})} \quad (5.62)$$

$$Z_{int} = \frac{Z_{op}^2(Z_{sh}+Z_{dut})}{(Z_{op}-Z_{DUT})(Z_{op}-Z_{sh})} \quad (5.63)$$

At microwave frequencies, the intrinsic impedance Z_{int} of the actual capacitor can be represented by a resistor (R_s) in series with the intrinsic capacitor (C_s). The equivalent circuit of the actual capacitor is shown in figure 5.39. Thus we have

$$Z_{int} = R_s + 1/(j\omega C_s) \quad (5.64)$$

The resistance (R_s) is caused by the dielectric loss of the thin film and the sheet resistance of the metal electrode of the MIM capacitor. The capacitance C_s is the actual capacitance of the capacitor.

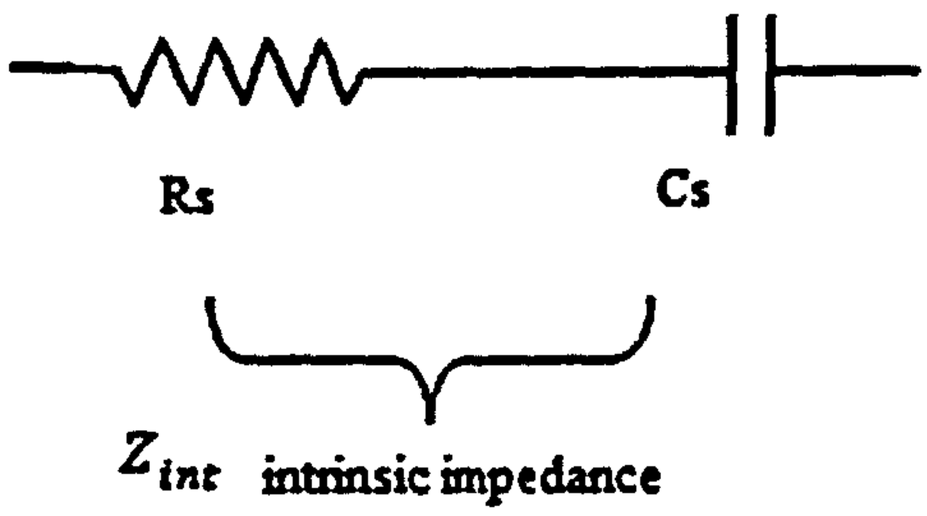

Figure 5.39 an equivalent lump circuit of the intrinsic capacitor

According to this capacitor model, the intrinsic capacitance of the actual capacitor is calculated from the imaginary part of the impedance (Z_{int}) by using $C_{int} = -\left(\frac{1}{2\pi f Im(Z_{int})}\right)$. On the other hand, the quality factor of the capacitor is obtained from the real part of impedance (Z_{int}) by using $Q_{int} = Im(Z_{int})/Re(Z_{int})$. The dielectric constant of the thin films can be determined from the capacitor's intrinsic capacitance (C_{int}) and intrinsic quality factor (Q_{int}) as follows:

$$\varepsilon_r = \frac{C_{int}d}{A\varepsilon_0} \tag{5.65}$$

where A is the area of the actual capacitor and d is the film thickness.

Because the top and bottom electrodes are so small, it is impossible to measure the conductor loss due to the metal electrodes. The dielectric loss tangent can only be roughly estimated as $\tan(\delta_{\varepsilon_r}) = 1/Q_{int}$.

5.3.4 An example of measuring the dielectric properties of ferroelectric BST thin film by the MIM capacitor method.

The thin film was prepared using the same chemical solution deposition method that has been discussed in section 6.1. To avoid damaging the metal electrodes, an annealing temperature of $(700C^o)$ was used to crystallize the thin film. This was lower than the temperature used in CPW method. The thickness of the metal thin film is again 140nm. The characterized results are also provided as a benchmark to be compared other materials.

The reflection coefficients (S_{11}) of the devices were measured using the methods described in section 5.1.6. A tuning voltage of 10V was applied to the device through the VNA's DC block. Since the thickness of the thin film was kept at 180nm, the tuning electric field was 556kV/cm. A photograph of the device under measurement is shown in figure 5.40.

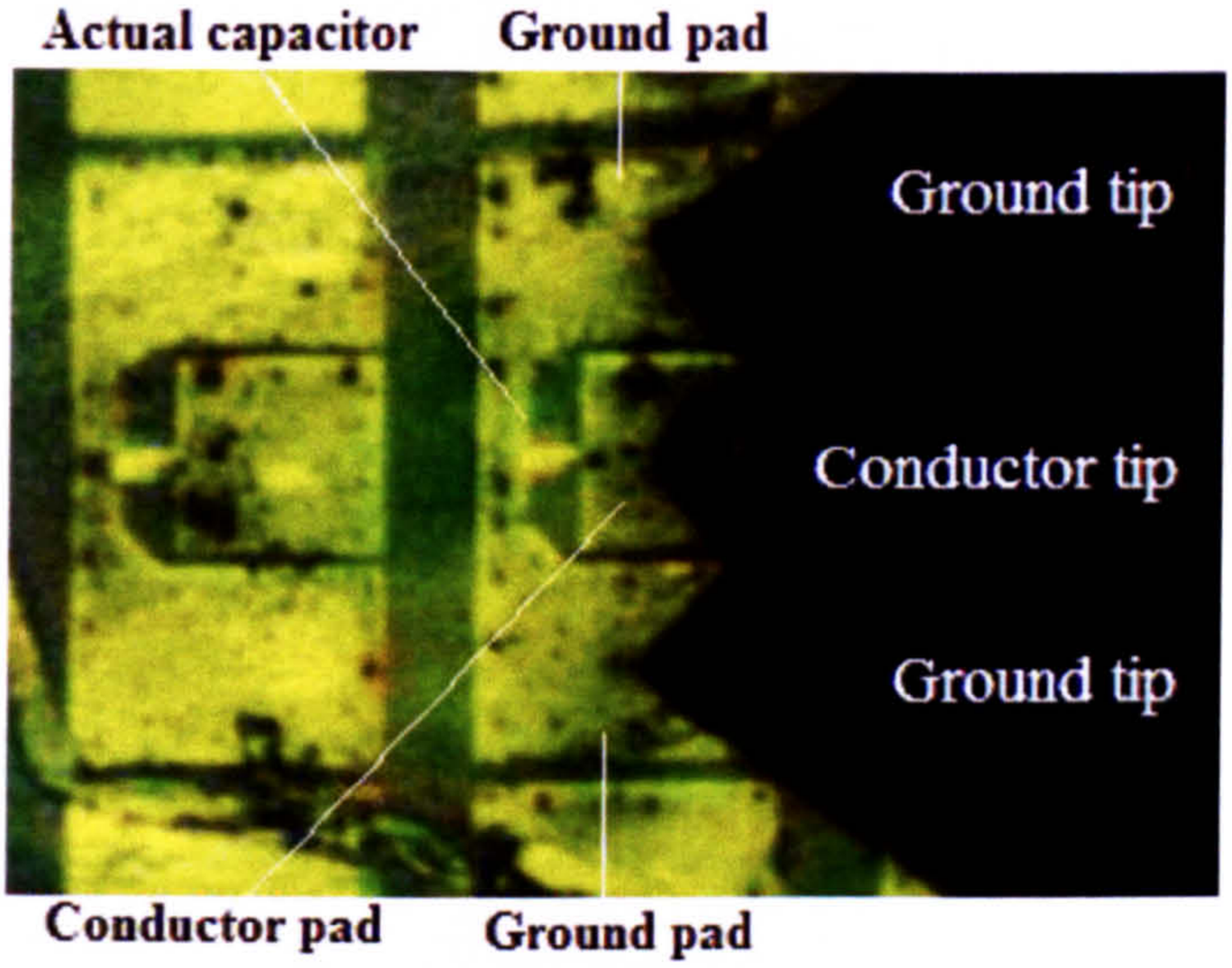

Figure 5.40 a real photograph through microscope of the MIM capacitor under measurement

Since the directly measured reflection coefficients (S_{11}) of the device are influenced by the parasitic capacitance and inductance due to the pads used to connect the BST thin film. A de-embedding process (Open and short) was employed to obtain the intrinsic characteristic impedance. All calculations include the de-embedding were carried out using Agilent's advanced design system 2007 (ADS) software. There are three steps to de-embed a MIM capacitor. Step (1): measuring the impedance of Open and short dummy pads. Step (2): measuring the impedance of MIM capacitor (DUT) and calculating the capacitor's intrinsic capacitance (Z_{int}). Step (3) converting the intrinsic impedance to the thin film's dielectric properties.

Step (1)

The measured reflection coefficients (S11) from the Open and Short pads are displayed in the Smith charts in figure 5.41(a) and (b).

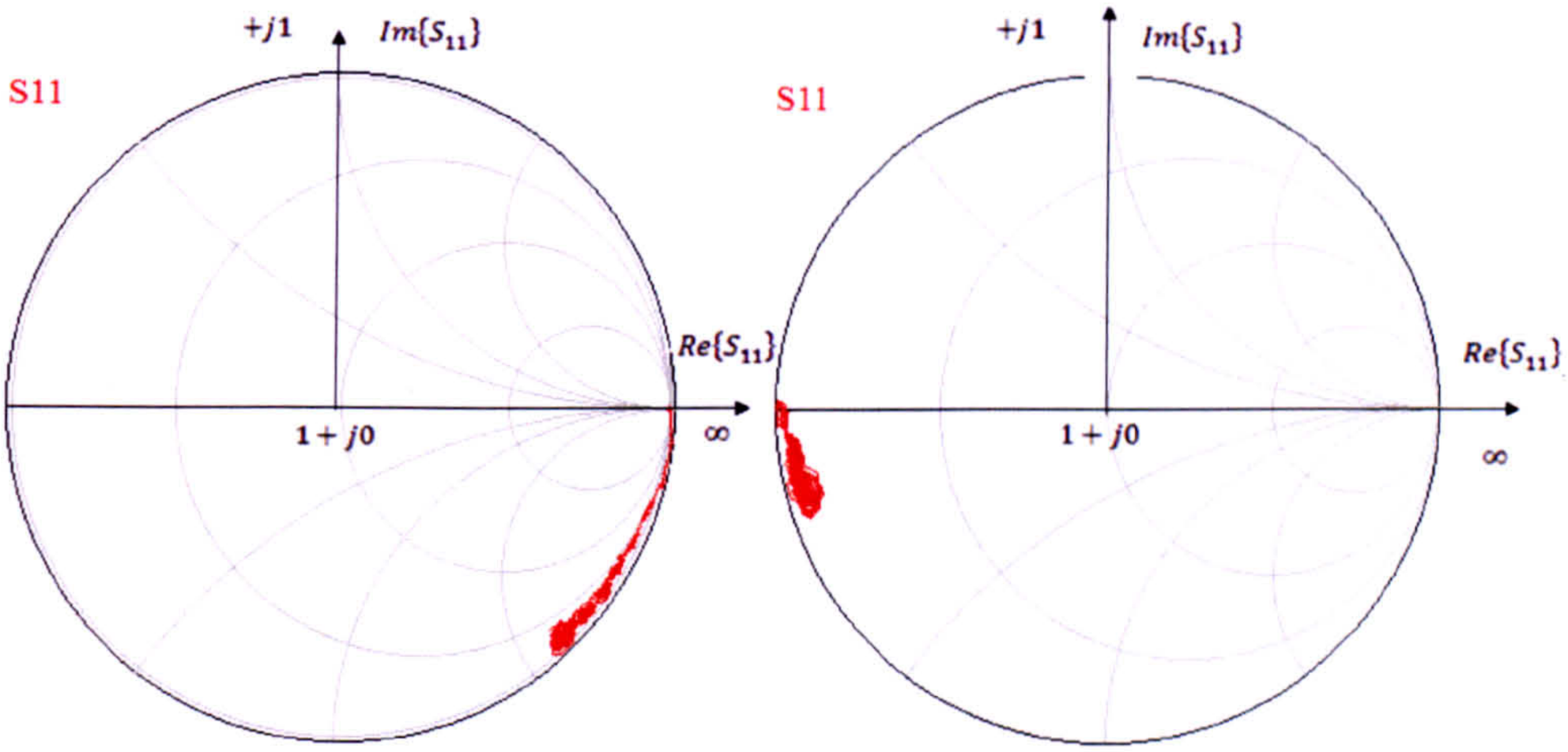

Figure 5.41 measured reflection coefficients (S11) of the Open (a) and Short pads (b)

The impedance of Open (Z_{op}) and short (Z_{sh})are calculated from the reflection coefficient S11 according to the following equations.

$$Z_{op} = Z_o \frac{\left(1 + S_{11(short)}\right)}{\left(1 - S_{11(short)}\right)} \tag{5.56}$$

$$Z_{sh} = Z_o \frac{(1+S_{11(op)})}{(1-S_{11(op)})} \tag{5.57}$$

Step (2)

The measured reflection coefficients (S_{11}) of the measured MIM capacitor (DUT) with and without electric tuning field are displayed in the complex plane with normalised impedance curves (Smith chart). Figure 5.42 shows the measured reflection coefficients (S11) of the capacitor (DUT) at 0V and 10V.

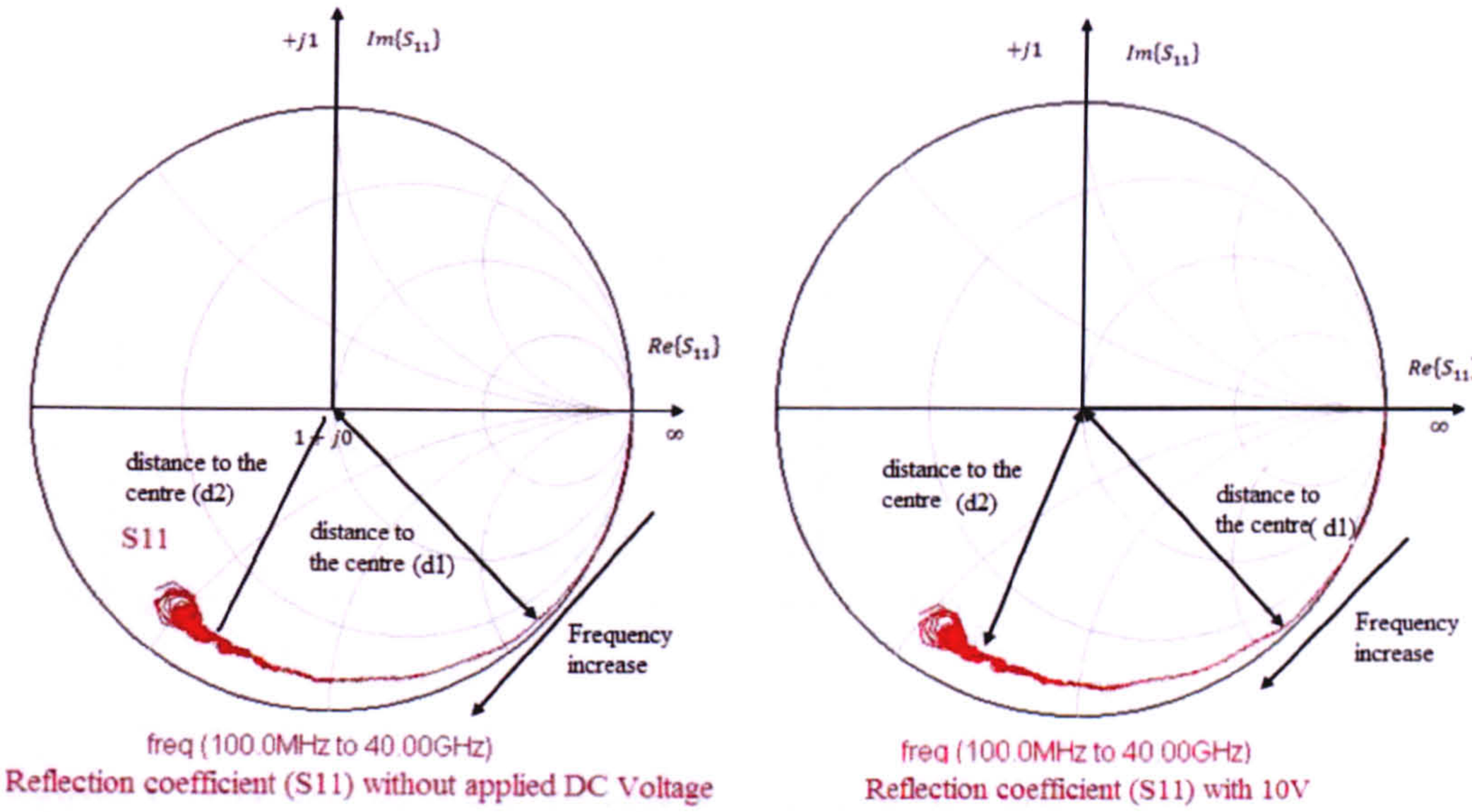

Figure 5.42 Measured reflection coefficients (S11) of the MIM capacitor under 0 and 10V (556kV/cm)

At lower microwave frequencies (<5GHz) the measured reflection coefficients are close to the outmost circle (d_1) of the Smith chart and the negative part (lower half) of the circle. This indicates that the imaginary part $Im(Z_{dut}) = \frac{1}{j\omega C_s}$ of the characteristic impedance due to the capacitance is far greater than the real part ($Re(Z_{dut}) = R_s$). This is the indication of a very high quality factor ($Q_{int} = Im(Z_{int})/Re(Z_{int})$). Hence, this device has shown excellent loss characteristics at frequencies lower than 5GHz. When the frequency increases (>5GHz), the measured data moves closer to the centre of the circle (d_2), indicating an increase of the characteristic loss in the device (DUT).

From the equation $Z_{dut} = Z_o \frac{(1+S_{11(dut)})}{(1-S_{11(dut)})}$, the impedance of the MIM capacitor can be obtained from the measured reflection coefficients (S11). Once, the characteristic impedance of Open, short and DUT capacitor are obtained, the intrinsic impedances of the capacitor can be determined from equation 5.62.

$$Z_{int} = \frac{Z_{op}^2(Z_{dut}-Z_{sh})}{(Z_{op}-Z_{dut})(Z_{op}-Z_{sh})} \qquad (5.62)$$

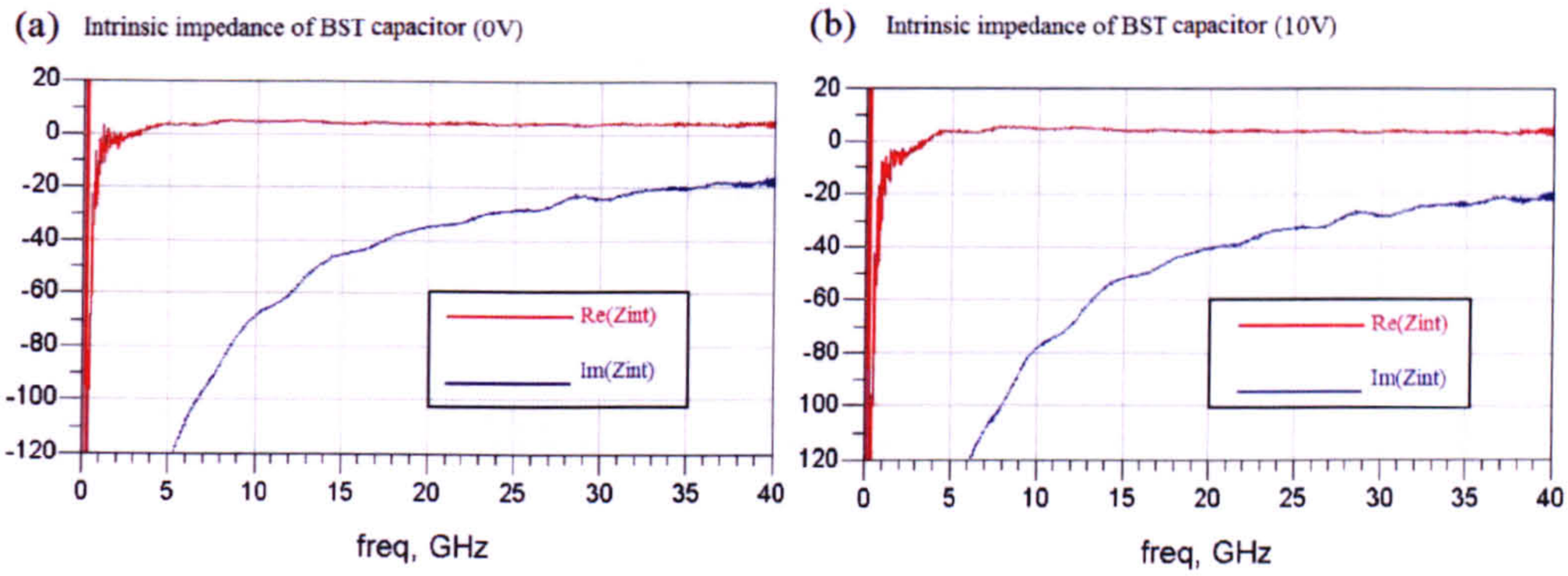

Figure 5.43 mathematically determined intrinsic impedances (Z_{int}) *of the capacitor at 0V (a) and 10V (b).*

The obtained intrinsic impedances for the capacitor voltages of 0V and 10 V are shown in figure 5.43(a) and (b). At lower frequencies (<3GHz), the real part (red line) of the intrinsic impedance is negative. This is caused by either the errors in de-embedding process or interference. Because the small size ($100\mu m^2$) of the MIM capacitor leads to a smaller capacitance, the intrinsic impedance of the capacitor ($Z_{int} = R_{int} + \frac{1}{j\omega C_{int}}$) is almost infinitely large at lower GHz and so it behaves like an open circuit.

In future work, a larger MIM capacitor with higher capacitance will be employed to characterize the dielectric properties of the thin film. The measured results can be strongly affected by the errors from de-embedding process and interference. Once the frequency increases to 5GHz or above, the experimentally determined real part of the intrinsic impedance remained constant around 10Ω. In contrast, the imaginary part of intrinsic impedance increases from -120Ω (5GHz) to - 20Ω (40GHz).

Step (3)

The intrinsic impedance (Z_{int}) of the MIM capacitor can be roughly represented as a capacitor connected in series with a resistor as: $Z_{int} = R_s + \frac{1}{j\omega C_s}$. Hence, the capacitance and quality factor of the actual capacitor can be determined from the following equations:

$$\text{Quality factor} = \frac{Im(Z_{dut})}{Re(Z_{dut})} \qquad \text{Capacitance} = \frac{-1}{2*\pi*f*Im(Z_{dut})}$$

By substituting the real and imaginary part of the intrinsic impedance into these equations, the quality factor and capacitance of the actual capacitor can be obtained. Figure 5.44 (a) (b) (c) and (d) shows the obtained quality factor Q_{int}, and capacitance C_{int}, for the actual capacitor with (10V) and without the applied DC voltage.

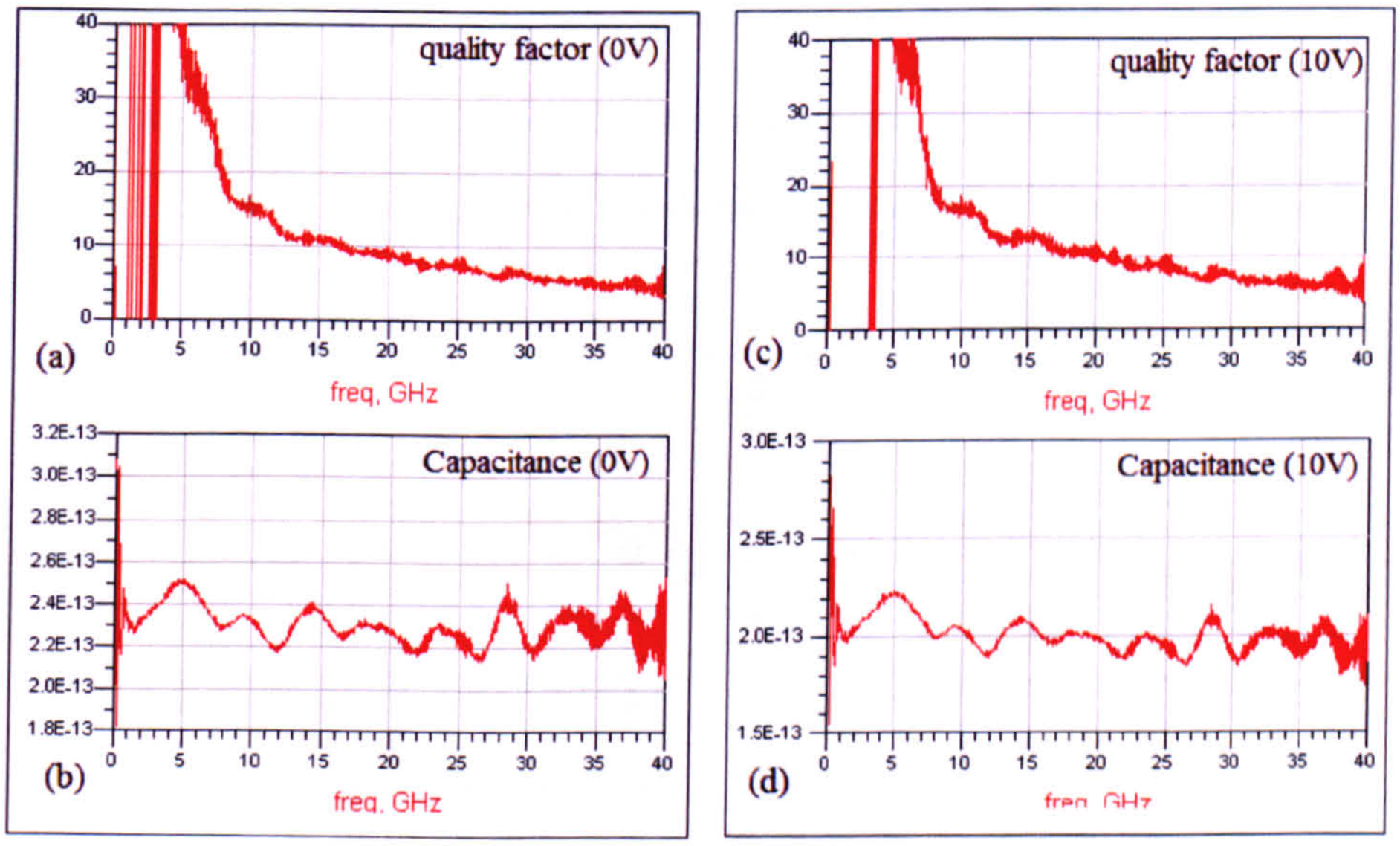

Quality factor and capacitance (in F) of the actual capacitor at 0V

Quality factor and capacitance (in F) of the actual capacitor at 10V

Figure 5.44 (a) and (c) quality factors of the MIM capacitor under 0 and 10V (556kV/cm); (b) and (d) De-embedded capacitance at 0V and 10V (556kV/cm).

In figure 5.44 (a) and (c), the quality factors of the capacitor are unrealistic below 7GHz. This is caused by the same reason that is described early in step (2) where the size of MIM capacitor is too small so that its impedance ($\frac{1}{j\omega C_{int}}$) is infinitely large at lower GHz. Therefore, the measured capacitor behaves like an open circuit. A small measurement error can affect the measured results significantly. Hence, the measured results below 7GHz are corrupted. Once the frequency increases to 10GHz or above, the values of the quality factors gradually decreases as a function of frequency. In contrast with the quality factors, the measured capacitances are independent of the frequency. According to figure 5.44, the quality factor and capacitance of the actual capacitor are 15 and 0.23pF at 10GHz when the applying DC voltage is not present. With an applied DC voltage of 10V or 556KV/cm, the capacitor's quality factor increases to 17 and its capacitance drops to 0.20 pF at 10GHz.

The thin film's dielectric constant is mathematically related to the intrinsic capacitance as: $\varepsilon_r = \frac{C_{int}\, d}{A\varepsilon_o}$ where A is the capacitor's actual area, d is the film thickness and C_{int} is the calculated intrinsic capacitance. The dielectric constants of the thin film at 0V and 10V calculated in this way are shown in figure 5.45(a) and (b).

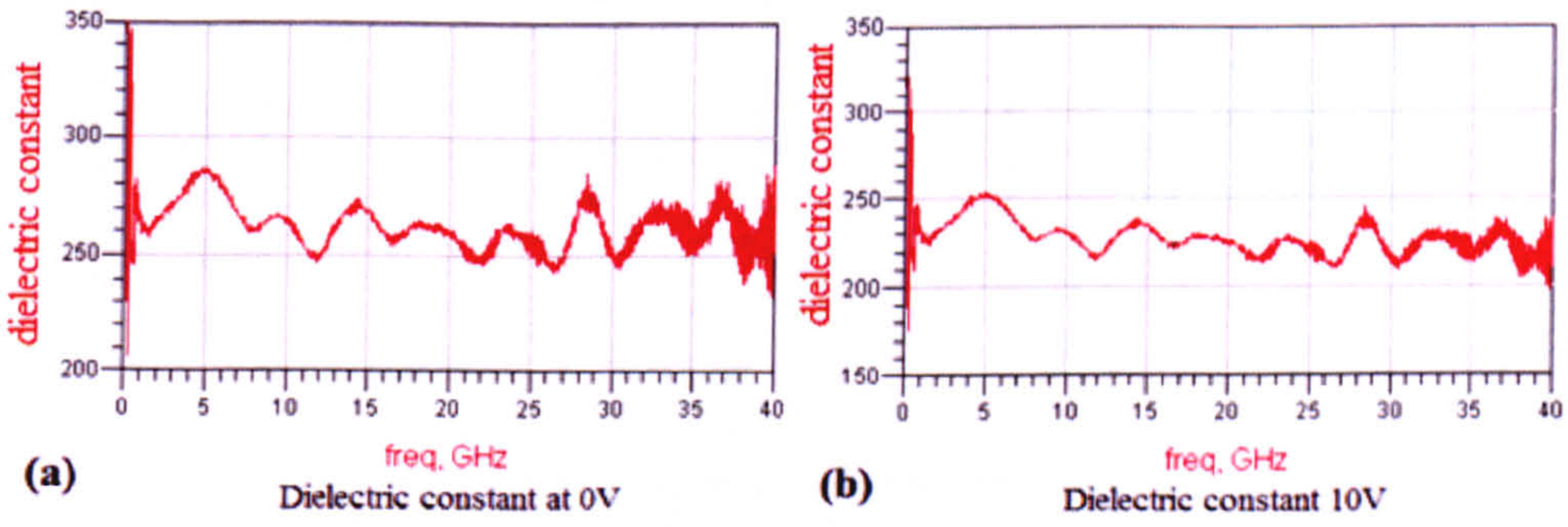

Figure 5.45 dielectric constant of the BST thin film under (a) 0V and (b) 10V

According to the above figure, the dielectric constants of the obtained BST thin film are 257 (0V) and 220 (10V) respectively at 10GHz. (**Deleted because there is no proof for it)** In other words, a dielectric tunability of 14% has been achieved with an applied DC voltage of 10V at 10GHz. Here the tunability is defined as $(Tunability = \frac{\varepsilon_r(0V)-\varepsilon_r(10V)}{\varepsilon_r(0V)})$.

To demonstrate the dielectric tunability of the thin film, figure 5.46 shows the variations of dielectric constant and tunability with respect to different DC tuning voltages (0V, 3V 5V, 8V and 10V). As mentioned in section 4.2, the misalignment of the photmask could result in a reduction of capacitor size from $100um^2$to $70um^2$(a 30% reduction of capacitor size). According to equation 5.65, a decrease in capacitor size (A) by 30% could also lead to an overestimation of the dielectric constant of BST thin film by 30%. In figure 5.46, several error bars have been employed to indicate the maximum possible errors (30%) in the measured dielectric constants at different DC voltages.

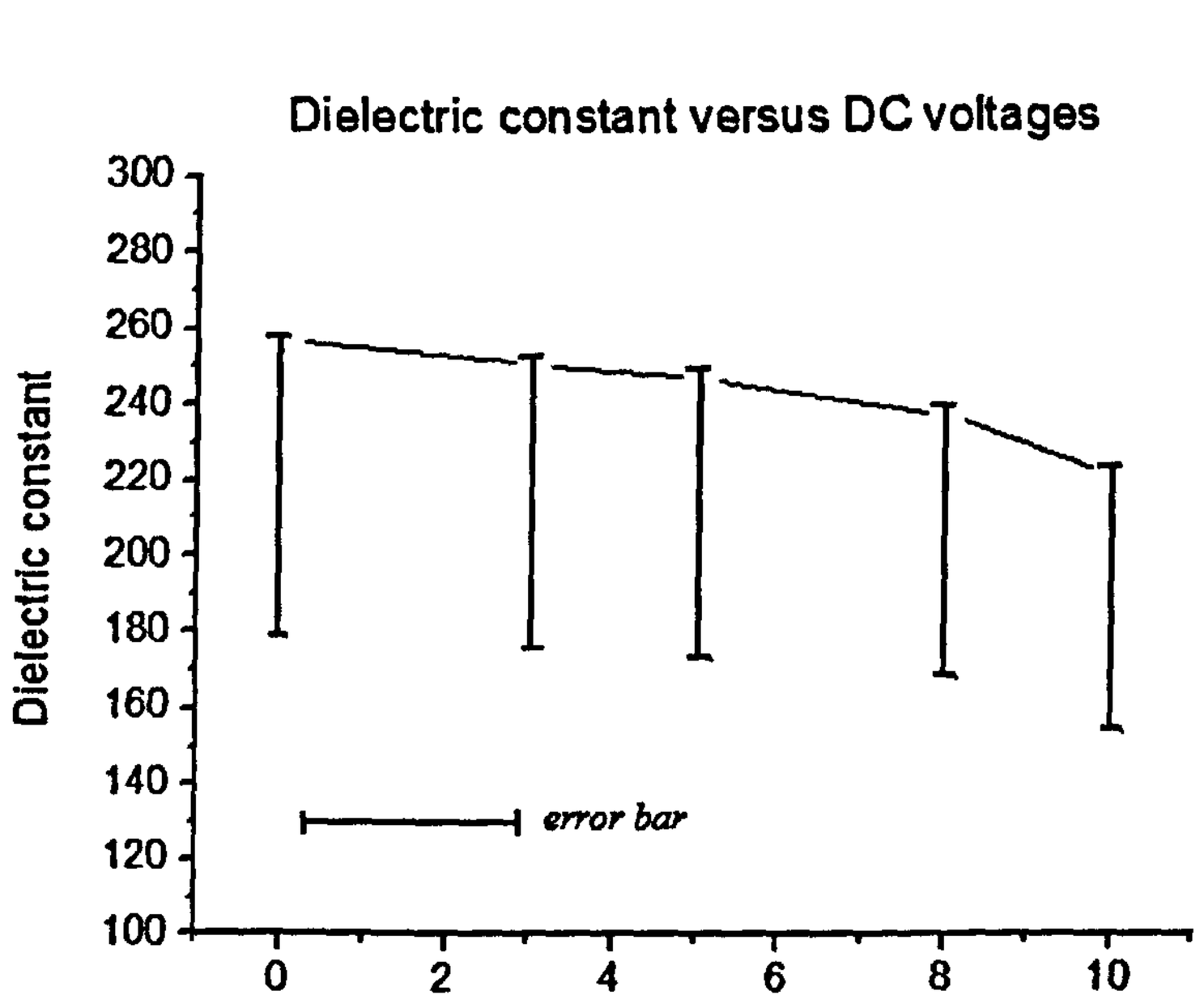

Figure 5.46: Dielectric tunability (in percentage) versus applied voltage from 0 to 10V

At lower frequencies, the thin film's dielectric loss tangent can be roughly estimated as: $\tan\delta_r = 1/Q_{int}$. Figure 5.47 shows the estimated loss tangent of the thin film versus frequency. From this figure, the estimated dielectric loss tangents are 0.075 (0V) and 0.06 (10V) at 10 GHz. At frequencies below 4 GHz, the loss tangent is unrealistically low (less than 0). This is caused by the errors of measurement at lower GHz frequency due to the small size of the capacitor.

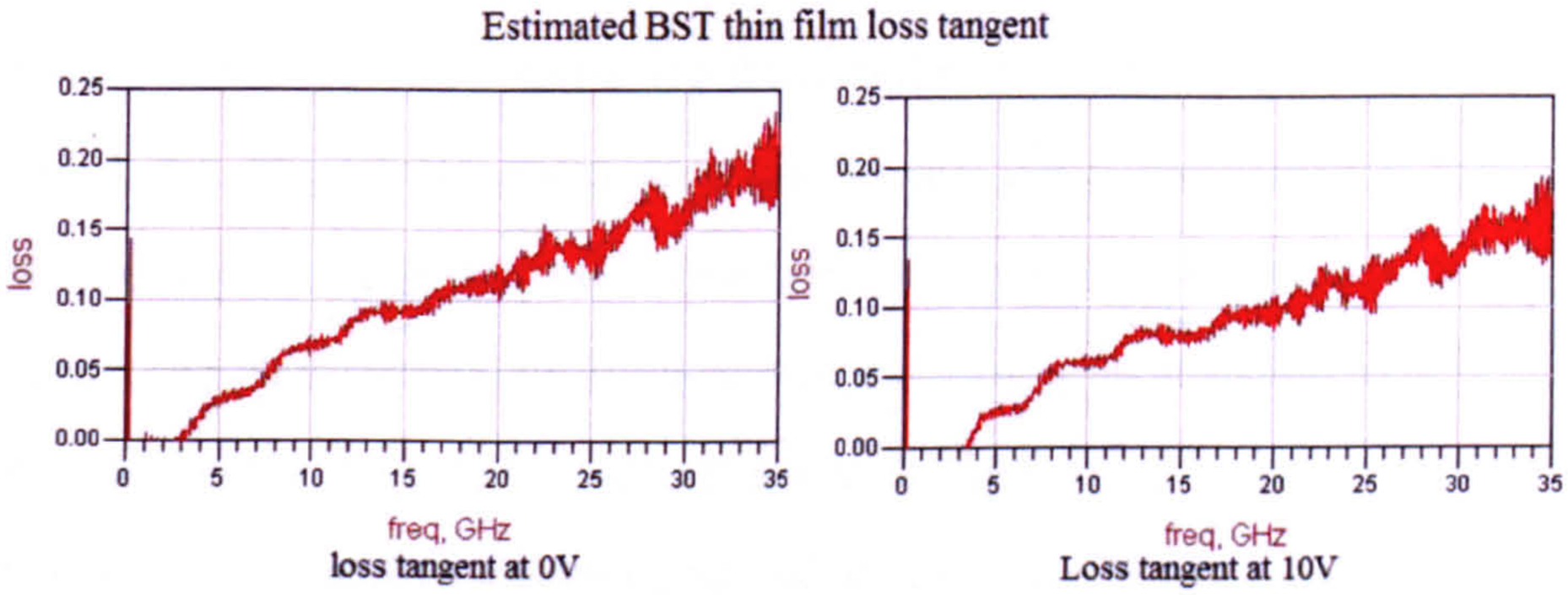

Figure 5.47 Estimated dielectric loss tangent of BST thin film

5.3.5 Conclusion of the capacitor method

In section 5.3, the process of capacitor characterization method has been discussed. An example of BST thin film characterized by this method is also presented. The measured dielectric constant and loss tangent of the BST thin film are 256 (0V) and 0.075 (0V) at 10GHz. The measured results are comparable to the values (260 and 0.07 at 10GHz under0V) given by a similar report which focused on multilayer BST thin film **[18].** The relatively low quality factor (15 at 10GHz) of the actual capacitor is caused by the Ohmic loss due to the thickness of metal electrodes. The obtained dielectric tunability (14%) is not good. This may be caused by two reasons, One: relatively lower annealing temperature at 700^o and very short annealing period of just 10min, Two: film thickness smaller than 180nm which was shown to resulted in a reduction of tunabilities **[19].** In general, the measured results are in agreement with

the previous work. To enhance the capacitance tunability, the thickness of the measured thin films were increased to 300 nm in chapter 8.

5.4 Conclusion of the work

In this work, two different methods (MIM capacitor and CPW) were selected to characterize the dielectric constant and dielectric loss of the thin films. In CPW method, the measured dielectric constant and dielectric loss are very similar to the previous report given by *Lue* and *Tsceng* **[10]**. The accuracy of the measurement depends only on the phase shift. The most accurate measurement results occurred at 90^o phase shift or $(2n \times 360^o + 90^o)$. Therefore, the CPW method is suited for the measurement of high GHz dielectric properties of thin film. The main drawback of the CPW method is that the tuning electric field is limited by the gap of the CPW.

In the present experiment, the maximum DC tuning voltage is limited to 30V and the gap of the CPW is 20um, the maximum allowed tuning electric field is only 15kV/cm which induced a very small dielectric tunability in the BST thin film. (deleted because the dielectric properties of the thin film has been successfully characterized).

This problem can be solved by using capacitor method since a very large tuning electric field can be built within an MIM capacitor. For an 180nm thick thin film and 10V DC voltage, the maximum tuning field is 556kV/cm. The BST dielectric constant measured using the capacitor method is slightly higher than the value reported by the CPW method. According to the measured results, the dielectric loss of BST thin film almost increases linearly as the frequency goes up. This is an

overestimation of dielectric loss due to the overestimation of overall capacitor microwave loss. The overestimated microwave loss is attributed to the thin metal electrodes of MIM capacitor which induced large Ohmic loss.

Another reason for the overestimation of dielectric loss is MIM capacitor's "equivalent circuit model". This model is an arbitrary mathematical model which is only reliable at low frequency measurement (several GHz). The errors of the model accumulated as the frequency goes higher. Therefore, capacitor characterization method should only be applied to measure the properties of BST thin film at lower GHz frequency. Both CPW and capacitor methods have their advantages and disadvantages. The choice of using which characterization method depends on the specification and requirement of the work. In this case, BST thin films were measured using CPW method, because it shows high dielectric tunability which can be tuned by applying a relatively low DC electric field. In contrast, pyrochlore BZN thin films were characterized using both CPW and MIM capacitor methods, since its dielectric tunability is lower than the BST thin film. The measured dielectric results are presented in chapter 6 and 7.

References:

[1]. L.F.Chen, C.K.Ong, C.P. Neo, V.V Varadan and V.K. Varadan, *Microwave electronics measurement and materials characterization*, John Wiley & Sons, Ltd, 2004.

[2]. G.H.Bryant, *Principles of Mircrowave Measurements*, Peter Peregrinuts Ltd, Revised Edition,1993.

[3]. A. J. Baden Fulle, *Microwaves: An introduction to microwave theory and techniques*, Wiley& Sons Australia, Limited, 1990.

[4]. Sinnema, W., *Electronic Transmission Technology Lines , waves , and antennas 2nd edition*: Prentice-Hall, 1979.

[5]. R.N.Simons, *Coplanar Waveguide Circuits, Components, and Systems*, John wiley & Son, Ltd, 2000.

[6]. M.J. Lancaster, J.Powell and A.Porch, "Thin-film ferroelectric microwave devices, *Supercond. Sci. Technol,* vol.11, 1323-1334, 1998.

[7]. Z.Y.Wang, J.S.Liu and L.T.Liu, "Permittivity Measurement of $Ba_{0.5}Sr_{0.5}TiO_3$Ferroelectric thin films on multilayered silicon substrate" *IEEE Trans on Instrumentation and Measurement*, vol.55, 1: 350-356, 2006.

[8]. C. Weil, P. Wang, H. Downar and J. Wenger, "Tunable coplanar waveguide phase shifters using ferroelectric thick films", Intitut fur Hochfrequenztechnik-TUD, 83-88, 2002.

[9]. C.L. Holloway and E.F. Kuester, " A quasi-closed form expression for the conductor loss of CPW lines , with an investigation of edge shape effects", *IEEE Trans Microwave Theory and Techniques*, vol. 42, 12, 2695-2701, 1995

[10]. T.Y.Tsceng and H.T.Lue, *et al*, "Application of on-wafer TRL calibration on the measurement of microwave properties of $Ba_{0.5}Sr_{0.5}TiO_3$ films". *IEEE Trans Ultrasonics, Ferroelectrics, and Frequency Control*, vol. 48, 6, 1640-1646, 2001.

[11]. D. M. Pozar, *Microwave Engineering 3rd*, John Wiley & Sons, Inc, 2005.

[12] F. John, A. Carl and S.Donald, "Low-frequency dielectric constants of α-quartz, sapphire, MgF_2, and MgO", *J. Appl. Phys,* vol. 45, 7, 2852-2854, 1974.

[13]. M. W. Cole, P.C.Joshi and M.H.Ervin, "La doped $Ba_xSr_{1-x}TiO_3$ thin films for tunable device applications". *J. Appl. Phys,* vol. 89, 11, 6336-6340, 2001.

[14]. F. M Pontes, E. R. Leite, E. J.H.Lee and J.A.Varela, "Preparation, microstrucutre and electrical characterization of $SrTiO_3$ thin films prepared by chemical route". *Journal of the European Ceramic Society,* vol. 21, 3, 419-426, 2001.

[15]. K. T. Kim and C. I. Kim, "Electrical and dielectric properties of Ce-doped $(Ba_{0.6}Sr_{0.4})TiO_3$ thin films". *Surface Coatings Techniques*, vol. 200,16-17, 4708-4712, 2006.

[16]. S. G. Yoon and A. Safari, "$Ba_{0.5}Sr_{0.5}TiO_3$ thin film preparation by r.f magnetron sputtering and its electric properties". *Thin Solid Films, vol.* 254, 211-215,1995.

[17]. C.H. Huang, M. Y. Yang, A, Chin, *et al*, "High density RF MIM capaciotrs using high k AlTaOx dielectrics". *Microwave Symposium Digest, IEEE MTT-S International*, 507-51,2003.

[18]. C.V.Weiss, M.B.Okatan and R.C.Tooneon, "Compositionally graded ferroelectric multilayers for frequency agile tunable devices". *J Mater Sci.* vol. 44, 19, 5356-5377, 2009.

[19]. J. Bellotti, E. K. Akdogan, A. Safari, W. Chang and S. Kirchoefer, "Tunable Dielectric Properties of BST Thin Films for RF/MW Passive Components", *Integrated Ferroelectrics,* vol. 49, 1, 113-122, 2002.

Chapter 6: Improvement of the dielectric properties of the BST thin film

As mentioned in section 2.2.6, the dielectric loss of the BST thin film is too high to be used to implementing the tunable microwave devices. Therefore, BST thin films with composition of $Ba_{0.5}Sr_{0.5}Ti_{1.0}O_3$ were doped with different concentrations of Li and Co ions were deposited onto sapphire substrates. The effects of ion doping on BST materials are studied as a function of ion doping concentrations. The microstructure and crystal structures of the crystal thin films are studied by a range of different modern characterization instruments such as XRD, SEM, AFM, XPS and EDX. Furthermore, the dielectric properties of crystallized thin films are measured at microwave frequencies using a vector network analyzer (VNA).

As mentioned in chapters 3 and 4, the yield of the device fabrication process and the thin film synthesis is too low. Therefore, only one sample for each doping concentration has been characterized. The experimental procedure and characterized results of Co and Li doped BST thin films are given in sections 6.1 and 6.2.

6.1: Co doped BST thin films

6.1.1 Introduction

To study the effect of Co doping, $Ba_{0.5}Sr_{0.5}Ti_{1.0}O_3$thin films doped with 0 mol%, 0.25 mol%, 0.5 mol% and 1.0 mol% of Co ions (BSTC0, BSTC1, BSTC2, BSTC5)

were deposited on to a sapphire substrate by spin coating. The starting compounds for preparing the as-deposited precursor were barium acetate, strontium acetate, titanium isopropoxide and cobalt acetate. The organic compounds were dissolved into a mixed organic solvent of acetic acid and acetyle-acetate to form the organic solution. These

precursors were coated onto the sapphire substrates by a spin coating process and crystallized by a 800C°annealing process. The details of the deposition procedures are presented in chapter 3.

The element compositions of the doped BST thin films were analyzed by the EDX technique. Once the compositions of the thin films were confirmed, the sample's crystal structures could be studied by the XRD technique using a Siemens D500 X-ray diffractometer with a CuK_α radiation source, which has a wavelength of 1.5402$\dot{A}$. A Philips XL30 ESEM was utilized to investigate the microstructure of the thin film. The surface roughness of the thin film was obtained by using the Atomic Force Microscopic (AFM) technique.

The dielectric properties of the doped thin films were measured by using CPW methods (discussed in chapter 5). A TRL calibration process was used to remove the measurement errors caused by the RF probing pads. To achieve higher dielectric tunabilities, the thickness of the thin films was increased to nearly 300 nm and the gap of the CPW was reduced to 10um. The maximum tuning voltage was limited to 30V because of the VNA's internal DC block. As a result, the maximum tuning electric field was 30kV/cm.

6.1.2 Composition analysis

EDX analysis

In this work, two sample films (BSTC1 and BSTC5) were analyzed using the EDX technique. Figure 6.1 shows the detected EDX pattern of the BSTC5 thin film between 0keV and 7keV.

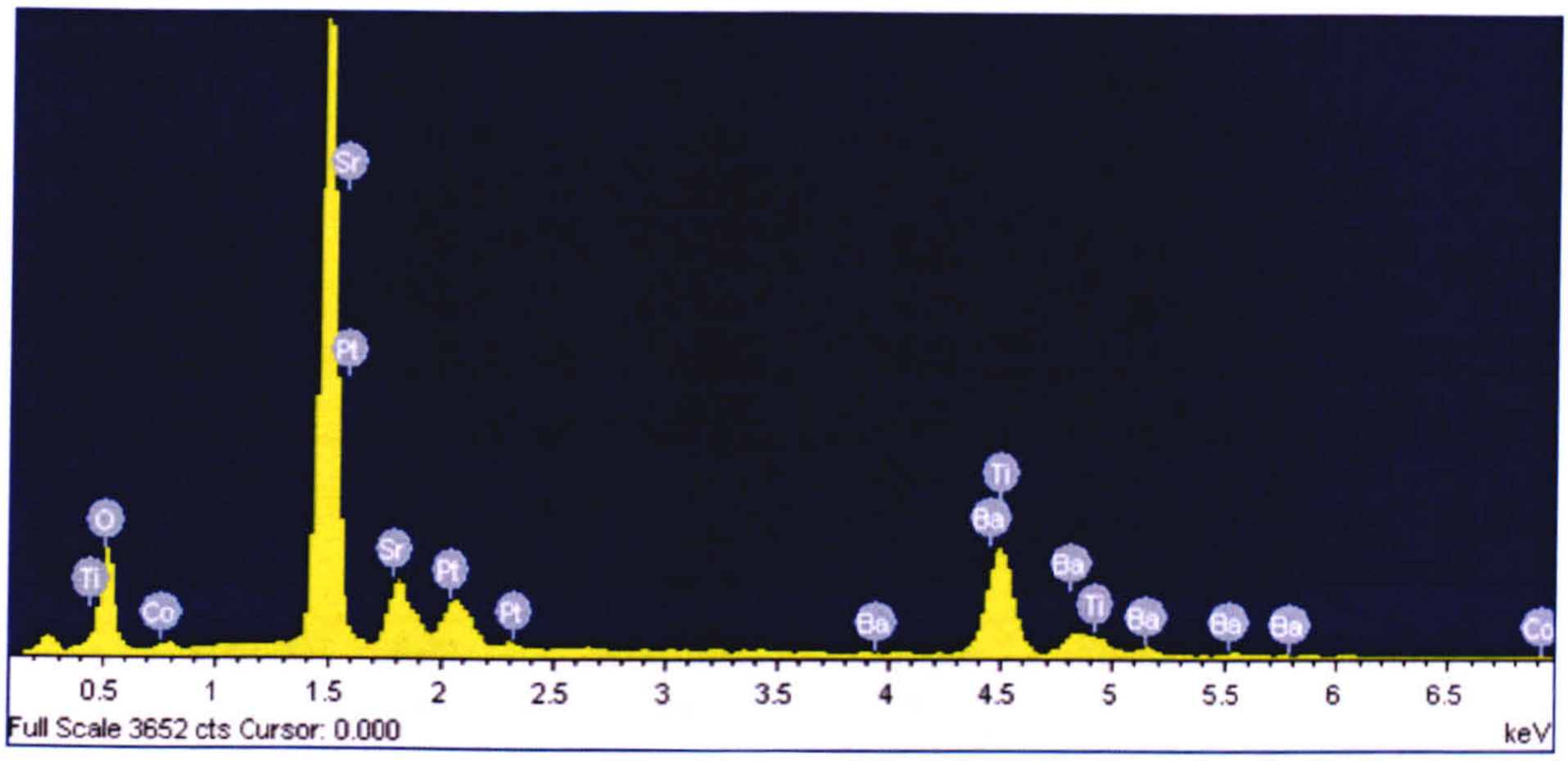

Figure 6.1: EDX pattern of BST thin film with 5mol% of Co

According to this pattern, the detected peaks of 3.9KeV, 4.4KeV, 4.8KeV, 5.2KeV; 1.5KeV, 1.8KeV and 0.4KeV, 4.5eV, 4.9KeVcorrespond to the Ba, Sr and Ti atoms in the BST thin film. Two weaker peaks are also detected at 6.9KeV and 0.75KeV, which indicate the existence of the doped Co atom. Since the EDX system was embedded into the Philips XL30 ESEM, a thin layer of Pt was also coated onto the sample surface to avoid the effect of electron charging. Thus, the detected peak at 1.5KeV also indicates the presence of Pt metal. The EDX technique can also be used to quantify the material's composition. Because two sample films (BSTC1 and BSTC5) were analyzed using EDX and therefore, an averaged results of the thin films' composition can be obtained. The quantified results of the Co doped BST thin film are given in table 6.1.

(a)

Element	App Conc.	Intensity Corrn.	Weight %	Weight% Sigma	Atomic%
O K	15.34	0.7021	40.12	1.42	79.29
Ti K	6.75	0.8980	13.80	0.68	9.11
Co Ti	0.25	0.8942	0.51	0.35	0.28
Sr L	5.48	0.7651	13.16	0.77	4.75
Ba L	9.15	0.8634	19.46	1.18	4.48
Pt M	4.79	0.6800	12.95	1.04	2.10
Total			100.0		

(b)

Element	App Conc.	Intensity Corrn.	Weight %	Weight% Sigma	Atomic%
O K	17.34	0.7448	46.55	1.46	83.40
Ti K	5.17	0.8826	11.70	0.66	7.00
Co Ti	0.03	0.8832	0.06	0.36	0.03
Sr L	5.40	0.7800	13.84	0.79	4.53
Ba L	6.47	0.8485	15.24	1.20	3.18
Pt M	4.29	0.6811	12.60	1.08	1.85
Total			100.0		

Table 6.1 the quantified results of EDX analysis of (a) BSTC5 and (b) BSTC1.

According to these tables, the average atomic ratio between Ba, Sr and Ti atoms are 1: 1.2: 2.0. The measured ratio is different to the desired atomic ratio (1:1:2) and the measured Co concentration is also smaller than the desired concentration of 5mol% in BSTC5.This is because the large penetration depth of X-ray beam (10μm) compared to the thickness of BST thin film which is only 300nm. The quantified results of the EDX analysis contain large errors. Therefore, this technique only provided a rough measurement of the composition of the material.

It is also shown that both samples have unexpectedly high concentrations of oxygen (79.29% and 83.40%) for BSTC1 and BSTC5. This is caused by the sapphire substrate (Al_2O_3) which contains large amount of oxygen atoms. Despite the problems, the results given by the EDX analysis have confirmed that the thin film contains the desired Ba, Sr and Ti ions. Meanwhile, a small percentage of Co ions have been doped into the thin film.

6.1.3 Crystal structure analysis

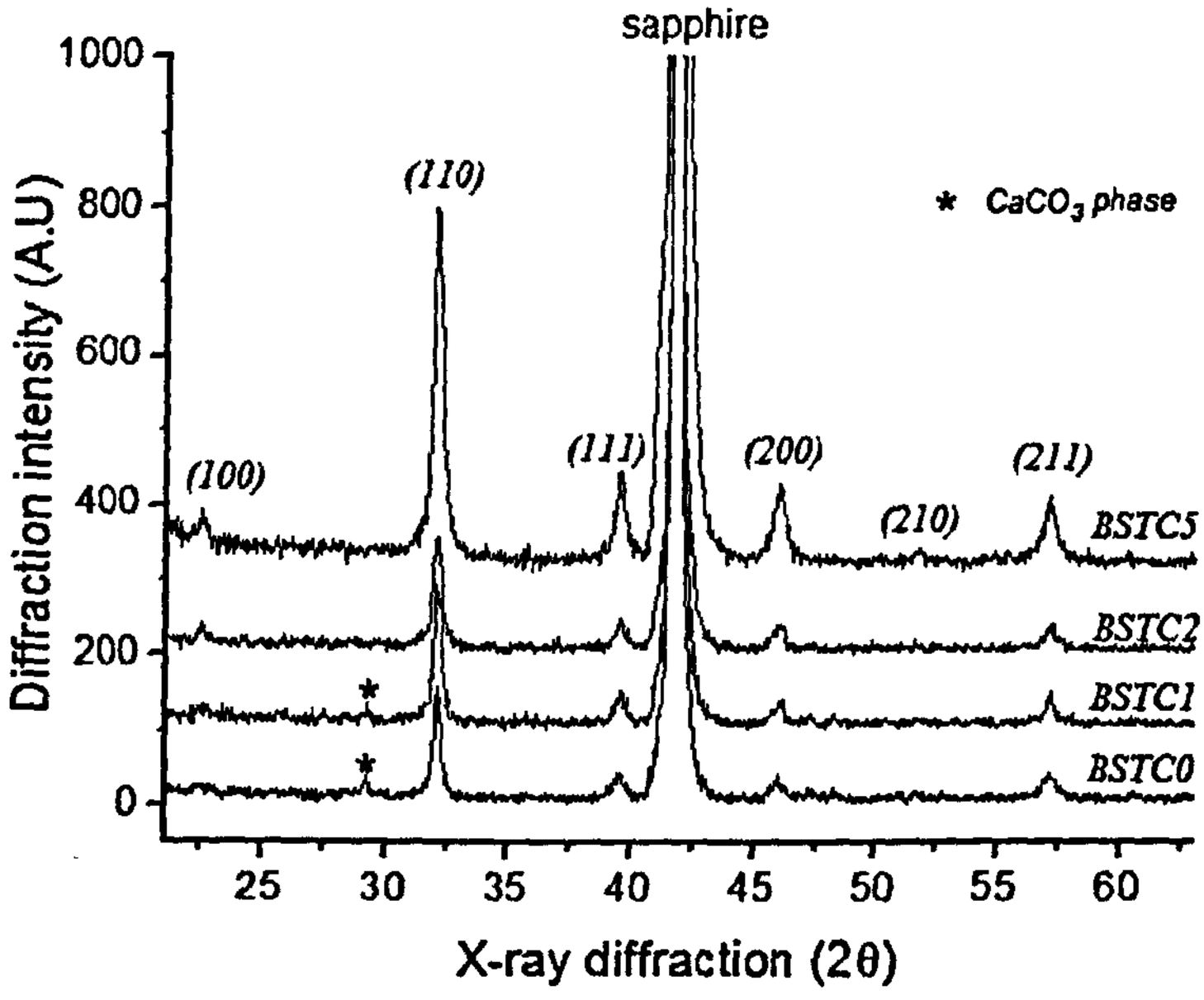

θ in degrees	*Intensity*	*h*	*k*	*l*
22.494	38	1	0	0
32.032	100	1	1	0
39.498	64	1	1	1
45.944	74	2	0	0
51.755	21	2	1	0
57.114	78	2	1	1
67.011	64	2	2	0
71.674	10	3	0	0
76.225	50	3	1	0
80.679	20	3	1	1
85.052	22	2	2	2
89.459	3	3	2	0
93.808	53	3	2	1
102.630	8	4	0	0
107.131	5	4	1	0
111.792	27	3	3	0
116.559	8	3	3	1
121.560	24	4	2	0
126.836	4	4	2	1
132.528	14	3	3	2

Figure 6.2: X-ray diffraction pattern of BSTC0, BSTC1, BSTC2 and BSTC5

The XRD patterns of $Ba_{0.5}Sr_{0.5}Ti_{1.0}O_3$ thin films doped with 0 mol%, 0.25 mol%, 0.5 mol%, 1.0 mol% of Co ions are shown in figure 6.2. The crystal orientations of the BST diffraction peaks are also illustrated in this figure. According to the JCPDS file (No: 00-039-1395), all of the BST thin films in figure 6.2 exhibits perovskite structure.

In the following sections, these samples will be referred to as BSTC0, BSTC1, BSTC2 and BSTC5. The thin films with 0.5 mol% (BSTC2) and 1.0 mol% (BSTC5) show a pure single cubic phase perovskite structure. However, both the undoped and 0.25 mol% Co doped BST films show a very weak secondary peak near 29°. The secondary phase is caused by the sample holder inside the XRD which contains Ca_2CO_3.

The intensities of the main (110) diffraction peaks vary slightly depending on the concentrations of Co in the BST films. The crystal orientation of the thin films was studied by using the orientation parameter α_{110}. The crystal (110)-orientation parameter α_{110}, was calculated from the heights of the (200), (110), and (111) diffraction peaks. Figure 6.3 shows the diffraction intensities of the three peaks.

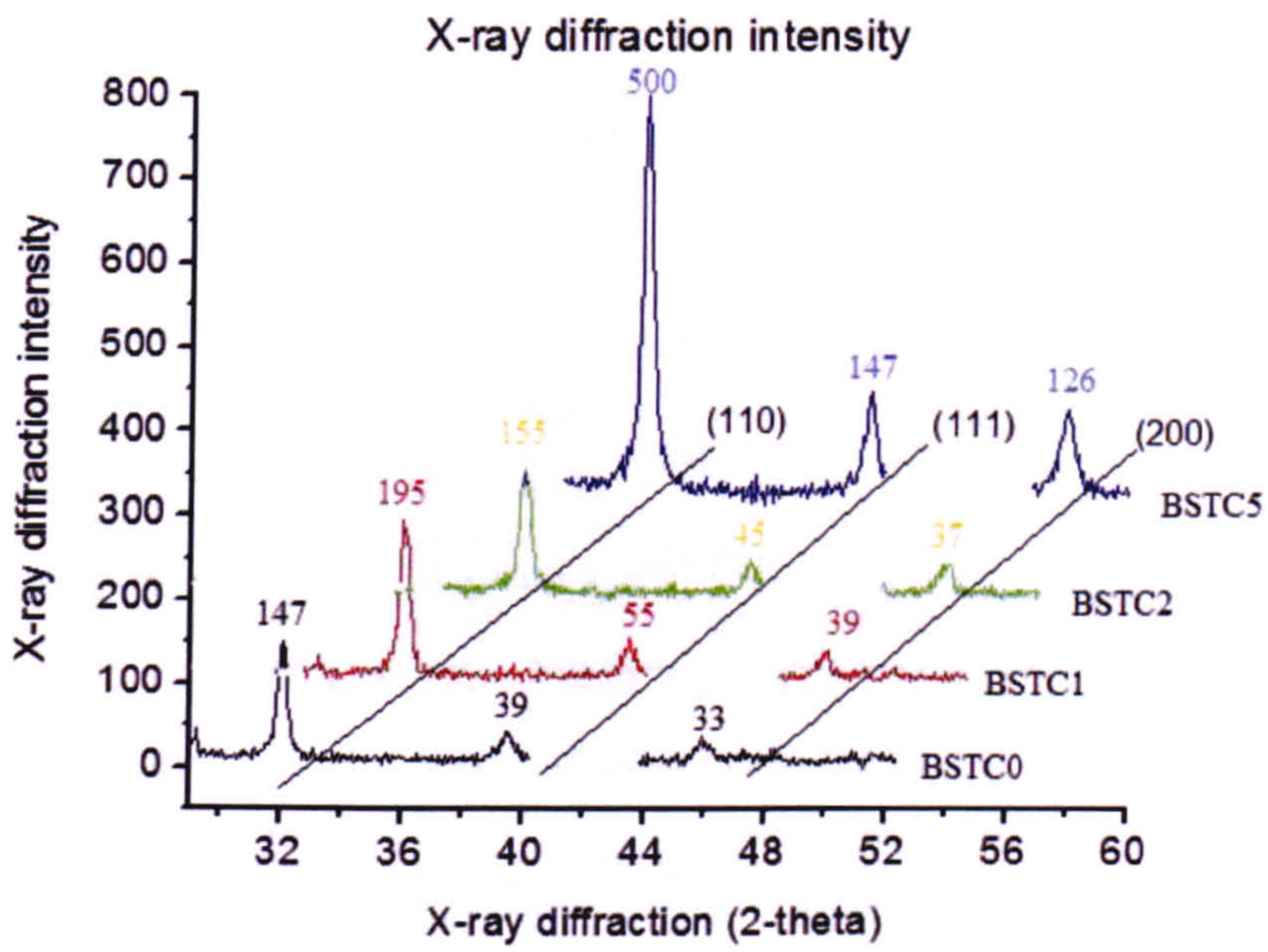

Figure 6.3: a comparison of diffraction peaks (110, 111 and 200) intensities

The mathematical equation to obtain the orientation parameter is expressed as: $\alpha_{110} = \frac{I_{110}}{(I_{110}+I_{200}+I_{111})}$ **[1, 2].** For samples such as BSTC0, BSTC1, BSTC2 and BSTC5, the obtained $\alpha_{110}$are 0.671, 0.674, 0.654 and 0.646 respectively. The results indicate that the crystallization and growth orientation of the thin films are not significantly influenced by the Co doping.

As mentioned in section 3.5.1, the grain size of the material can be calculated from the full width half maximum (FWHM) of the diffraction peaks using "Scheerer" equation. In this work, the FWHM were obtained from the (110) main diffraction peak of each thin film shown in figure 6.4. The measured FWHM were0.381°,

0.384°, 0.436° and 0.434° for BSTC0, BSTC1, BSTC2 and BSTC5 respectively. The mathematically calculated grain size were 37.2nm, 36.7nm, 29.8nm and 30.0nm for BSTC0, BSTC1, BSTC2 and BSTC5, respectively. The results indicate a decrease of grain size as Co concentration moved up from 0 mol% to 1.0 mol%.

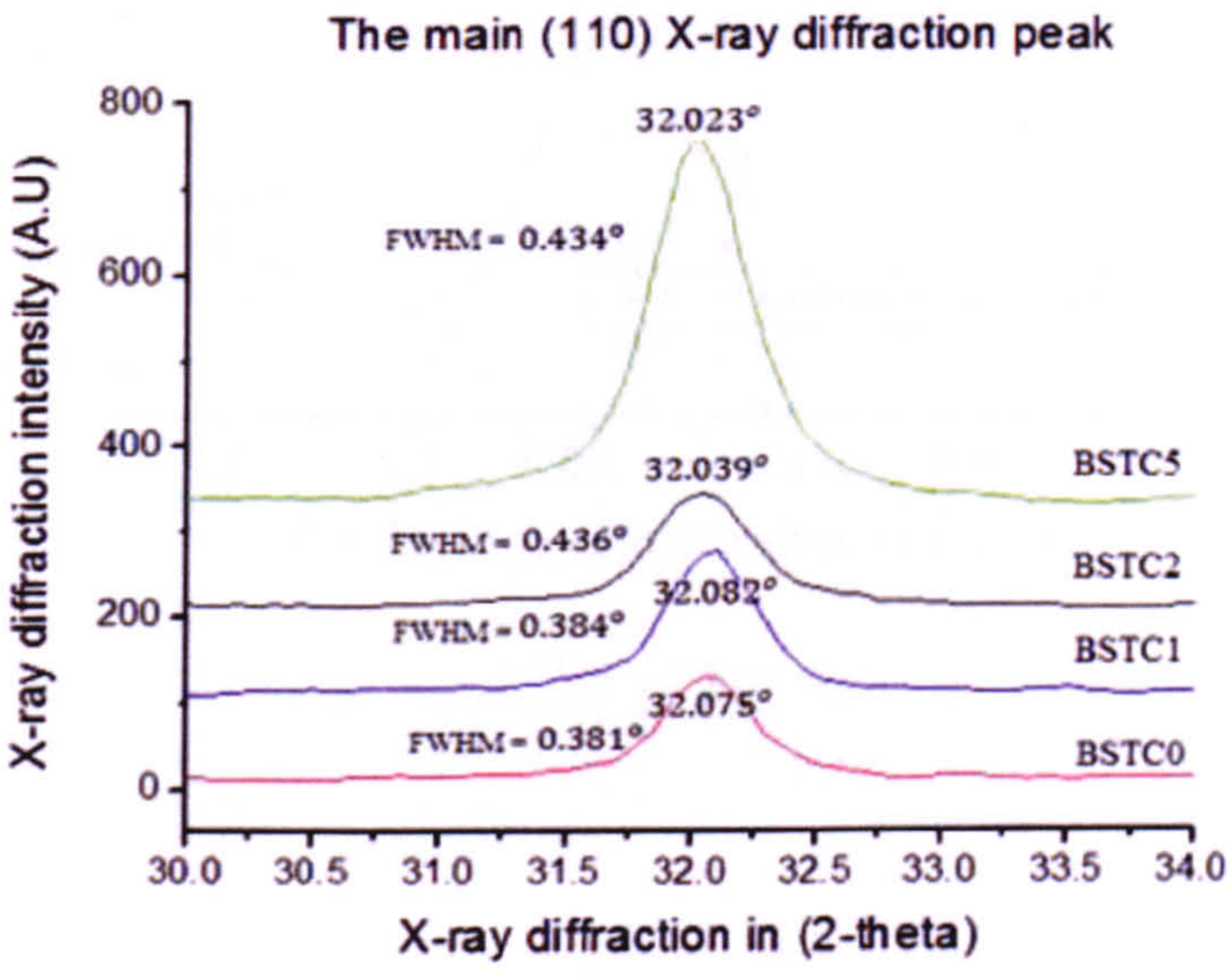

Figure 6.4 main diffraction peaks (110)

According to figure 6.4, the positions of (110) peaks depend on the Co concentrations in BST thin films. The in-plane *(a)* lattice parameters were calculated from the position of the main (110) diffraction peaks by using the "Bragg" equation. The in-plane lattice parameters are shown in figure 6.5 with respect to Co concentrations.

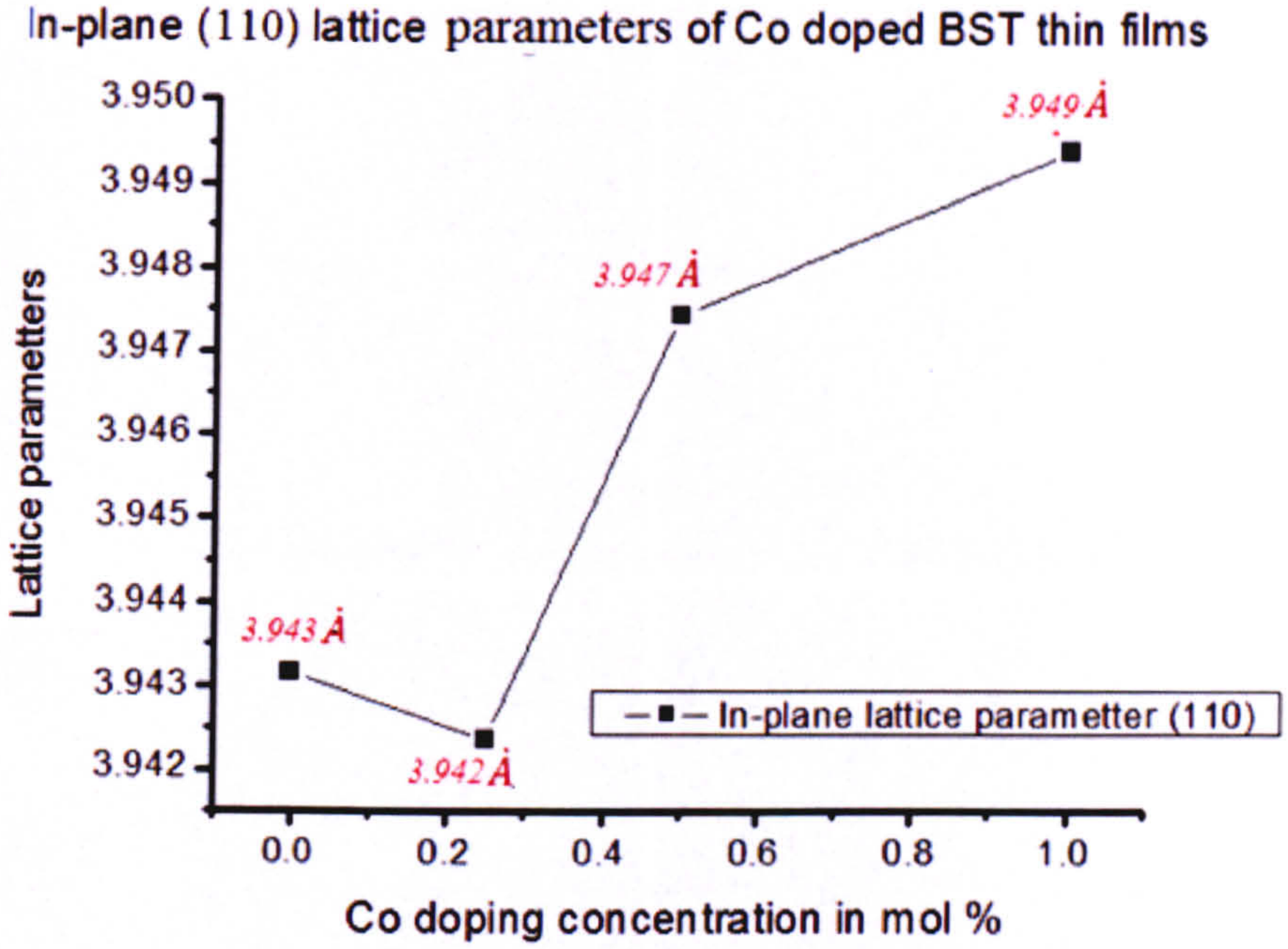

Figure 6.5 in-plane lattice parameters of BST thin films with respect to the concentrations of Co ions

As is shown, the in-plane lattice parameter measured from the main diffraction peak (110) changes slightly between 3.942 Å and 3.949 Å. The variation in the lattice parameters of BST thin films due to Co doping is small. This indicates that the Co^{3+} ion had substituted into the B site (Ti^{4+}) of the ABO_3 structure, because the radius of Co^{3+} (0.68Å) ion is very close to Ti^{4+} (0.63Å) ion. Therefore, the substitution of Co^{3+} ion in BST crystal does not result in a significant change in the lattice parameter of the crystal.

6.1.4 Microstructure and surface morphology

The microstructure, such as grain size and surface roughness, is the key factor that determines the dielectric properties of BST thin films. The SEM images of BSTC0, BSTC1, BSTC2 and BSTC5 are shown in Figures 6.6 (a), (b), (c) and (d) respectively

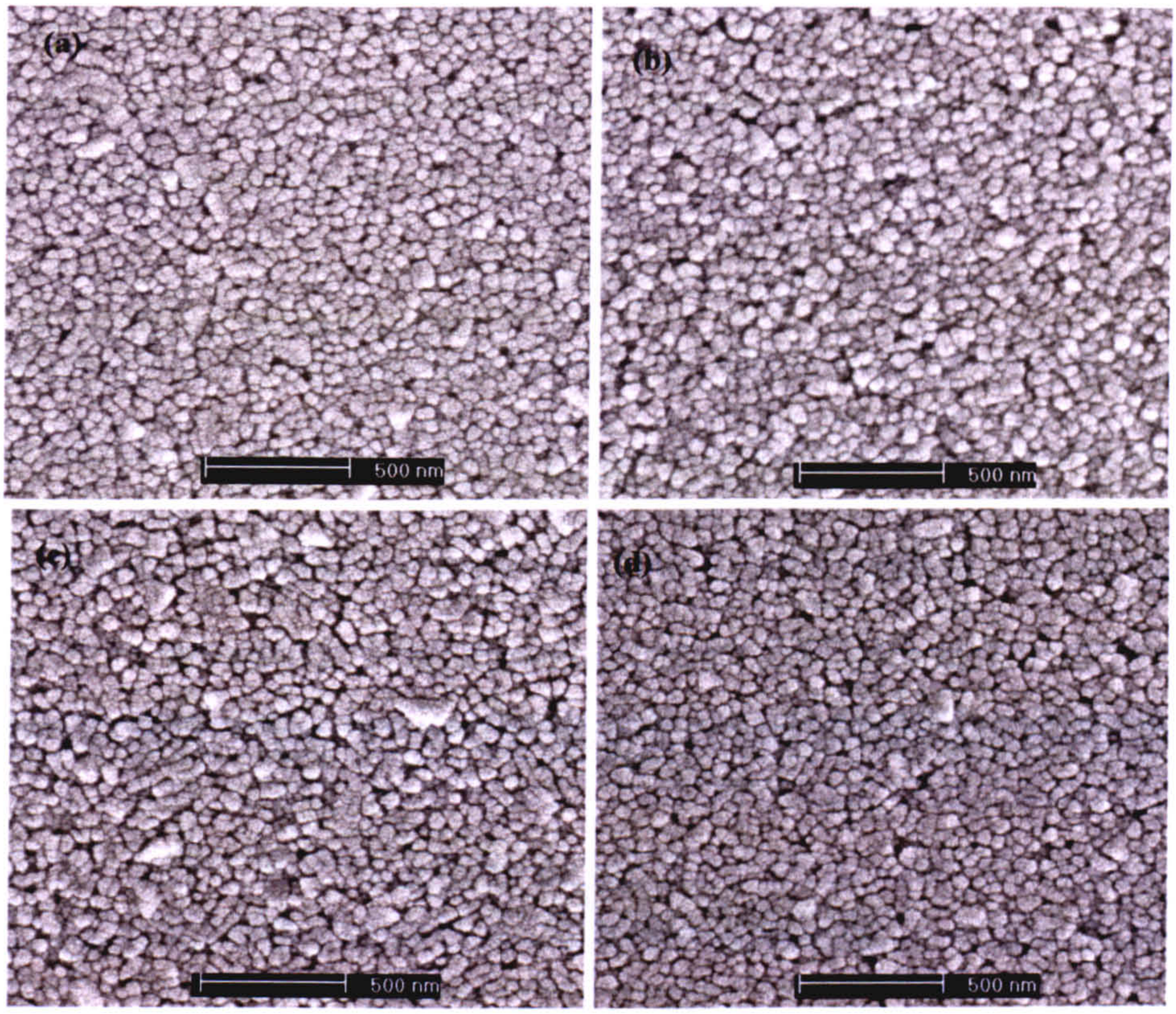

Figure 6.6 (a) (b) (c) and (d): SEM images of BSTC0, BSTC1, BSTC2 and BSTC5.

According to the images above, both the doped and un-doped BST thin films contain smooth, dense and well crystallized microstructures. No major voids or defects were observed on the thin films' surfaces. Figure 6.6 also shows that the films were composed of granular grains randomly distributed. Some of the large grains appearing on the thin films were actually clusters of small particles due to the high annealing process. The same effects were also reported in 2007 **[3]**. In general, the grain sizes for all BST thin films were nearly the same despite the Co doping.

6.1.5 Dielectric properties of Co doped BST thin films

The dielectric properties of BSTC0, BSTC1, BSTC2 and BSTC5 were characterized using the CPW method (chapter 5).To avoid the calibration errors, the thin films were usually measured when the CPW phase shift was between 20 and 160 degrees. Hence

the measured dielectric results below 4GHz are not shown in the figure. In this work, the dielectric properties of the thin film were measured from a 1500μm CPW with 10um gap and a track width of 20μm.

Measurement of dielectric constant

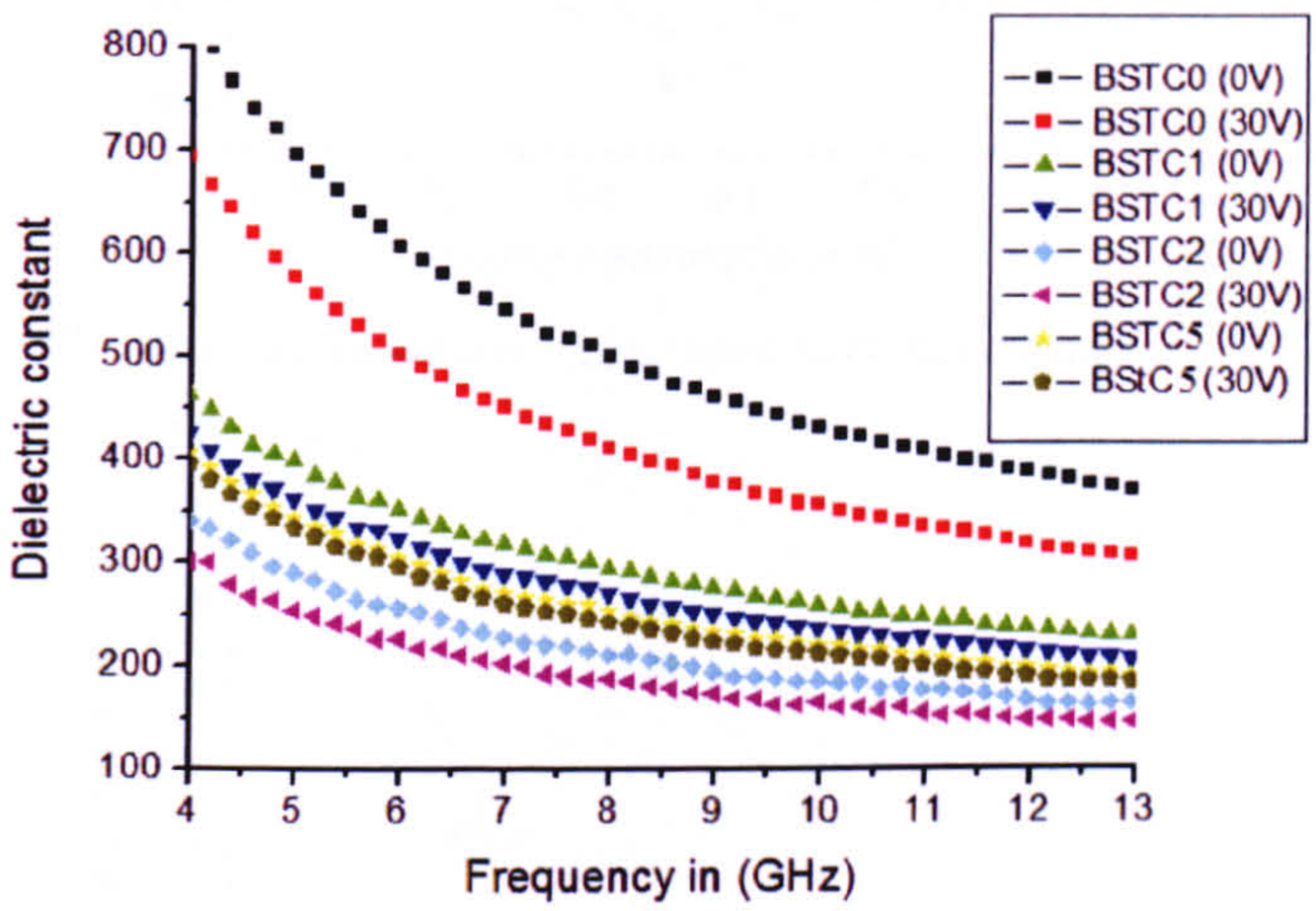

Figure 6.7: the dielectric constant of doped and undoped BST thin films between 4 and 13 GHz

Figure 6.7 shows the dielectric constants of BSTC0, BSTC1, BSTC2 and BSTC5 thin films between 4GHz and 13GHz under a tuning voltage of 0V or 30V (30kV/cm). In general, the dielectric constants of all doped thin films were lower than for the undoped BST. According to this figure, the dielectric constants of all thin films decreased as the frequency increased, until 10GHz where the phase shift of the CPW was near to 90 degrees. The variations of measured dielectric constants below10 GHz (<90 degrees) could be caused by the errors from TRL calibration or the natural dielectric relaxation **[4].** The thin films' dielectric constant and tunability were only compared when the CPW phase shift reached 90 degrees at 12GHz.

(a)

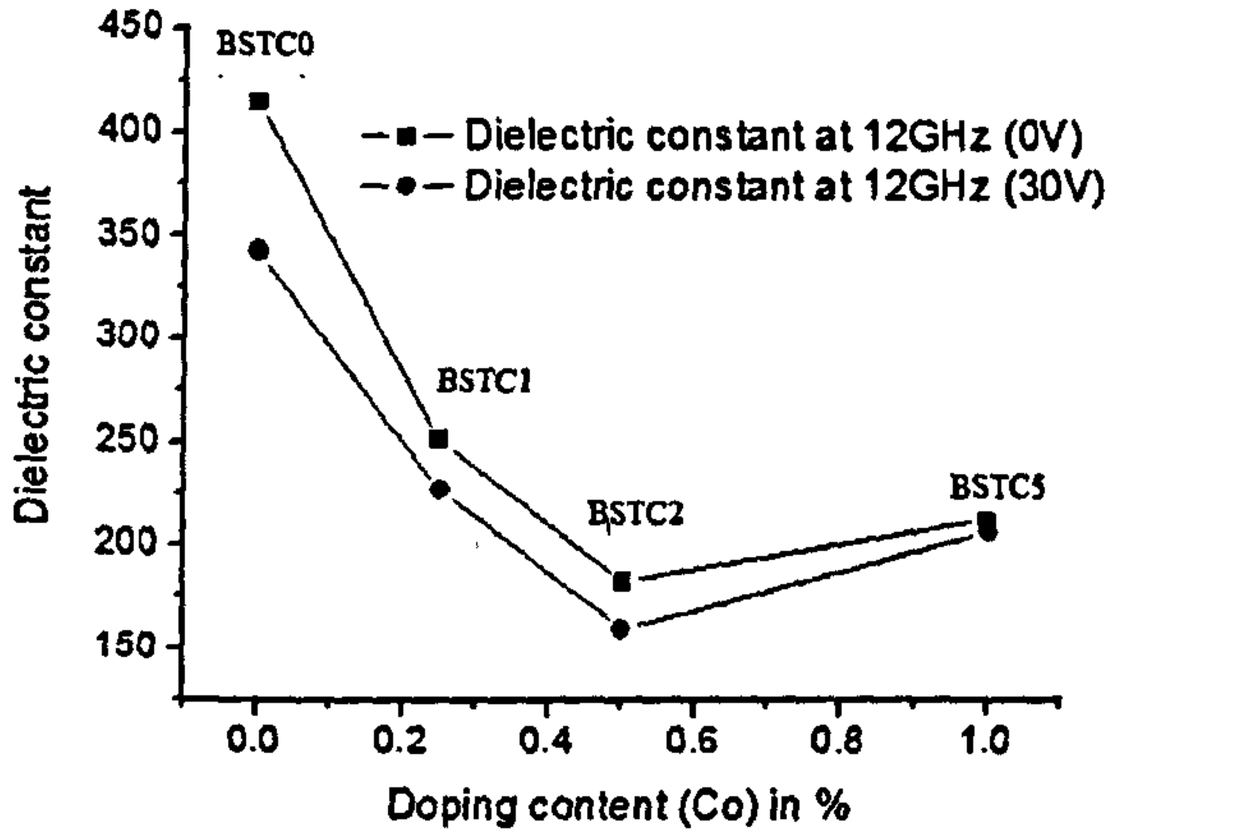

(b)

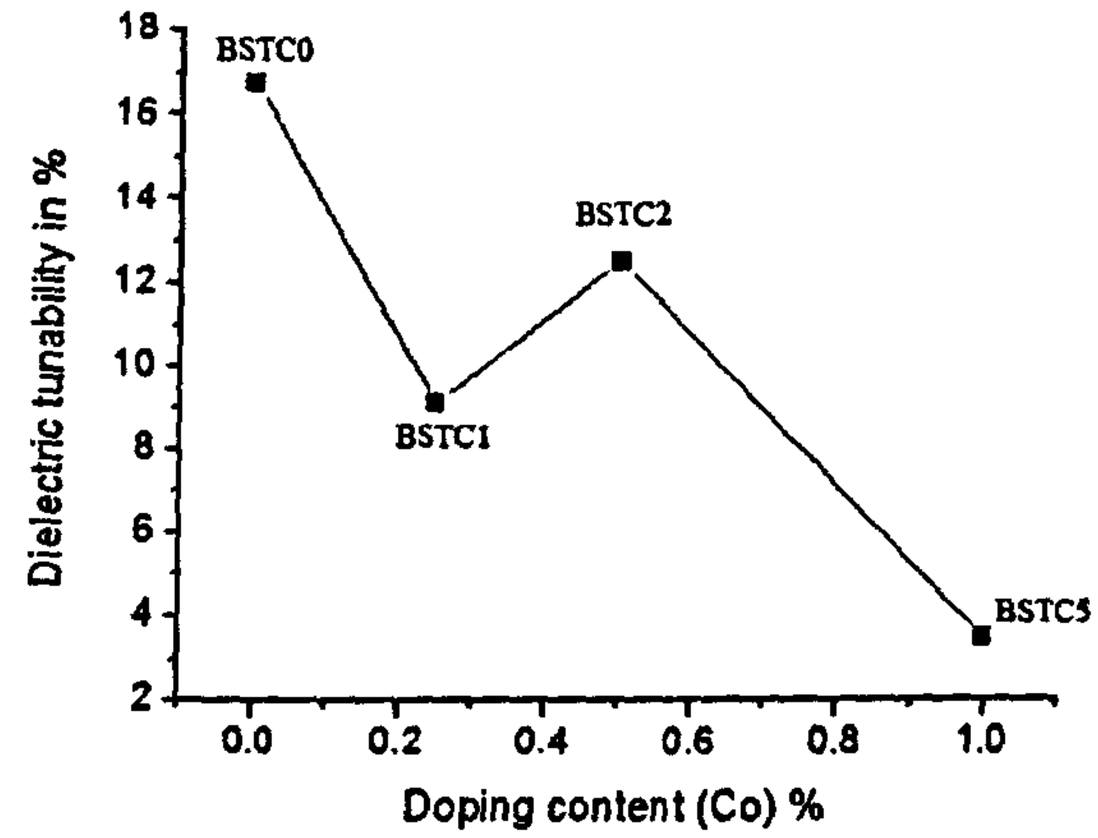

Figure 6.8 (a) Tunabilities of the thin films versus Co concentrations (b) dielectric constants of the BST thin films versus Co doping concentrations

Figure 6.8 (a) and (b) show the measured dielectric constants are 415 (0V) 343 (30V); 251 (0V) 227 (30V); 183 (0V) 160 (30V); and 212 (0V) 206 (30V) for BSTC0, BSTC1, BSTC2 and BSTC5, respectively. As mentioned in section 5.2, the measured dielectric constants of the thin films contain a maximum error of 24%.

In general, the doped BST films have lower dielectric constants than the undoped films. However, the dielectric constant does not decrease any further by doping with a higher concentration of Co. The thin film BSTC5 with 1mol% Co actually has a higher dielectric constant than the 0.5 mol% Co doped BST. In this work, the

dielectric tunabilites are defined as: $\frac{\varepsilon_{r(0V)}-\varepsilon_{r(30V)}}{\varepsilon_{r(0V)}}$. By applying the measured dielectric constant into this equation, the obtained dielectric tunabilites for BSTC0, BSTC1, BSTC2 and BSTC5 were 16.5%, 9.2%, 12.3% and 3.8% respectively.

Similar to the measured dielectric constant, the tunability also decreased as the concentration of Co increased. The decreases in tunability and dielectric constant are caused by (a): the reduction of grain size due to Co doping which leads to a smaller polarization in BST thin film **[5]**. (b): the substitution of Co ion in the B site of the BST crystal breaks the Ti-O chain which lowers the *Curie* temperature **[6]**. BST material with a lower *curie* temperature has smaller dielectric constant and tunability. Similar result has already been reported by previous works who studied the low frequency response of Co doped BST thin films **[7, 8]**.

Measurement of dielectric loss

The dielectric loss of BSTC0, BSTC1, BSTC2 and BSTC5 thin films between 4GHz and 14GHz are shown in figures 6.9(a). As can be seen, Co doped BST films have a significantly lower dielectric loss than the undoped BST material. The dielectric losses of the thin films measured at 12GHz (CPW phase shift is 90 degrees) are given in figure 7.9(b) for comparison.

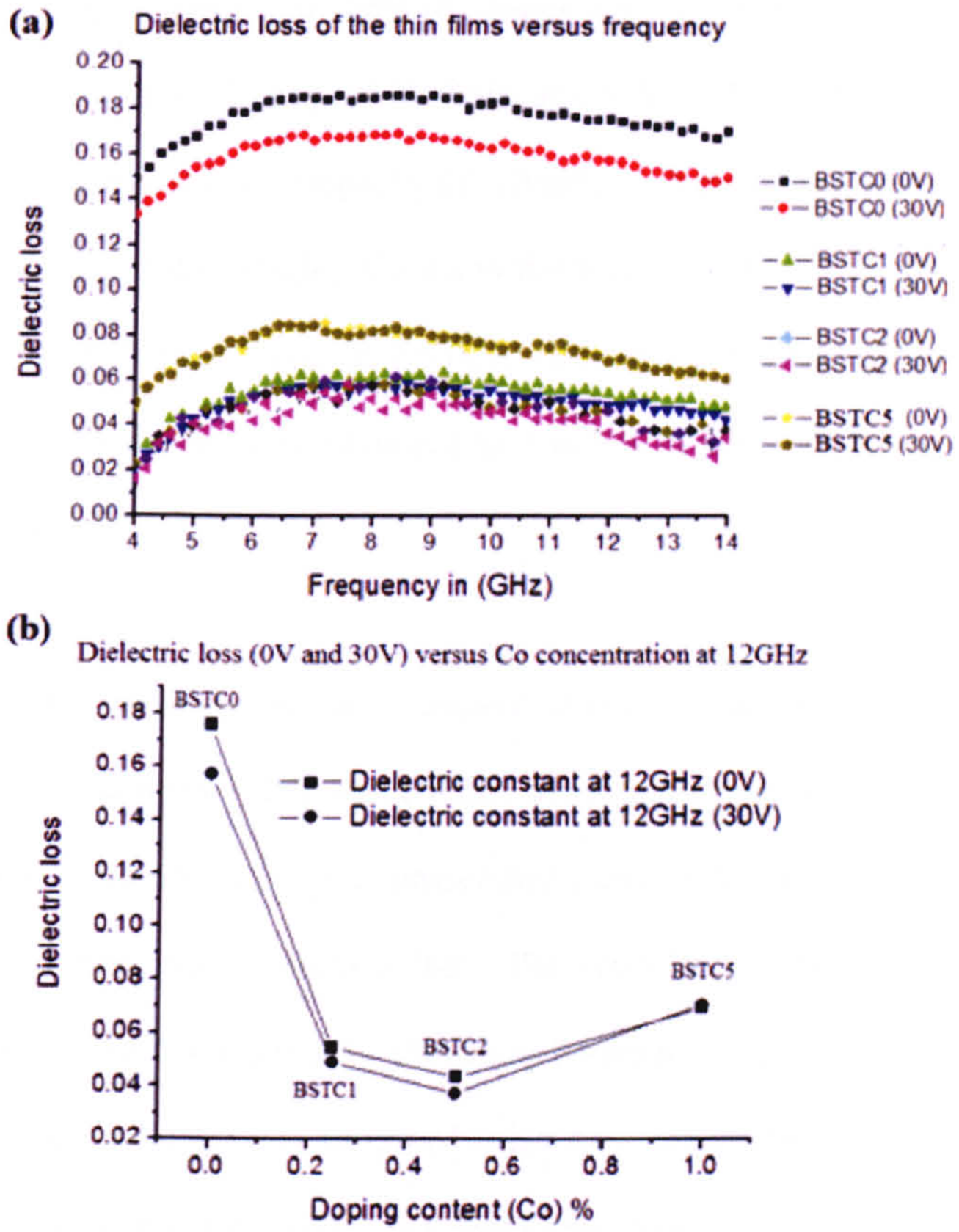

Figure 6.9 (a) tunabilities of the thin films versus Co concentrations (b) dielectric loss of the BST thin films (12GHz) versus Co doping concentrations (c) the error bars for the dielectric loss (between 7GHz and 14GHz) of the Co doped BST thin films at 0V

According to Figure 6.9(b), the dielectric losses were 0.176 (0V) 0.157 (30V), 0.054 (0V) 0.048 (30V), 0.0433 (0V) 0.038 (30V) and 0.069 (0V) 0.07 (30V) for BSTC0, BSTC1, BSTC2 and BSTC5 respectively. Clearly, a dramatic reduction of dielectric loss has been achieved by doping Co ion in the BST thin films. The lowest dielectric loss of 0.38 (30V) was found in BSTC2. Although the dielectric loss increased slightly when Co doping was increased to 1 mol%, it was still lower than for the undoped BST.

Meanwhile, the variations in the measured dielectric loss of the thin films are relatively small between 7GHz and 14GHz. This indicates a good TRL calibration. As mentioned in section 5.1.2, the measurement error is estimated by recording the minimum and maximum dielectric loss. The recorded minimum and maximum dielectric loss of the Co doped BST thin films between 7GHz (0V) and 14GHz (0V) are compared in figure 6.9 (c). An error bar has been used to indicate the error in the measured dielectric loss for each Co doped BST thin film.

Figure of Merit

An easier way to analyze the dielectric properties of thin film is to use the figure of merit (FOM). FOM is defined as $FOM = \frac{(Dielectric\ tunability\ in\ \%)}{Dielectric\ loss\ at\ 0V}$ where the tunability and dielectric loss are obtained from figures 6.9(a) and 6.9(b). The FOM of all thin films are compared in the following figure (6.10).

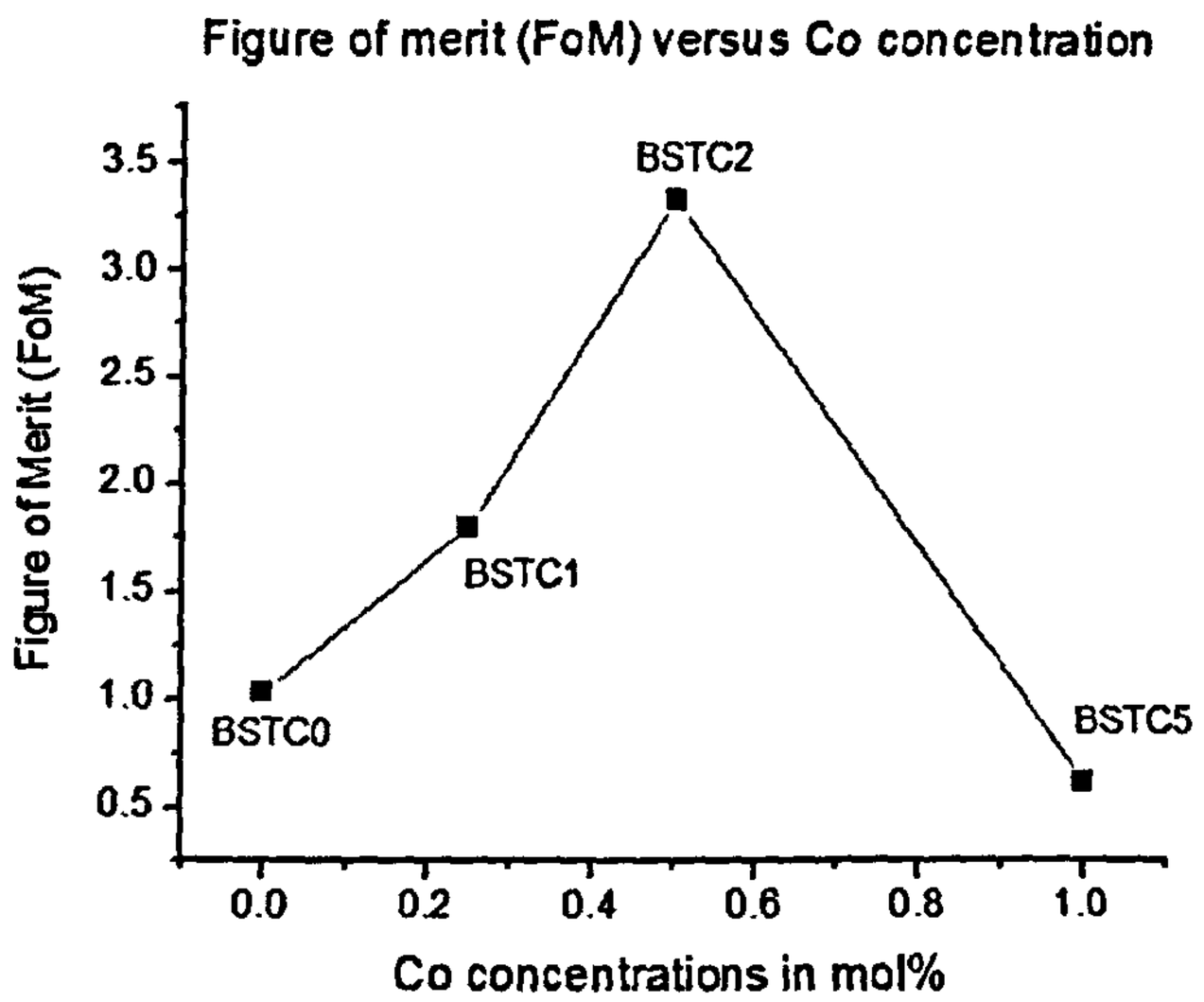

Figure 6.10: figure of merit (FoM) for thin films with different Co concentrations.

As can be seen, BSTC2 with 0.5mol% Co has the highest value of FoM = 3.3, which is three times higher than for the undoped BST. However, the smallest FoM was observed when1.0mol% of Co was doped into BST film. The decrease in FoM is mainly caused by the dramatic reduction in tunability. Because the small tuning electric field of just 30kV/cm resulted in lower tunability, the obtained FoM values were relatively small.

Measurement of leakage current

The leakage current of the thin films (BSTC0, BSTC1, BSTC2 and BSTC5) was measured as a function of DC voltages range from 0 to 30V (30kV/cm) with a step size of 2V (2kV/cm). The leakage current measured from the doped BST thin films is given in figure 6.11 which compares the leakage current of the doped BST thin films only.

(a) *Leakage current (Amp) versus tuning DC voltages*

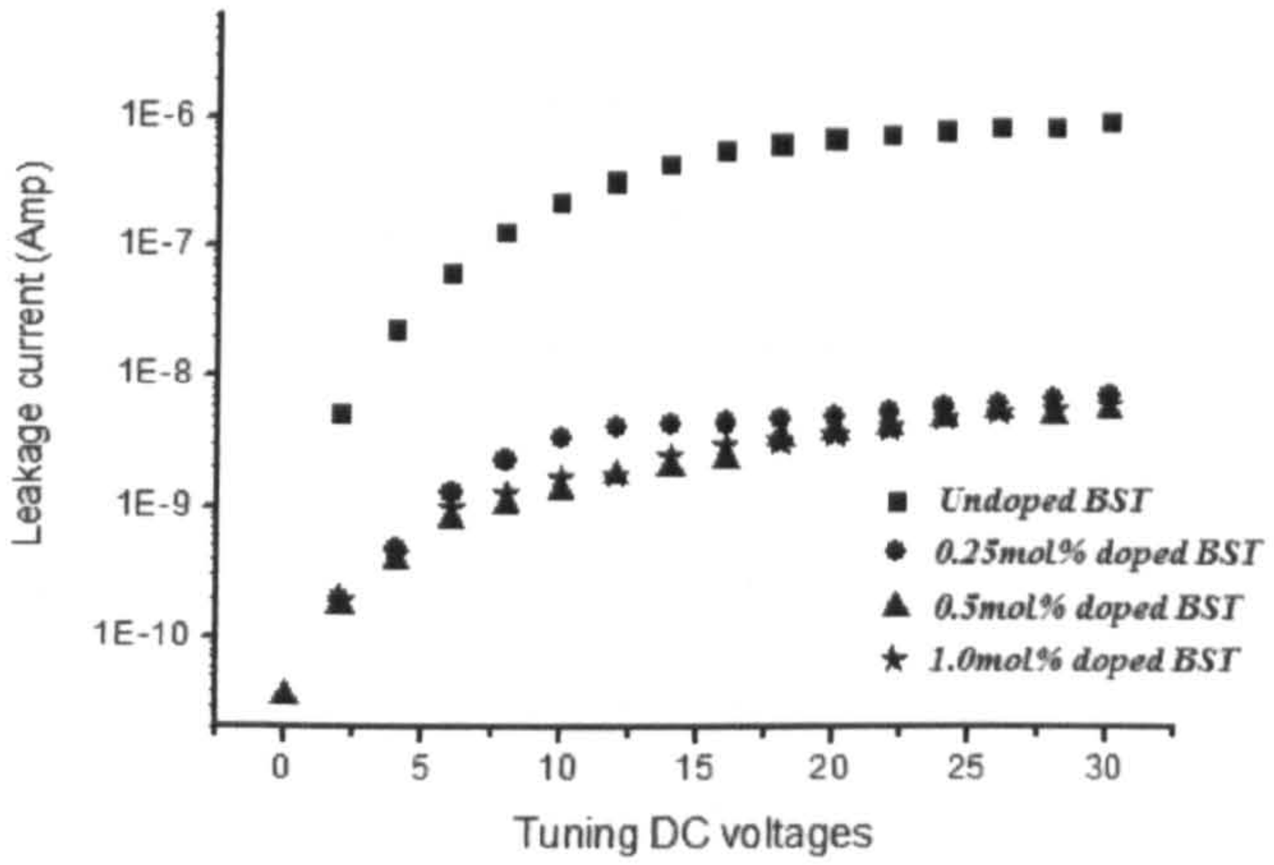

(b) *A close look of leakage current (Amp) versus tuning DC voltages*

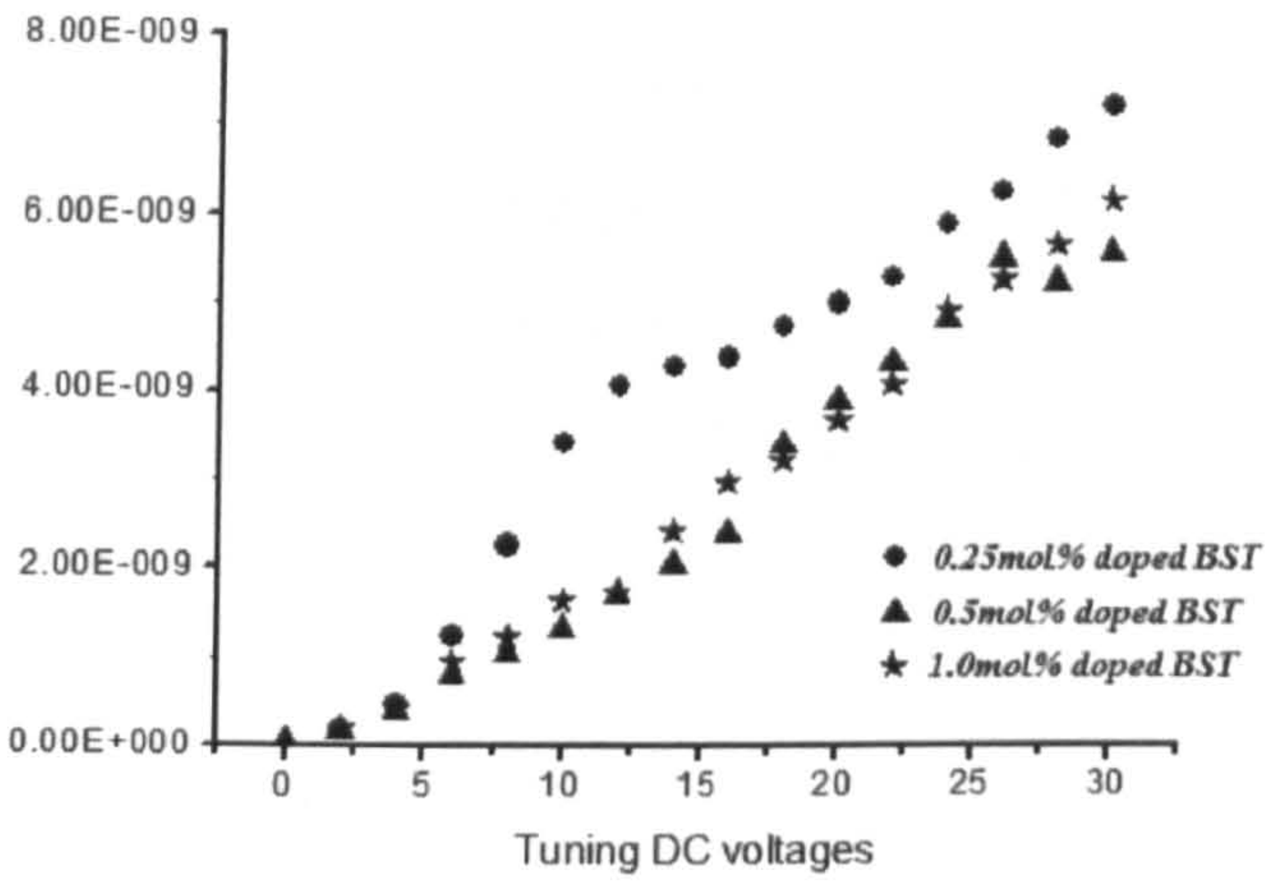

Figure 6.11: leakage current (Amp) for different thin films as a function of DC tuning field

At the maximum tuning electric field of 30V, the leakage currents for BSTC0, BSTC1, BSTC2 and BSTC5 were 0.91μA, 7.2nA, 6.1nA and 5.5nA respectively. In general, the measured leakage current for the Co doped BST film was much smaller than for the undoped film.

6.1.6 Results and discussion

In this work, $Ba_{0.5}Sr_{0.5}Ti_{1.0}O_3$ thin films doped with 0.25mol%, 0.5mol% and 1.0mol% of Co ions have been fabricated to investigate the effect of acceptor Co doping. The XRD pattern of BST thin films showed that all BST thin films contain cubic phase perovskite structures. The crystal orientation was calculated from the relative height of (110), (200) and (111) peaks. The results suggest that the orientation parameter of (110) peak only slightly changed in the presence of Co doping. The in-plane lattice parameters of the thin films were calculated from the positions of (110) peak using the "Bragg" equation. The change in the lattice parameters of the BST thin films due to Co doping is very small, because the radius of Co ion (0.68Å) is very close to the radius of the substituted Ti^{4+}ion. Meanwhile, the measured FWHM of the main (110) diffraction peak implies a decrease of grain size as the Co concentration is increased. The microstructures of the thin films studied by the SEM technique show all BST thin films are well crystallized and composed of dense grains.

A summary of dielectric properties of various Codoped BST

Sample names	Dielectric constant (0V)	Dielectric constant (30V)	Dielectric tunability In %	Dielectric loss (0V)	Dielectric Loss (30V)	Leakage current In Amp	Figure of Merit
BSTC0	415	343	16.5%	0.176	0.157	9.1e-7	1.1
BSTC1	251	227	9.2%	0.054	0.048	7.2e-9	1.6
BSTC2	183	160	12.3%	0.043	0.038	5.5e-9	3.3
BSTC5	212	206	3.8%	0.069	0.07	6.1e-9	0.75

Table 6.2 a summary of dielectric properties of BST thin film with different Co concentrations

The measured dielectric properties are given in table 6.2. According to this table, the dielectric constants and tunabilites of all Co doped BST films have decreased, while the loss tangents and leakage currents are lower. The reduction of tunability and dielectric constants can be attributed to two reasons. **One**: the acceptor ion (Co) which occupies the B site of the ABO_3 breaks the Ti-O chain and so lowers the Curie temperature. This results in a reduction of dielectric constant and tunability of BST thin film. **Two**: the decrease of the grain size in Co doped BST thin films results in smaller polarization and so lowers the dielectric tunability **[9]**.

The reduction of dielectric loss in Co doped BST thin films is also attributed to the substitution of B site ion in BST's ABO_3. As mentioned in section 7.2, it is widely known that the doped Co ions would reduce the concentration of free electrons which can hop between the Ti^{4+}ions of the BST crystal and so provide a loss mechanism for BST thin film **[8]**. Table 6.2 also points out that Co doped thin films have much lower leakage current than the undoped thin film. The reduction of leakage current can be explained by the theory reported by *Wencheng Hu* and *Chuanren Yang* **[10]**. They suggested that a dopant ion occupying either A or B site in BST's perovskite ABO3 structure could suppress the donor action of the oxygen vacancy, which reduces the charge carrier density (electron) **[10]**. The reduction of charge carry (electrons) prevents the current passing through the material and so lowers the leakage current. On the other hand, the grain boundary also prevents the charge carries passing through the films **[10]**. In this case, the decrease of grain size due to Co doping results in an increase of grain boundary area and so lowers the concentration of charge carriers.

Based on the measured results, the overall performance of $Ba_{0.5}Sr_{0.5}Ti_{1.0}O_3$thin films can be improved slightly by doping with Co (0.25 mol% and 0.5mol%). However, the improvement in overall performance (FoM) is at the cost of dielectric constant and tunability. This makes Co doped BST thin films unsuitable for the tunable microwave

devices. Furthermore, the dielectric loss of Co doped BST is still higher than the desired dielectric loss ($tan\delta_2$< 0.01). Therefore Co doped BST materials do not fully satisfy the desired parameters of a tunable thin film. However, it is a step forward in the direction of developing low loss tunable material.

6.2: Li doped BST thin films

6.2.1 Introduction

$Ba_{0.5}Sr_{0.5}Ti_{1.0}O_3$ thin films doped with 0 mol%, 1 mol%, 2 mol% and 4 mol% (BSTL0, BSTL1, BSTL2, BSTL4) of Li ions were deposited on a (0001) sapphire substrate by spin coating. The procedure of fabricating Li doped BST thin films was identical to the process used in making Co doped BST films. Instead of using cobalt acetate, lithium acetate was used as the starting compound to prepare the as-deposit precursor. The thickness of the crystallized thin film (300nm) was the same as Co doped BST film.

The composition and crystal structure of the thin films was analyzed by EDX, XPS and XRD techniques. An XL30 ESEM was employed to study the microstructure of the thin films. The dielectric properties of the doped thin films were measured using CPW, and the TRL calibration method was employed to reduce the errors caused by RF probes and CPW pads. Because of calibration errors at lower frequencies, the measured results below 3 GHz are not shown in this work. The tuning voltage was provided by a "Keithley" voltage source with a maximum tuning voltage of 30V or 30kV/cm.

6.2.2 Composition analysis

EDX results

The composition of Li doped BST thin films were analyzed by EDX. In the present work, two of the Li doped BST films (BSTL0 and BSTL4) were characterized using EDX technique. The obtained EDX pattern (BSTL4) is shown in figure 6.12. The large peak at 1.6 keV indicates the existence of Pt metal, which was coated onto the surface of the sample to prevent charging effects. The diffraction peaks at 3.9keV, 4.4keV, 4.8keV, 5.2keV; 1.5keV, 1.8keV and 0.4keV, 4.5keV, 4.9keVcorrespond to Ba, Sr and Ti atoms in the BST thin film. Because the lithium atom has a very low energy peak < 0.2keV (below the lower limit of the equipment), the corresponding peaks cannot be observed in this figure. A very large diffraction peak at 1.4KeV corresponds to aluminium metal which is used to fabricate the metal electrode of the CPW. An unexpected carbon peak (0.3KeV) was also observed. The existence of carbon atoms may be attributed to sample contamination.

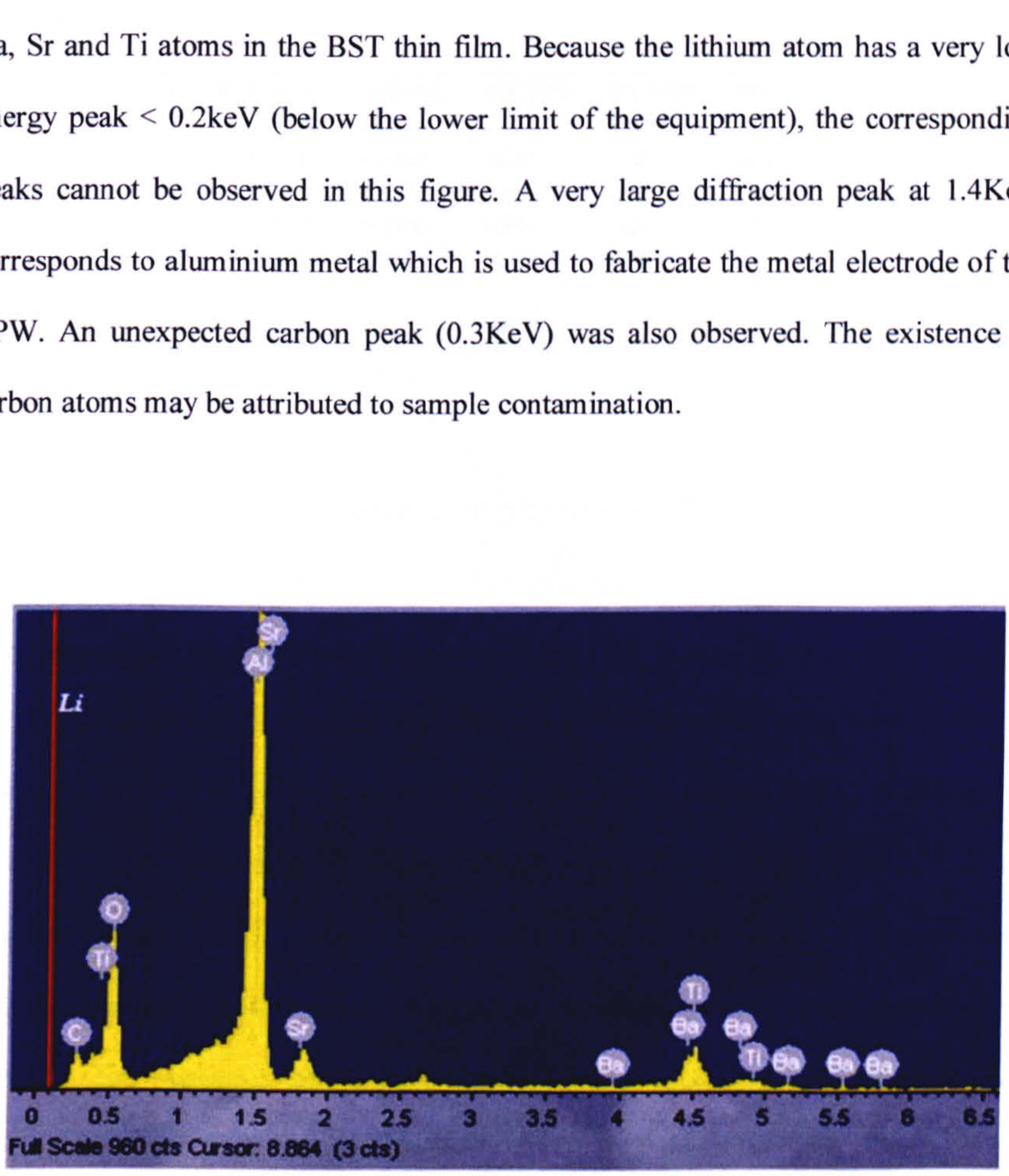

Figure 6.12 EDX pattern of sample BSTL4

EDX analysis can also provide the quantified results of the composition. Table 6.3 (a) and (b) list the quantified compositions of BSTL0 and BSTL4 thin films.

(a)

Element	App Conc.	Intensity Corrn.	Weight%	Weight% Sigma	Atomic%
O K	59.53	0.7460	50.75	0.61	82.01
Ti K	15.90	0.8803	11.48	0.29	6.20
Sr L	22.43	0.7605	18.75	0.40	5.53
Ba L	20.44	0.8160	15.36	0.54	2.89
Totals			100.00		

(b)

Element	App Conc.	Intensity Corrn.	Weight%	Weight% Sigma	Atomic%
O K	4.99	0.8548	59.47	3.02	68.16
Ti K	0.50	0.8473	5.96	1.04	2.28
Sr L	0.43	0.7470	5.89	1.27	1.23
Ba L	0.89	0.8141	11.09	2.09	1.48
Totals			100.00		

Table 6.3 quantified composition results of (a) BSTL0 and (b) BSTL4

The composition ratio between Ba, Sr and Ti are 1.48: 1.23: 2.28 and 2.89: 5.53: 6.20 for BSTL0 and BSTL4, respectively. The average composition ratio between Ba, Sr and Ti is 1:1.55:1.9. Since the peak corresponding to lithium atoms could not be observed, quantified results for lithium are not given. The substrate of the thin film is sapphire (Al_2O_3) which contains a large amount of oxygen atoms. Therefore, very high percentages (68.16% and 82.01%) of oxygen atoms were detected in both of the samples. The measured composition ratio (1:1.55:1.9) of BST thin film is very different from the desired composition (1:1:2) of BST thin film. This is because the penetration depth (10μm) of the X-ray beam is much deeper than the thickness of the thin film (300nm). To overcome this problem, BSTL4 was characterized using the XPS technique which provides the composition analysis of the BST thin film.

XPS results

The elementary composition of the BST thin film was also investigated by using the XPS technique. In this case, a XPS (VG Scientific, ESCALAB MARK 2) with a MgK_{α} radiation source of kinetic energy hv = 1253.6 eV was employed to analyze the composition of the film. As mentioned in chapter 3, the XPS analysis is strongly affected by its sensitivity, chamber, sample cleanness and etc. In this case, the film was measured twice by the same XPS so that averaged results of the film composition could be obtained. Figures 6.13(a) and (b) show the scanned XPS spectrums (between 0eV and 1250eV) and the composition ratios between each of the elements.

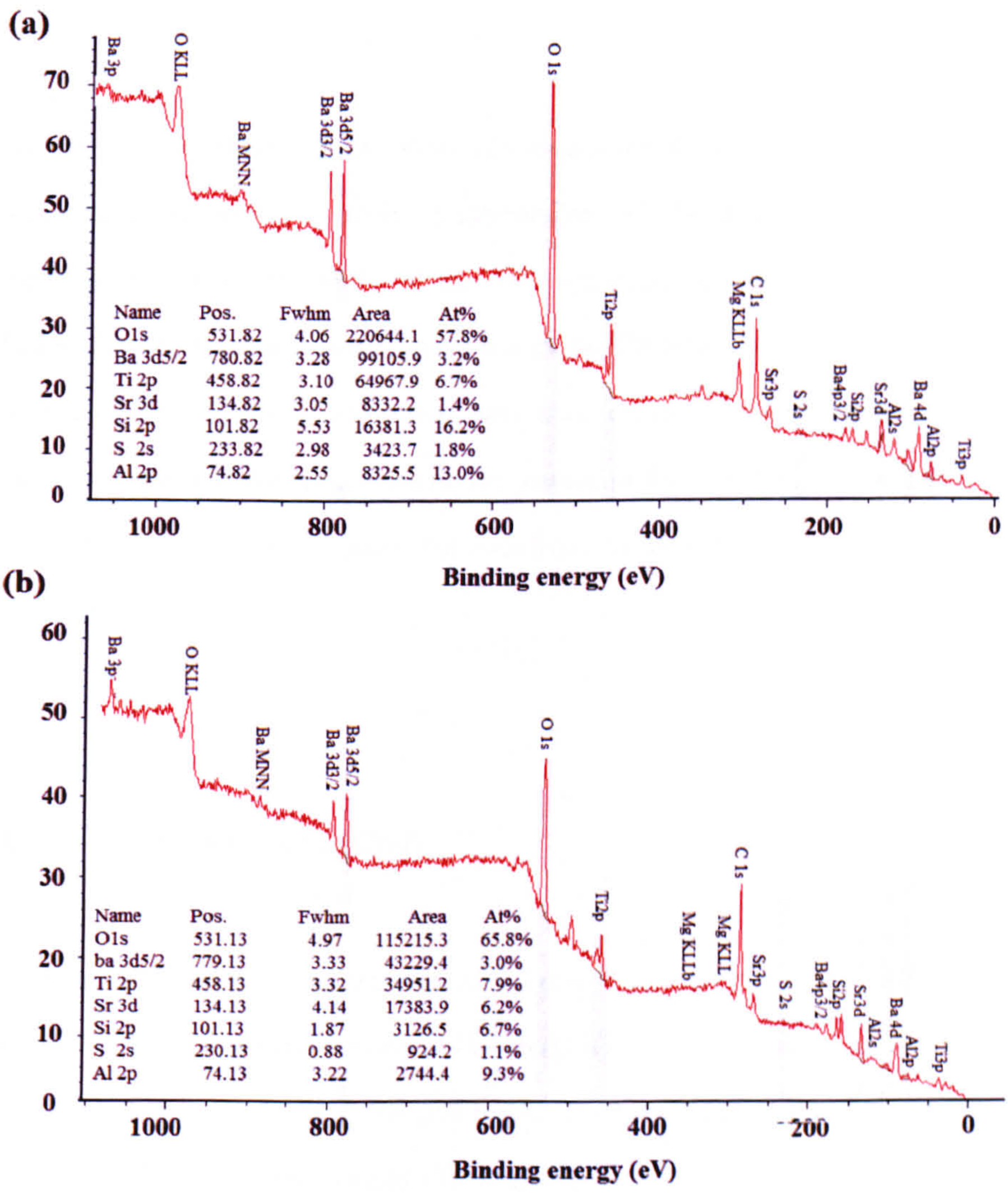

Figures 6.13 (a) and (b). X-ray spectrums of a Li doped BST thin film with 4mol% of Li ion

In both figures, energy peaks that correspond to Ba, Sr and Ti were detected. The ratio between Ba, Sr and Ti was calculated from their concentrations (in %). Then an averaged composition ratio between these elements could be calculated mathematically. The calculated composition ratio between Ba, Sr and Ti is 1: 0.815: 2.13. This result is close to the desired ratio of 0.5: 0.5: 1.0 or 1: 1: 2.0. However, the doped Li ions were not detected in these spectrums. This may caused by the poor sensitivity of the XPS. Meanwhile, both figures indicate that the sample film contained many unwanted elements such as C, S, Mg and Si.

As mentioned in chapter 3, the X-ray can only penetrate into the sample for few nanometers. Therefore, a slight contamination of the sample surface could significantly change the results of the XPS spectrum. In this case, the XPS is frequently used by other researchers who work on different types of materials. The existence of C, S and Si atoms may have been caused by contamination in the vacuum chamber of the XPS. Because the surface of the thin film was covered by CPWs made from Al metal, peaks that correspond to Al atom were also detected in the spectra.

6.2.3 Crystal structure analysis

Figure 6.14 shows the XRD patterns of $Ba_{0.5}Sr_{0.5}Ti_{1.0}O_3$ thin films doped with 0 mol%, 1mol%, 2 mol% and 4 mol% of Li ions (BSTL0, BSTL1, BSTL2 and BSTL4) on a sapphire substrate. The X-ray diffraction pattern indicates that all samples are cubic perovskite and polycrystalline. No secondary crystal phase can be observed in the patterns.

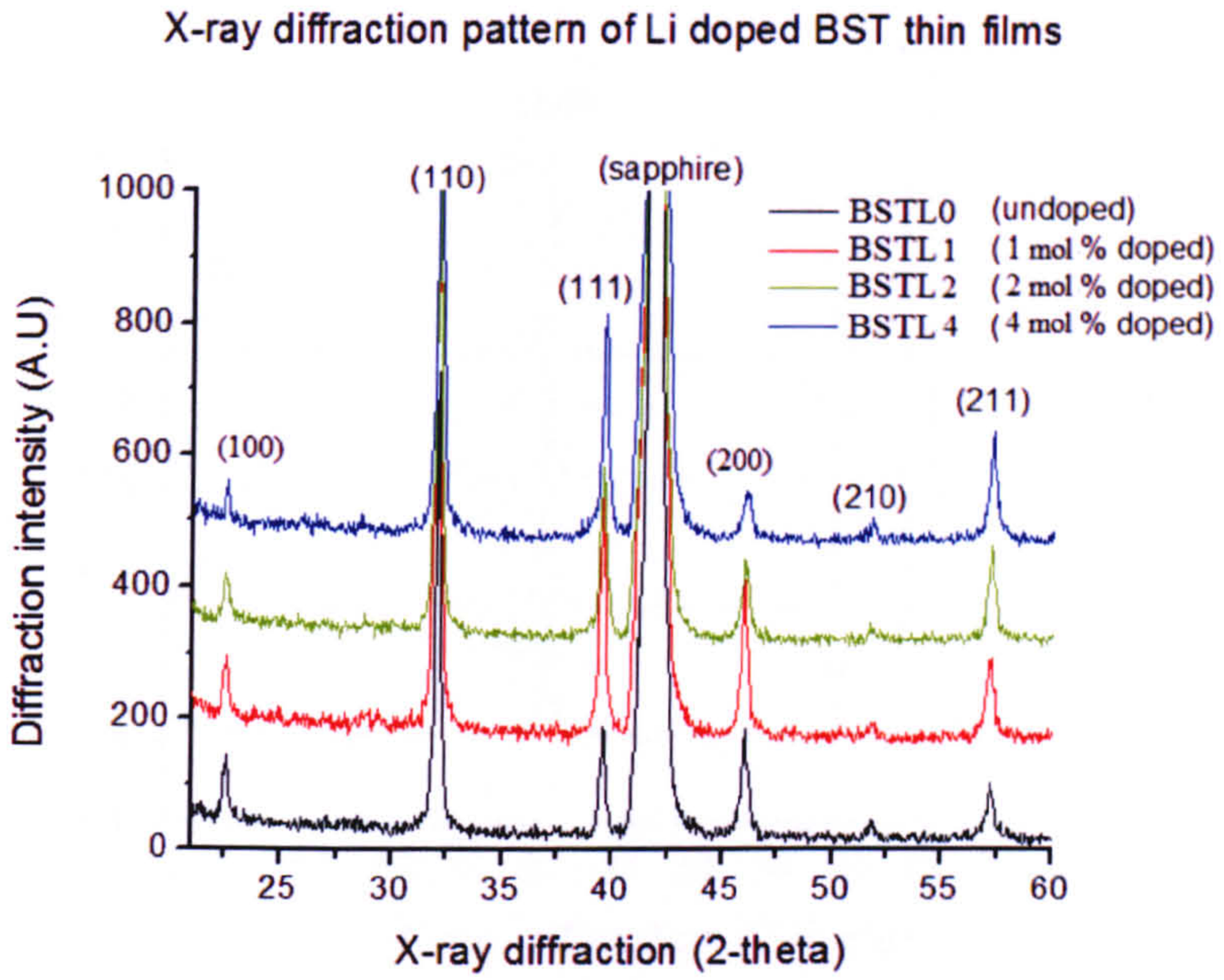

Figure 6.14 the X-ray diffraction pattern of BSTL0, BSTL1 BSTL2 and BSTL4.

The (110) crystal orientation was analyzed by using orientation parameter α_{110}which was calculated from the relative heights of the (200), (110) and (111) peaks using the equation $\alpha_{110} = I_{110}/(I_{110} + I_{200} + I_{111})$. The intensities of the diffraction peaks are given in figure 6.15.

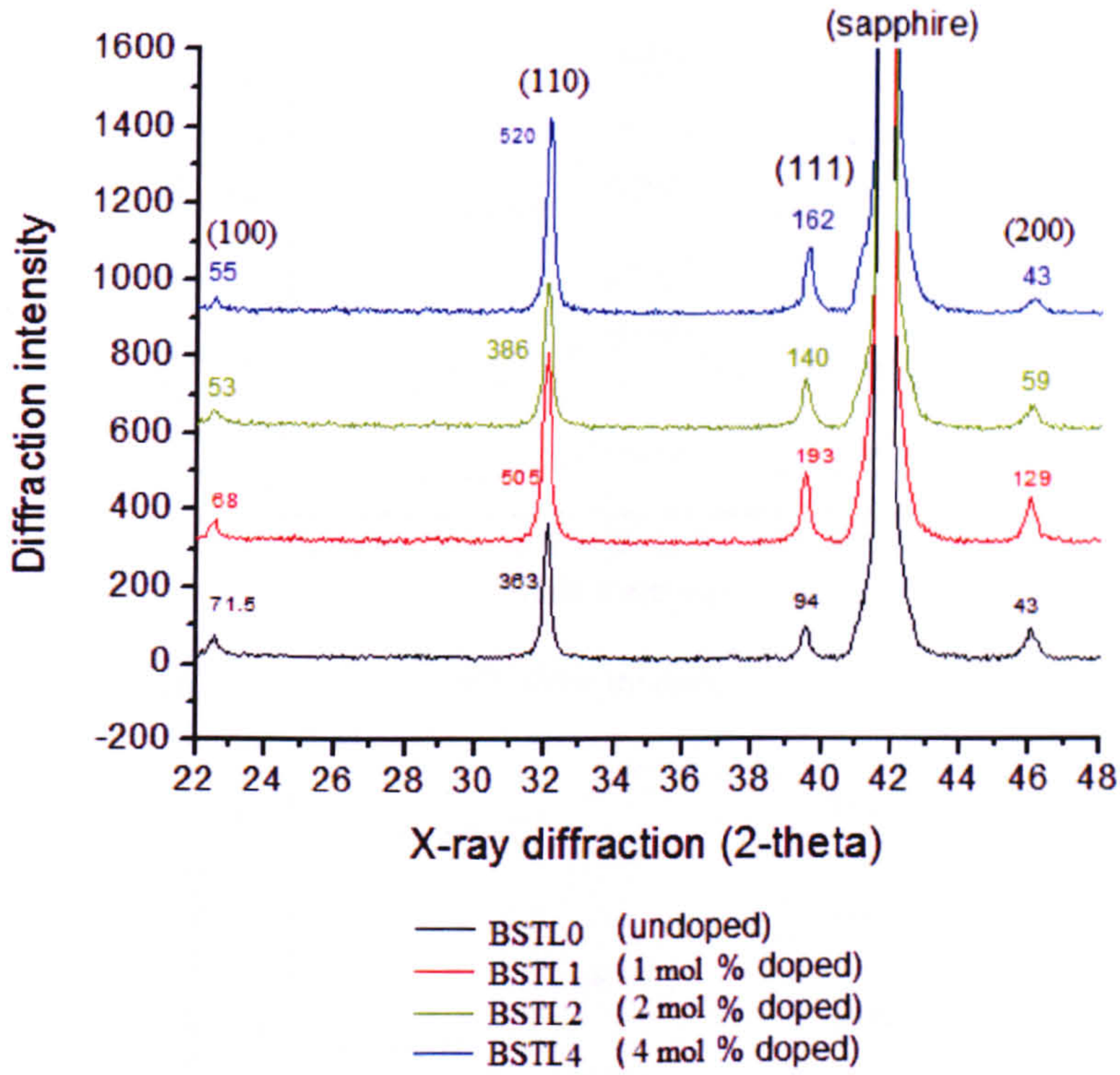

Figure 6.15 X-ray diffraction intensities of (110), (111) and (200) peaks in BSTL0, BSTL1, BSTL2 and BSTL4

For BSTL0, BSTL1, BSTL2 and BSTL4, the obtained orientation parameters were 0.72, 0.61, 0.66 and 0.72 respectively. This indicates that the crystal growth orientation of the thin films was not significantly affected by the Li doping. The (110) peak is still the main X-ray diffraction peak for all BST films regardless of the Li concentration.

Figure 6.16 shows a close look at the diffraction curves of the 110 and 200 peaks. The out-of-plane *(c)* and in-plane lattice *(a)* parameters of the thin films were calculated from the diffraction angles of (200) and (110) peaks using the "Bragg" equation.

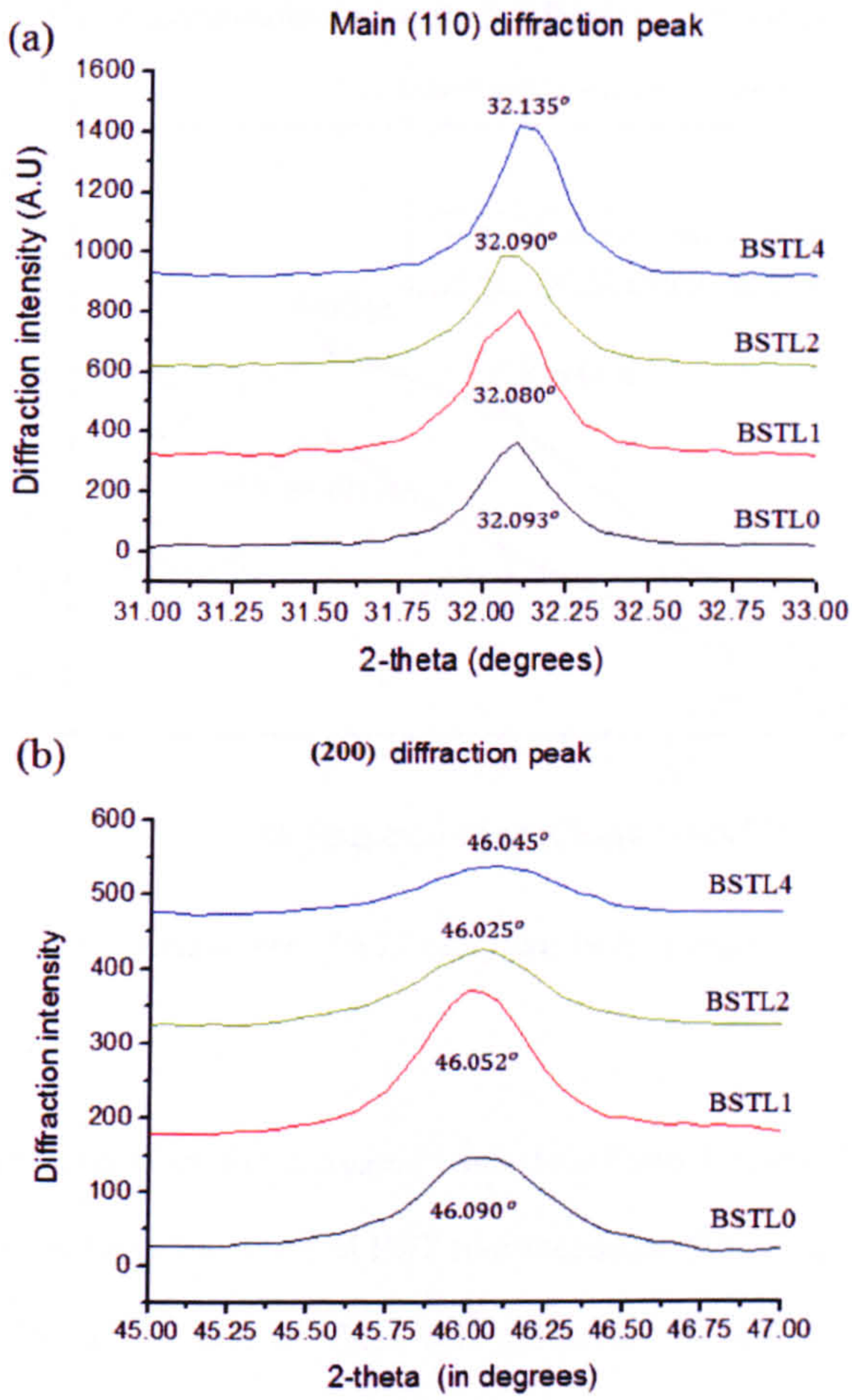

Figure 6.16: X-ray diffraction peaks of (a) (110) and (b) (200)

The calculated *in-plane (a) and out-of-plane (c)* lattice parameters of each BST thin film with respect to different Li concentrations are given in figure 6.17. The figure also compares the lattice parameters of BST thin films with bulk $Ba_{0.5}Sr_{0.5}Ti_{1.0}O_3$ ($a = c = 3.947\dot{A}$). As it shows, all films exhibit a slightly in-plane $c < a$ tensile strain **[11].**

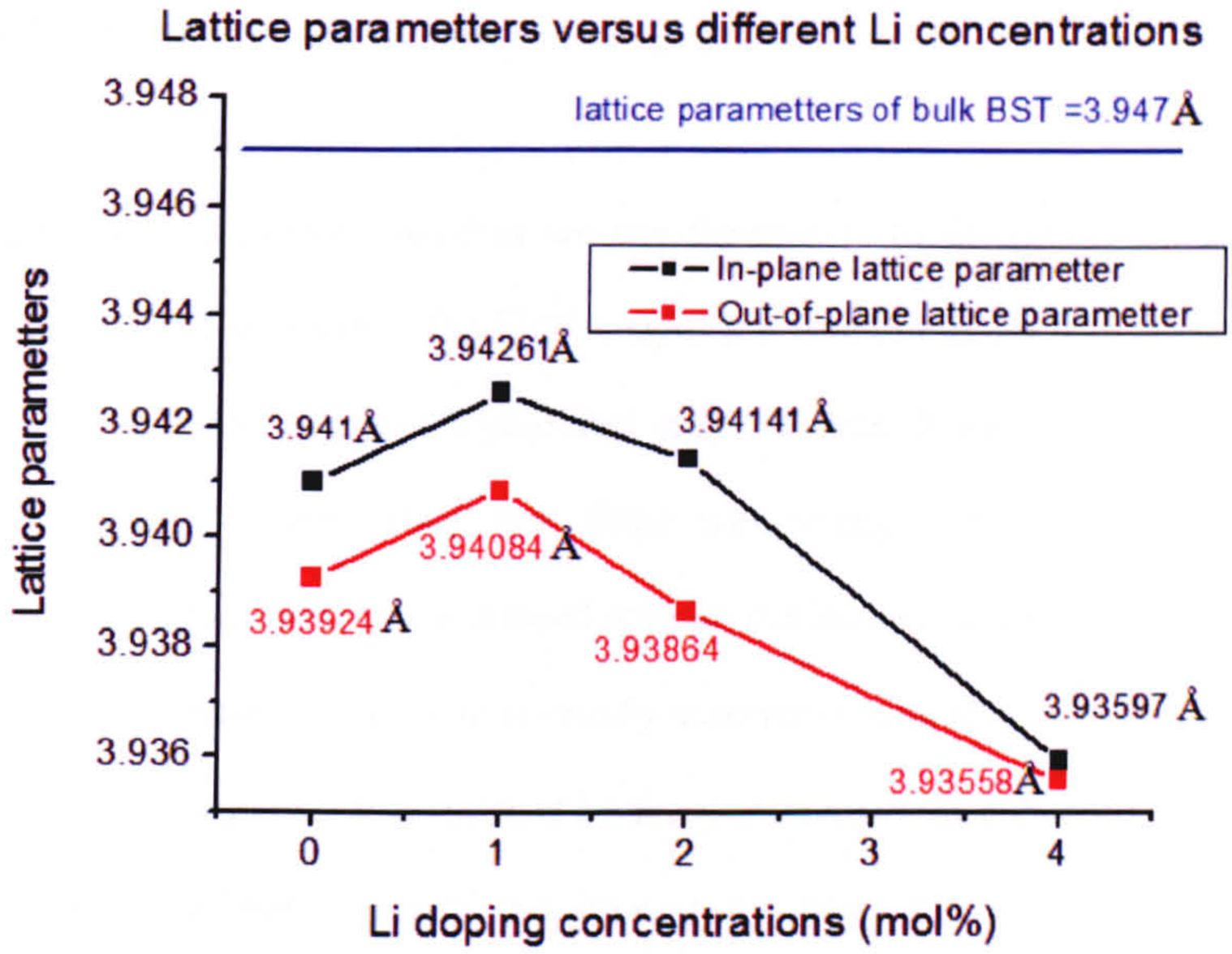

Figure 6.17 lattice parameters of BST thin films with respect to Li concentration

When the Li concentration was increased from 0 mol% to 1 mol%, both the in-plane and out-of-plane lattice parameters of BST film increased. Since the radius of a Li ion (ie, Li^{1+} = 0.76 Å) is smaller than the radius of A site Ba^{2+}(1.34 Å) and Sr^{2+}(1.12Å) in the perovskite ABO_3 structure, and larger than the radius of B site Ti^{4+}(0.68 Å) ion, the increase of lattice parameter indicates that the majority of Li ions have substituted into the B site of perovskite.

However, a further increase in Li doping concentration from 1mol% to 4mol% led to a decrease in BST's lattice parameter. This implies that most of the Li ions were substituted into the A site of BST's perovskite structure when Li concentration was higher than 1 mol%. These results suggest that Li ions can enter into either the A site or B site of BST's perovskite structure depending on the doping concentration. This unique feature could affect the dielectric properties of BST thin films significantly.

6.2.4 Microstructure analysis

The grain size and microstructures are key parameters to determine the dielectric properties of BST thin films. The SEM images presented in figure 6.18 show that all of the BST thin films are well crystallized and crack free. It was also found that the grain size of Li doped BST thin films was strongly influenced by the Li concentrations. The grain size increased with an increase in Li concentration up to 4 mol %. The increase of grain size is usually associated with an increase of dielectric constant. This suggestion is confirmed by the measurement of dielectric constants in the following sections. Some of the large grains appearing on the thin films are actually clusters of small particles due to the high annealing process.

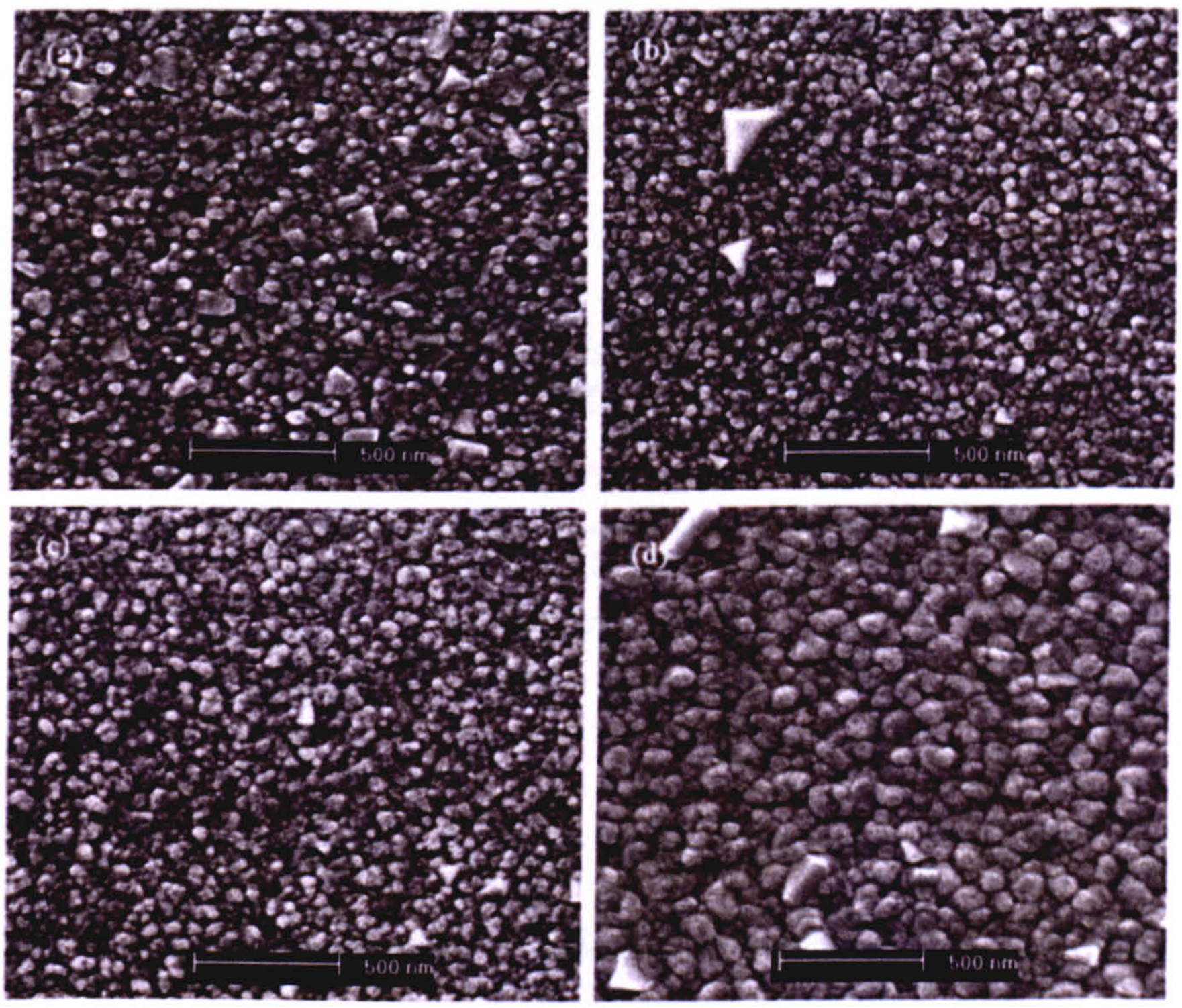

Figure 6.18 SEM images for BST thin films with (a) 0 mol% Li (b) 1 mol% Li (c) 2 mol% Li and (d)4 mol% Li

6.2.5 Measured dielectric properties

The dielectric properties of the Li doped BST thin films were measured using the same CPW method described in sections 5.1 and 5.2. However, the length of the CPW used in this work was reduced to 800μm, while the track width and gap remained at 20μm and 10μm, respectively.

Measurement of dielectric constant

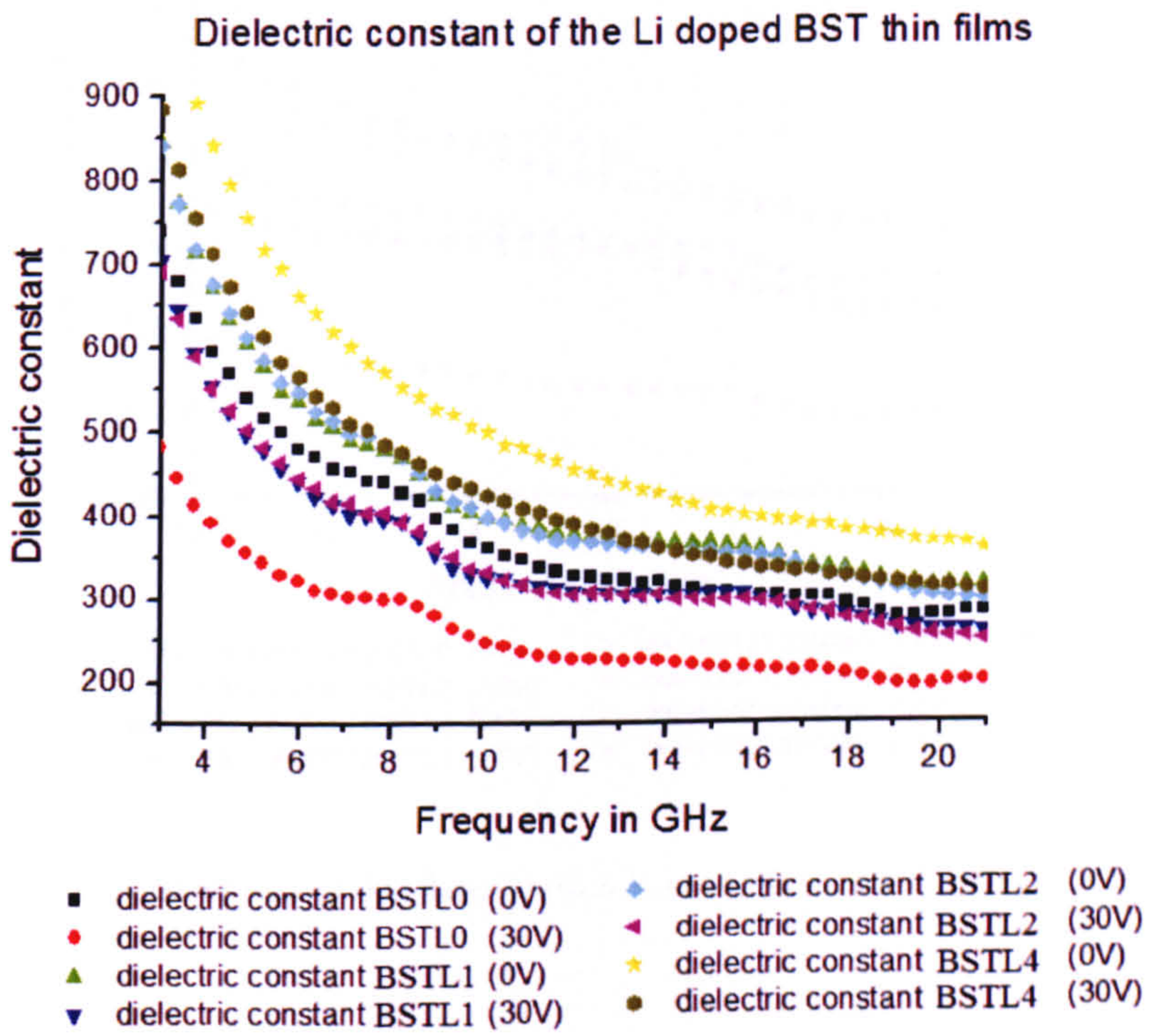

Figure 6.19: the measured dielectric constant of (a) BSTL0, (b) BSTL1, (c)BSTL2 and (d) BSTL4.

The measured room temperature dielectric constants of the $Ba_{0.5}Sr_{0.5}Ti_{1.0}O_3$ with different Li concentration from 0% to 4 mol% are given in figure 6.19. As can be seen, the measured dielectric constants of all thin films decreased with frequencies up

to 21GHz. Because of the calibration errors, the dielectric constants varied sharply below 12GHz. As mentioned in chapter 2, the decrease in dielectric constants with respect to increasing frequency may also be attributed to the effect of dielectric relaxation.

The measured results stabilised at around 12 GHz since the CPW phase shift was close to 90 degrees. Figure 6.20 provides a close look at the measured results between 10GHz and 21GHz.

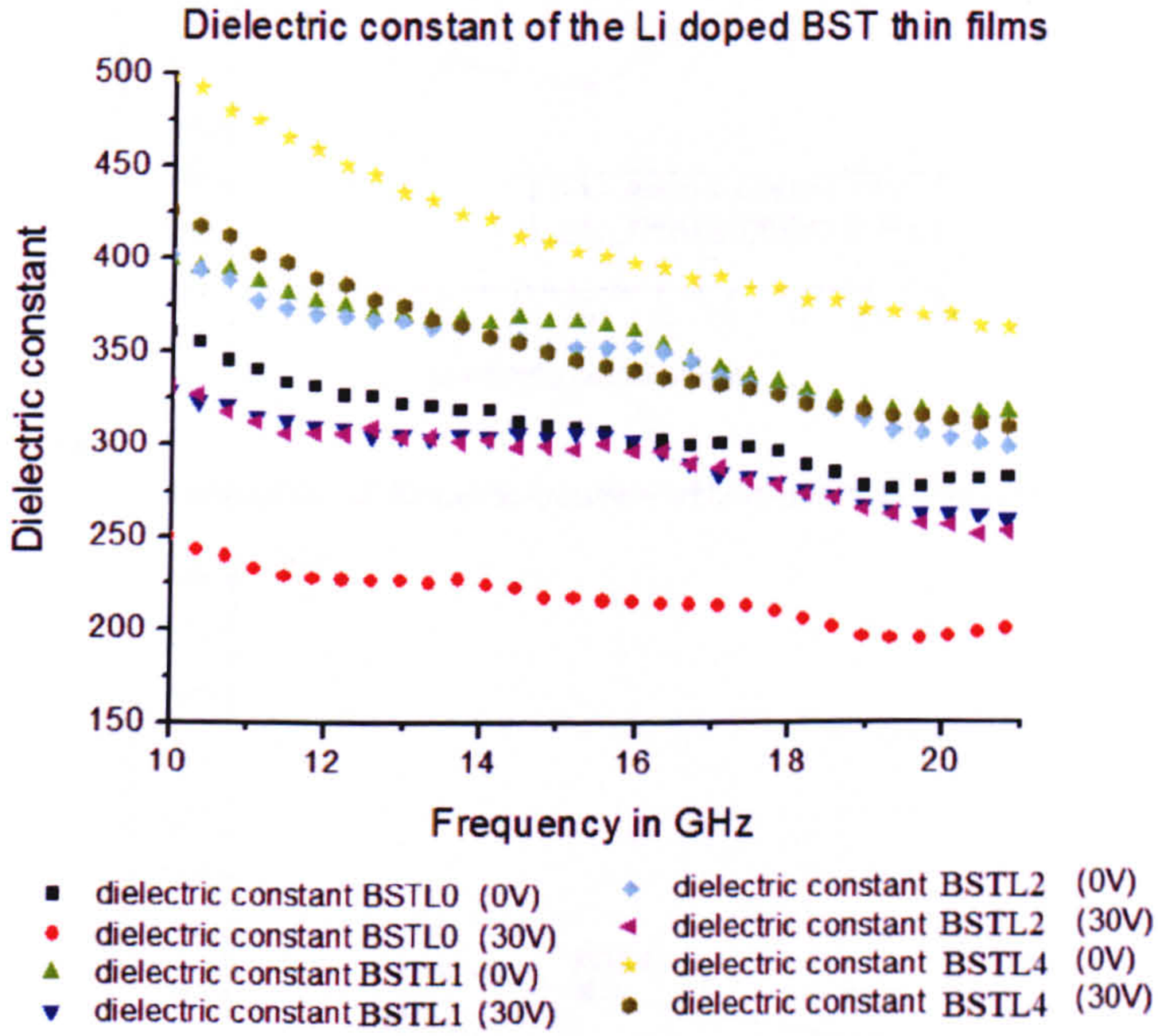

Figure 6.20: a close look of thin films' dielectric constants between 10GHz and 21GHz.

This figure shows that all of the doped thin films had higher dielectric constants than the undoped BST. BSTL4 with 4 mol% of Li under an applied voltage of 0V had the highest dielectric constant between 500 (10GHz) and 380 (21GHz). Both BSTL1 and BSTL2 had similar dielectric constants between 400 (10GHz) and 340 (21GHz) under 0V. The dielectric constant of undoped BST thin film (BSTL0) under 30V was the lowest of all (between 250 at 10GHz and 220 at 21GHz) samples. The measured

dielectric constant and dielectric tunability of BST thin films at 20GHz where the CPW phase shift is 90 degrees are shown as a function of different Li concentrations in figures 6.21(a) and (b). The errors in the measured dielectric constants are below 24%.

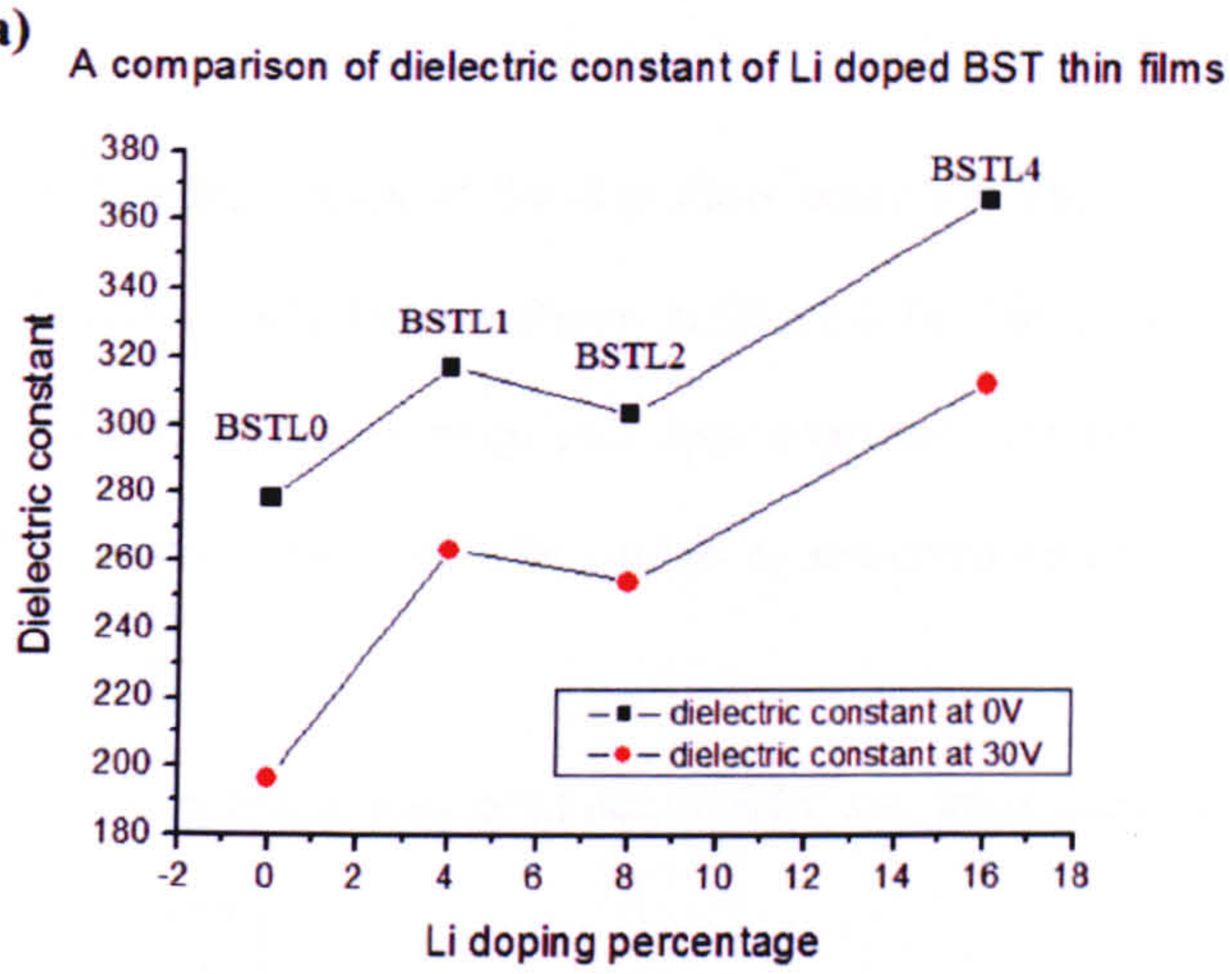

Figure 6.21 dielectric constant of BST thin films with respect to Li concentration (a) at 0V and (b) 30V.

The dielectric constant of BST thin film under both tuning voltages (0Vand 30V) increased as the Li concentration increased from 0 mol% to 4 mol%. BSTL4 with 4 mol% Li doping had the highest dielectric constant of 370 (20GHz) while the undoped BST film showed the lowest dielectric constant of 280 (20GHz). In contrast,

a decrease in dielectric tunability from 30% to 15% was found as Li concentration increased from 0 mol% to 4 mol%.

Measurement of dielectric loss

The measured dielectric losses of the thin films under 0V and 30V were measured between 3GHz and 21GHz and are shown in figure 6.22. The dielectric losses of all thin films decreased with frequency until approximately 12 GHz and then became approximately constant. This could be caused by dielectric relaxation or from TRL calibration artefacts.

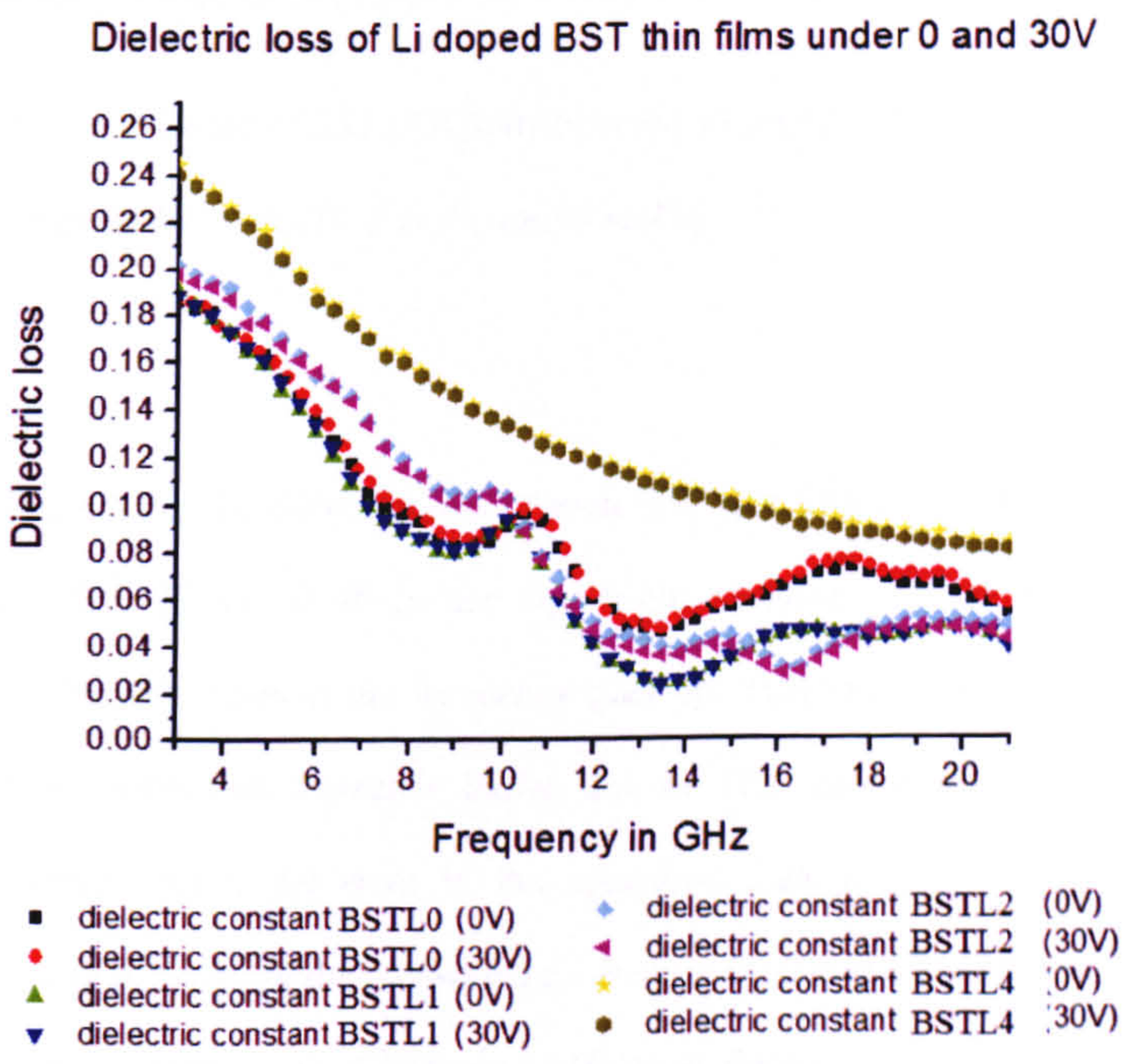

Figure 6.22: dielectric losses of BST thin films with different Li content (0 mol%, 1 mol%, 2mol% and 4 mol%)

A close look of the measured dielectric losses between 12GHz and 21GHz are shown in figure 6.23.

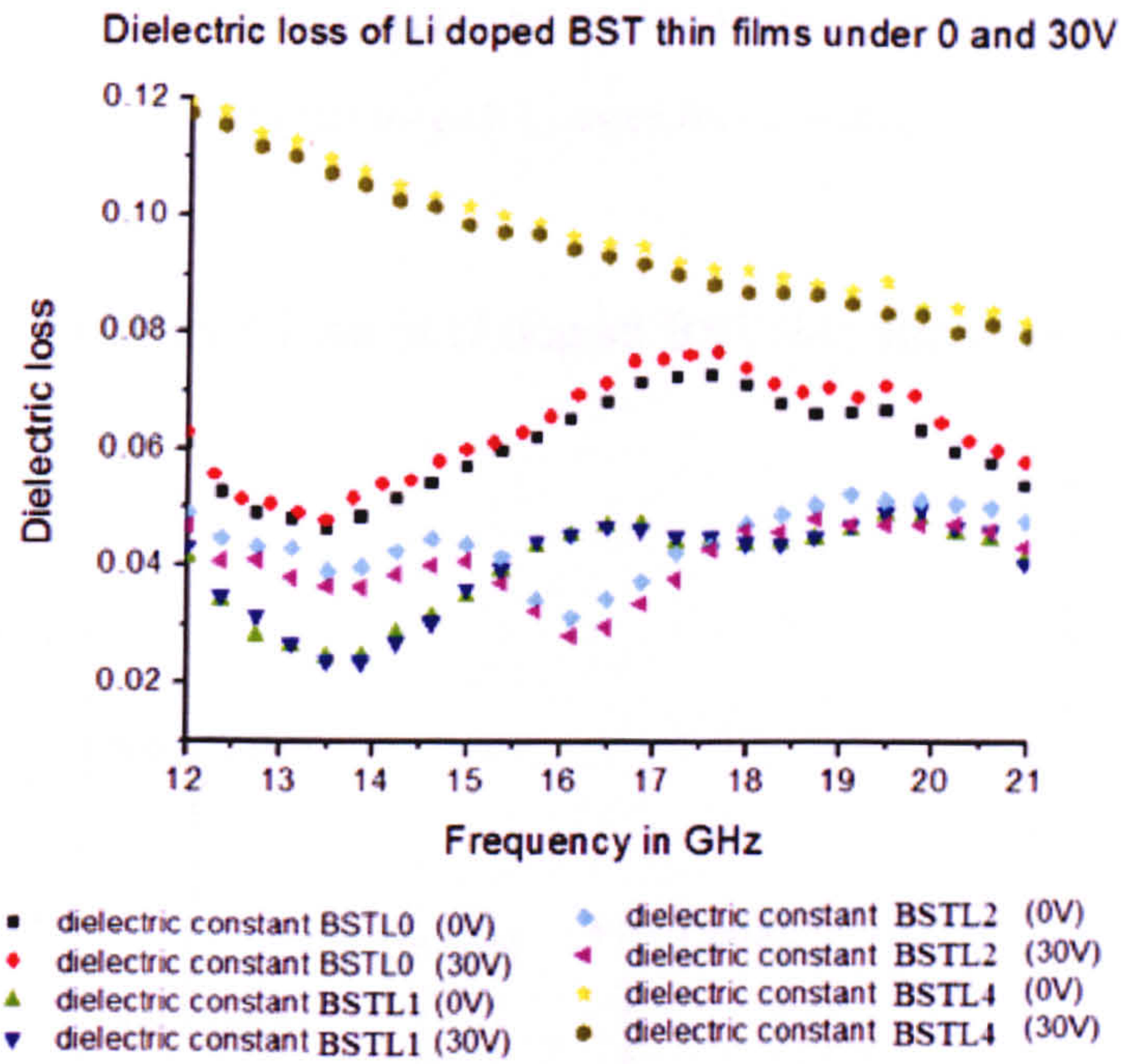

Figure 6.23: dielectric losses of BST thin films between 12 and 21GHz with respect to Li concentration (0 mol%, 1 mol%, 2 mol% and 4 mol%)

According to figure 6.23, the dielectric loss of each BST thin film changed very little between 0 and 30V. However, there are significant variations in the measured dielectric loss of the thin films as the frequency goes up. This implies that there are large errors in the measured dielectric losses due to TRL calibration errors. As mentioned in section 5.1.2, the error in the measured dielectric loss is hard to determine. One way to estimate the measurement error is to record the minimum and maximum dielectric loss between 12GHz and 21GHz in figure 6.23. The estimated error in the dielectric loss is between the measured minimum and maximum dielectric loss.

Therefore, the measured dielectric losses of the thin films are not compared at a single frequency. The dielectric losses of BSTL0, BSTL1, BSTL2 and BSTL4 are compared between 12GHz and 21GHz. The recorded minimum and maximum dielectric loss of the Li doped BST thin films between 12GHz (0V) and 21GHz (0V)

are compared in the following figure. An error bar has been used to indicate the error in the measured dielectric loss for each Li doped BST thin film.

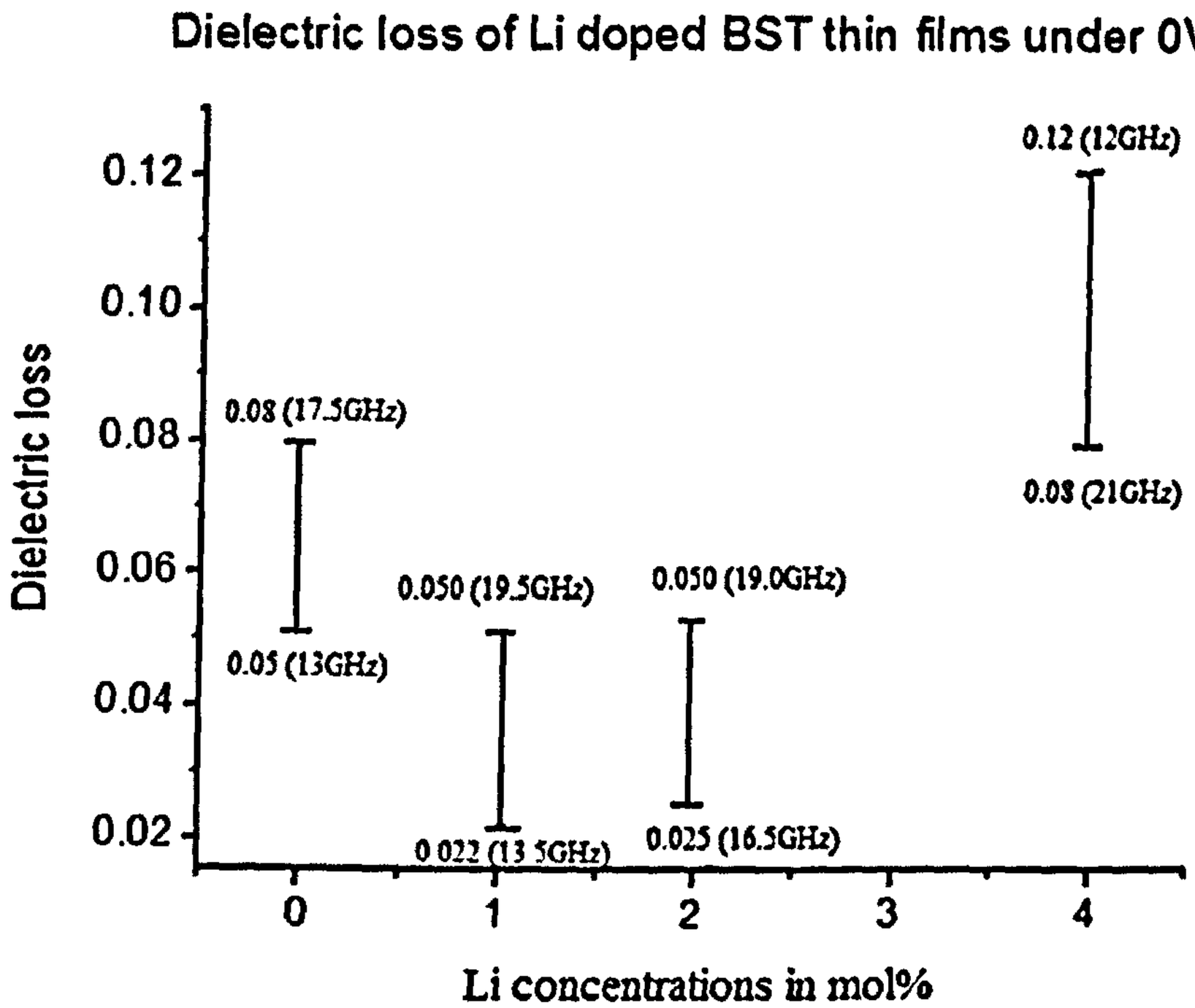

Figure 6.24: a comparison of dielectric losses of BST thin films (BSTL0, BSTL1, BSTL2 and BSTL4)

According to figure 6.24, BSTL1 had the lowest dielectric loss between 0.022 (13.5GHz) and 0.05 (19.5GHz). The dielectric loss of BSTL2 was very similar to the loss of BSTL1. The undoped BST film had the second highest dielectric loss (between 0.05 at 13GHz and 0.08 at 17.5GHz) of all the samples. The highest dielectric loss was measured from BSTL4 where the measured results dropped from 0.12 to 0.08 between 12 and 21GHz. In general, the dielectric losses of 1 mol% (BSTL1) and 2 mol% (BSTL2) Li doped BST films were lower than those for undoped BST. The 4 mol% (BSTL4) had the highest dielectric loss.

Figure of merit (FoM)

An easier way to analyze the dielectric properties of the thin film is to use the figure of merit (FOM). FOM is defined as $FOM = \frac{(Dielectric\ tunability\ in\ \%\ at\ 20GHz)}{Dielectric\ loss\ at\ 0V\ (20GHz)}$ .The measured FoM of all thin films are compared in figure 6.25.

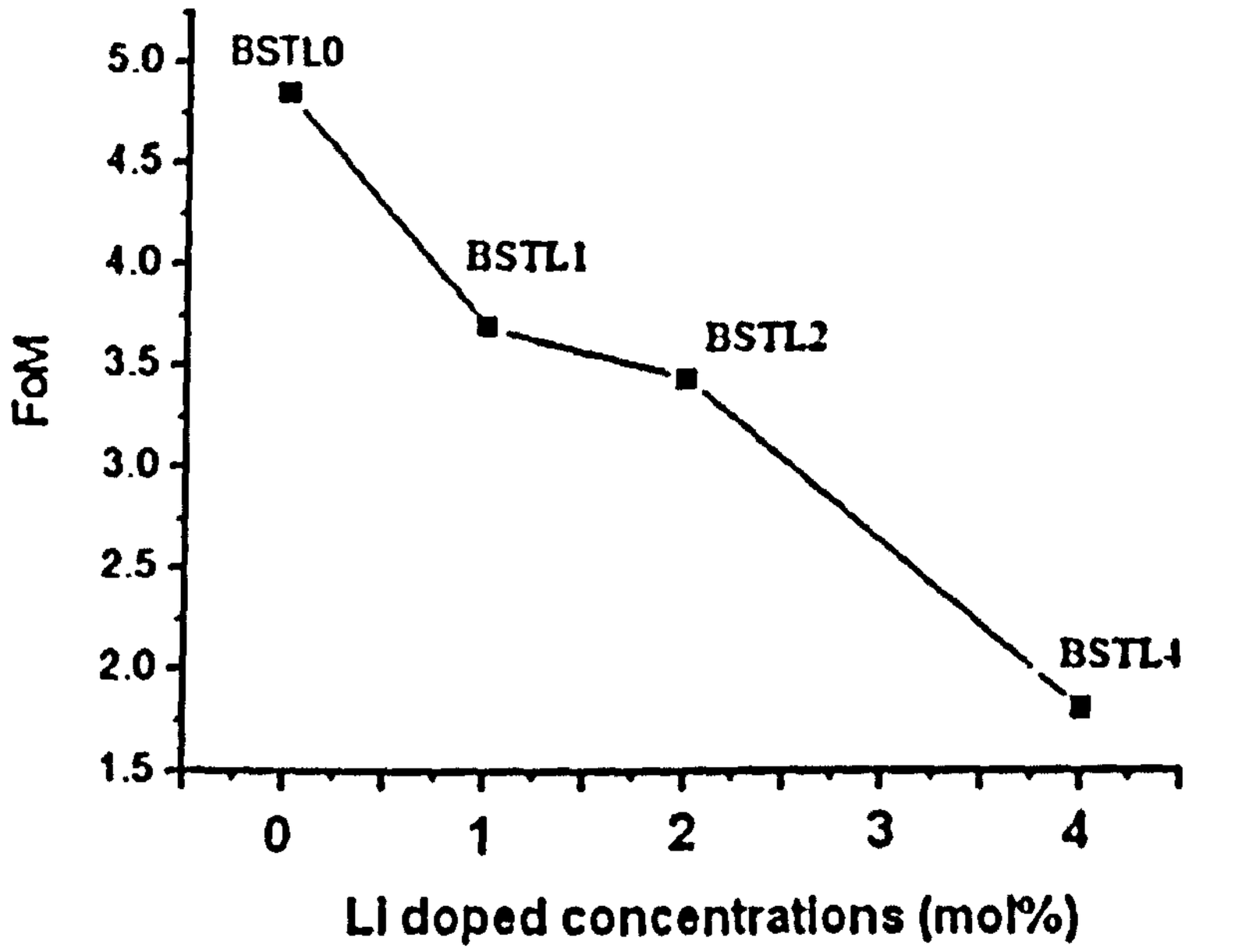

Figure 6.25: the measured figure of merit (FoM) of BST thin films with different Li concentration

The measured FoM of the undoped BST in figure 6.25 was much higher than the FoM of undoped BST thin film displayed in figure 6.13. The difference in FoM was caused by the precursor synthesizing method (chelation) which has difficulties in repeatability. As mentioned in chapter 3, one of the major drawbacks of this method is that the synthesized organic precursor is under constant attack from the water in air and, therefore, the quality of the precursor degrades as time pass. This leads to a variation of dielectric properties of BST thin films. In future, more work should focus on improving the repeatability of the chelation method. Figure 6.25 also shows that the doping of Li ions resulted in a decrease of the overall performance of the material.

Due to the small tuning voltage, the recorded FOM was relatively small for all the samples.

Table 6.4 compares the dielectric constant and tunabilities of 1mol% Co and 1mol% Li doped BST thin films which are measured at 12GHz. The dielectric results are obtained from figure 6.23 and 6.8.

Sample Names	Dielectric constant (0V)	Dielectric constant (30V)	Tunability
BSTC1	251	310	9.8%
BSTL1	375	227	17%

Table 6.4: a comparison of dielectric results of BSTC1 and BSTL1.

The Li doped BST (BSTL1) thin film has higher dielectric constants at both tuning voltages (0V and 30V) and exhibits greater tunability than Co doped BST. However, the comparison of dielectric loss between BSTC1 and BSTL1 is not straight forward due to the large variations in the measured dielectric loss of BSTL1 thin film. In figure 6.23, the measured dielectric loss of BSTL1 (0V and 30V) vary between 0.022(14GHz, 0V) and 0.05(19.5GHz, 0V). These values are still lower than the dielectric loss of BSTC1 (0.054) measured at 14GHz (0V). All in all, the dielectric properties of Li doped BST (BSTL1) thin film outperforms the Co doped BST (BSTC1).

Measurement of leakage current

The leakage currents of BST thin film with different Li concentrations of 0 mol%, 1 mol%, 2 mol% and 4 mol% (BSTL0, BSTL1, BSTL2 and BSTL4) were measured by

applying DC voltages from 0 to 30V with a step size of 2V. The measured results are shown in figures 6.28(a) and (b) as a function of different DC voltages.

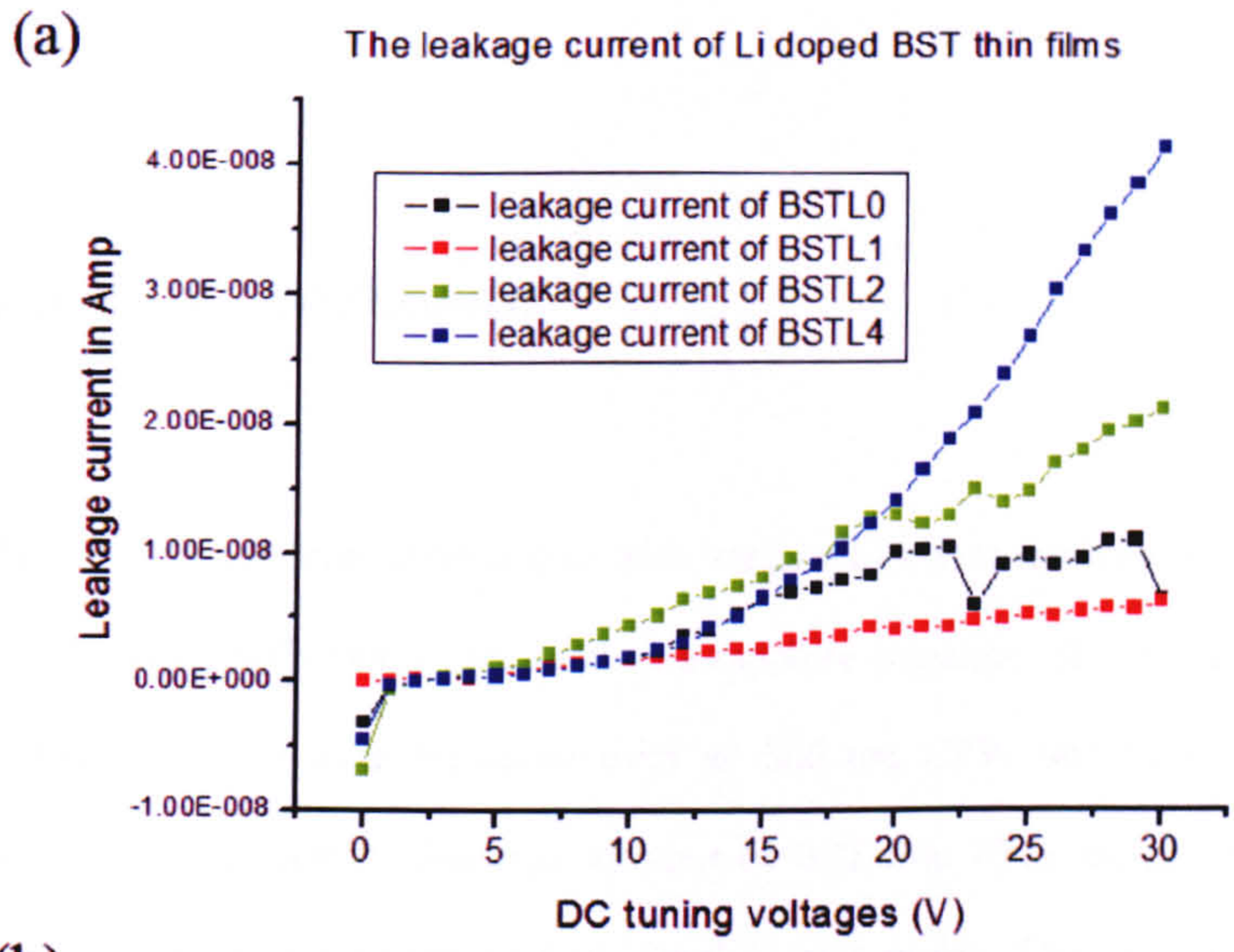

(b)

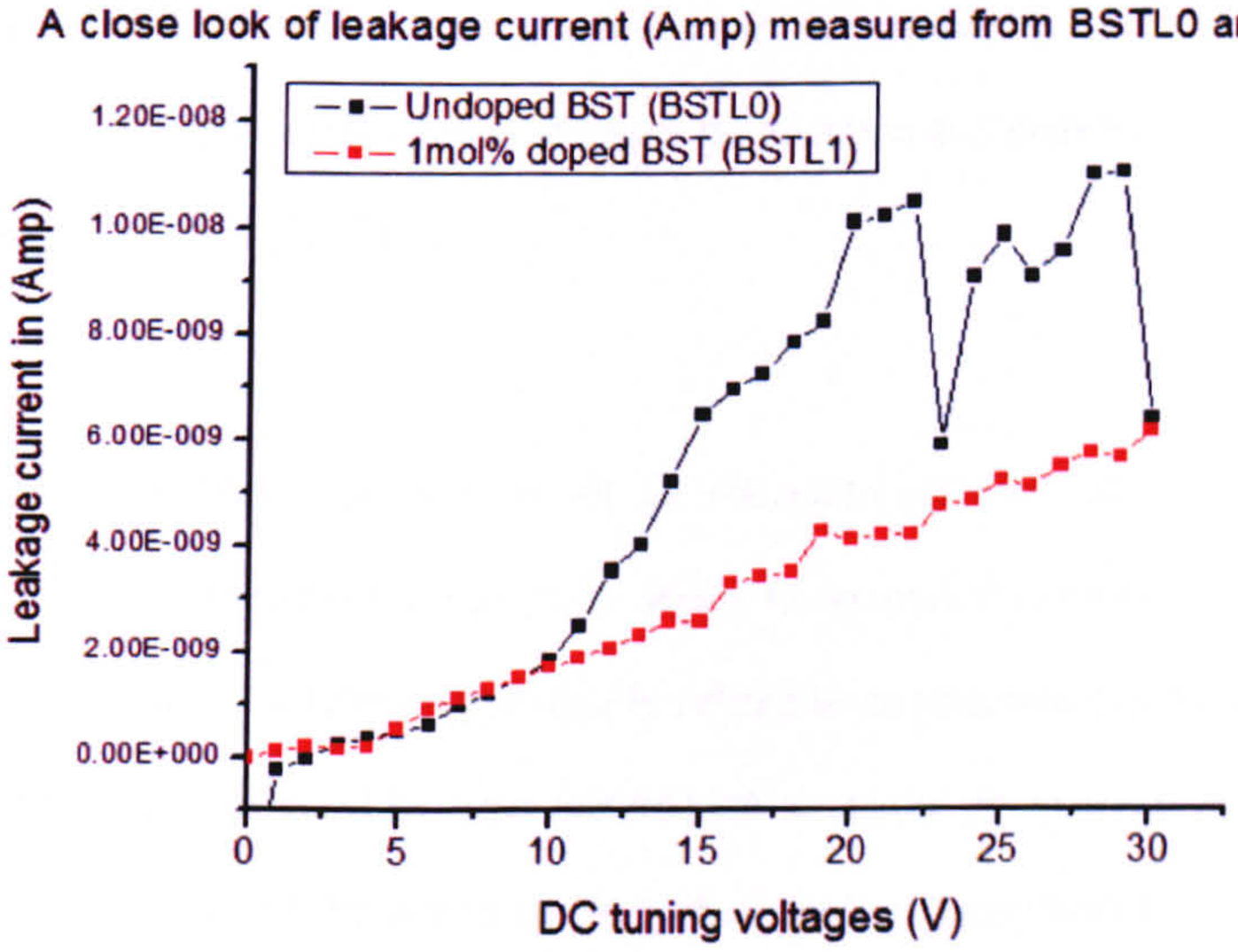

Figure 6.28(a): leakage current of BST thin films (BSTL0, BSTL1, BSTL2 and BSTL4) with respect to varied DC tuning voltages and (b): a close look at leakage current measured from BSTL0 and BSTL1

As shown in Figure 6.28(b), the leakage current of BSTL1 (1mol% Li) is lower than the current measured from BSTL0 (undoped BST). A further increase in Li concentration from 1mol% to 4mol% resulted in an increase of leakage current in

BSTL2 and BSTL4. Because of the poor repeatability of chelation method, the measured leakage current of the undoped BST was significantly smaller than the undoped BST in figure 6.11.

6.2.6 Results and discussion

$Ba_{0.5}Sr_{0.5}Ti_{1.0}O_3$ thin films doped with various Li concentrations (0mol%, 1mol%, 2mol% and 4mol%) were deposited on a sapphire substrate. The dielectric properties of the thin films were measured from an 800 um CPW line between 4GHz and 21GHz. The measured dielectric constant of BST thin films increased gradually as the Li concentration increased from 1mol % to 4 mol%. The increase in dielectric constants is attributed to the increase in grain size caused by Li doping, particularly since larger grains usually result in larger polarization and therefore a higher value of dielectric constant **[9, 12]**.

On the other hand, the increase of Li concentration also led to a reduction in tunability. The reduction in tunability seems to contradict the increase of grain size since tunability is always proportionally related to polarisation **[5]**. In fact, dielectric tunability is also affected by other factors such as crystal phase and Curie temperature. In this case some of the doped Li ion (when doping concentration is 1mol%) were substituted into the B site of the ABO3 structure which broke the Ti-O bond and so decreased the Curie temperature of the BST thin film. This will lead to a reduction of the dielectric tunability in Li doped BST thin films **[9]**.

According to the measured results, the BST thin films doped with 1mol% and 2mol% of Li had significantly lower dielectric losses than the undoped material. This was

caused by the doping of Li ion which prevented the reduction of Ti^{4+} to Ti^{3+} by neutralizing the donor action of the oxygen vacancies. This led to fewer electrons that could hop between the Ti ions, which caused the dielectric loss mechanism **[13]**.

Interestingly, there was a sharp increase in dielectric loss in BST thin film when it was doped with 4 mol% of Li ions. The sudden increase of dielectric loss may have been caused by the high concentration of Li dopants being above the solubility limit. The excessive Li would be in oxide form and have different dielectric properties. The oxides would be located at the grain boundaries of the BST material. Hence, the doped BST films consisted of high dielectric constant BST with low dielectric constant metal oxide precipitates. These oxides may have greater dielectric loss, which would increase the overall loss of the thin film.

According to the FoM, the overall performance of Li doped BST thin film was actually worse than that of undoped thin films. Despite this, there are still good reasons for Li doped BST thin films to be used to implement microwave devices. First and foremost, the Li doped BST thin film (BSTL1) exhibited a significant improvement in dielectric constant while reducing the dielectric loss and leakage current of BST thin film.

6.3 Conclusion

In this chapter of the thesis, we have presented two reports on Co and Li doped $Ba_{0.5}Sr_{0.5}Ti_{1.0}O_3$ thin films separately. The effects of doping were analyzed by modern instruments such as XRD, SEM, EDX, XPS and AFM. According to the X-ray diffraction analysis, the crystal structure of the BST thin films remained the same regardless of doping concentration. However, the microstructures of the thin films including surface roughness and grain sizes were strongly affected by the ion doping.

These changes greatly affected the dielectric properties of the thin films, as discussed in sections 6.1 and 6.2.

For Co doped BST thin film, an increase of overall performance (FoM) and decrease of dielectric loss was observed. These benefits were obtained at the cost of tunability and dielectric constant, which are essential to implement high agile devices such as phase shifters. On the other hand, the Li (1mol% and 2mol%) doped BST thin films showed an increase in dielectric constant and a decrease in dielectric losses at the same time. This type of material is highly attractive for implementing small size passive microwave devices due to the increase in dielectric constant. Based on the measured results, it is reasonable to conclude that Li doped BST can be used to implement different kinds of microwave devices depending on the application of those particular devices.

Despite the fact that neither Co or Li doped BST thin films achieved the desired dielectric properties (dielectric loss <0.01), doping by acceptor ions such as Co and Li resulted in a significant improvement in the dielectric properties compared with the undoped BST thin film. In particular, Li doped BST thin films showed improvements in both dielectric constant and dielectric loss at the same time. This feature makes it even more attractive to be used to implement frequency agile devices.

References:

[1] G. S. Wang, Y. Y. Zhang, Y. Chen, F. Cao, *et al*, "Effect of donor, acceptor, and donor-acceptor codoping on the electrical properties of $(Ba_{0.6}Sr_{0.4})TiO_3$ thin films for tunable device applications,"*J. Am. Ceram. Soc*, vol. 92, 11, 2759-2761, 2009.

[2] Y.Y. Zhang G. S. Wang, C.L Mao and X. L. Dong, "Composition dependence of structural and optical properties for sol-gel derived (100)-oriented $Ba_xSr_{1-x}TiO_3$ Thin films," *Applied Physics Letters,* vol. 91, 061104, 2007.

[3] R. Dewi, I. A. Talib, *et al,* "The effect of spin coating rate on the microstrucutre, grain size, surface roughness and thickness of $(Ba_{0.6}Sr_{0.4})TiO_3$ thin film preparation by the sol-gel process," *Materials Science-Poland*, vol. 25, 3, 657-662, 2007.

[4] Z. Y. Chen, L.E. Cross and A. S. Bhalla, "Dielectric relaxation and conduction in $SrTiO_3$ thin films under dc bias," *Applied Physics Letters,* vol. 79, 6, 818-820, 2001.

[5] K.T. Kim and C. I. Kim, "The effect of Cr doping on the microstructural and dielectric properties of $(Ba_{0.6}\ Sr_{0.4}TiO_3)$ thin films", *Thin Solid Films, vol.* 472, 26-30, 2005.

[6] L. Xiao, K. L. Choy and I. Harrison, " Co-doped BST thin films for tunable microwave applications", *Surface and Coating Technology,* vol.205, 8-9, 2989-2993, 2011.

[7] J. W, Zhai, X. Yao and L. Gao, "The influence of Co doping on the dielectric, ferroelectric and ferromagnetic properties of $Ba_{0.7}Sr_{0.3}TiO_3$ thin films," *Applied Surface Science,* vol. 255, 4521-4525, 2006.

[8] B.L Cheng, S.Y Wang, C. Wang, H. B. Lu, *et al*, "Dielectric properties of Co-doped $Ba_xSr_{1-x}TiO_3$ thin films fabricated by pulse laser deposition," *Journal of Crystal Growth,* vol. 259, 1-2, 137-143, 2003.

[9] B. L. Zhu, X. H. Sun, T. Liu, M.Y Li and X. Z. Zhao, "Dielectric and tunable properties of K-doped $Ba_{0.6}Sr_{0.4}TiO_3$ thin films fabricated by sol-gel method," *J. Appl. Phys*, vol. 99, 8, 084103, 2006.

[10] C. R. Yang, W. L. Zhang, W. C. Hu, "Fabrication and characteristics of La, Cd and Sn doped BST thin films by sol-gel method," *J mater Sci: Mater Electron*, vol.19 , 1197-1201, 2008.

[11] W. Chang, L. M. B Alldredge, S. W. Kirchoefer, and Jeffrey M. Pond, "Phase transitions and the temperature dependence of the dielectric properties in tetragonally strained Barium Strontium Titanate films," *Applied Physics Letters*, vol. 94, 053904 ,2009.

[12] M. W. Coel, C. Hubbard, E. Ngo, M. Ervin, *et al*, "Structure-property relationships in pure and acceptor-doped $Ba_xSr_{1-x}TiO_3$ thin films for tunable microwave device applications," *J. Appl. Phys*, vol. 92, 475-483, 2002.

[13] P. C Joshi M. W. Cole, M.H Ervin, M.C Wood and R.L Pfeffer, "The influence of Mg doping on the materials properties of $Ba_xSr_{1-x}TiO_3$thin films for tunable devices applications," *Thin Solid Films*, vol. 371, 1, 34-41, 2000.

Chapter 7 Non-ferroelectric material BZN

Bismuth Zinc Niobium Oxide (BZN) is considered as a non-ferroelectric material that can be used in microwave tunable devices. As mentioned in chapter 2, the literature review, BZN has two different crystal phases: (a) cubic (α phase) $Bi_{1.5}Zn_{1.0}Nb_{1.5}O_7$ (b) monoclinic (β –phase) $Bi_2Zn_{2/3}Nb_{4/3}O_7$. Since the cubic (α phase) has a higher dielectric constant and greater tunability than the monoclinic (β phase), the majority of work focus on using cubic BZN thin films to implement tunable microwave devices.

Cubic pyrochlore BZN has several attractive features for implementing microwave devices: (1) compositionally controllable temperature coefficients of capacitance (TTC) **[1]**, (2) lower crystallization temperature <1000 ^oC **[1]**, (3) less sensitive to substrate properties **[2]**, (4) very low dielectric loss of 0.0005 at 1MHz **[3]** and (5) excellent quality factor (around 100 at 10GHz) **[3]**.

BZN's microstructure varies with annealing temperature. Therefore, it is important to find out the optimized crystallization temperature. Because of the low cost of silicon substrate, several BZN thin films with composition of $Bi_{1.5}Zn_{1.0}Nb_{1.5}O_7$ were coated onto Si<111> substrates and the annealing temperatures varied from 500°C to 800°C. Although *Hiroshi Funakuba's* work had already indicated that BZN thin film is less sensitive to the strain induced by the substrate **[3]**, this work is carried out at very low frequency (100kHz) which may not be applicable to the response of BZN thin film at microwave frequencies. To study the influence of substrate, BZN thin films with composition $Bi_{1.5}Zn_{1.0}Nb_{1.5}O_7$ were deposited onto four different types of substrates: Si<111> (low resistance), Si<100> (high resistance>10,000Ω), quartz and Sapphire <0001>. The microwave dielectric properties of the BZN thin films were measured

from the metal insulated metal (MIM) capacitor and coplanar waveguide (CPW). The purpose of this work is to investigate the potential of implementing microwave devices using cubic BZN thin film.

In the following section (7.1), a brief discussion of the experimental work is presented. Sections 7.3 and 7.4 investigate the variations of properties of BZN thin films with respect to different annealing temperature and substrates. Section 7.5 investigates the tunability of BZN thin film in the MIM capacitor.

7.1 Experimental work

Organic precursor preparation

In this work, $Bi_{1.5}Zn_{1.0}Nb_{1.5}O_7$ thin films were synthesized using a modified sol gel or method which has already been discussed in section **3.4.** Previously reported processes employed 2-methoxyethanol as a solvent to improve the solubility of zinc acetate in the precursor **[4]**. However, on exposure to air, 2-methoxyethanol can be dangerous which prevents its use in many facilities **[5]**. To overcome this safety hazard, acetic acid was used in this work as the solvent.

The precursors used for the synthesis of BZN thin films were bismuth acetate (Sigma Aldrich 99.99%), zinc acetate (SigmaAldirch 99.0%) and niobium ethoxide (Sigma Aldrich, 99.95%). Bismuth acetate was dissolved in acetic acid (Sigma Aldrich 99.0%) and distilled at 120 °C on a hot plate for 10 minutes. At the same time, zinc acetate was mixed with absolute ethanol (Sigma Aldrich, 99.5%) in an ultrasonic bath at 55 °C until it had dissolved completely. Both precursors were cooled down to room temperatures and mixed in one beaker to form a clean and transparent solution. Niobium ethoxide was added to acetic acid at room temperature and subsequently dissolved into a mixture of solution containing bismuth/zinc solution to form an organic precursor solution for spin coating.

Thin film deposition methods

The procedures of thin film deposition and crystallization varied depending on the microwave devices. As mentioned earlier, two kinds of devices: coplanar waveguide (CPW) and metal insulated metal capacitor (MIM) were used to characterize the dielectric properties of the thin films. In CPW, BZN thin films were deposited onto Si<100>, Si<111>, quartz and sapphire <0001> substrates by a spin-coating process using a spin rate of 2000 rpm for 10 seconds. After the spinning, each layer was pre-annealed at 300 °C for 3min to remove organic residue and further annealed at 800 °C for 5min in a furnace. This process was repeated 12 times to reach a desired thickness of 200 nm. Finally, the thin films were fully crystallized by a 2hrs 800 ^{o}C anneal in an open furnace. The thickness of the thin film was determined by two cross section SEM images with different scales in figure 7.1(a) and (b). The distance (figure 7.1(a)) between the top and bottom of the BZN thin film is very close to 200nm. The errors in the estimated thickness are +10nm or -10nm.

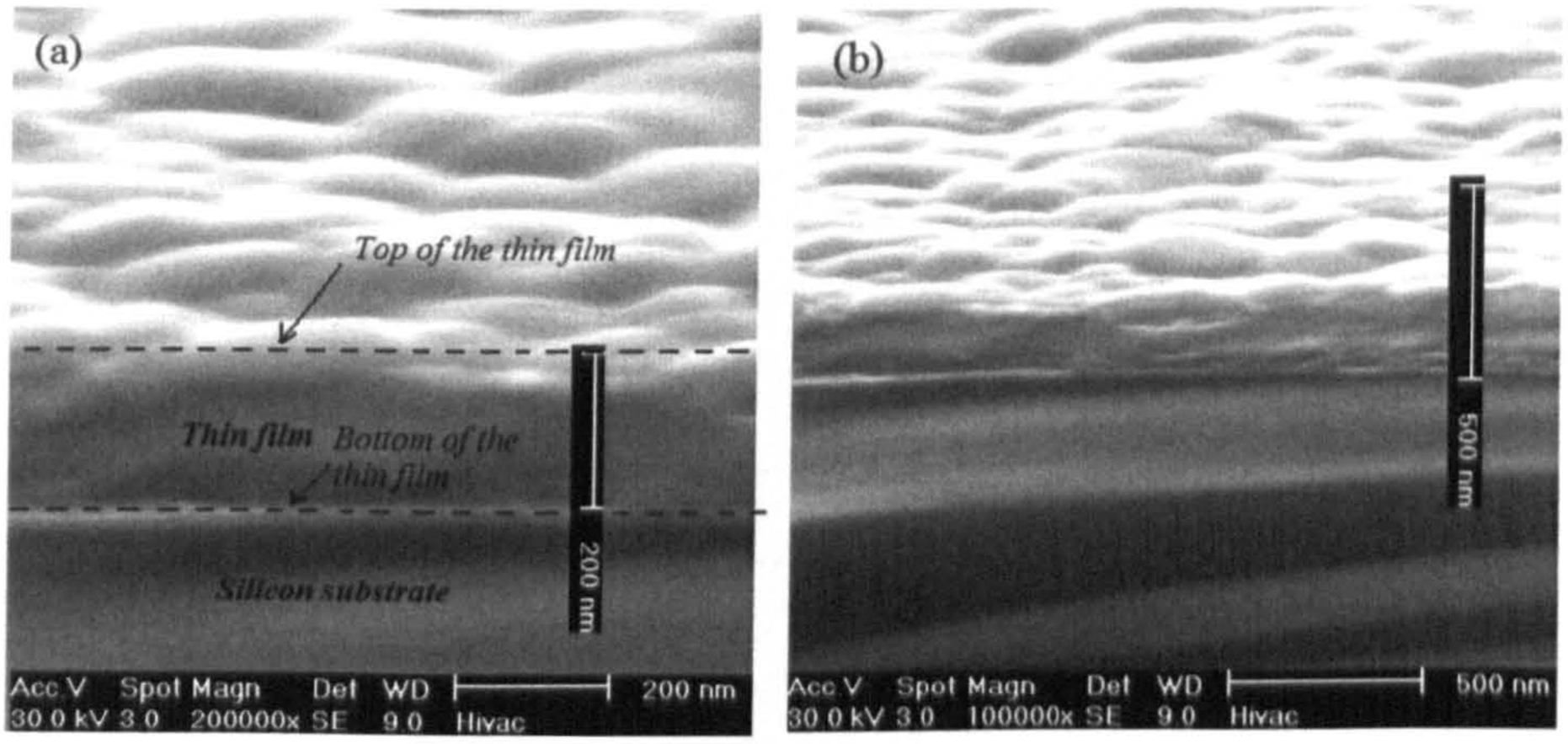

Figure 7.1 (a) the cross section image of a BZN thin film measured by a 200nm scale (b) the cross section image of the same thin film with a 500nm scale.

In MIM capacitor fabrication, BZN thin film was also spin coated onto the substrates using a spin rate of 2000rpm for 10seconds. Again, each layer was pre-annealed at 300°C for 3 min. This process was repeated for 12 times to reach the desired thickness of 200nm. Since the bottom electrodes of MIM capacitors are made of 120nm of gold, the final annealing temperature is kept at 700°C for only 10 min to avoid damaging the bottom electrode.

Characterization methods

The element compositions of the thin films are co-studied by XPS and EDX techniques. A D500 X-ray diffractometer (XRD) has been employed to identify the crystal phase of the thin films. The microstructure and surface roughness of the thin films are investigated by an environment microscopic ESEM (Philips XL30).

The dielectric properties of BZN thin film are characterized by using the CPW methods which were discussed in chapter 5. The scattering parameters (S-parameters) of the devices are measured by an Antritsu ME7808B vector network analyzer (VNA). A TRL calibration process was employed to remove the measurement errors caused by the RF probing pads. The tuning DC voltages are provided by a "Keithley" voltage source. The maximum tuning voltage was kept below 30V due to the limitation of VNA's internal DC block. The width and gaps of the CPWs used in this work were 20um and 40um respectively. As a result, the maximum tuning electric field for the CPW was $E = \frac{V}{CPW\ gap}$ =15KV/cm or 1.5V/μm. The maximum tuning field for the MIM capacitor was limited to 10V by the breakdown voltage of the thin film which corresponds to a maximum tuning electric field of $E = \frac{V}{film\ thickness}$ =500kV/cm.

7.2 Composition analysis of BZN thin film

EDX analysis

The EDX pattern of a $Bi_{1.5}Zn_{1.0}Nb_{1.5}O_7$thin film (200nm) annealed at 800°C with a Silicon <111> substrate is shown in figure 7.2. Since the deposition process and organic precursor are exactly the same for all BZN thin films with different substrates and crystallization temperatures, the compositions of BZN thin films should be identical for all samples.

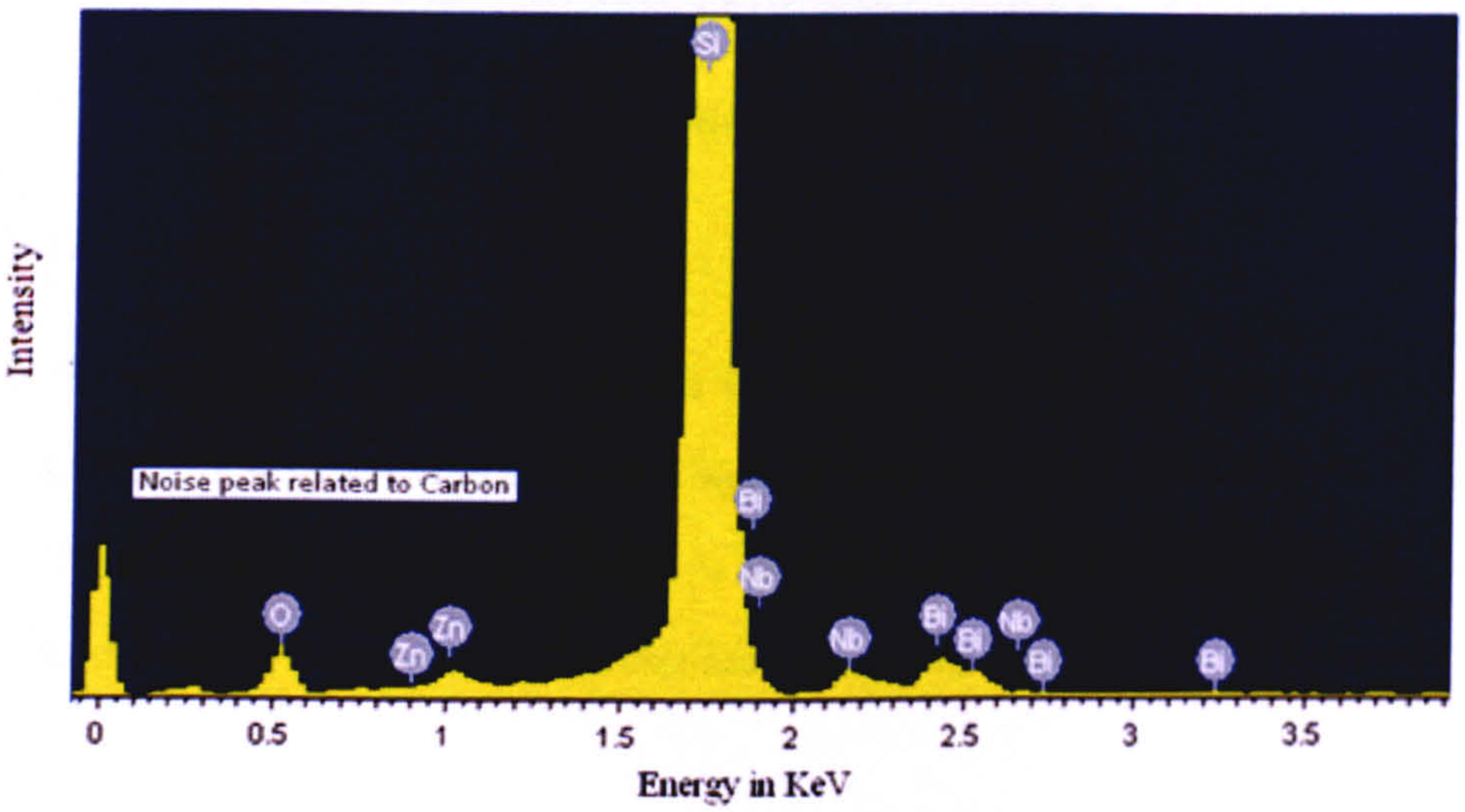

Figure 7.2 EDX pattern of cubic pyrochlore BZN thin film

According to this pattern, the detected peaks at 3.25keV, 2.75keV, 2.5keV, 1.9keV; 0.9keV, 1.0keV and 1.9keV, 2.18keV, 2.7keVcorrespond to Bi, Zn and Nb atoms of the BZN thin film. In addition, a strong silicon peak caused by the substrate was also detected between 1.6keV and 1.9keV. The EDX also quantifies the compositions of BZN thin film as shown in table 7.1. As mentioned in section, the quantified results of the EDX analysis contain large errors, because the penetration depth of the X-ray (10um) is much deeper than the thin film (200nm). Therefore, this technique only provides a rough measurement on the composition of the material. The ratio between Bi, Zn and Nb atoms is 4.15: 2.53: 4.89 or 1.64: 1.0:1.377. When these are compared

with the desired composition of $Bi_{1.5}Zn_{1.0}Nb_{1.5}O_7$, the measured results have significant deviations. Despite this, the EDX results still proves that the BZN thin film only contains the wanted Bi, Zn and Nb atoms.

Element	App Conc.	Intensity Corrn.	Weight%	Weight% Sigma	Atomic%
O K	13.90	0.7886	48.78	2.30	88.44
Zn K	1.88	0.9151	5.69	1.43	2.53
Nb L	4.91	0.8678	15.66	1.52	4.89
Bi M	8.46	0.7838	29.87	2.29	4.15

Table 7.1 the quantified results of EDX analysis

XPS analysis

The composition of the BZN film was also analyzed by employing a XPS (VG Scientific, ESCALAB MARK 2) with a MgK_α radiation source of kinetic energy hv = 1253.6 eV. The recorded kinetic energy is between 0 and 1250eV. Figure 7.3 shows the detected XPS spectrums and the obtained sample compositions.

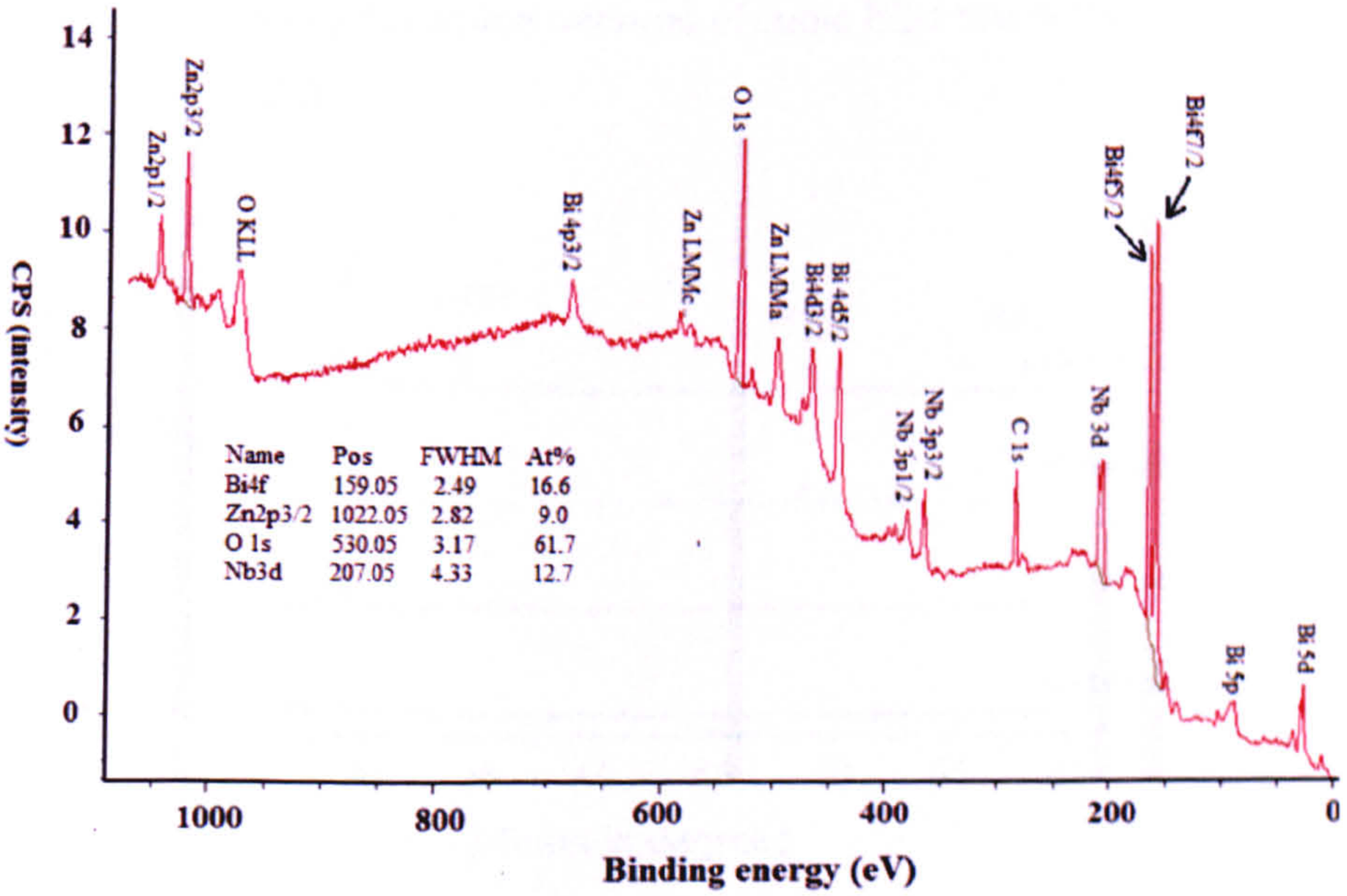

Figure 7.3 the XPS spectrum of BZN thin film

According to the figure 7.3, all expected elements including Ba, Sr and Ti have been detected. The composition ratio between Ba, Sr and Ti is 1.844: 1.0: 1.3. However, the measured composition ratio is different to the desired ratio of 1.5: 1.0 :1.5. This could be attributed to the poor sensitivity of the XPS. Due to the poor cleanness of the vacuum chamber, the unwanted element such as carbon is also detected in this spectrum.

7.3 The effect of annealing temperature on BZN thin films

7.3.1 Crystallization

To study the effects of annealing temperature, BZN thin films were deposited onto low cost Si<111> substrate with different annealing temperatures of 500°C, 600°C, 700°C and 800 °C for 2hrs. The XRD patterns of $Bi_{1.5}Zn_{1.0}Nb_{1.5}O_7$ thin films annealed at varies temperatures are shown in figure 7.4.

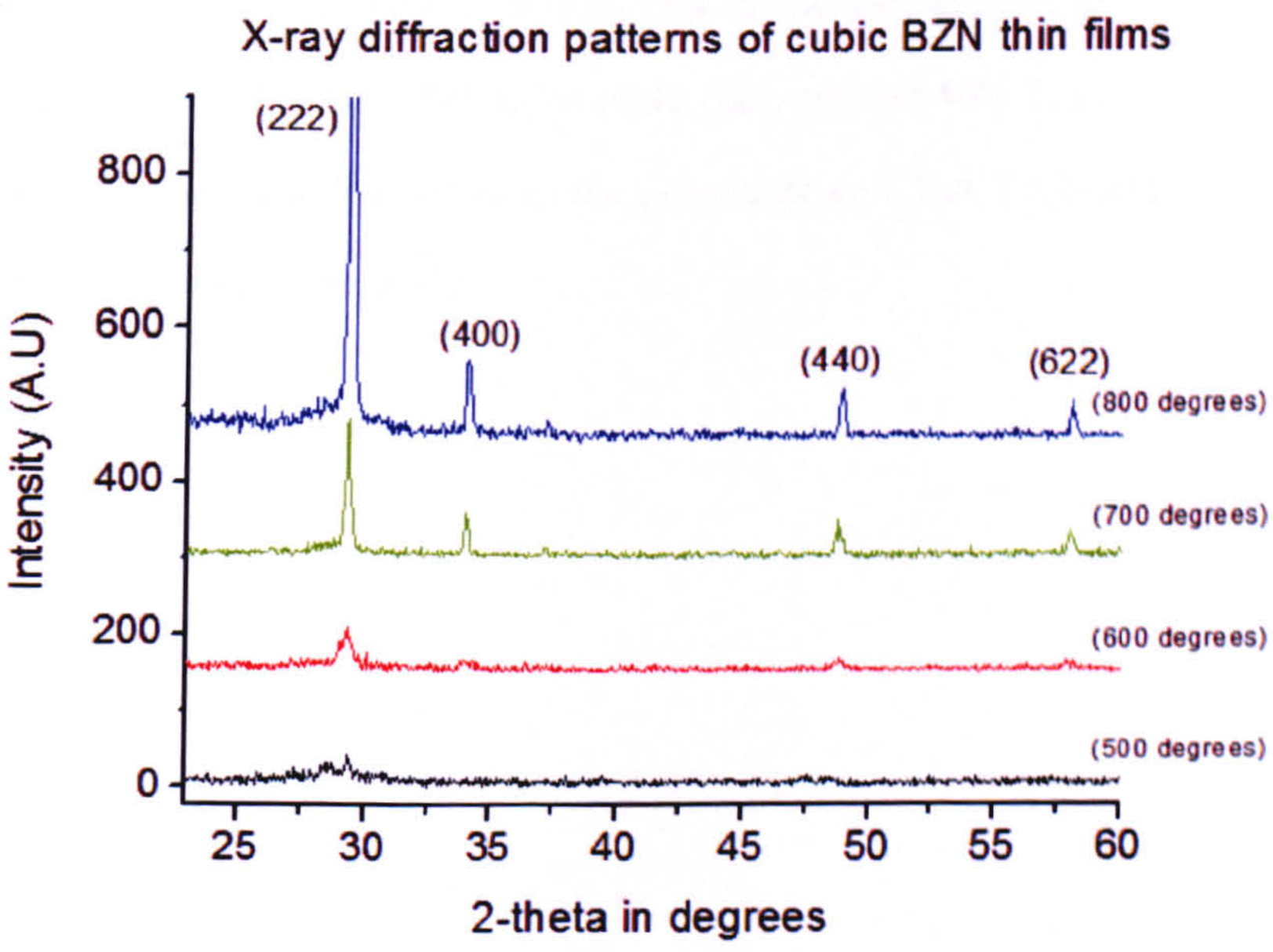

Figure 7.4 XRD patterns of the BZN thin film annealed at 500, 600, 700 and 800 °C.

The XRD pattern indicates that BZN thin film starts to crystallize at 700 °C and exhibit pure cubic pyrochlore structure. No secondary phases were detected in the diffraction pattern. The intensity of all diffraction peaks increases with increasing annealing temperature from 600°C to 800°C. The lattice parameter (calculated from "Bragg" equation) of main (222) diffraction peak and its corresponding full width half maximum (FWHM) at 800°C are 10.52Å and 0.189°, respectively.

The grain size of the thin film can be mathematically deduced from the values of FWHM of each diffraction peak by using the "Scherrer equation" (discussed in section 3.5.1).

$$D = \frac{0.9\lambda}{\sqrt{b_{sp}{}^2 - b_{st}{}^2 \cos(\theta)}} \qquad (7.1)$$

where b_{sp} is the FWHM of diffraction peak, b_{st}= 0.14° is the FWHM of the standard silicon substrate, θ is the diffraction angle of the X-ray and λ = 1.5402Å is the wavelength of the X-ray.

In this case, the grain sizes of the thin films are actually an average value calculated from the FWHM of three diffraction peaks (222, 400 and 440). The rocking curves of 222, 400 and 440 diffraction peaks are given in figure 7.5(a), 7.5(b) and 7.5(c) (in the following page), respectively.

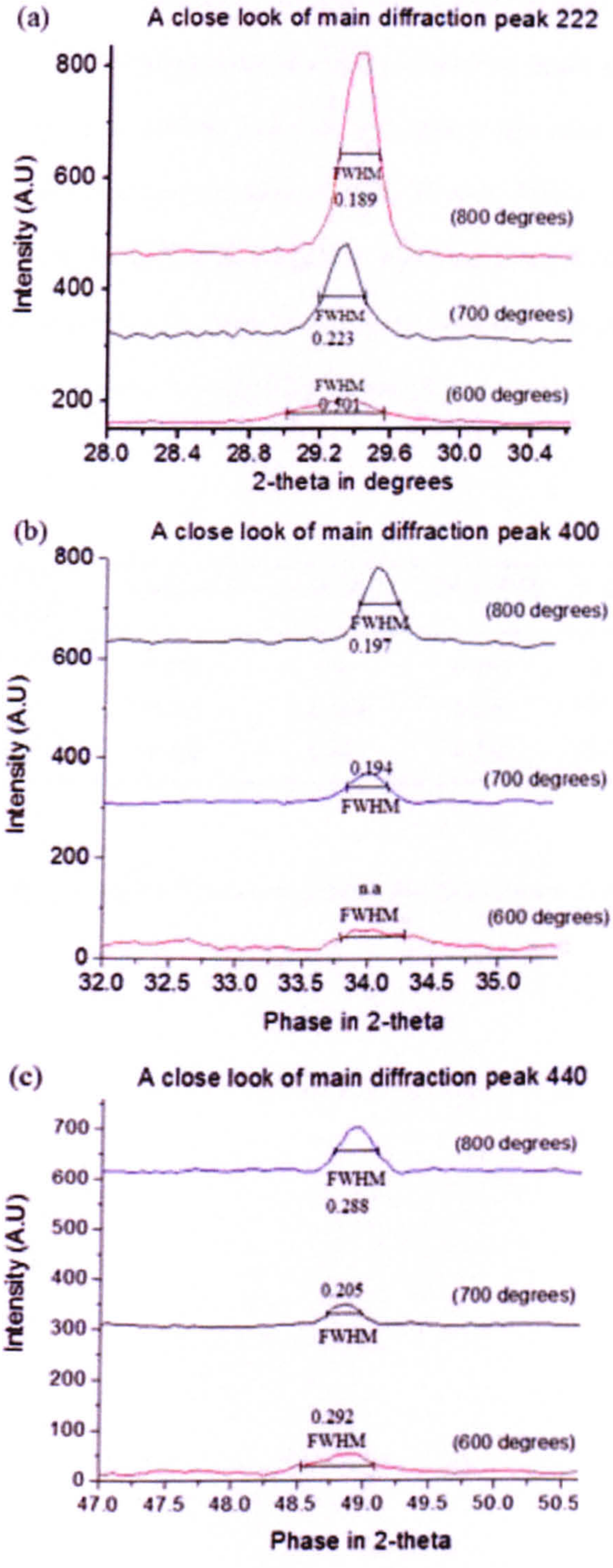

Figure 7.5: X-ray diffraction curve of (222), (400) and (440) peaks at different annealing temperature of 600, 700 and 800 °C.

The calculated grain size for each of the thin film is listed in table 7.2. Since BZN film annealed at 500°C is amorphous, the X-ray diffraction peaks are not identified and so the corresponding FWHM cannot be provided in this table. From 600°C to 700°C, the grain size increased significantly from 35nm to 146nm. However, only a slight increase in grain size (156 nm) has been observed as the temperature reaches 800°C. The increase in grain size with respect to crystallization temperature is further confirmed by SEM images in the following section (8.3.2).

Annealing temperature	peak (222)	peak (400)	peak(440)	grain size
600 degrees	0.501	n.a.	0.292	35 nm
700 degrees	0.223	0.294	0.205	146 nm
800 degrees	0.189	0.197	0.288	156 nm

Table 7.2 FWHM of the diffraction peaks of the BZN films annealed at 600, 700 and 800 °C

7.3.2 Microstructure

Figure 7.6 (a), (b), (c) and (d) shows the surface images of the BZN thin films annealed at 500, 600,700 and 800°C respectively.

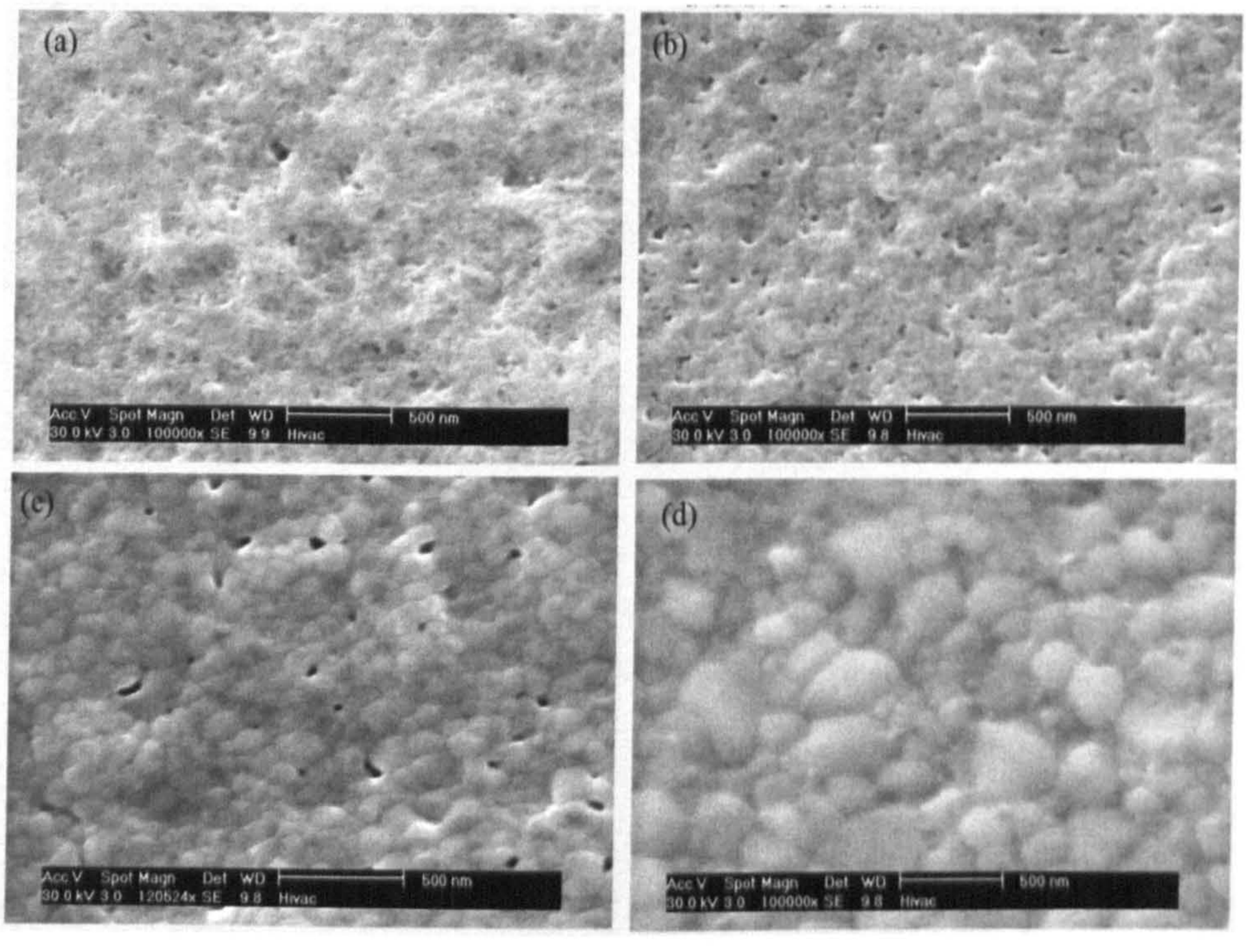

Figure 7.6 the SEM images for BZN thin films annealed at 500 (a), 600 (b), 700 (c) and 800°C (d) respectively.

In figure 7.6(a), the thin film is amorphous due to the low annealing temperature (500°C). Therefore, no grains or grain boundaries can be observed. The thin film only starts to crystallize when the annealing temperature is 600°C or above and it is fully crystallized at 800 °C. The fully crystallized thin film in figure 7.6(d) exhibits no voids or cracks and has the largest grain size. Similar to the obtained grain size (in section 7.3.1), the SEM images indicated a general trend of increasing grain size with higher annealing temperature.

7.3.3 Conclusion

The micro and crystal structures of the BZN thin films have been studied by using SEM and XRD techniques. Both SEM and XRD results indicated an increase of crystallization as the annealing temperature goes up. BZN thin film is fully crystallized at 800°C and so this is the optimum annealing temperature. The dielectric properties of the thin films were not measured for these samples because the Si<111> substrate has very high conductivity which induces large dielectric losses.

7.4 BZN crystal structure influenced by the substrates

To investigate the influence of substrate, Cubic pyrochlore BZN thin films with composition $Bi_{1.5}Zn_{1.0}Nb_{1.5}O_7$ have been deposited on four types of substrates include Si<100>, Si<111>, quartz and sapphire<0001>. In the following sections, the influence of substrate on the crystal structure, growth orientation and lattice mismatch of the BZN thin films will be discussed.

7.4.1 Crystal structure

BZN Crystal structure

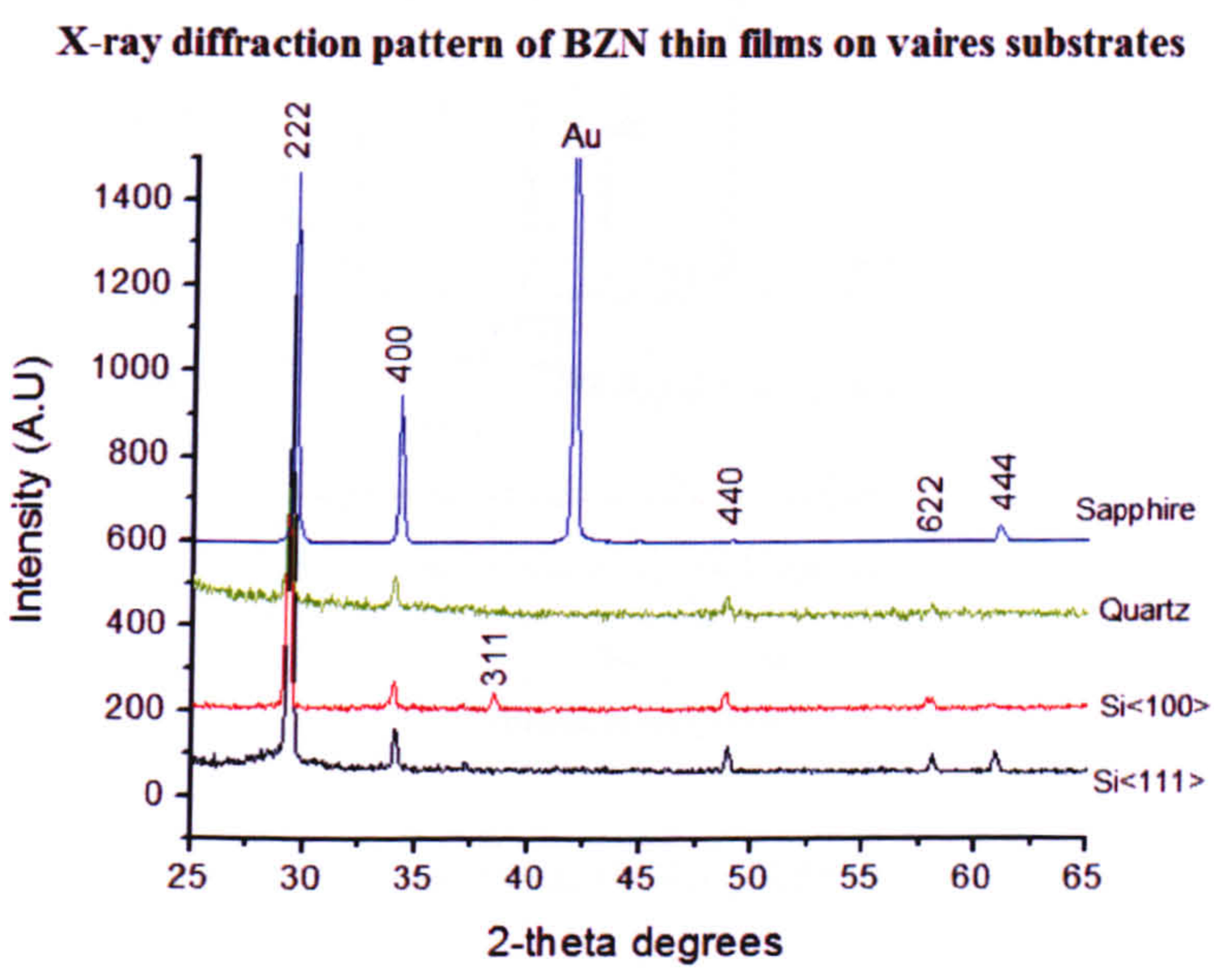

Figure 7.7: X-ray diffraction patterns of BZN thin films grown on Si<111>, Si<100>, quartz and Sapphire <0001> substrates.

Figure 7.7 shows the XRD patterns of the BZN thin films on four different substrates. The X-ray diffraction peaks of all samples show the cubic phase pyrochlore structure. There is no secondary crystal phase. However, the X-ray diffraction intensities of

BZN thin film on quartz substrate are very weak. The diffraction peak (444) can not be observed in this sample. This indicates poor crystallization of the material.

BZN crystal orientation

Although the crystal phase of BZN films is not affected by the substrates, the crystal orientation for each thin film varied significantly. The crystal orientations of the thin films are studied from X-ray diffraction intensities of each peak.

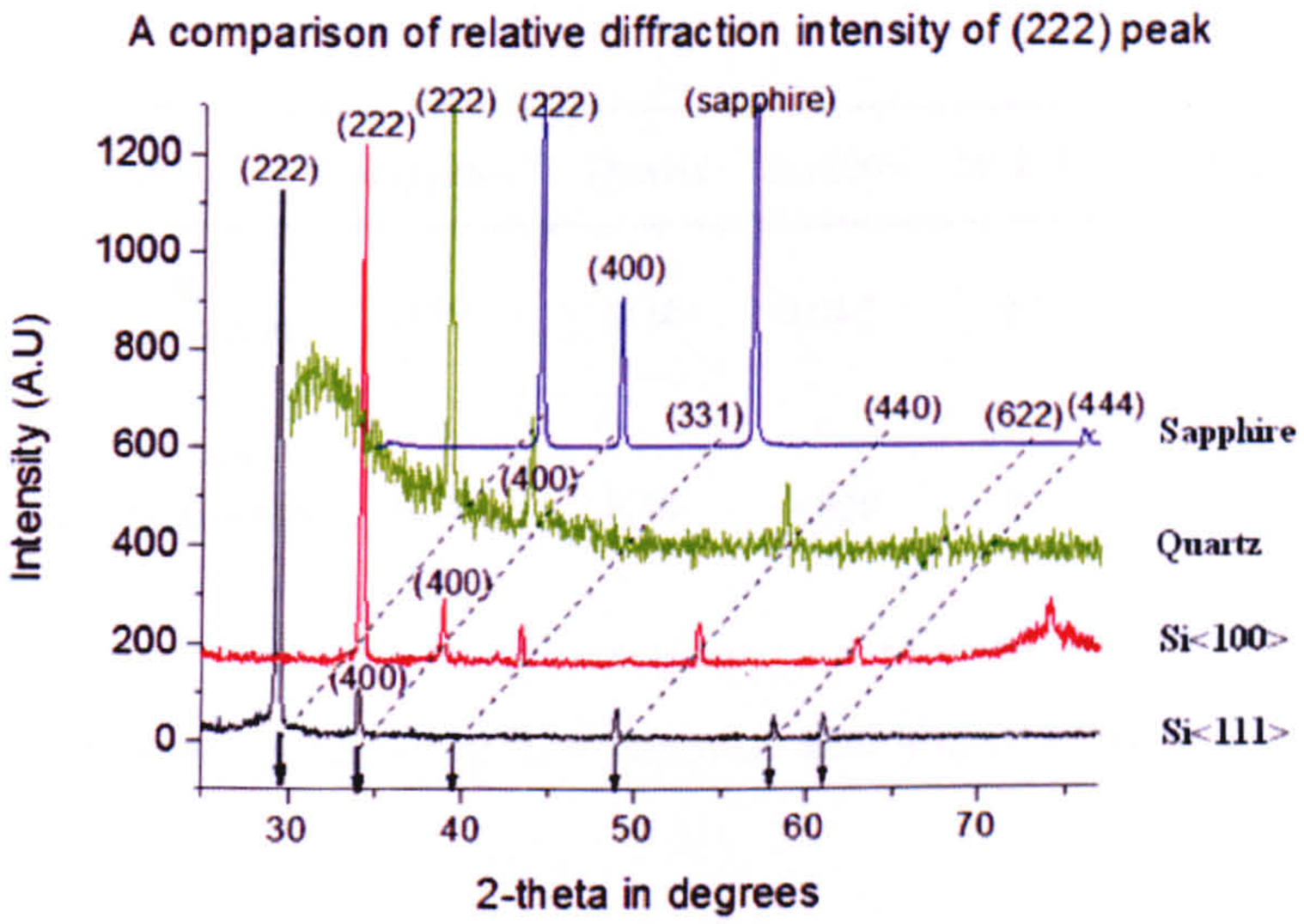

Figure 7.8 a close look of the X-ray diffraction intensity

Figure 7.8 compares the X-ray diffraction intensity of (222) main peak with respect to the other peaks. Although all of the BZN films have the preferred crystal growth (222) orientation, the thin film on the sapphire <0001> substrate shows stronger growth intensity in the c-axis (400). The orientation of the BZN thin films can also be analyzed by using the orientation factor. Based on "Lotgering's theory" **[6],** the orientation factors are calculated from the following equations:

$$F = (P - P0)/(1 - P0) \qquad (7.2) \qquad P = \sum I(abc) / \sum I(hkl) \qquad (7.3)$$

In equations 8.1 and 8.2, *F* is the orientation factor with respect to a reference plane *(abc)*, where *(abc)* indicates the Miller indices. *P* is the textured thin film and so it means the ratio of the sum of intensities of a particular diffraction of plane *(abc)* to the sum of all diffractions. *P*0 is the equivalent ratio for "BZN powder" of the target with random orientation. The orientation factor F lies between 0 and 1. When F = 0, it indicates a film with no preferred crystal orientation or random orientation while F=1 indicates an epitaxial film with only one preferred growth orientation [6]. Using equations 8.1 and 8.2, the orientation factors of the BZN thin films with different substrates were determined and are listed in the following table (7.3).

Substrate	Sapphire	Quartz	Si<100>	Si<111>	BZN powder
the texture of the thin film p(400)	0.29	0.16	0.087	0.08	0.08
Orientation factor (C-axial oreintation) (400)	0.30	0.10	0.008	0.0	0.0

Table 7.3 Orientation factors of BZN thin films with respect to different types of substrates

According to this table, the growth orientation factors of the (400) peaks are 0.0, 0.008, 0.10 and 0.30 for BZN thin film deposited on Si<111>, Si<100>, quartz and sapphire respectively. This indicates that the crystal orientations of BZN thin films can be affected by the substrate materials. This may lead to a change in the dielectric properties of BZN thin films.

Strain induced by the substrate

Figure 7.9 shows the rocking curve of the main (222) diffraction peaks with different substrates. The diffraction angles of BZN 222 peaks are 29.300^o, 29.345^o, 29.351^o and 29.388^o for BZN thin films on Si <111>, Si <100>, quartz and sapphire <0001> substrates respectively.

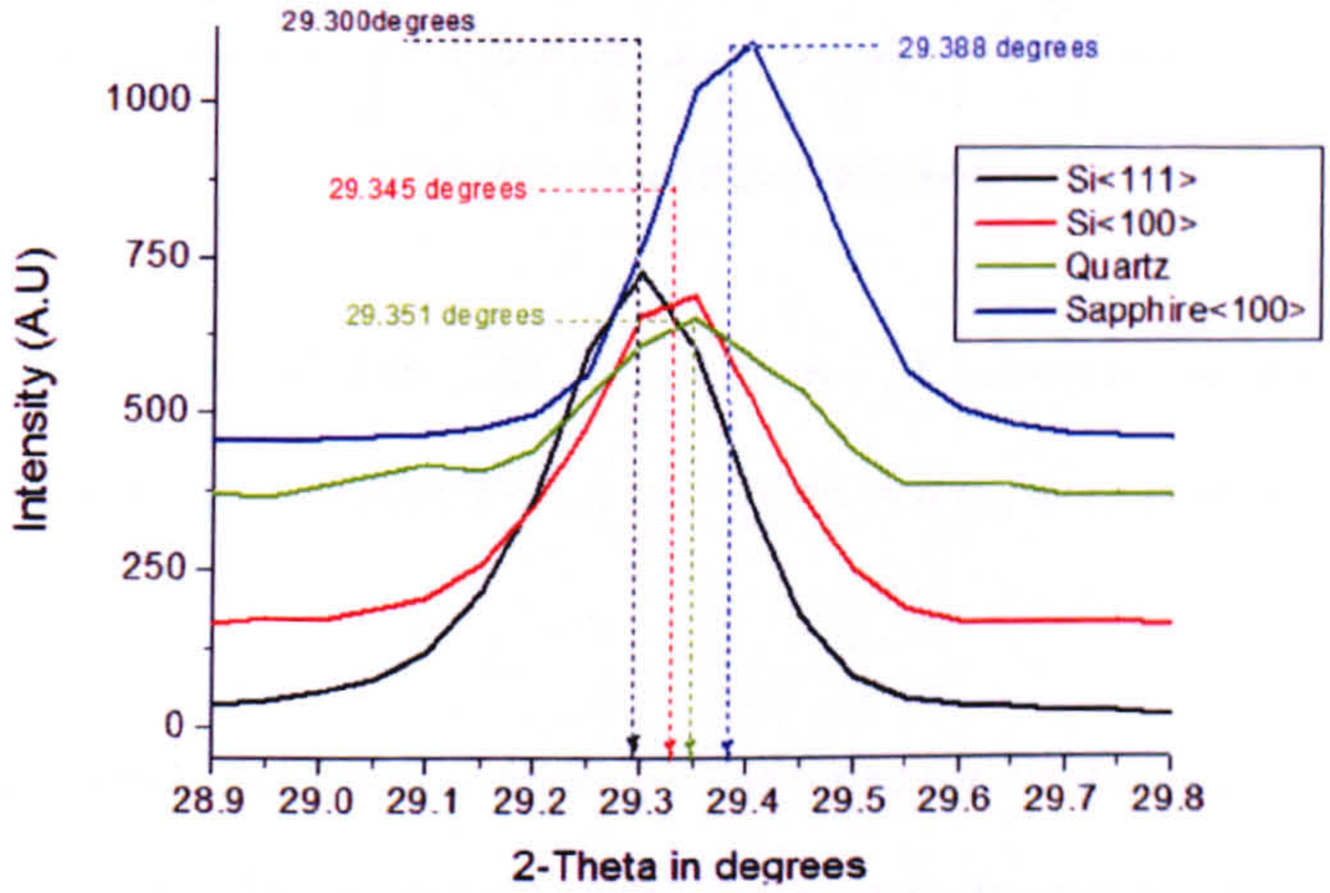

Figure 7.9 the diffraction curves of 222 diffraction peaks with Si<100>, Si<111>, quartz and sapphire <0001> substrates

By using the "Bragg" equation, the lattice space or (*d-space)* of BZN (222) can be calculated from the positions of the diffraction angles of 222 peaks (given by figure 7.9). Figure 7.10 plots the d-space as a function of substrate thermal expansion coefficient.

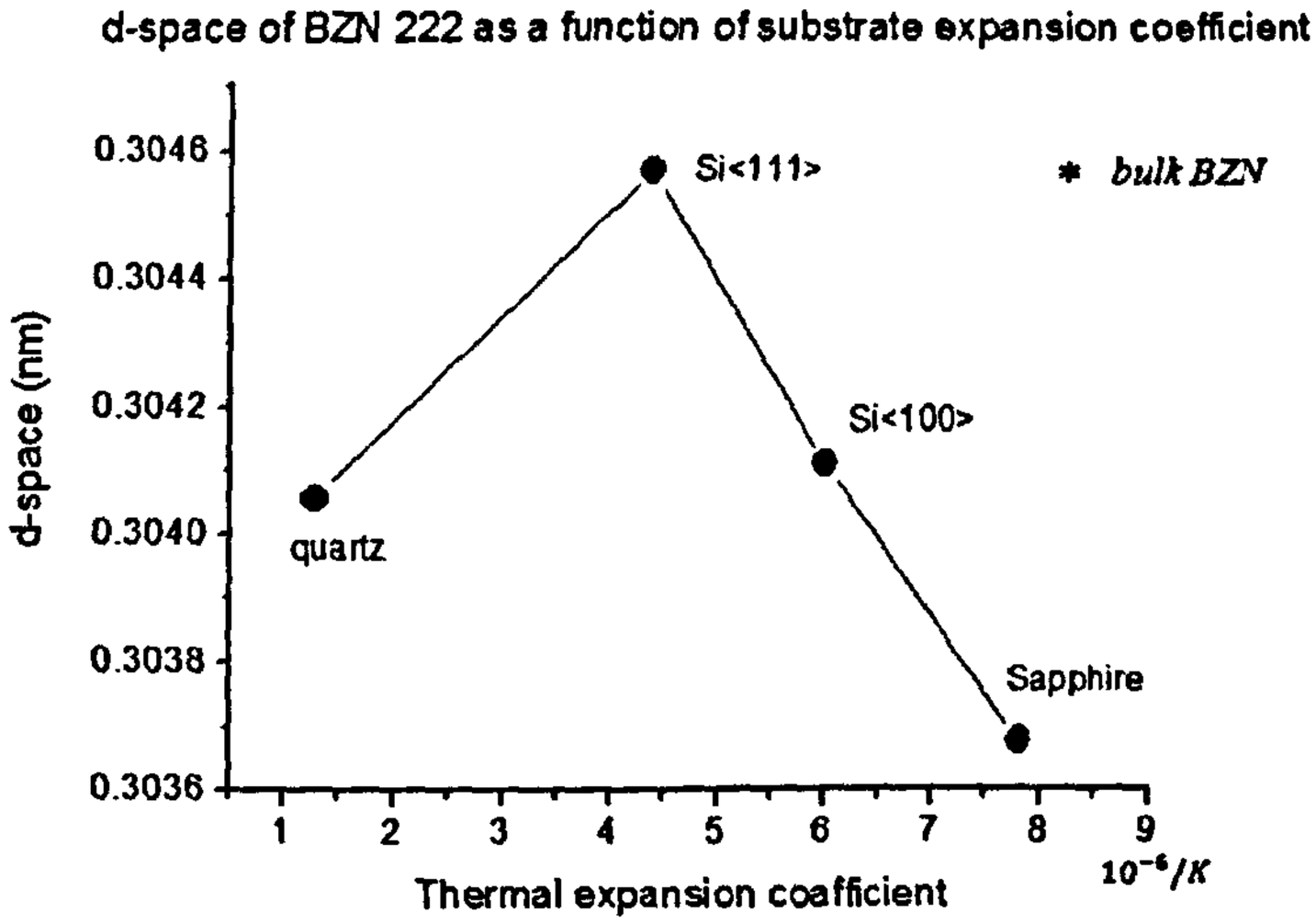

Figure 7.10 d-space of BZN 222 as a function of substrate thermal expansion coefficient. The d-space of bulk BZN is also given in this figure indicated by symbol of (*).

The *d-space* of bulk BZN is also shown on this figure for comparison. As shown, the *d-space* of BZN thin film on Si<111> substrate is nearly the same as the lattice of the *bulk* BZN. The maximum *d-space* mismatch between the BZN thin film (on sapphire) and bulk BZN is 0.32%.

7.4.2 Microstructure

The microstructures of the BZN thin films are investigated by using AFM and SEM. Figure 7.11(a), (b) and (c) shows the SEM images for the surface of BZN thin films with Si<111>, Si<100> and sapphire<0001> substrate respectively. Due to the poor conductivity of quartz, a clear SEM image can not be taken from the surface of BZN thin film with quartz substrate.

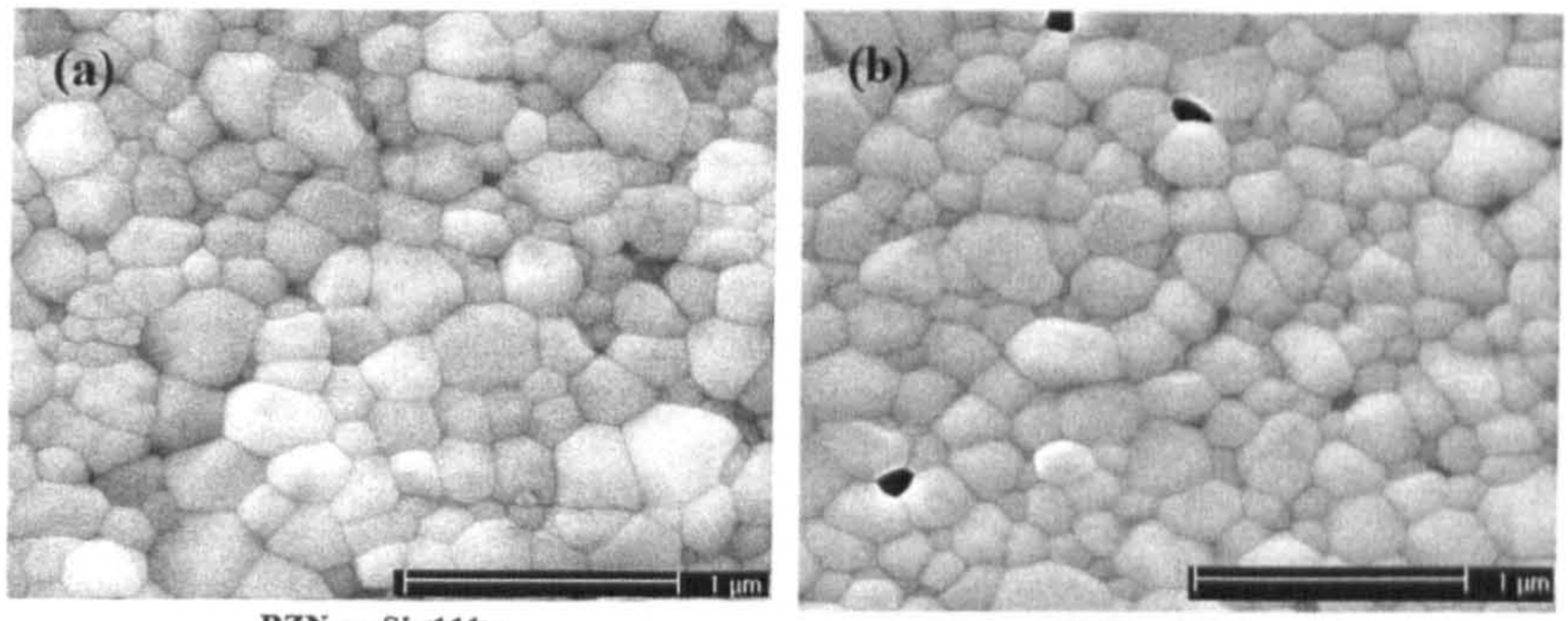

BZN on Si<111> **BZN on Si<100>**

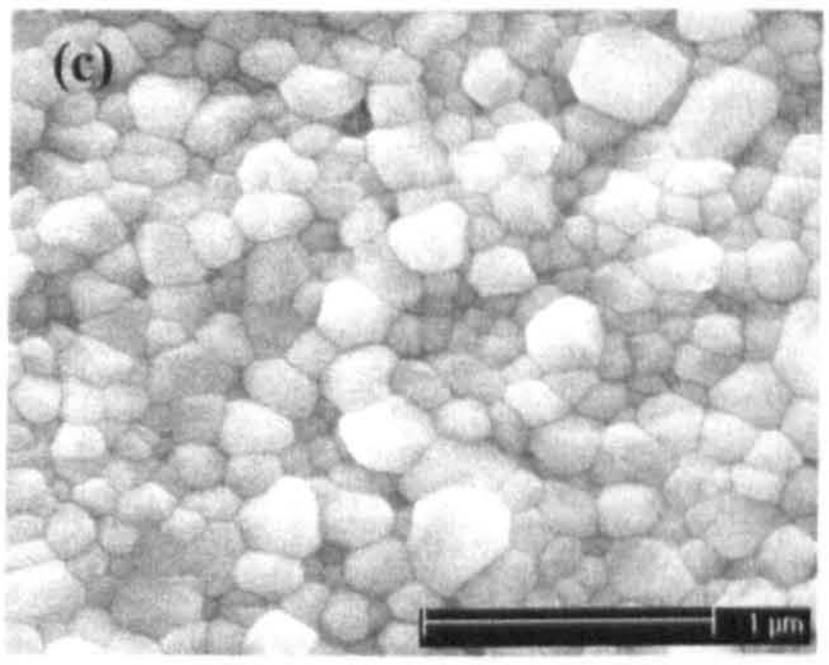

BZN on Sapphire

Figure 7.11: SEM images for BZN thin films on (a) Si<111>, (b) Si<100> and (c) Sapphire substrates.

According to the figure, all the BZN thin films are crystallized and crack free. However, voids are clearly observed on the surface of BZN thin film (figure 7.11(b)). Due to the rough surface of BZN thin films, the observed grain size of the BZN thin film varies between 100nm and 400 nm. AFM images in figure 7.12 provide more meaningful information about the thin films' grain size and their corresponding surface roughness. According to figure 7.12(a) and (c), BZN thin film with Si <111> and Si<100> substrates have similar grain sizes between 400nm and 500nm. The thin film on a sapphire substrate shows a smaller grain size of 300nm. The smallest grain size (less than 200nm) is found in figure 7.12(g) where BZN thin film is deposited on amorphous quartz substrate.

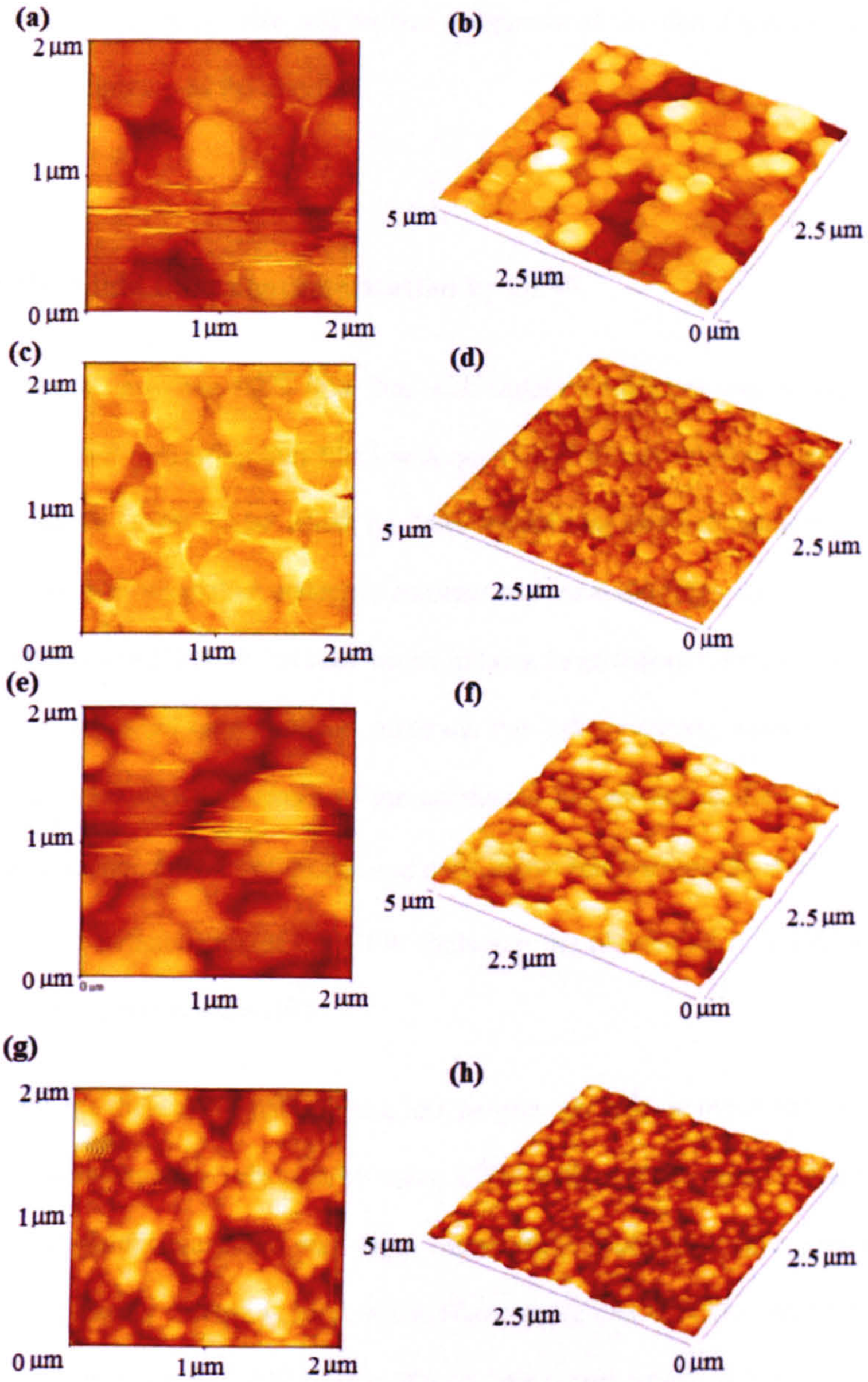

Figure 7.12(a, b): AFM images for BZN thin film on Si<111> (c, d): AFM images for BZN on Si<100>; (e, f) AFM images for BZN thin film on sapphire; (g, h): AFM images for BZN thin film on quartz.

According to the AFM results, the surface roughness are: 6.8nm, 2.99nm, 27.37nm and 17.56nm for BZN thin films deposited on Si <111>, Si <100>, sapphire and quartz respectively. In general, both the SEM and AFM results show that the microstructures of the BZN thin films are highly dependent on the types of substrates.

The variations in grain size and surface roughness of the thin films can affect the dielectric properties of the thin film.

7.4.3 BZN thin films characterization by CPW

In this work, only one BZN thin film with sapphire substrate was measured. The reasons for not measuring thin films with quartz and silicon substrates are: (1) BZN film grown on quartz wafer which has poor crystal structure and smaller grain size. This could lead to smaller dielectric constant and tunability [7]; (2) Si<111> wafer has very low resistivity of 20Ω/cm which induces large leakage current loss; (3) For thin films deposited onto a silicon substrate, the leakage current caused by the DC tuning field between the centre of the conductor and ground of the CPW is large enough to change the bias of diodes and other active components [8]. This effect will change the characteristics of the CPW including the phase shift of CPW which is related to the phase constant (β).

Therefore, the dielectric tunability and loss tangent can only be measured from BZN thin film with sapphire substrate by using CPW method. The gap and width of the CPW wave guides are 20um and 40um respectively. Since the upper limit for the applied DC tuning voltage is 30V, a 15kV/cm tuning electric field can be built up between the gaps of the CPW (gap = 20um). The actual length of the CPW line is 1500μm. The measured results for the dielectric constant and dielectric loss between 1GHz and 20GHz are shown in figure 7.13(a) and (b). According to this figure, the dielectric loss and dielectric constant have not been altered despite applying a DC voltage of 30V. In both figures, the dielectric constant drops sharply from 500 (1 GHz) to 140 (10GHz) and stabilizes above 10GHz. The unexpected high dielectric constant at lower frequency (<5GHz) could be the result of TRL calibration errors at the lower frequency. As mentioned in chapter 6 and 7, the TRL calibration has very large errors when the phase shift of the measured transmission line at below20°.

Furthermore, the dielectric relaxation may also contribute to the decrease in dielectric constant.

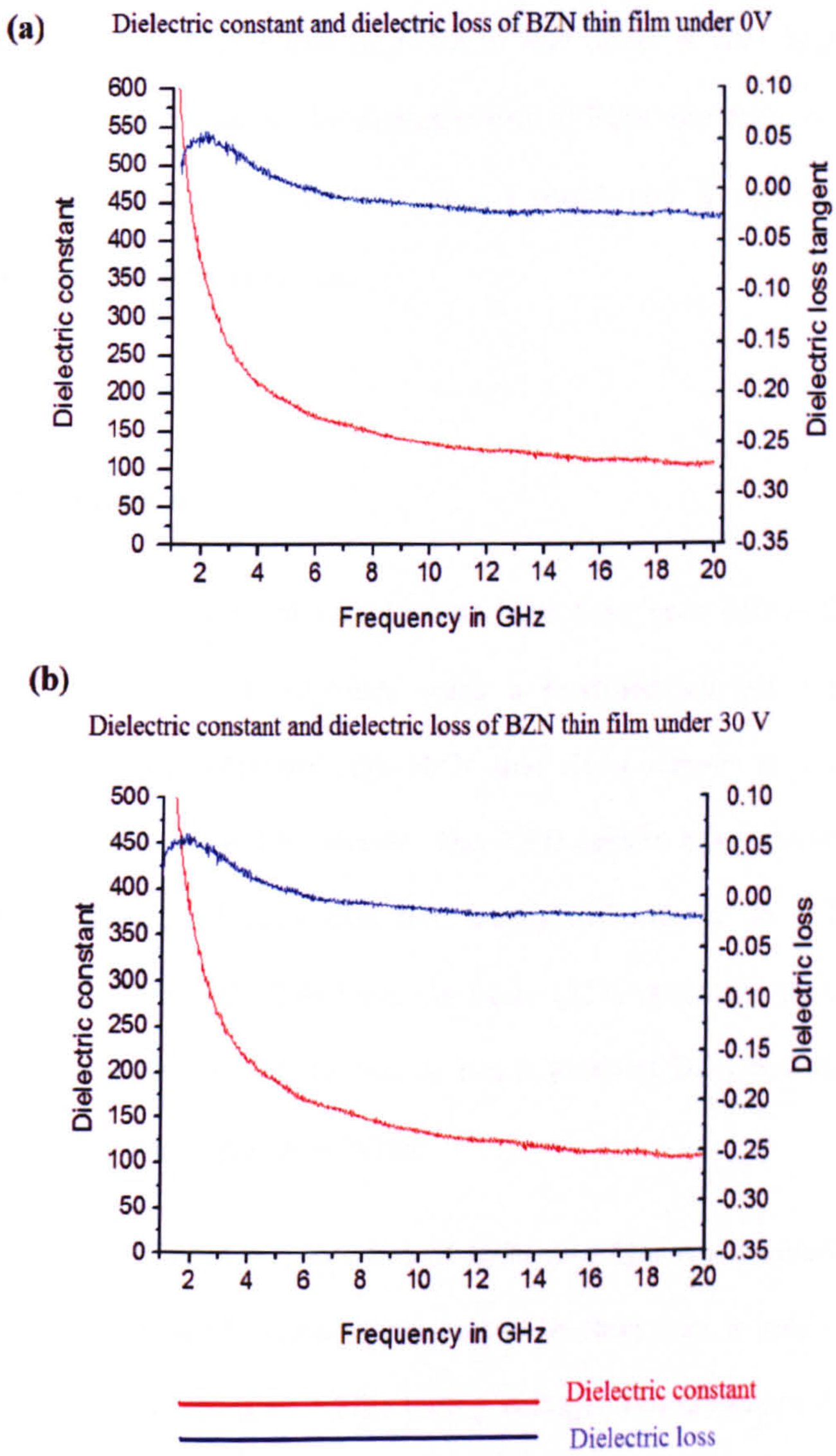

Figure 7.13 (a) Dielectric constant and loss tangent for BZN thin film with DC voltage of 0V (b) Dielectric constant and loss tangent for BZN thin film with DC voltage of 30V (15kV/cm)

The measured dielectric losses for BZN thin films are lower than 0.0, which is unrealistic. According to equation 5.26, this is caused by the overestimation of the

conductor attenuation (α_c) which is related to the skin effect. In this case, the influence of skin effect is particularly strong, since the thickness (140nm) of the metal (aluminium) conductor is much smaller than its skin depth (0.8um) at 10GHz. Therefore, the conductor loss (α_c) due to skin effect is very large compare to the attenuation (α_d) caused by the dielectric loss of BZN thin film. A small error in the measurement of CPW attenuation (α_{cpw}) could have a significant effect on the dielectric loss of BZN thin film.

7.4.4 Conclusion

In this work, cubic pyrcohlore BZN thin films have been successfully deposited on four different types of substrates using a modified sol gel method (chelation). Regardless of the substrates, the BZN thin films remain in a cubic pyrochlore structure without secondary phases. The XRD results have shown that the crystal growth orientation of BZN thin film varies with respect to different substrates. Although, all BZN thin film have the same (222) preferred growth orientation, a relatively strong growth orientation in c-axis (400) of BZN has also been found in BZN thin film with sapphire substrate.

The microwave dielectric properties of BZN thin film was measured using a CPW method. The measured dielectric constant of the thin film is between 140 (10GHz) and 100 (20GHz) regardless of the tuning voltage. The measured dielectric constant is much smaller than the value (190 at 0V) reported by *Jiwei Lu and Jaehoon Park* [9] who measured the thin film at 1MHz. The measured results also show that the applied DC voltage of 30V has not resulted in a change of dielectric constant. Thus it is reasonable to conclude that cubic pyrochlore BZN materials are unsuitable for implementing planar microwave devices due to the poor tunability. As mentioned in chapter 2, a large electric field allows the source of polarization to be clamped out and so provides a mechanism for the dielectric tunability of BZN material. Therefore,

a much larger DC electric field is required to tune the dielectric constant of the thin film.

7.5 BZN thin films employed by MIM capacitors

To enhance the tuning field while keeping the DC voltage below 30V, a MIM capacitor was fabricated to characterize the dielectric tunability of BZN thin film. In this MIM capacitor, a BZN thin film was synthesized by a chelation method and deposited onto gold (Au) electrode on quartz substrate. To avoid damaging the gold electrode, the annealing temperature is kept at 700°C for only 10min. This leads to a variation in the crystal and microstructures of BZN thin films in MIM capacitor. Therefore, the micro and crystal structures of the thin film in the capacitor are re-examined by XRD and AFM techniques.

7.5.1 Crystallization of BZN thin films

Figure 7.14 compares the XRD patterns of the BZN thin films deposited on Au/quartz and pure quartz substrates. According to this figure, both BZN thin films have a cubic pyrochlore structure. However, the thin film deposited on Au/quartz substrate shows a tiny (021) peak corresponding to monoclinic phase. The appearance of monoclinic phase in BZN thin film may be caused by the shorter (10min) and lower temperature (700°C) anneal.

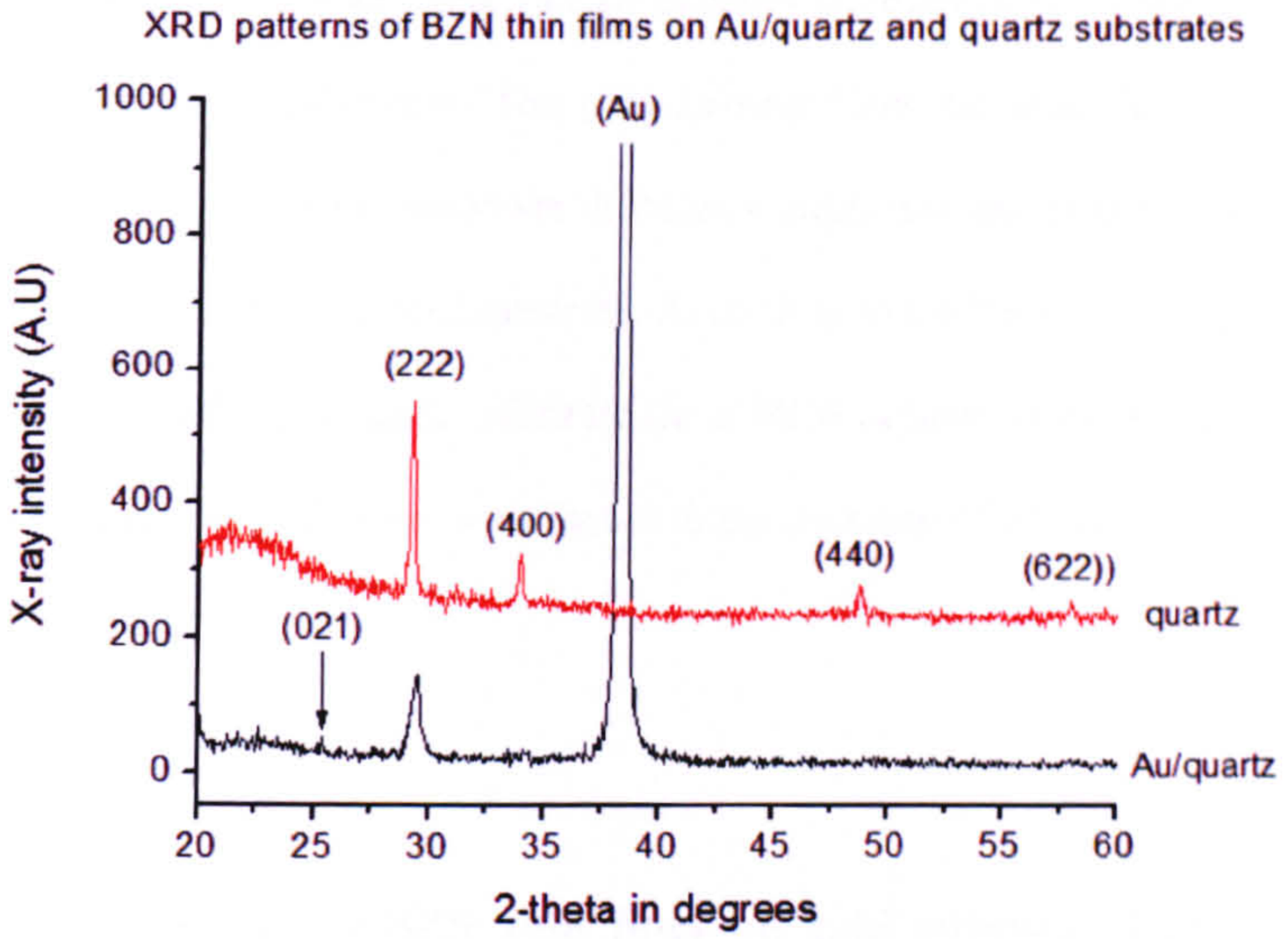

Figure 7.14 XRD pattern of BZN thin film on Au/Quartz and quartz substrates

The figure also shows that the thin film on Au/quartz substrate has only one main 222 diffraction peak and the rest of the peaks (400, 440, 622) are not observed. This implies that BZN thin film grown on Au/quartz substrate with lower annealing temperature (700°C) is not fully crystallized.

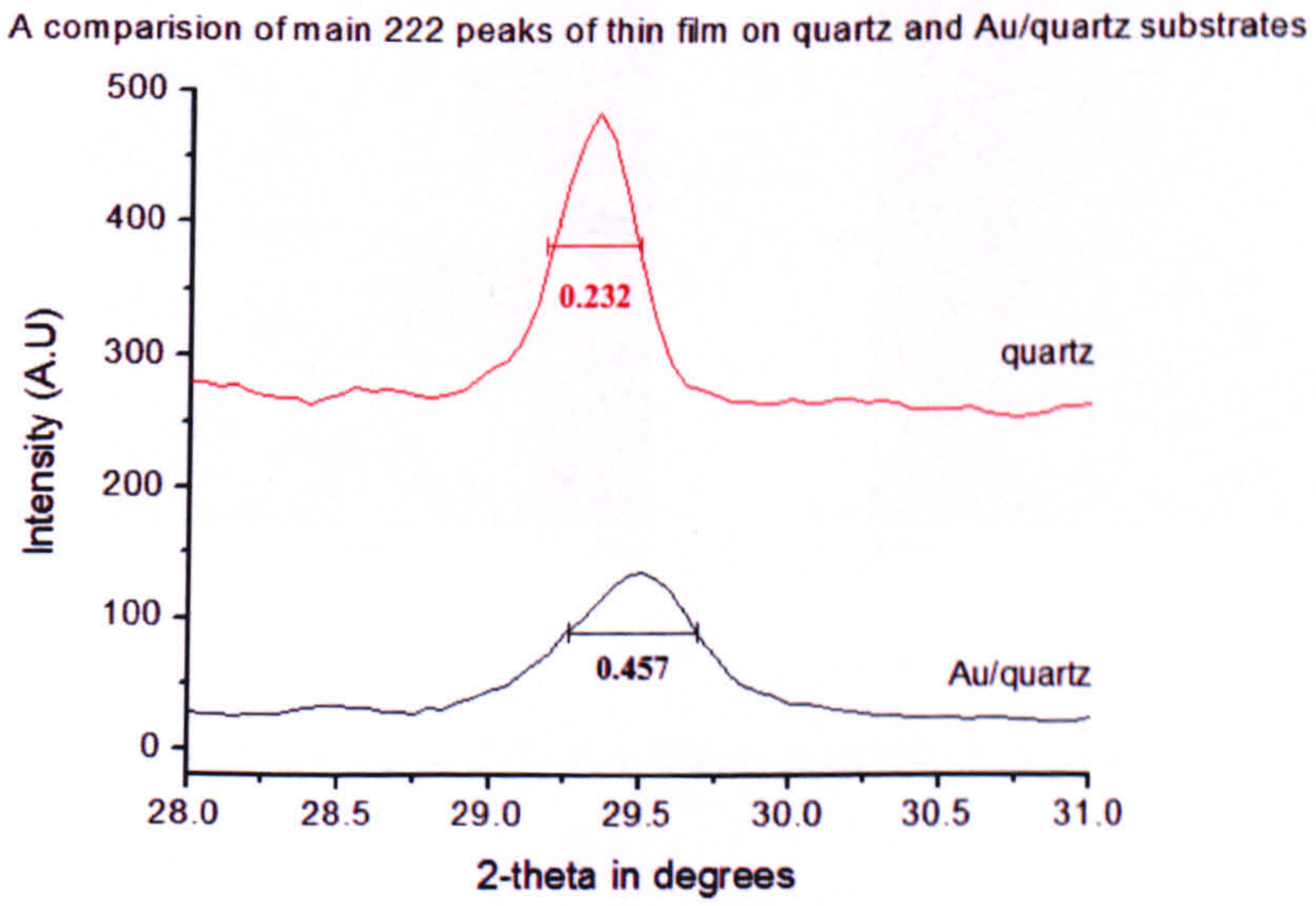

Figure 7.15: diffraction curves of BZN 222 peaks with Au/quartz and quartz substrate

Figure 8.18 provides a closer look of 222 diffraction peaks of BZN thin films with quartz and Au/quartz substrates. The peak arising from the thin film with quartz substrate is slightly shifted to the lower diffraction angle and has smaller FWHM than the thin film grown on Au/quartz substrate. According to the "Scherrer" equation, the BZN thin film on the Au/quartz substrate (in a MIM capacitor) has a smaller grain size. The decrease of grain size is attributed to the decrease of annealing temperature from 800°C to 700 °C.

7.5.2 Microstructure of BZN thin films on gold covered Si and quartz substrates

Since the surface of the BZN film is not perfectly flat, the SEM images cannot provide meaningful information about the grain size of the thin films. The microstructures of the BZN thin films were analyzed by using AFM images. Figure 7.16(a) and (b) shows the AFM images of BZN thin films on quartz and Au/quartz respectively.

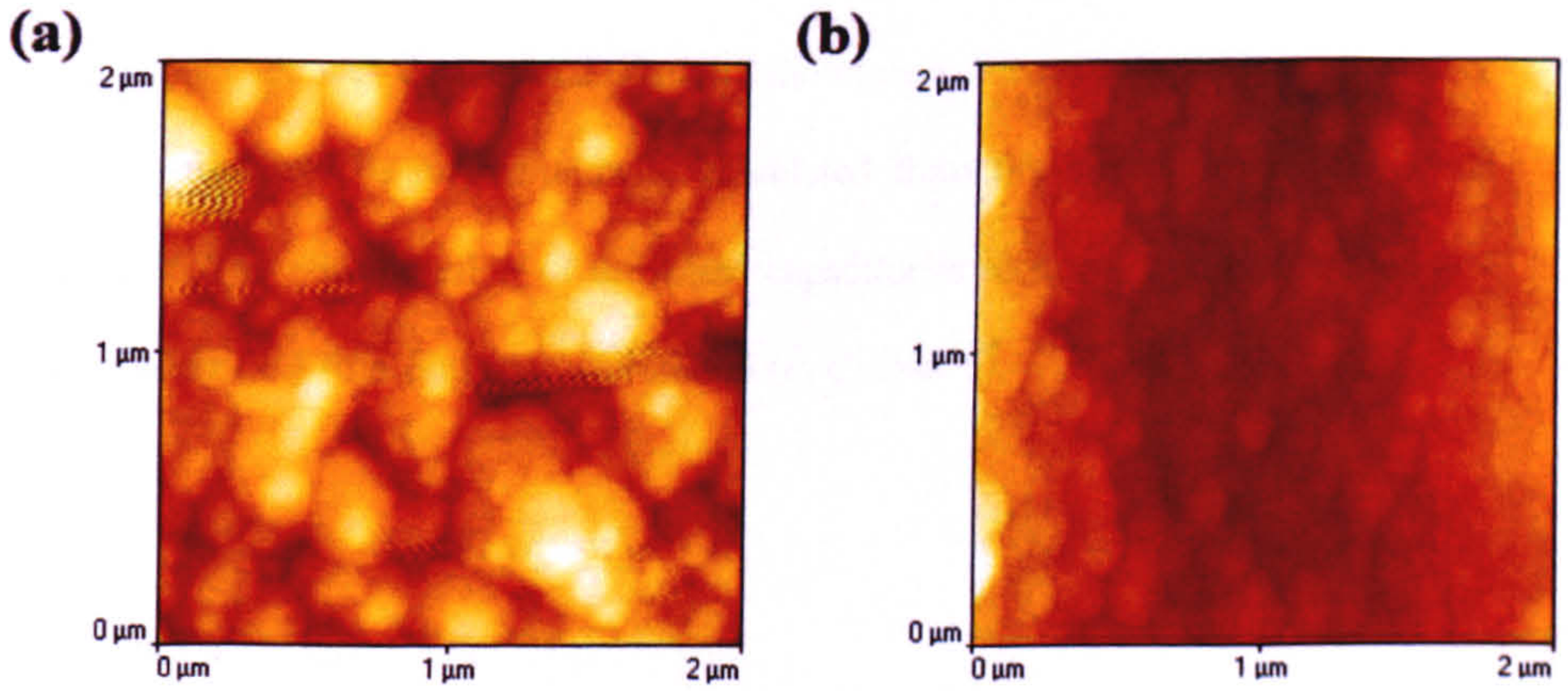

Figure 7.16 (a) AFM image of BZN thin film on quartz (b) AFM image of BZN thin film on Au/quartz

According to the above figures, the grain size of BZN film on Au/quartz substrate is smaller than the grain size of thin film deposited on quartz. This observation matches

the mathematical analysis using "Scherrer equation". The measured surface roughness is 17.56nm and 2.06nm for BZN thin films on quartz and Au/quartz.

7.5.3 MIM capacitor measurement

The microwave dielectric properties of BZN thin film are characterized by measuring a MIM capacitor between 0GHz and 40GHz with different DC tuning voltages. In this work, the size of the capacitor is 100 um^2 and the thickness of the top/bottom electrodes are made of 140nm gold metal. To avoid electric field breakdown, the DC voltage was kept below 10V for which a maximum field of 500kV/cm can be achieved in the capacitor. The tuning DC voltages are 3V, 5V, 8V and 10V or $E = \frac{V}{d}$ are 150kV/cm, 250kV/cm, 400kV/cm and 500kV/cm where d is the thickness of thin film (200nm) and V is the applied voltage. A "lightning" vector network analyzer (VNA) has been used to measure the reflection coefficient (S11) of the MIM capacitor. Then the measured data is transformed into the impedance of the capacitor. As discussed in chapter 5, an Open-through de-embedding process has been used to remove the parasitic capacitance of the MIM capacitor so that the actual impedance of the capacitor was determined. Finally, the dielectric constant and loss tangent of the thin film can be mathematically calculated from the impedance of the actual capacitor. The configuration of the MIM capacitor is identical to the capacitor that was used in BST thin film characterization (in chapter 5).

Dielectric tunability

The measured dielectric constants with different DC voltages are displayed in the following figure (7.17). In general, the dielectric constant of BZN thin film gradually decreases as the frequency goes up from 0GHz to 20GHz. As the tuning voltage increased from 0V to 10V, the dielectric constant of the BZN thin film drops from 130 to 126 at 10GHz. The calculated dielectric tunability is 3.0%.

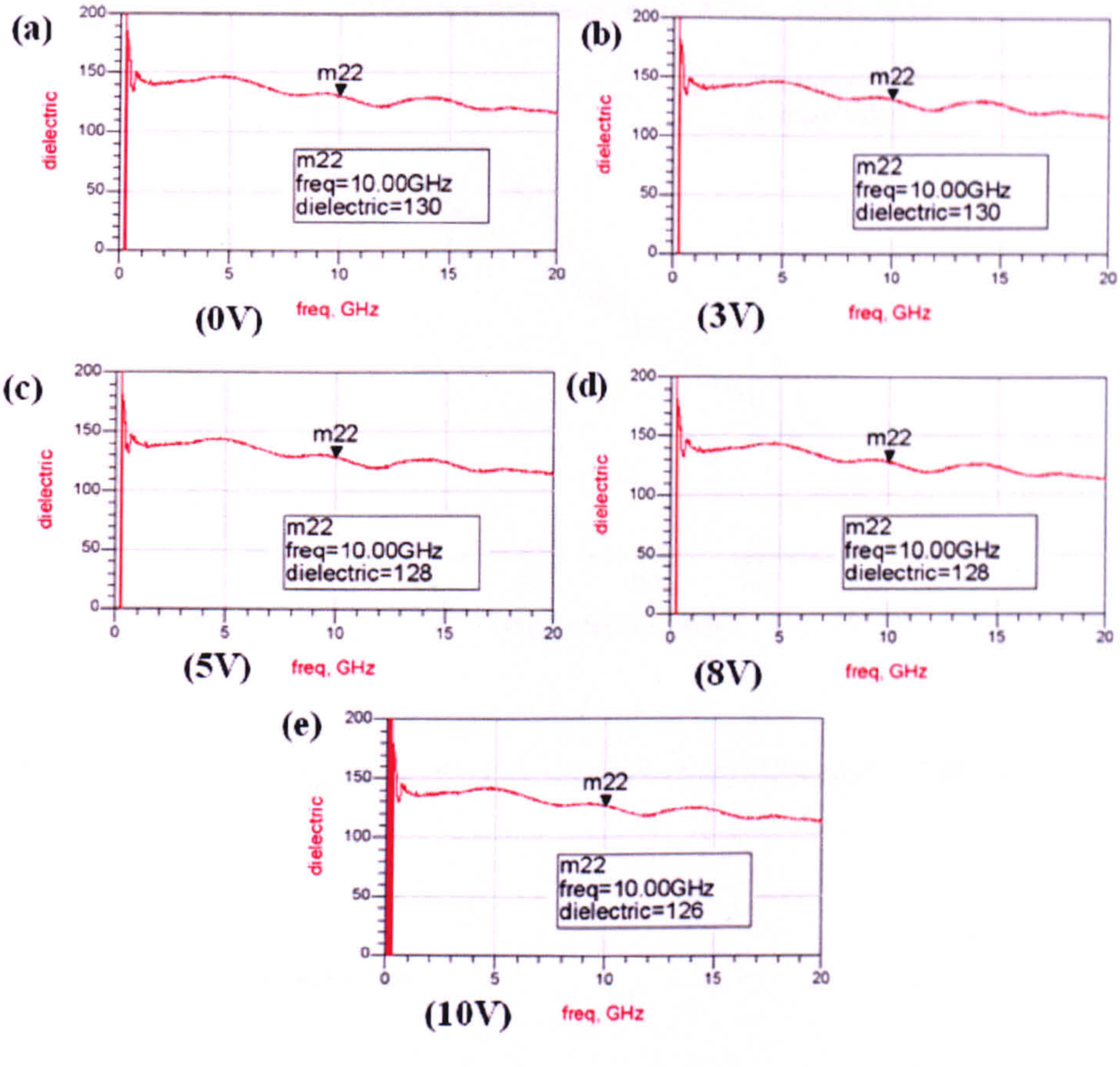

Figure 7.17 measured dielectric constant between 0GHz and 20GHz with a tuning DC voltage of 0V (a), 3V (b), 5V (c), 8V (d) and 10V(e).

The decrease in the dielectric constant with respect to the applied DC electric field is shown in figure 7.18. Because there are only five measurement points, the averaged results of the measurement are also displayed in this figure. The measured dielectric constants could be overestimated by 30% due to the overestimation of the capacitor size.

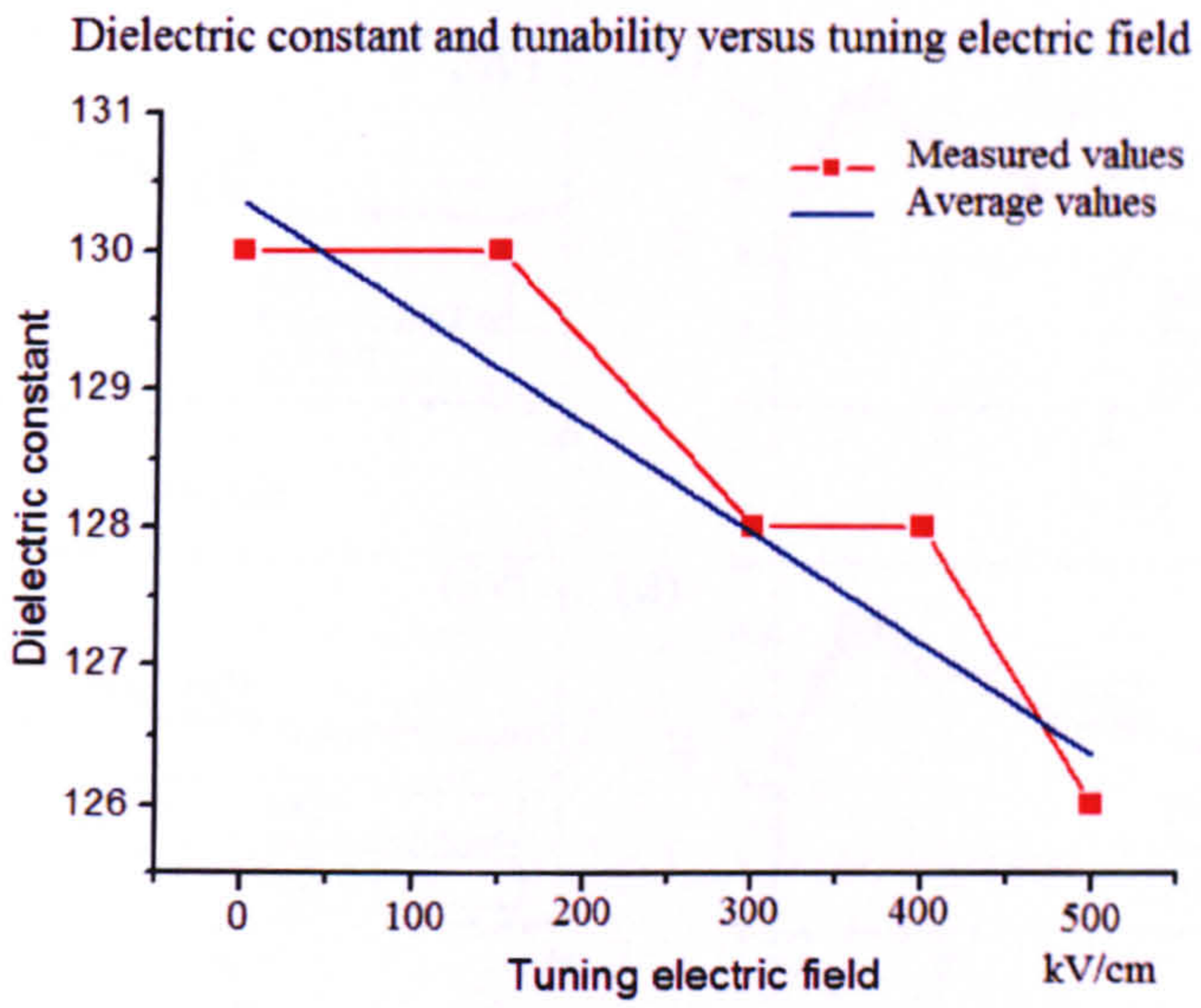

Figure 7.18 the dielectric constant versus tuning electric field from 0 to 500kV/cm

Quality factor and dielectric loss

The capacitor quality factors, for different DC voltages, measured between 0GHz and 20GHz, are shown in figure 7.19. In all of the figures, the measured quality factors rises sharply from 0GHz to 3GHz and subsequently decreases as the frequency goes up to 10GHz. The variations of quality factors at lower GHz were explained in chapter 5.2. The intrinsic capacitance is small and so its impedance ($\frac{1}{j\omega C_{int}}$) is very large at lower GHz. Therefore, the measured capacitor behaves like an open circuit. A small measurement error can affect the measured results (quality factor) significantly. The measured quality factors stabilized between 10GHz and 20GHz. In this case, the quality factors of the capacitor with different DC voltages are compared at 10GHz. As the tuning voltage increases from 0V to 10V, the quality factor at 10GHz increases slightly from 8.9 to 9.1. This indicates a small enhancement of overall electrical performance of the capacitor with higher DC voltages.

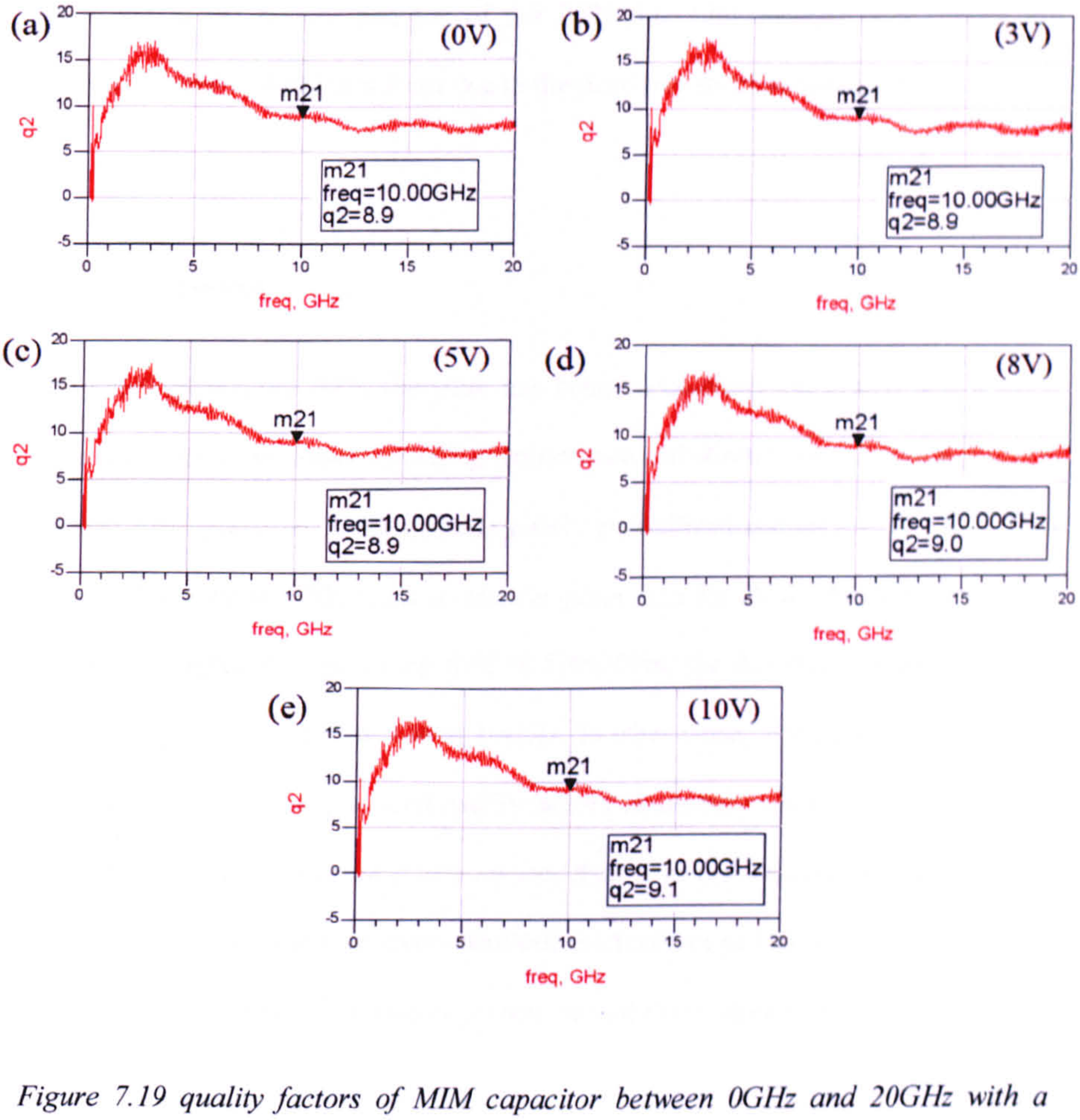

Figure 7.19 quality factors of MIM capacitor between 0GHz and 20GHz with a tuning voltage of (a) 0V, (b) 3V, (c) 5V, (d) 8V and (e) 10V.

The dielectric losses of the BZN thin films are roughly estimated as $tan_\delta = \frac{1}{Q}$ where Q is the quality factor shown in the above figure. The estimated dielectric losses of BZN thin films are 0.112, 0.112, 0.112, 0.111 and 0.109 for 0V, 3V, 5V8V and 10V, respectively. The dielectric loss of the thin film decreased slightly from 0.112 to 0.109 as the tuning voltages increases from 0V to 10V.

Figure 7.19 also shows that the measured dielectric losses are actually much higher than the expectation. The measured loss of BZN film is even higher than ferroelectric BST thin (0.075 at 10GHz and 0V given in chapter 5). This unexpected high dielectric loss are attributed to (a) large conductor loss caused by thin (120nm) metal

electrodes at the bottom and top of the BZN thin film and (b) poor crystal and microstructures of BZN thin films due to the relatively short annealing process.

7.5.4 Conclusion

The cubic pyrochlore BZN thin film has been successfully integrated into a MIM capacitor. Due to the lower annealing temperature and shorter crystallization process, the thin film grown on Au/quartz was poorly crystallized compare to the BZN film deposited on quartz. This leads to smaller grain size for BZN film with Au/quartz substrate. Despite of large tuning field of 500kV/cm, the dielectric constant of BZN changes slightly from 130 to 126 at 10GHz. In other word, a tunability of just 3.0% has been achieved. The measured quality factors varies between 8.9 (10GHz 0V) and 9.1 (10GHz 10V) which are much smaller than previous reports. The low quality factor should be attributed to metal electrode thickness of just 120nm. This could lead to large Ohmic losses, which causes greater overall microwave loss.

7.6 Overall summary

In this work, cubic pyrochlore $Bi_{1.5}Zn_{1.0}Nb_{1.5}O_7$ thin films were successfully synthesized by using a modified sol gel (chelation) method. To study the effects of annealing temperatures, cubic pyrochlore BZN thin films were crystallized at varies temperatures between 500 °C and 800 °C. Their crystal and microstructures are analyzed by XRD and SEM techniques. According to XRD results, all BZN thin films exhibit pure cubic pyrochlore structure despite the variations in annealing temperatures. It is believed that the thin film is fully crystallized at 800°C .

Cubic pyrochlore BZN thin films were also deposited onto different kinds of substrates to study the influence of substrates. According to XRD analysis, BZN thin films with different substrates have slightly different crystal growth orientations. It

was also observed that the grain size of BZN thin films varies significantly depending on different substrates. The microwave dielectric properties of BZN thin film on a sapphire substrate were measured by using CPWs. The measured dielectric constant of BZN thin film on sapphire substrate is 140 (0V) at 10GHz, which is less than half of the dielectric constant of the (1mol%) Li doped BST thin film reported in chapter 6. It was also found that the thin film shows no dielectric tunability despite a tuning electric field of 15kV/cm being applied. Therefore, cubic pyrochlore thin films (BZN) are not suitable for implementing planar microwave devices such as CPW.

On the other hand, BZN thin film was also characterized using the MIM capacitor. The tuning electric field within the capacitor is far greater than the electric field in the CPW so that a higher dielectric tunability can be achieved. Since the bottom electrode of the MIM capacitor is made of 120nm thick gold metal, the annealing temperature is lowered to 700°C. According to figure 8.17, some of the X-ray diffraction peaks (400, 440, 622) of the BZN thin film annealed at 700°C are not observed. This indicates poor crystallization in BZN thin film. Meanwhile, the grain size of BZN thin films determined by AFM images is also reduced.

The measured dielectric constant is 130.0 at10GHz (0V). Under a tuning field of 500KV/cm, the dielectric constant was reduced to 126.0, a tunability of just 3.0%. This small tunability is not useful for making microwave tunable devices. To further increase the tunability of the thin film, a greater DC voltage is required. However, higher electric field obtained by using higher DC voltage isn't comparable with MMIC. This makes BZN thin film unattractive to be integrated into a MMIC that operated at lower DC voltage.

References:

[1] H. Wang, X. Yao and M. L. Zhang, "Effect of Ca substitution on structure and dielectric properties of bismuth-based microwave ceramics," *J Electronceram,* vol. 21, 1- 4, 461-464 ,2008.

[2] S. Okaura and H. Funakuba, "Low strain sensitivity of the dielectric properties of pyrochlore Bi-Zn-Nb-O films," *Applied Physics Letters,* vol. 92, 18, 18290, 2008.

[3] J. W. Lu, S. Stemmer and J. Park, "Microwave dielectric properties of tunable capacitors employing bismuth zinc niobate thin films," *J Appl Phys,* vol. 97, 084110, 2005.

[4] C. A. Randall, R. L. Thayer, "Medium permittivity Bismuth Zinc Niobate thin film capacitors," *J Appl Phys,* vol . 94, 3, 1941-1947, 2003.

[5] M. Paranthaman, K. Salama and M. S. Bhuiyan, "Solution-derived textured oxide thin films-a review," *Supercond.Sci.Technol,* vol. 19, R1, 2006.

[6] W. Y. Fu, L. Z. Cao, S. F. Wang and Q. Wang , "C-axial oriented $(Bi_{1.5}Zn_{0.5})(Zn_{1.0}Nb_{1.5})O_7$ thin film grown on Nb doped SrTiO3 substrate by pulsed laser deposition," *J Phys. D: Appl. Phys,* vol. 40, 1460, 2007.

[7] J. J. Choi, J. H. Jang, *et al* ," Electrical properties of Lead Zinc Niobate-Lead Zirconate Titanate thick films formed by aerosol deposition process", *Solid State Phenomena,* vol.124-126, 169-172, 2007.

[8] G. E. Ponchak, "RF transmission lines on silicon substrates", *Microwave Conference , 2pth European* , 158-161,1999.

[9] J. W. Lu, J. Park, S. Stemmer and R. A. York, "Microwave Planar capacitors Employing Low Loss, High-K, and Tunable BZN Thin Films", *IEEE MTT-S International Microwave Symosium*, vol. 2, 607-610, 2005.

Chapter 8: Conclusion and suggested future work

In this thesis, three types of dielectric tunable thin films including: Co doped BST ($Ba_{0.5}Sr_{0.5}Ti_{0.5}O_3$), Li doped BST ($Ba_{0.5}Sr_{0.5}Ti_{0.5}O_3$) and pyrochlore BZN ($Bi_{1.5}Zn_{1.0}Nb_{1.5}O_7$) thin films were successfully synthesized using a chemical solution deposition (CSD) method. The synthesized thin films were characterized by numerous techniques including XRD, SEM, AFM, XPS and EDX. The dielectric properties of the thin films were characterized by measuring the response of coplanar waveguide (CPW) and metal insulated metal (MIM) capacitors which were fabricated on the surface of the thin films.

8.1 Conclusions

Several conclusions can be made based on the measured dielectric results of the BST and BZN thin films.

1) **Li doped BST thin film is more attractive for implementing microwave devices than Co doped BST:** The dielectric properties of ferroelectric BST materials can be improved by doping acceptor ions including Co and Li ions. However, the Li doped BST thin film is a more attractive candidate for implementing tuneable microwave devices than the Co doped BST. Table 8.1 compares the dielectric properties of Li and Co doped BST thin films.

(a)

Sample names	Dielectric constant (0V)	Dielectric constant (30V)	Dielectric tunability In %	Dielectric loss (0V)	Dielectric Loss (30V)
BSTC0	415	343	16.5%	0.176	0.157
BSTC1	251	227	9.2%	0.054	0.048
BSTC2	183	160	12.3%	0.043	0.038
BSTC5	212	206	3.8%	0.069	0.07

(b)

Sample names	Dielectric constant (0V)	Dielectric constant (30V)	Dielectric tunability In %	Dielectric loss (0V)	Dielectric Loss (30V)
BSTL0	278	196	30%	0.0623	0.064
BSTL1	317	263	17%	0.048	0.047
BSTL2	303	256	16%	0.051	0.048
BSTL 4	369	315	15%	0.083	0.081

Table 8.1 the dielectric properties of (a) Co doped BST thin films and (b) Li doped BST thin films.

According to the table 8.1, both Li and Co doped BST thin films have their advantages and disadvantages. The Li doped BST (BSTL1 and BSTL2) have greater tunability and dielectric constant than the BST thin films doped with Co ions (BSTC1 and BSTC2). In contrast, BST doped with Co (BSTC2) has the lowest dielectric loss (0.043(0V) and 0.038 (30V)) than all other thin films. However, the improvement in BST's dielectric loss is at the cost of dielectric constant and tunability. BSTC2 also has the lowest dielectric constant and tunability of 12.3%. This makes Co doped BST unsuitable for implementing microwave tunable devices that are integrated in a microchip such as CMOS, since a larger device or higher tuning DC voltage is required to achieve a large phase shift and high tunability. The most likely applications for Co doped BST thin films are areas that have less constraints on space and operation voltages, and are highly sensitive to microwave losses. For example, a phase shifter could be made of a cascade of tuneable MIM capacitors where a large tuning electric field can be built with a very small DC voltage.

On the other hand, Li doped BST films show a decrease in dielectric loss from 0.0623 (undoped, 0V) to 0.051 (2mol% doped, 0V), while the measured dielectric constant also increases from 278 to 303 as the Li concentration was increased from 0mol% to 2mol%. In other words, there is no compromise of dielectric constant in Li doped BST thin films. This unique feature is particularly important for the miniaturization of tuneable microwave devices.

2) **BZN thin film can not be considered as a real alternative to the traditional BST:** Pyrochlore BZN cannot be considered as a real alternative to the tuneable ferroelectric BST material, because their poor dielectric tunability and dielectric constant. As mentioned in section 7.53, a tunability of only 3.0% has been achieved by applying a DC electric field of 500kV/cm, while the dielectric tunability of the undoped BST with a tuning field of 15kV/cm is 14%. This tunability is too small to be used to implement any practical tunable microwave devices. To achieve a bigger tunability, a much higher DC tuning voltage is required which drives up the power consumption in the device. In addition, the dielectric constant of BZN thin films measured from CPW (140 at 10GHz and 0V) and MIM capacitor (130 at 10GHz and 0V) methods are still smaller than that of BST's. Therefore, the size of a microwave device made of BZN thin films will be relatively large. Pyrochlore BZN material should be considered as an alternative to the traditional high dielectric materials such as TiO_2 and SiO_2. The real application of BZN thin film is to implement fixed bandwidth microwave devices on a PCB.

8.2 Unsolved problems and solutions

As discussed in chapters 4, 5, 6 and 7, the measured dielectric results contain large errors which are caused by the TRL calibration and the metal conductors of the

measured devices. The following improvements need to be made to improve the characterizations of the thin films.

1) **Reducing conductor loss:** The biggest unsolved problem is the low quality factors of the MIM capacitors. As mentioned in chapter 5, the top and bottom electrodes have a significant influence on the microwave energy loss in the capacitor. In this work, the thickness of metal electrodes is just 140nm, which results in a large ohmic loss and so leads to an overestimation of the microwave loss in the MIM capacitor. In future work, the capacitor's electrodes should be made from thicker metal layers (>1um). The increase of the conductor thickness in CPW can also reduce the skin effect which is related to the conductor loss of the CPW.

2) **Improvement on the error analysis:** The measured dielectric properties are strongly affected by the TRL calibration process. Because there has been no report on the TRL calibration errors, it is difficult to calculate the errors in the measured dielectric properties. In this case, the errors in the measured dielectric constant and dielectric loss of the thin films are estimated by comparison. In future work, a mathematical model should be built to analyse the errors in the measured dielectric results, which provide more accurate dielectric results.

3) **Improving the repeatability:** The third unsolved problem is the repeatability of the thin film synthesis method (chelation). To avoid the degrading of the organic precursor over a period of time, the synthesized organic precursors should be coated onto the substrate immediately after the precursor is prepared. In addition, the prepared precursor should be stored in a controlled environment which prevents the degradation of organic precursor.

8.3 Future work

Although significant improvement has been achieved in Li doped BST thin films, much of these results were achieved based on sapphire substrates and high annealing temperatures (800°C) which are incompatible with the manufacturing processes of the microchips. In the long term, it is also important to integrate Li doped BST thin films with a commercial MMIC. This will help to demonstrate the viability of using BST thin film technology to develop affordable microwave electronic circuits in the future.